THE DEVELOPMENT OF HYDROGEL MICROFIBER SCAFFOLDS FOR PERIPHERAL NERVE REPAIR

By

Brian P. Ginn

A dissertation submitted to Johns Hopkins University in conformity with the requirements for the degree of Doctor of Philosophy

Baltimore, Maryland

August 2017

Abstract

This thesis provides a description of the development of electrospun hydrogel fiber strings, fiber sheets, and fiber tubes by characterizing their property changes with variations in spinning properties such as collector rotation speed, solution concentrations, and crosslinking conditions, for biologically derived materials such as alginate, fibrin, collagen, and hyaluronic acid. The basic, as spun, fibers were applied to several clinical applications including guidance of axons and Schwann cell outgrowth in peripheral nerve repair using fibrin and collagen fibers, where guidance by the collagen fiber sheets improved neurite outgrowth by 2.5 mm over 14 days compared to anisotropic collagen gels; alignment and maturation of cardiomyocytes, adipose-tissue derived stem cells (ASCs), and microvessel network formation in cardiac patches composed of fibrin; skeletal muscle implants formed through use of porous fibrin generated by removing co-spun alginate via sodium citrate treatment; and fibrin fiber-based vascular grafts to demonstrate the versatility and utility of the material for enhancing ECM deposition from vascular cell types and perfusibility. These hydrogel fibers were then modified to serve as growth factor delivery vehicles to enhance cellular interaction and provide the topographical guidance to promote neurite outgrowth for improving peripheral nerve regeneration through local release of GDNF. A robust protective nerve guide outer conduit, to serve as a carrier for hydrogel fibers, was developed in collaboration with a corporate partner, the Secant Group (Telford, PA, USA) using poly(glycolic acid) (PGA) braided tubes that were coated with a biodegradable elastomer, poly(glycerol sebacate) (PGS). The fibrin-loaded PGA/PGS conduits were implanted in a rat sciatic nerve defect model to assess their effect on nerve regeneration, the local inflammatory microenvironment, and improvement in coated tube mechanical properties to ease surgical handling of the guide. PGS-coated conduits improved the M2/M1 macrophage ratio and improved action potential amplitudes compared to the uncoated nerve guide group. In addition, PGS-coated conduits containing electrospun fibrin hydrogel fibers and collagen fibers with uniform and gradient presentation of loaded neurotrophic factor were evaluated in a rat sciatic defect model to determine the potential feasibility of hydrogel fibers for peripheral nerve repair. Nerve guide groups containing collagen fiber sheets showed high permissivity of cells through the aligned hydrogel structure. These studies demonstrate the broad potential and unique properties of the hydrogel fibers for regenerative engineering applications.

Readers:

Hai-Quan Mao, Ph.D. (Advisor)

Sharon Gerecht, Ph.D.

Defense Committee:

Hai-Quan Mao, Ph.D. (Advisor)

Ahmet Höke, M.D., Ph.D.

Kalina Hristova, Ph.D.

Sharon Gerecht, Ph.D.

Honggang Cui, Ph.D.

Acknowledgments

Research and development of innovative engineered products requires the interaction with, and contribution of ideas from, many people. This Ph.D., in particular, was primarily focused on the generation of new electrospun materials technologies and engineering products for use in many tissue engineering applications including: peripheral nerve guides, cardiac patches, vascular grafts, therapeutic delivery systems, ocular patches, liver regeneration scaffolds, and the development of a plethora of tools and methods to quickly prototype solutions to other potential needs and problems as they arise. Out of the many people who helped along the way, the first and foremost person I would like to thank is Dr. Hai-Quan Mao for allowing me to join his lab effectively as a walk-on whose only relevant background was Mrs. Geesman's 9th grade biology from before the human genome was fully sequenced and some experience with biological coatings while working in the orthopaedics industry prior to starting a master's at JHU. Dr. Mao gave me a fair opportunity to develop my skills as I caught up with the field of tissue engineering, developed my soft materials science knowledge, and learned many new lab techniques. I would particularly like to thank Dr. Mao for giving me way too much freedom in determining my own workflow and projects during my Ph.D. studies. Both Dr. Mao and I were awful at saying no to projects and collaborations, which made my six years at Hopkins incredibly stressful, but I wouldn't have learned nearly as much during my time here if this weren't the case.

There are several people I'd like to thank from before my time at Johns Hopkins while I was working DePuy Orthopaedics (now DePuy Synthes). Jim Smous helped coordinate a position for me at DePuy in R&D that allowed me to escape the nightmare

year I had stuck in limbo trying to find employment after graduating from Purdue University directly into the Great Recession of 2008. I want to thank Craig Ernsberger for his patience as my engineering skills transitioned from the theoretical style of problem solving that plagues undergraduate thinking to a more practical based thought process that proved to be invaluable during my Ph.D. studies. Dr. Weidong Tong took me under his wing while at DePuy and was a great mentor during my time there and taught me, along with Craig, that sometimes when you need to determine the adhesion of something, to just throw it on the ground. Lastly from DePuy I'd like to thank Dr. Jason Langhorn for his constant willingness to help me solve practical problems that arose in my labwork there and for being the only other one there that would get excited when it was World Cup time.

I'd like to thank the fellow Mao lab members that served in the trenches with me during my time in the lab. Dr. Russ Martin has been a great person to go to for advice and was always willing to share his experiences of his Ph.D. process at Hopkins, which was very helpful for my own preparation for big milestones such as the thesis proposal and dissertation. Dr. Kellin Krick and Dr. Jose Roman were always great sounding boards for more outlandish ideas and were great resources for getting BME perspectives on potential solutions. Dr. Markus Tammia helped jumpstart my skill acquisition early on in my Ph.D. research with anything related to cells or immunostaining and was an incredible source of knowledge on anything related to Schwann cells and peripheral nerves. Dr. Herdeline Ann Ardoña was consistently one of my favorite people to talk engineering shop with during my Ph.D. and I look forward to seeing the great things she does as a PI in a few years. I'll always look back fondly on the horribly doomed "electrospinning boat" method that we attempted to electrospin some of her self-assembling peptides at one point.

The undergraduates I had the pleasure of mentoring were all great troopers with their willingness to put up with any electrospinning tasks they were delegated. I want to give special thanks to Brook Jeang who was the first undergraduate student I mentored. Brook was incredibly helpful during the early to middle stages of the project where there was still a lot of flux in the spinning processes for many of the materials that were standardized by the end of this Ph.D. She helped to push forward potential modification methods of the fibrin fibers with her research into heparinization of the material and the subsequent release of growth factors during her senior design and master's work. It was fantastic seeing her develop from a highly dependent undergraduate student researcher to one able to independently determine what important experiments needed to be run to test her own independent hypotheses. Lucy Li helped to advance some of the later fibrin fiber bundle spinning work during her time in the lab. Zachary Olah helped with the fibrin and collagen fiber sheet development. Haoze Duan was a great help with his production of alginate sheets for liver regeneration projects.

The postdocs in the lab were always a great help and I want to thank Dr. Shuming Zhang for the training he provided me in the electrospun hydrogel platform he initially developed and the trust he placed in me to carry the technique forward as his successor. Dr. Huanhuan Liu was instrumental in the characterization of macrophage response results in Chapter 4 with the PGS coated materials and Dr. Jisuk Choi was of great assistance during the pilot PGS experiments with Schwann cell adhesion on the coating. Dr. Xiaowei Li was an indispensable source of knowledge on soft hydrogel materials and neural stem cell biology and provided much of the early cell training I received early in my Ph.D. Of all the postdocs, I want to give greatest thanks to Dr. Xuesong Jiang who had the unfortunate pleasure to sit directly behind me in lab and surely came to dread the sound of my chair spinning around followed by “Hey Xuesong…” with whatever random idea I had at the moment.

A key cornerstone of this Ph.D. are the collaborations that occurred and I want to thank all of those who placed their trust in the materials developed in this thesis for their own research. Dr. Sebastian Barreto-Ortiz was one of the earliest adopters of the electrospun hydrogel materials with his use of electrospun fibrin fiber bundles for vascular applications and characterizing the deposition and orientation of ECM from vascular support cells. Dr. Pinar Huri and Jordie Gilbert-Honick utilized alginate-fibrin composite fiber bundles to tune mechanical properties and porosity for skeletal tissue engineering projects. Justin Morrissette-McAlmon has been the source of one of my favorite collaborations with our development of implantable cardiac patches that mimic the properties of heart myocardium using aligned fibrin fiber sheets. This collaboration is particularly special as it was initiated by the two of us bumping into each other one weekend leading to a conversation about the issues Justin was having using isotropic fibrin gels and was started without instigation by either of our respective PIs. Morgan Elliot has continued on collaboration that was started with Sebastian with her use of aligned fibrin fiber tubes as a perfusable vascular graft providing some of the most complex, challenging, and fun engineering problems to solve during this Ph.D.

The nerve guide in vivo studies could not have happened without the support of several groups and I’d like to also thank them for their help during these studies. Our collaborators at the Secant Group including Dr. Peter Gabriele, Dr. Steven Lu, and Dr. Jeremy Harris have been incredibly supportive during the two major peripheral nerve guide animal studies that were done as part of this Ph.D. The assistance of the lab of Dr. Ahmet Hoke was invaluable to the first implantable PGS nerve guide study and I want to thank Dr. Ruifa Mi for his eagerness to help with the surgeries and data collection, as the study would not have been possible without his help. I also want to thank all the people who helped with the second nerve guide study at SYSU in the lab of Dr. Zhu, particularly Shuai for his willingness to perform the surgeries on a huge number of animals to test so many nerve guides. I want to thank Dr. Mao, Dr. Hoke, Dr. Gerecht, Dr. Cui, and Dr. Histrova for their help serving on my defense committee.

Most importantly I want to thank my family for their support during the six years of my Ph.D. study and through all the trials and tribulations I've had to go through to get to this point. My parents were both incredibly patient to put up with an excessive number of SkypaP calls during my Ph.D. whose sole purpose was to see whatever our two dogs, Mackey and Meili, were doing while I was going through data, looking up papers at home, eating dinner, etc. My little sissy has constantly forced me to keep pushing myself forward to keep up with her ever since we were little guppies to avoid her gaining the clear status of 'I win' and I want to thank her for doing that even though she has already won!

Table of Contents

Chapter 1 Hydrogels and Topographical Alignment Cues in Tissue Engineering……………………………………………………………………………1

1.1 Tissue engineering……………………………………………………………..1
1.2 Hydrogels and the native extracellular matrix.. 4
1.3 Structural anisotropy in biological tissues………………………………………10
1.4 Topographical and neurotrophic guidance for nerve repair................................ 12
1.5 Peripheral nerve regeneration and current clinical repair options………………15
1.6 Electrospun hydrogel microfibers……………………………………………… 17
1.7 Study design……………………………………………………………………. 18
1.8 Conclusion………………………………………………………………………19
1.9 Figures…………………………………………………………………………..20
1.10 References……………………………………………………………………… 26

Chapter 2 Development and Modification of Fibrin, Collagen, Alginate, and Other Hydrogel Microfibers…………………………………………………………... 34

2.1 Background…………………………………………………………………….. 34
  2.1.1 Alginate as a hydrogel material……………………………………………..34
  2.1.2 Fibrin as a tissue engineering material and physiological role…………….. 35
  2.1.3 Collagen as a tissue engineering material and physiological role…………..37
  2.1.4 Hyaluronic acid as a tissue engineering material and physiological role…...39
2.2 Methods………………………………………………………………………… 40
  2.2.1 Alginate hydrogel fiber spinning……………………………………………40
  2.2.2 Fibrin hydrogel fiber spinning………………………………………………42
  2.2.3 Collagen hydrogel fiber spinning…………………………………………... 44
  2.2.4 Gelatin hydrogel fiber spinning……………………………………………..46

2.2.5 Hyaluronic acid hydrogel fiber spinning……………………………………47

2.2.6 Synthetic 3D microfiber bundle spinning – PLGA…………………………48

2.2.7 Mechanical property testing of electrospun hydrogel fibers………………..49

2.2.8 Optical transparency measurements of electrospun hydrogel fiber sheets….50

2.2.9 Graded ethanol drying and lyophilization of fibrin fiber tubes for vascular graft preparation……………………………………………………………………. 51

2.3 Results and Discussion……………………………………………………….52

2.3.1 Effect of biological material type on mechanical properties………………..52

2.3.2 Precursor solution weight % effect on fiber strength………………………. 53

2.3.3 Effect of additional strain on fibrin fiber mechanical properties…………... 54

2.3.4 Collector rotation speed effect on resultant dry alginate fiber diameter…… 55

2.3.5 Effect of flow rate on diameter of short duration alginate fiber spins……... 56

2.3.6 Effect of PEO and PVA composition on diameter of one-minute alginate fiber spins…………………………………………………………………….... 58

2.3.7 Alginate as a porogen: effect on fibrin fiber mechanical properties……….. 59

2.3.8 Effect of total spin time on fibrin fiber diameter and swelling…………….. 60

2.3.9 Effect of flow rate at constant spin time on fibrin filament diameter…….... 61

2.3.10 Effect of spin time at constant flow rate on fibrin filament diameter……… 62

2.3.11 Effect of drying method on fibrin tube mechanical properties…………….. 63

2.3.12 FXIII treatment effect on fibrin tube mechanical properties………………..64

2.3.13 Layering and drying processing effect on fibrin tube stability and cracking. 65

2.3.14 Comparison of fibrin fiber diameters holding total mass flow constant…… 66

2.3.15 Swelling ratios of fibrin and collagen fibers during rehydration…………... 68

2.3.16 Rehydration of alginate, fibrin, and collagen fibers with time……………...69

2.3.17 Degradation of alginate and fibrin fibers……………………………….... 71

2.3.18 Effect of landing position of fiber jet during sheet formation………………72

2.3.19 Optical properties of electrospun hydrogel fibers………………………….. 74

2.3.20 Spinning of synthetic PLGA fiber bundles………………………………… 75

2.4 Conclusions…………………………………………………………………….. 76

2.5 Figures…………………………………………………………………………..77

2.6 References…………………………………………………………………….. 106

Chapter 3 Cellular Organizational and Migratory Effects using Aligned Hydrogel Microfibers and Neurotrophic Cues In Vitro…………………………… 109

3.1 Background…………………………………………………………………… 109

3.1.1 Interaction of cells with extracellular matrix…………………………….... 109

3.1.2 Topographical and neurotrophic guidance cues…………………………...110

3.1.3 Cardiac tissue engineering…………………………………………………111

3.1.4 Vascular graft engineering……………………………………………….... 112

3.1.5 Skeletal muscle tissue engineering………………………………………...114

3.2 Methods………………………………………………………………………..114

3.2.1 Spreading of primary Schwann cells along fibrin and collagen fiber sheets……………………………………………………………………… 114

3.2.2 Neurite extension from DRG explant as function of fiber alignment…….. 115

3.2.3 Outgrowth of neurites from DRG explants on uniformly loaded GDNF collagen fiber sheets……………………………………………………….116

3.2.4 Consumption of free amines during collagen fiber sheet formation………117

3.2.5 Release of GDNF from heparinized collagen fiber sheets..................... 118

3.2.6 Effect of fibrin fiber sheet heparinization on neural stem cell spreading and FITC-lysozyme release.. 119

3.2.7 Physical loading and release of FITC-lysozyme from fibrin and alginate fibers.. 120

3.2.8 In situ spinning of live cells during formation of electrospun hydrogel fibers.. 121

3.2.9 Fibrin cardiac patch spinning.. 122

3.2.10 Fibrin fiber sheet alignment effects on microvessel formation and cardiac cell alignment.. 125

3.2.11 Electrospun hydrogel fibrin fiber bundles and tubes for generation of vascular grafts... 126

3.3 Results and Discussion.. 129

3.3.1 Spreading of primary Schwann cells on fibrin and collagen fiber sheets... 129

3.3.2 Neurite extension from DRG explant as function of fiber alignment........ 130

3.3.3 Outgrowth of neurites from DRG explants on uniformly loaded GDNF collagen fiber sheets.. 131

3.3.4 Consumption of free amines during collagen fiber sheet formation......... 132

3.3.5 Release of GDNF from heparinized collagen fiber sheets..................... 133

3.3.6 Effect of fibrin fiber sheet heparinization on neural stem cell spreading and FITC-lysozyme release.. 135

3.3.7 Physical loading and release of FITC-lysozyme from fibrin and alginate fibers.. 136

3.3.8 In situ spinning of live cells during formation of electrospun hydrogel fibers.. 137

3.3.9 Fibrin fiber sheet alignment effects on microvessel formation and cardiac cell alignment……………………………………………………………….. 139

3.3.10 Electrospun hydrogel fibrin fiber bundles and tube for engineered vascular grafts…………………………………………………………………….140

3.4 Conclusions………………………………………………………………… 143

3.5 Figures……………………………………………………………………… 145

3.6 References………………………………………………………………….. 167

Chapter 4 Poly(glycerol sebacate) (PGS) Coated Braided poly(glycolic acid) (PGA) Nerve Guides……………………………………………………………….. 170

4.1 Background………………………………………………………………… 170

4.1.1 Academic nerve guide designs…………………………………………….170

4.1.2 PGS coatings……………………………………………………………… 171

4.1.3 Role of macrophages in nerve regeneration……………………………….172

4.2 Methods……………………………………………………………………..173

4.2.1 Macrophage isolation and culture for PGS contact effect on differentiation…………………………………………………………... 173

4.2.2 Effect of PGS degradation product on macrophage phenotype…………... 173

4.2.3 Preparation of PGS coated braided PGA conduits and glass coverslips…..174

4.2.4 Nerve guide preparation…………………………………………………... 175

4.2.5 Outgrowth of neural stem cells as function of fiber filler density and luminal filler preparation for nerve guide usage…………………………………... 176

4.2.6 In vivo sciatic nerve critical gap defect animal model…………………….178

4.2.7 Presence of autophagy in nerve guide groups……………………………..178

4.2.8 Foot angle of inclination and characterization of atrophy…………………179

4.2.9 Electrophysiological assessment of functional recovery using Secant PGS nerve guide..... 179

4.2.10 Histological analysis of axon and myelination characteristics.....180

4.2.11 Immunofluorescence imaging..... 180

4.2.12 In vivo inflammatory response.....181

4.3 Results and Discussion.....182

4.3.1 Attachment of BMDM to PGS.....182

4.3.2 PGS coating effect on BMDMs in M1 differentiation media..... 182

4.3.3 Effect of PGS degradation product on macrophage differentiation and viability in vitro..... 183

4.3.4 Outgrowth of neural stem cells as function of Secant collagen fiber density..... 184

4.3.5 Presence of autophagy in nerve guide groups..... 185

4.3.6 Foot angle of inclination and characterization of atrophy.....186

4.3.7 Onset latency measurements..... 186

4.3.8 Peak latency measurements.....187

4.3.9 Action potential amplitudes.....188

4.3.10 Histological analysis of axon and myelination characteristics.....189

4.3.11 Secant PGS braided tube in vivo macrophage response..... 191

4.3.12 Pro-inflammatory M1 macrophage population..... 193

4.3.13 Pro-regenerative M2 macrophage population..... 195

4.3.14 Comparative M1 and M2 macrophage populations..... 198

4.4 Conclusions..... 199

4.5 Figures……………………………………………………………………201

4.6 References…………………………………………………………………..247

Chapter 5 In Vivo Study of Fibrin-Collagen Hydrogel Fiber Based Nerve Guides to Promote Peripheral Nerve Regeneration………………………………………… 249

5.1 Background………………………………………………………………… 249

5.1.1 Use of fibrin and collagen in nerve guide design………………………….249

5.1.2 Gradient platform modification and development………………………... 250

5.2 Methods…………………………………………………………………..251

5.2.1 Rat sciatic nerve defect repair model and study overview using electrospun hydrogel microfibers…………………………………………………… 251

5.2.2 Preparation and growth factor loading of fibrin-collagen composite nerve guides…………………………………………………………………252

5.2.3 Hydrogel fiber loading into PGS coated nerve guide luminal space........... 253

5.2.4 Examination of implanted nerve guides following 8 weeks implantation... 255

5.2.5 Functional recovery assessment………………………………………... 256

5.2.6 Gait analysis using Sciatic Functional Index (SFI) after 8 weeks implantation………………………………………………………………..256

5.2.7 Histological analysis of implanted nerve guides after 8 weeks implantation………………………………………………………………..257

5.3 Results and Discussion……………………………………………………...257

5.3.1 Gradient formation in collagen hydrogel fiber sheets……………………..257

5.3.2 Examination of explanted nerve guides following 8 weeks implantation…258

5.3.3 Gait analysis results after 8 weeks implantation………………………….. 259

5.3.4 Histological analysis of explanted nerve tissue after 8 weeks NGC implantation……..260

5.4 Conclusions……262

5.5 Figures……264

5.6 References…….. 278

Curriculum Vitae……...280

Page left intentional blank

Table of Figures

Figure 1-1: Electrospun hydrogel fiber generation. 20

Figure 1-2: Individual distinct fibers formed during electrospinning of alginate hydrogel microfibers 21

Figure 1-3: Fiber alignment is enhanced by hydrogel fiber spinning compared to isotropic cast gels. 22

Figure 1-4: Hydrogel fiber geometries that can be generated with the method.............. 23

Figure 1-5: Cells can directly interact and align with orientation of electrospun hydrogel fiber surfaces... 24

Figure 1-6: Improved mechanical properties of PGA multifilament braided tubes after PGS coating.. 25

Figure 2-1: Effect of biological material type on mechanical properties....................... 77

Figure 2-2: Mechanical properties of fibrin fibers increases as wt % of fibrinogen in precursor solution increases.. 78

Figure 2-3: Effect of additional strain on fibrin fiber strength...................................... 79

Figure 2-4: Increasing rotation speed of collection wheel reduced alginate fiber bundle diameter... 80

Figure 2-5: 1.5 wt% vs 0.75 wt% alginate fiber diameters after 15s spin time varying flow rate. 81

Figure 2-6: Effect of PEO composition on 1 wt% alginate fiber diameters after one-minute spins 82

Figure 2-7: Effect of PVA composition on 1 wt% alginate fiber diameters after one-minute spins. 83

Figure 2-8: Alginate lyase treatment of alginate-fibrin fiber composites increases porosity and reduces elastic modulus. 84

Figure 2-9: Fibrin bundle dry and rehydrated size as a function of spin time. 85

Figure 2-10: Flow rate effects on fibrin filament diameter 86

Figure 2-11: Small fibrin filament size as a function of spin time 87

Figure 2-12: Fibrin filament swelling at different spin times. 88

Figure 2-13: Drying treatment effect on fibrin fiber tube stiffness. 89

Figure 2-14: Factor XIII effect on fibrin tube stiffness. 90

Figure 2-15: Factor XIII effect on fibrin tube strain to failure 91

Figure 2-16: Factor XIII effect on fibrin tube ultimate tensile strength 92

Figure 2-17: Comparison of lyophilization and ethanol drying of fibrin tubes. 93

Figure 2-18: Cracking occurring in fibrin tube during drying 94

Figure 2-19: Application of mass flow constant to achieve similar fiber diameters with different spin conditions. 95

Figure 2-20: Swelling ratios of fibrin and collagen hydrogel fibers 96

Figure 2-21: Rapid rehydration of alginate, fibrin, and collagen hydrogel fibers. 97

Figure 2-22: Degradation of alginate fibers in alginate lyase, PBS, Schwann cell media, and DI water. 98

Figure 2-23: Fibrin fiber bundle degradation with plasmin treatment ranging from 0.1 CU/ml to 15 CU/ml. 99

Figure 2-24: Degradation of fibrin fiber sheets by DRG explant without addition of aprotinin. 100

Figure 2-25: Modifying fiber sheet width by changing landing position of fiber jet 101

Figure 2-26: Optical transparency properties of collagen and fibrin fiber sheets..........102

Figure 2-27: Effect of collagen fiber sheet thickness on optical properties..................103

Figure 2-28: Comparison of optical properties of collagen, AM membrane, and calcified cornea...104

Figure 2-29: 3D PLGA microfiber bundle spinning. 105

Figure 3-1: Measurement method of neurite outgrowth from DRG explant.................145

Figure 3-2: Capture of heparin in collagen fibers during spin. 146

Figure 3-3: Spreading of primary Schwann cells from spheroid over 6 days on electrospun collagen fiber sheets 147

Figure 3-4: Spreading of primary Schwann cells from spheroid over 6 days on electrospun fibrin fiber sheets. 148

Figure 3-5: Extension of neurites from DRG explants as a function of fiber alignment.149

Figure 3-6: Maximum neurite outgrowth and aspect ratio of outgrowth show Matrigel coating does not enhance untreated collagen fiber sheets. 150

Figure 3-7: Distribution of neurite outgrowth as a function of GDNF loading level on aligned collagen fiber sheets after seven days..151

Figure 3-8: Quantity of collagen free amines drastically depleted following electrospinning onto EDC-based crosslinking bath solution. 152

Figure 3-9: Release profiles of GDNF$_{488}$ from collagen hydrogel fiber sheets at different heparin levels...153

Figure 3-10: Burst and sustained release of GDNF$_{488}$ from collagen hydrogel fiber sheets at different heparin levels. 154

Figure 3-11: Outgrowth of NSC spheroids on fibrin and heparinized fibrin sheets after seven days. 155

Figure 3-12: Conjugation of EDC activated 0.1 wt % heparin solution to fibrin fiber sheet surface reduces release rate of FITC-lysozyme. 156

Figure 3-13: Physical loading of FITC-lysozyme *in situ* during alginate and fibrin fiber formation. 157

Figure 3-14: ASCs spun *in situ* within 0.4 wt% fibrin fibers are viable after four days culture. Schwann cells show minimal migration between fiber regions after one week. 158

Figure 3-15: Preparation of 6-layer fibrin fiber sheets for cardiac tissue engineering applications 159

Figure 3-16: Alignment of vasculature formed from different concentrations of HUVEC's co-cultured with ASCs on fibrin fiber sheets. 160

Figure 3-17: Vasculature formed from ECFCs co-cultured with ASCs on fibrin fiber sheets show high alignment and interconnectivity. 161

Figure 3-18: Vessel organizational differences on random fibrin gels and aligned fibrin hydrogel microfiber sheets 162

Figure 3-19: Cardiomyocyte culture on aligned fibrin fibers show striations indicating maturity is promoted by fiber sheets 163

Figure 3-20: Pericytes secrete several cell adhesive molecules and collagens along direction of alignment of 200+ μm diameter fibrin bundles after 5d culture. 164

Figure 3-21: Hollow vascular graft tubes made from aligned fibrin fiber hydrogel sheets. 165

Figure 3-22: Perfusable hollow fibrin fiber tube with longitudinal alignment as vascular graft in rat aortic replacement model. 166

Figure 4-1: Suture retention test for PGS coated and uncoated PGA multifilament braided tubes. 201

Figure 4-2: Coating of multifilament poly(glycolic acid) (PGA) braided tubes with poly(glycerol sebacate) (PGS). 202

Figure 4-3: Collagen fiber loading into PGS coated PGA braided tubes......................203

Figure 4-4: 25, 50, and 100% Secant collagen filament fill density within PGS coated nerve guide conduit. 204

Figure 4-5: Topographical guidance features of Secant collagen filaments 205

Figure 4-6: Poor attachment of BMDMs on PGS coated coverslips. 206

Figure 4-7: Healthy attachment of BMDMs and successful differentiation in absence of PGS coating. 207

Figure 4-8: Effect of PGS coating on M1 differentiation of BMDMs in vitro using different levels of M1 differentiation cytokines LPS and IFNγ. 208

Figure 4-9: Effect of PGS coating on M2 differentiation of BMDMs in vitro using different levels of M1 differentiation cytokines LPS and IFNγ. 209

Figure 4-10: PGS degradation product (DP) interferes with normal cell morphology an attachment on TCPS as concentration increases. 210

Figure 4-11: PGS degradation product (DP) reduces BMDM viability due to increased media acidity...211

Figure 4-12: Relative mRNA expression of M1 markers when BMDMs are exposed to PGS degradation product and M1 differentiation media 212

Figure 4-13: Relative mRNA expression of M2 markers when BMDMs are exposed to PGS degradation product and M2 differentiation media. 213

Figure 4-14: Differentiated neural stem cells show higher outgrowth as collagen fiber density decreases. 214

Figure 4-15: Increased incidence of autophagy in uncoated PGA braided nerve guides after implantation using rat sciatic nerve defect model. 215

Figure 4-16: Nerve guide groups show reduced mobility of ankle joint after three months compared to autograft and positive controls 216

Figure 4-17: Combined atrophy of gastrocnemius and soleus muscle is highest in uncoated PGA braided nerve guidance conduits. 217

Figure 4-18: Onset latency measurements of foot and ankle for all nerve guide groups after 12 weeks implantation in rat model. 218

Figure 4-19: Peak latency measurements of foot and ankle for all nerve guide groups after 12 weeks implantation in rat model 219

Figure 4-20: Action potential amplitudes of foot and ankle as % of control leg for all nerve guide groups after 12 weeks implantation in rat model..220

Figure 4-21: Representative mid-graft cross sections of nerve guide explants after three months. 221

Figure 4-22: Axon count per whole nerve cross section data. 222

Figure 4-23: Higher magnification images showing capillary formation within collagen fiber and vessel formation near PGA braid. 223

Figure 4-24: Average axon cross sectional area in nerve guide conduit and autograft after three months of nerve regeneration. 224

Figure 4-25: Calibers of axons with and without myelin layer inclusion for nerve guide groups and autograft...225
Figure 4-26: Higher magnitude histology of nerve guide groups and myelin...............226
Figure 4-27: Distribution of axon diameters for nerve guide groups and autograft........227
Figure 4-28: Myelin sheath g-ratio measurements..228
Figure 4-29: Distribution of g-ratios and axon diameters..229
Figure 4-30: Logarithmic fit of g-ratio - axon diameters distribution. 230
Figure 4-31: Total macrophage population in proximal and distal sections of nerve guide groups...231
Figure 4-32: Immunostaining of representative proximal and distal section sliced after 7d 232
Figure 4-33: Aggregate cellular infiltration into proximal and distal nerve stump regions. 233
Figure 4-34: Absolute macrophage infiltration into proximal and distal stumps. 234
Figure 4-35: M1 subpopulation of macrophages in proximal and distal regions. 235
Figure 4-36: Expression increase of iNOS after seven days in nerve guide groups. 236
Figure 4-37: Increase of iNOS expression in proximal regions after seven days...........237
Figure 4-38: ELISA of tissue homogenate to measure iNOS levels in proximal and distal nerve stumps...238
Figure 4-39: M1 macrophage marker mRNA expression of TNFα, CD86, and IL-1β after seven days. 239
Figure 4-40: Proximal and distal M1 macrophage marker mRNA expression for TNFα, CD86, and IL-1β. 240

Figure 4-41: Increased M2 subpopulation present in PGS coated nerve guide groups compared to uncoated NGCs. 241

Figure 4-42: Higher levels of ARG1 expressed in PGS coated nerve guides containing collagen fibers as measured by qPCR...242

Figure 4-43: ELISA of tissue homogenate to measure ARG1 levels in proximal and distal nerve stumps..243

Figure 4-44: M2 macrophage marker mRNA expression of CD206, IL-10, and PPARγ after seven days. 244

Figure 4-45: Proximal and distal M2 macrophage marker mRNA expression for CD206, IL-10, and PPARγ 245

Figure 4-46: Relative inflammatory environment of NGCs given by M2/M1 ratio. 246

Figure 5-1: SYSU *in vivo* rat sciatic nerve defect model animal study groups. 264

Figure 5-2: Loading of PGS coated braids with hydrogel fibers.................................265

Figure 5-3: Fill density of lumen cross section as a function of fibrin filament loading level for 40, 100, and 200 μm hydrated fibrin filaments 266

Figure 5-4a: Preparation of fibrin-collagen hydrogel fiber nerve guide. 267

Figure 5-4b: Preparation of fibrin-collagen hydrogel fiber nerve guide. 268

Figure 5-5: Diffusible gradient generation in collagen sheets utilizing modified Krick method...269

Figure 5-6: Testing of diffusible gradient generation in collagen fiber sheets using FITC-lysozyme. 270

Figure 5-7: Gross histological examination of fibrin filament containing groups after 8 and 12 weeks..271

Figure 5-8: Gross histological examination of PGS coating only and unloaded collagen sheet only groups after 8 weeks. 272

Figure 5-9: Sciatic functional index (SFI) results after 8 weeks NGC implantation. 273

Figure 5-10: Longitudinal sections of steep GDNF and no GDNF groups stained with Masson’s trichrome after 8 weeks. 274

Figure 5-11: Toludine blue stained while cross sections of PGS coating only and collagen fiber sheet only groups mid-graft after 8 weeks 275

Figure 5-12: High magnification images of myelinated axons in PGS coating only, autograft, and collagen fiber sheet only groups after 8 weeks. 276

Figure 5-13: Myelinated axon density and myelin sheath thickness for unfilled PGS coated PGA braid, autograft, and collagen fiber sheet only group after 8 weeks 277

Page left intentionally blank

Chapter 1 Hydrogels and Topographical Alignment Cues in Tissue Engineering

1.1 Tissue engineering

Modern tissue engineering is an excellent example of a rapidly evolving field that has developed as a result of the intersection of two previously unrelated fields of study, biomaterials science and cellular engineering, for solving tissue related medical problems with many advances in the field being made as a result of collaboration between surgeons and engineers. In essence, modern tissue engineering is focused on restoring or improving function though a combination of: 1) scaffold design, 2) cellular interactions between scaffolding and native tissue, and 3) the application of biological factors to enhance cellular response. Application of these three key design factors present the tissue engineer with the flexibility required to improve patient recovery from injury and disease to a plethora of tissues in the body, all having unique properties and function.

Very early instances of tissue engineering were generally related to applications involving the grafting of skin with modern grafting applications being established by Webster's studies in graft preservation during the twilight days of World War II [1]. Prior to World War II, implantation of biomaterials was primarily focused on biocompatibility. It wasn't until following the war that a shift occurred leading to improved focus on performance materials following implantation. Noteworthy with this is the development of early metal-on-polymer hip implants by Sir John Charnley who first developed hip implants where the wear properties were first taken into account as a design parameter during the engineering of the device. Whereas previously hip implants had been metal-on-metal, Charnley developed metal on ultra-high molecular weight poly(ethylene) (UHMWPE) implants to reduce wear, reducing inflammation and extending the lifetime of the implant before revision surgery was needed [2]. Improvements in cell culture and expansions techniques were made throughout the 1940s through 1960s that truly opened the door for the tissue engineering field to begin to coalesce. Shortly thereafter, rapid advancements were made in the cryopreservation techniques for cells, leading to early off-the-shelf skin allograft products by Genzyme in the late 1970s and 1980s [3-6].

It was around this time that the term “tissue engineering” began to be used to describe the developing field at the intersection of material science engineering and cell based therapies to create combinatory products for replacing or promote the healing of damaged tissue [7]. The 1990s saw approval of several tissue engineered products by the FDA including coral-derived bone grafts (Pro-Osteon, Interpore), non-biological artificial skin (Integra), and living skin treatments for leg and foot ulcers (Apligraf, Organogenesis Inc). In the orthopedic industry, focus began to shift towards improving bioactivity of implants through the addition of calcium phosphate coatings to enhance osseointegration of regenerating bone with the implant [8]. This marked a turning point of engineering implants from minimizing unwanted negative biological responses to designing materials that actively interact with the body in an engineered manner. Early excitement for the field peaked in the late 1990’s with the widespread media circulation of the “Vacanti Mouse” where tissue engineered cartilage was grown using chondrocytes on the back of a mouse utilizing a PLGA scaffold in the shape of a human ear [9].

Despite the emerging commercial market in the late 1980s and 1990s for tissue engineered products, the field remained high risk for investors and suffered a downturn in the early 2000s after the tech bubble collapse [10]. It has taken the past decade for the field to recover from the loss of investment and we are currently in a second tissue engineering boom. The largest driving force behind the current second boom of tissue engineering has been the development improved knowledge of stem cells and their use [11]. Recent leaps in tissue engineering caused by improvement in characterization and production techniques have yielded engineered tissue with increased complexity compared to skin grafting [12], cartilage [13], and bone regeneration [14], tissue which are predominantly avascular. Amongst these are artificial bladders containing cells cultured in vitro that are later implanted [15] and trachea constructs composed of decellularized extracellular matrix that complimented with stem cell derived cells [16]. Engineered tissues with even higher complexity will soon be realized as further advancements are made in materials processing techniques such as 3D printing, electrospinning, decellularized matrices, self-assembled nanofibers, microfluidics, and others technologies. Further maturity of these technologies along with our continually improving understanding of the manipulation, plasticity, and materials interaction of cells offer great hope that the early excitement and promises of tissue engineering in the 20th century will soon finally be realized.

1.2 Hydrogels and the native extracellular matrix

Hydrogels are crosslinked networks of hydrophilic natural or synthetic polymers that are composed of mostly water by weight. Due to their 3D crosslinked structure, hydrogels behave much like solids despite being mostly solution. They make an excellent implantable tissue engineering material due to their mimicry of the structural and mechanical properties of the native extracellular matrix [17]. Hydration of hydrogels are a result of high negative or positive charge along the polymer chains causing an attraction of water due to water's dipole structure. Because of this, both naturally derived and synthetic materials can be used for hydrogel formation through a variety of crosslinking methods such as ionic [18], changes in pH [19], addition of photocrosslinkable molecules [20], or even combinations of orthogonal crosslinking methods to create interpenetrating networks of different hydrogel materials [21, 22]. Gelation for many materials can be induced through either a physical process such as repeated freeze-thaw cycles [23] or through chemically induced crosslinks [24]. Hydrogel materials are particularly important for recreating the native 3D microenvironment that is home to cells and their use enables cells to avoid unusual integrin binding patterns that are forced to exist in 2D cell culture systems [25].

Synthetic materials typically used for gel formation include poly-L-lactide (PLA), polyurethane, polyethylene glycol, and others [26-28]. Usage of hydrogels are highly dependent on the material and its specific properties, such as the high oxygen permeability of poly(2-hydroxethyl methacrylate) (Poly(HEMA)) for creation of contact lenses [29], or the temperature dependent swelling and contraction of poly(N-isopropylacrylamide) which will shrink and exclude water when heated above its lower critical solution temperature, making the material excellent for easily releasing engineered cell sheets [30]. The good biocompatibility of poly(ethylene oxides) (PEO) make them excellent materials for modifying the surfaces of other implantable materials to induce ‘stealth’ like properties that bypass immune system response due to this high hydrophilicity minimizing protein adsorption [31] although they have low biodegradability without copolymerization with hydrolysable materials [32]. PEO is frequently used for drug delivery applications though block copolymer formation with other materials such as poly(propylene oxide) to create thermally reversible gels [33] and can enhance drug uptake [34].

Synthetic hydrogel materials are particularly applicable where high batch-to-batch consistency is required as the precursor materials will be more homogeneous than naturally derived materials that may have variation in properties due to differences in materials sourcing or age. Additionally, synthetic materials allow the generation of highly tuned modification chemistries to control mechanical, release, and degradation properties. Such an example is the modification of PEO chain ends with photocrosslinkable acrylate groups for gelation upon exposure to UV light and photoinitiatior or addition of polymers in a block copolymer that are more susceptible to hydrolytic degradation [35]. Peptide engineering has gained significant traction in the past decade, enabling researchers to generate specific amino acid sequences to control hydrogel properties. These polypeptides can be directly gelled with themselves to form structures such as self-assembling aligned gels [36] or electrically active peptide-π-peptide triblock self-assembled peptides that have excellent energy transport properties in aqueous environments [37] that have great potential as tissue engineering constructs for action potential propagating tissues such as cardiac tissue or nerve. Other synthetic hydrogels have been developed for delivery of BMP-2 during remodeling of bone defects [38], or particular structures like ECM-like poly(lactic acid) (PLL) foams [39] and poly(glycolic acid) (PGA) fibers to reinforce coating collagen sponges [40]. Synthetic hydrogels have excellent biocompatibility and can be designed to have extensive structural lifetimes while retaining high strength after implantation or have more rapid degradation as needed based on copolymerization techniques, enabling highly application-specific hydrogel engineering and furthermore can be combined with natural biomaterials to make hybrid structures.

Naturally derived hydrogel materials such as alginate, chitosan, collagen, fibrin, silk, fibronectin, and decellularized ECM provide improved biocompatibility and can better mimic the native extracellular matrix compared to synthetic hydrogels [41-45]. Even DNA itself has been used to create natural hydrogel materials [46]. While naturally these materials have great biocompatibility, there exists several potential problems with their use including high chance of xeno-immunogenic response, difficulty in tuning their degradation due to the presence of native degradation enzymes, and the weak mechanical properties of the materials make them difficult to handle and process [47, 48].

Generation of decellularized ECM began in the late 1940s with the first removal of cells to isolate muscle tissue ECM by Poel [49]. Use of decellularized ECM truly did not become in vogue until Stephen Badylak used decellularized pig small intestine ECM to enhance Achilles tendon repair strength in a canine model in 1995 [50]. Since then, there has been some clinical investigation of the usage of decellularized porcine heart valves and decellularized trachea, though in both cases some complications arose either due to incomplete decelluarization in the case of the heart valves or development of stenosis in the decellularized trachea [51, 52].

The extracellular matrix provides the structural support for cells throughout the body by providing the mechanical framework to help tissues maintain their shape and is generally produced by resident fibroblasts and epithelial cells in a given tissue [53]. Additionally, the ECM provides adhesive cues for cells to provide cues for migration, proliferation, and differentiation [54]. The ECM is under a constant state of remodeling by cells and is generally composed of fibrous proteins such as collagens and elastin serving as the main structural support and providing elasticity respectively [55]. Hydrophilic proteoglycans such as hyaluronic acid uptake water and provide tissues with resistance to compressive forces [56]. A critically important structure in the body, ECM takes up around 25% of protein mass in mammals [57] with collagen types I, III, IV, V and XI being highly ubiquitous collagens within the ECM [58] providing structural support and sites for other ECM components to bind. Another role of the ECM is uptake and capture of soluble growth factors and adhesion molecules for cellular signaling [56].

Adhesive proteins such as fibronectin and laminin are produced by fibroblasts and other cell types and captured by the ECM. Integrins in the cell membrane link signaling from ECM mechanical, directional, and adhesive cues to the cytoskeleton which can remodel itself in response to these cues [59, 60]. Fibronectin can bind to collagen and heparin sulphate proteoglycans through its fibronectin type III domain, a pair of anti-parallel β-sheets containing RGD amino acid sequence (Arg-Gly-Asp) for cellular integrin binding and heparin binding domains; other smaller fibronectin binding domains help bind the adhesive cue to other fibronectin molecules or fibrin [61]. Laminins are found more frequently in the basement membrane of the ECM and are composed of three subunits, α,β, and γ domains forming a cross-shaped structure that binds to other laminins and components of the ECM [62].

The final main component of the extracellular matrix are heparan sulfate proteoglycans (HSPGs) such as perlecan, collagen XI, syndecan, and others that consist of protein backbones containing heparan sulphate side chains that interact with other structural proteins and water. HSPGs can be either secreted from cells or cleaved from the cell membrane [63, 64]. HSPGs play a role much like glue in the ECM by binding to many different ECM proteins and capturing soluble growth factors to control their diffusion and release kinetics. Heparin binds an incredible number of ECM and soluble factors including VEGFs, GDNFs, HGFs, PDGFs, FGFs; cytokines like the interleukin series, interferons; and to adhesive cues such as laminin and fibronectin [65, 66].

Mechanical properties of the extracellular matrix have a substantial impact on the cellular behavior, often providing a driving force for differentiation of stem cells to specific lineages [67]. Stiffness of the ECM directly impacts the organization of actin filaments within the cell that form the cytoskeleton by increasing filament organization with stiffness increases by altering the formation and organization of focal adhesion [68]. Additionally, stiffness of the extracellular matrix can affect the migration, proliferation, and survival of cells [69].

Cellular interaction with the ECM is primarily through transcellular membrane integrins that act as receptors for cellular adhesion for specific peptide sequences within adhesion proteins [70]. These receptors are heterodimeric composed of a combination of one of eighteen α subunits pairing with one of eight β subunits [71]. The pairing of the specific α and β domains in the cell membrane determines the ECM proteins that it can bind with [72]. Primary integrin binding is through the RGD motif found in fibronectin and other ECM proteins such as laminin and vitronectin [70]. Specificity of integrin binding to RGD sequences are impacted by the amino acids surrounding the RGD site and the overall density and spacing between RGD binding sites [73, 74]. Integrin activation is driven by the polymerization and depolymerization of actin filaments within the cytoskeleton allowing cells to effectively deactivate integrin binding to the ECM when cells need to remain in circulation such as red blood cells or for turnover during extension of lamellipodia and its restructuring of the cytoskeleton during cellular traction to enable cell motility [60, 75, 76]. Addition of these adhesive motifs to synthetic biocompatible grafting materials has been found to substantially improve cellular response [77, 78].

Proteins that make up the ECM have binding sites for not only adhesive cues, but also for growth factors to prolong their lifetime and control the spatial distribution and release for cell signaling. Capture of growth factor or adhesion peptides by the ECM as the factors diffuse away from their source provides a natural mechanism for generation of soluble growth factor gradients that play a particularly important role during wound repair and development [79, 80] as well as establishment of adhesive ligand gradients [81]. Soluble growth factors will frequently be captured by HSPGs and then released from the proteoglycan after cleavage of heparan sulphate by heparinase [82]. Integrins specific for particular growth factors such as the VEGFR2 receptor work together with adhesion site integrins to promote improves specificity to ECM captured signals based on the integrin expression profile of particular cell types [83].

Remodeling of the ECM is primarily driven by interaction of matrix metalloproteinases (MMPs) or heparanases with the matrix structure. There exists at least 24 different types of MMPs that are either presented as transmembrane structures or solubilized and secreted by cells to cleave extracellular matrix proteins, captured adhesion cues, and growth factors [84, 85]. Tissue inhibitors of metalloproteinases (TIMPs) regulate the levels of MMP present to ensure excessive degradation of the ECM does not occur [86]. Heparanase also plays an important role in ECM remodeling by cleaving heparan sulphate groups from HSPGs, causing a reduction in the crosslinking of the ECM and releasing captured growth factors [87].

1.3 Structural anisotropy in biological tissues

Anisotropy in biological tissue is critically important for the function many tissues including tendons, ligaments, muscle, nerves, cardiac, vascular, and bone. Tendons require high strength along their long axis and are composed of highly aligned collagen fiber bundles [88]. Loss of tendon function with age is generally due to changes in the collagen fiber structure, with additional crosslinking of collagen over time reducing elasticity by increasing collagen aggregation [89]. These issues are further compounded by slower degradation and remodeling of collagen as collagenases are generated in lower amounts with age [90].

Alignment of the vascular epithelium with direction of blood flow is critically important to provide flexibility for blood vessels and give them sufficient tensile properties to avoid rupture during pulsatile blood flow [91]. Circumferential alignment of the exterior ECM of vasculature provides the mechanical feedback during flow to maintain smooth muscle cells (SMCs) in a healthy contractile phenotype, as opposed to a repair phenotype present in several disorders that deposits ECM [92]. Longitudinal alignment in the blood vessel lumen helps enhance shear flow stress induction of endothelial cell alignment and polarization [93]. Disruptions in the ECM and therefore endothelial alignment can cause many issues including altered permeability, increased inflammation due to disruptions in flow, and other vascular problems [94].

Muscle cells require axial alignment for effective contraction [95, 96], thus any tissue engineering solution for implantable muscle must provide an aligned matrix or function will be compromised. The fusing of muscle cells into striated myotubes that run the entire length of the muscle needs alignment features to be a major consideration of design or muscle tissue will have function severely impacted [97]. Two dimensional substrates can provide the alignment cues needed for muscle cell organization but even so, function is highly limited without a consistent method for generation of muscle tissue in 3D [98].

The ECM of cardiac tissue has native alignment to it that provide organizes cardiac cells to ensure contractility is strong enough to pump blood throughout the body [99]. Conduction of the action potential propagates most rapidly along the direction of alignment and many pathological heart conditions are the result of disruption to the anisotropy of cardiac ECM organization [100]. Organization of engineered cardiac tissue is currently generated through several strategies including mechanical stimulate of cells [101], cardiomyocyte entrapment in fibrin gel scaffolds [102], or aligned collagen substrates [103]. Electrically conductive nanofibers have also been investigated to form 3D meshes for cardiac tissue patches through the weaving together of multiple layers of aligned fibrous PCL-silk-carbon nanotube composites [104].

1.4 Topographical and neurotrophic guidance for nerve repair

As the regeneration speed of axons act as a primary limiting factor for successful nerve regeneration, much of the recent work has been focused on improving the speed of axonal outgrowth and SC migration rates, as a primary function of immature SCs are to lead the axons across the injury gap through secretion of NFs [105]. Strategies employed to improve nerve guidance conduits (NGCs) include incorporation of growth factors, surface modification, substrate patterning, usage of porous foams, aligned fibers, and combinatorial approaches attempting to enhance regenerative speed [106]. Aligned electrospun nanofibers have previously been used to artificially provide topographical guidance cues for Schwann cell migration that are normally provided by the axon in healthy tissue [107]. Topographical alignment has been shown to have strong effect on the orientations of both axons and SCs relative to random fiber meshes or planar tissue culture surfaces and lead to an improved regenerative outcome due to the guidance cue they provide, although they have yet to reach the performance level of the autograft [108]. Topographical guidance by nanofiber-based conduits typically improves the number of myelinated axons throughout the conduit relative to empty tubes. Although topographical guidance could be provided by electrospun nanofibers, they fail to upregulate specific proliferative or phenotypic responses during their interaction with cells and typically do not match the mechanical properties of the native microenvironment that the cells are accustomed to. Other methods of generating topographical guidance cues to improve nerve regeneration have included strategies such as forming oriented channels in scaffolds through use of degradable templates [109] and directed freeze processes [110] to mimic the endoneurial tube structure for guidance of axonal outgrowth.

Guidance of endogenous SCs is of particular importance in enhancing nerve regeneration due to the numerous roles of SCs in the PNS repair process [111-113]. Immediately following nerve injury, SCs precede the axons into the lesion site, self-assembling into cord-like structures, and secrete extracellular matrix to form tracks upon which regenerating axons grow while producing a cocktail of NFs that promote neuron survival and growth of regenerating neurons to the distal stump. To maximize neuronal infiltration into the nerve guide, it is imperative to design fibers that maximize SC migratory speed through a combination of fiber alignment and neurotrophic cues. Neurotrophic factor gradients provide directional cues to maximize SC infiltration towards the distal end of the nerve guide where they can continue to secret soluble factors that drive axonal outgrowth. SCs have been shown to respond strongly to GDNF as a migratory cue [114] and gradient steepness plays an important role in cellular response such as in the study by Cao *et. al.* showing improved migratory rates of PC12 cells as NGF steepness increased [115].

As a method of enhancing the regeneration of nerves, various approaches of delivering exogenous NFs to the injury site have been explored using hydrogels, microspheres, and viral-based gene transfection methods to promote neural survival and enhance axonal outgrowth across the injury gap [116-120]. Delivery of uniform concentrations or excessively high concentrations of NFs have been shown to trap axon growth within the conduit, referred to as the “candy store effect”, results in poor functional outcome by limiting the number of axons that exit the conduit into the distal stump due to how beneficial the conduit microenvironment becomes for the cells [116-118]. Localized delivery and presentation of diffusible or immobilized NF gradients within nerve conduits could provide an avenue for improvement in regeneration of nerves compared to isotropic delivery of NFs by better driving a higher number of axons towards the distal portion of the nerve guide more rapidly. Depletion of gradient loaded soluble NFs, or degradation of collagen fibers loaded with immobilized NFs, over time provides a reliable mechanism to eliminate any “candy store effect” that might be present.

While there are a myriad of neurotrophic factors beneficial to nerve regeneration, well studied heparin-binding factors include GDNF, PTN, and NGF as these have significant phenotypic dependent effects on regenerative outcome. GDNF has been shown to have many benefits for nerve regeneration including Schwann cell viability, motility, and myelination capacity, and primarily enhances neuron survival [121]. Upregulation of PTN expression after peripheral neuropathy enhances motor neuronal survival and leads to increased myelination [122]. NGF provides a similar overarching role as GDNF but has increased beneficial effects for sensory nerve outgrowth [120]. By selective usage of specific neurotrophic factors, we can selectively design fibers to maximize functional outcome for motor, sensory, and mixed neural populations. Several strategies for delivering GDNF and NGF gradients have been proposed to enhance unidirectional migration of axons *in vitro* over short lengths [123-125]. However, the lack of technical platforms for preparing and testing tuneable gradient patterns on a multi-centimeter scale has limited advancement in applying gradient delivery methods *in vivo*, minimizing their potential use for long gap injuries where the therapeutic need is greatest. Our diffusion-based gradient method presents a technological advance that enables generation of multi-centimeter length gradients for use in critical nerve gap regeneration.

1.5 Peripheral nerve regeneration and current clinical repair options

Undamaged nerve tissue consists of numerous fascicles containing paired axons and Schwann cells (SCs) organized anisotropically within a protective endoneurial structure that acts as the blood-nerve barrier and is surrounded by an extracellular matrix consisting predominantly of collagen and laminin [126, 127]. Within the nerve fascicles, mature SCs will anchor themselves to the basal lamina and collagen IV and wrap themselves around their partner axon with multiple layers of myelin that prevent loss of signal during action potential conduction [128]. Disruption of the nerve structure following injury causes axons within the damaged distal nerve to die off through the process of Wallerian degeneration where SCs react to dying axons by dedifferentiating from a mature myelinating state, to an immature proliferative state as they, and macrophages, phagocytize the axonal and myelin debris [129]. Circulating fibrinogen accumulates in the wounded nerve due to blood vessel rupture to form a disorganized fibrin clot that guides the migration of the newly proliferating SCs across the injury site [130]. During their migration after injury, SCs form cellular tubes, known as bands of Büngner, that guide the growth of regenerating axons from the proximal region to reinnervate the distal target and secrete neurotrophic through contact and chemotrophic guidance [131]. Once the axons have successfully reconnected with the distal target, SCs revert back to their mature pro-myelinating phenotype in response to axonal membrane-bound NRG1 type III signaling amongst other factors including repair of the ECM [108, 132].

The degree of functional recovery rapidly decreases with increasing gap size due to a combination of factors including: regenerating axons reestablishing connections with incorrect distal targets, atrophy of downstream motor targets due to prolonged lack of neural connection, and axons being unable to navigate through the buildup of collagenous scar tissue secreted by fibroblasts over time [133]. Due to these factors, the critical gap distance at which human nerves can no longer successfully regenerate unassisted is around 5 cm which can take up to two months for repair at typical axonal outgrowth rate of 1-2 mm/day [134-136].

Over short injury gaps, up to 2–5 centimeters in length, treatment options include usage of commercially available nerve guides in the form of collagen (NeuroMatrix and NeuraGen) or porcine submucosa (AxoGuard) hollow tubes. These provide a protective, biodegradable environment for nerve regeneration but lack guidance cues or growth factor incorporation to enhance regeneration and are limited to use with injury gaps lengths of up to 3 cm. The gold standard for larger gaps are the nerve autograft and to lesser extent, the allograft. The autograft provides a preconstructed extracellular microenvironment like healthy nerve but has several distinct disadvantages. Autografting requires donor nerve from the patient thus a second surgery to take out a graft nerve, which can result in donor site morbidity and loss of function for the donor nerves previously associated target, and typically a sensory nerve from the patient’s leg that has smaller caliber nerves than the motor nerve it replaces [137]. To date, the only long gap autograft alternative is processed nerve allografts (Avance®), which uses decellularized nerve to preserve the axon-SC tubular structure for guiding axonal regeneration. However, it also has several disadvantages relating to potential immunogenicity, difficulty in storage and transport of the grafts, and limited availability of donor nerve tissue for decellularization; the latter two issues increase downstream cost to the patient. Moreover, structural mismatch between the graft nerve caliber and the damaged nerve also decreases the potential effectiveness of graft nerves.

1.6 Electrospun hydrogel microfibers

Electrospun hydrogel microfibers are created through a modification of traditional electrospinning processes where an electrical field is applied to an extruded polymer solution, drawing out a polymer jet that then lands on a grounded rotating collector (Fig. 1.1). To generate collagen or fibrin hydrogel fibers and sheets, collagen or fibrinogen are spun onto a rotating collection dish that contains aqueous crosslinking agents that rapidly form fibers and capture the electrically induced alignment of the biopolymer chains. Individual fiber diameters can be adjusted by variation in parameters such as flow rate, polymer concentration, needle size, and collector spinning speed (Fig. 1.2) [138]. Inducing molecular alignment (Fig. 1.3) of the biopolymer chains via electrospinning enhances the mechanical properties beyond that can be obtained with as-cast bulk isotropic hydrogels of similar composition and crosslinking properties. The tensile moduli of several biopolymer hydrogel fibers were measured using dynamic mechanical analysis and found to range from

10s to 100s of kPa when hydrated. Electrospun fibrin hydrogel tensile moduli after drying and rehydration are similar in range to sciatic nerve tissue (580 kPa) [139]. By varying the method of collection, an array of hydrogel fiber geometries can be generated, including collection as fiber bundles, filaments, sheets, and tubes (Fig. 1.4). The combined topographical guidance cues and tunable ECM-like mechanical properties of electrospun hydrogel fibers provide a material that can be applied to many tissue engineering applications such as nerve, cardiac, vascular, and skeletal muscle repair where direct interaction of cells with topographical guidance by the substrate is beneficial (Fig. 1.5).

1.7 Study Design

The study design was focused on development of electrospun hydrogel fibers and characterization of mechanical property changes with variations in spinning properties such as collector RPM, solution concentrations, additional crosslinking following the spin, etc. The basic, as spun, fibers will be applied to several tissue engineering applications to demonstrate the versatility of the material and its ability to be used in multiple geometric configurations. Next, several methods of modification of the base fibers will be investigated, targeting the development of these materials as a growth factor delivery vehicle to enhance cellular interaction. The effect of the hydrogel fiber materials on cellular outgrowth, using both modified and unmodified fibers, will be characterized along with the organizational capacity of the fibers to induce oriented cells along the topographical guidance cues presented. As an improved potential nerve guide carrier for hydrogel fibers over electrospun nanofibers, an industrial collaboration with the Secant Group (Telford, PA, USA) was established and a poly(glycerol sebacate) (PGS) coated tube composed of poly(glycolic acid) (PGA) was implanted in a sciatic nerve defect to examine the effect of PGS on nerve regeneration, the local inflammatory microenvironment, and improvement in coated tube mechanical properties (Fig. 1.6). Finally, a collaboration with Sun Yat-Sen University (SYSU) (Guangzhou, P.R. China) was established to test PGS coated tubes containing electrospun hydrogel fibrin and collagen fiber materials with uniform and gradient loaded neurotrophic factor as a method of peripheral nerve repair of the sciatic nerve in a rodent animal model.

1.8 Conclusion

Development of electrospun hydrogel materials enables the generation of ECM-like materials that can be used to provide topographical guidance cues for the outgrowth of Schwann cells and the axonal growth cone. Use of native materials for these microfibers enables remodeling of the implanted materials using the same cellular mechanisms that are present during remodeling of the ECM. As these materials are at the intersect between traditional biologically derived hydrogels and electrospun nanofibers, techniques used in both classes of materials can be used for tailoring hydrogel microfiber structural and physiochemical properties.

1.9 Figures

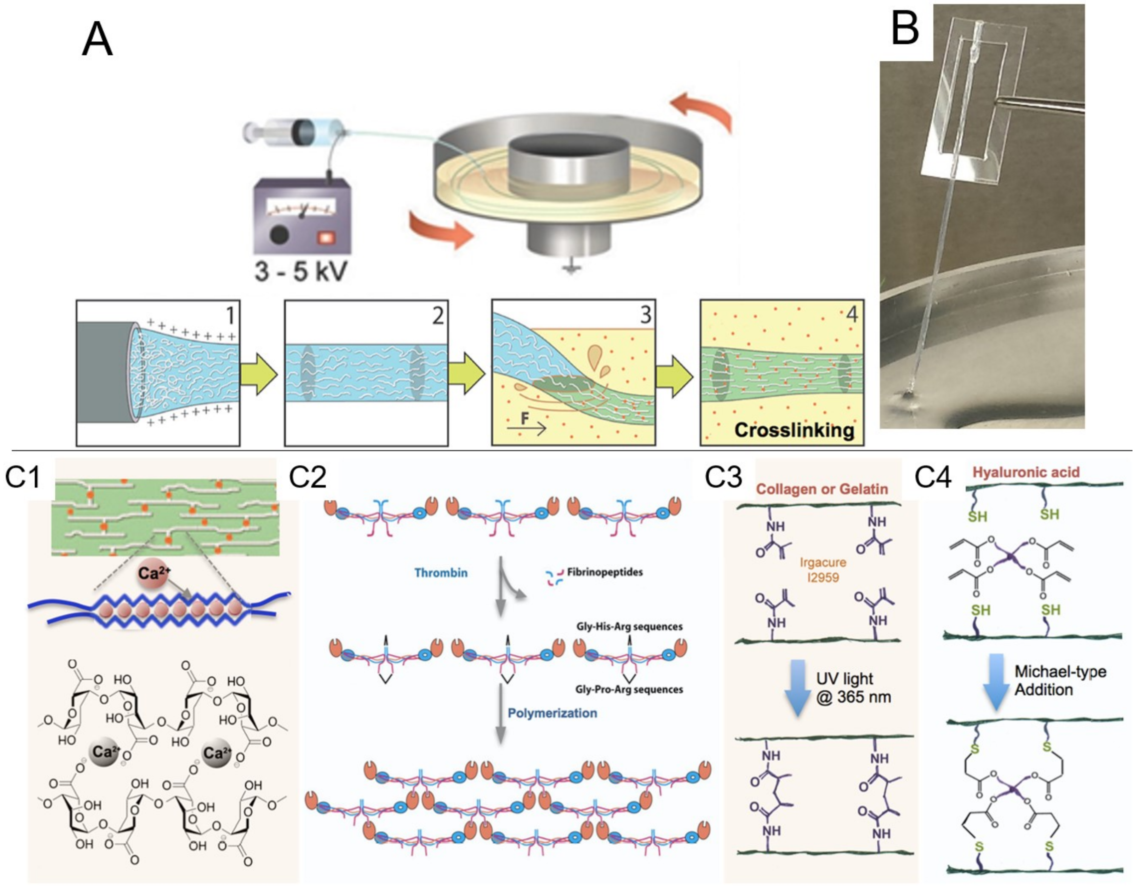

Figure 1-1: Electrospun hydrogel fiber generation.

Electospun hydrogel fibers are prepared by electrospinning precursor solution onto rotating collection bath containing crosslinker (a) that provides additional mechanical strain to further align the hydrogel polymer chains during crosslinking, thereby improving strength compared to cast hydrogels to the point where hydrogel fibers can be directly manipulated (b). Several biologically derived and modified polymers are compatable with hydrogel fiber spinning including, but not exclusively, alginate (c1), fibrin (c2), collagen derived materials (c3), and hyaluronic acid (c4).

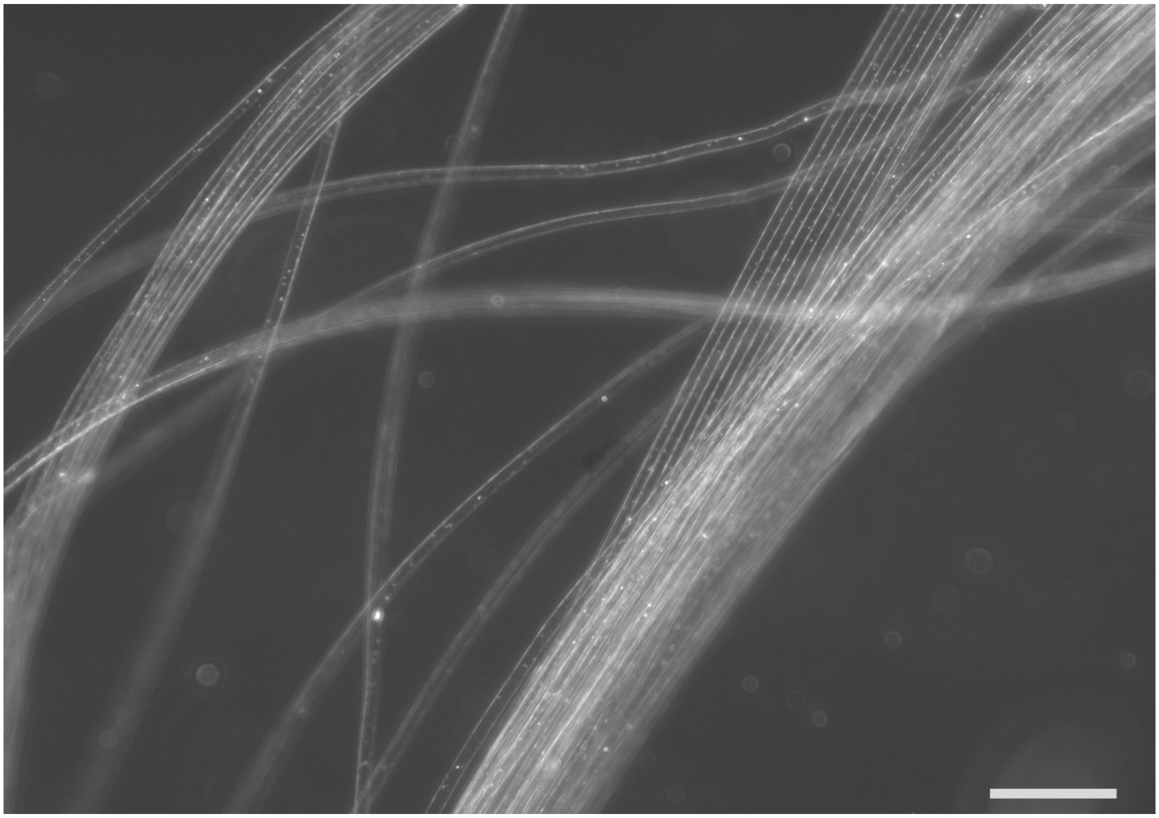

Figure 1-2: Individual distinct fibers formed during electrospinning of alginate hydrogel microfibers.

Micron scale individual fibers aggregate together to form bulk electrospun hydrogel fiber structures. The size of the individual hydrogel fiber strands are in the same range as the diameter of a typical cell. Scale bar: 300 μm.

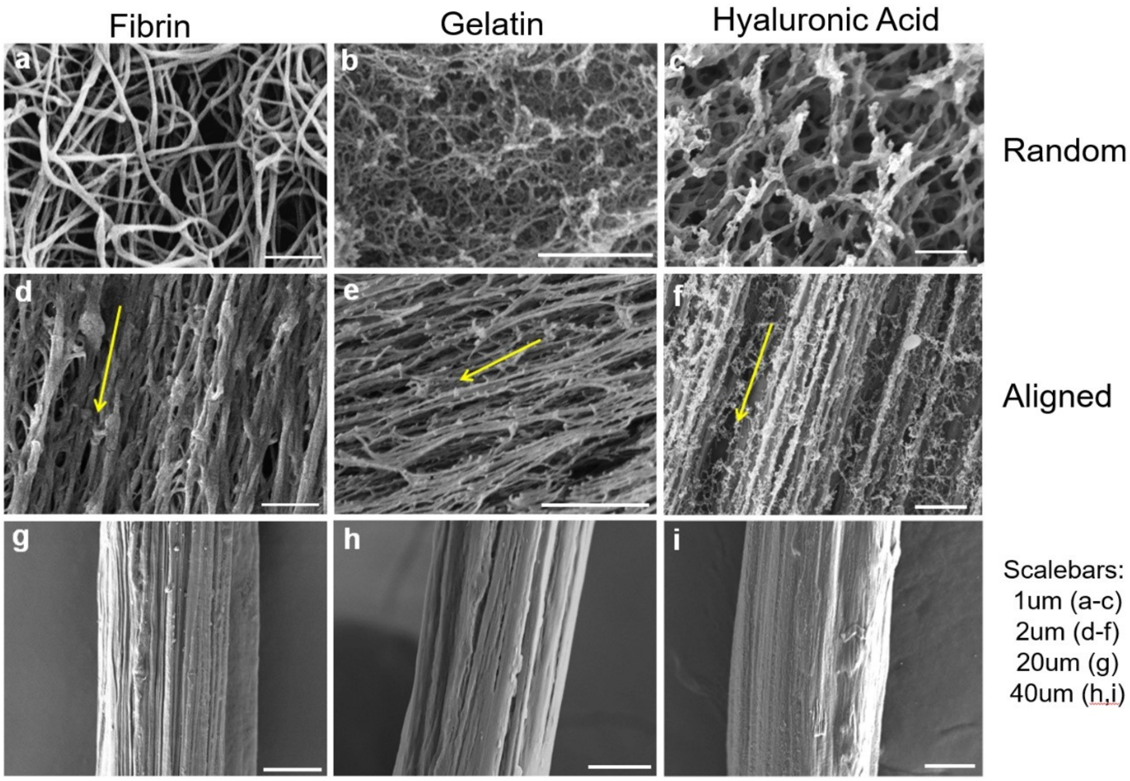

Figure 1-3: Fiber alignment is enhanced by hydrogel fiber spinning compared to isotropic cast gels.

Cast gels (a-c) show random orientation of fibrin, gelatin, and hyaluronic fibers, generating the isotropic bulk properties of these hydrogels. Electrospinning these materials into hydrogels (d-f) induced molecular alignment of the polymer chains, providing topographical guidance cues and anisotropic mechanical properties. Collection onto a rotating solution bath permits the generation of 3D structures such as fiber bundles for any of the materials electrospun with this technique (g-i).

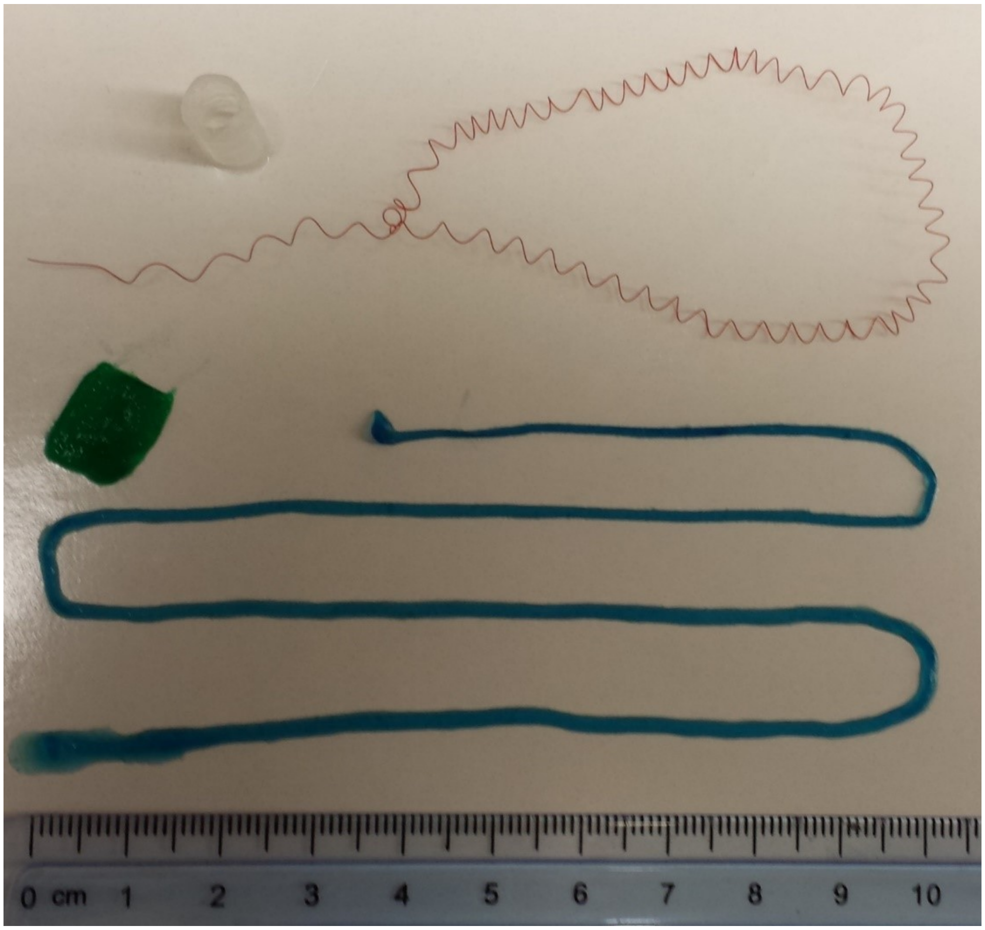

Figure 1-4: Hydrogel fiber geometries that can be generated with the method.

Depending on the method of collection following hydrogel fiber spinning, the material can be collected, going from top to bottom, 1) in the form of tubes by wrapping fibers or sheets around a secondary cylindrical structure, 2) straight or coiled dry strings by drying long fiber bundles in air for several hours to overnight, 3) sheets by spinning fibers with a rastering movement to distribute fibers across a wide band of the collection solution, and 4) hydrated fiber bundles of various sizes by directly pulling hydrogel fiber strings off the collection solution after several minutes of spinning.

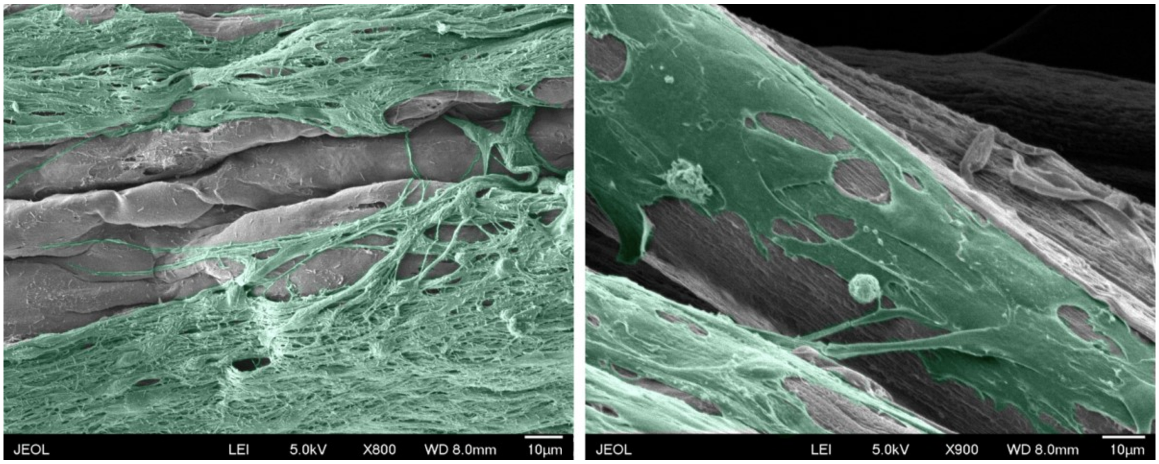

Figure 1-5: Cells can directly interact and align with orientation of electrospun hydrogel fiber surfaces.

False color images of neurites from DRG explants extending along collagen fibers aggregated in sheet form (left). Fibroblasts spreading along the length of fibrin filaments are able to extend filopodia between adjacent filaments and show elongation of the cell body with the long axis of the filament (right).

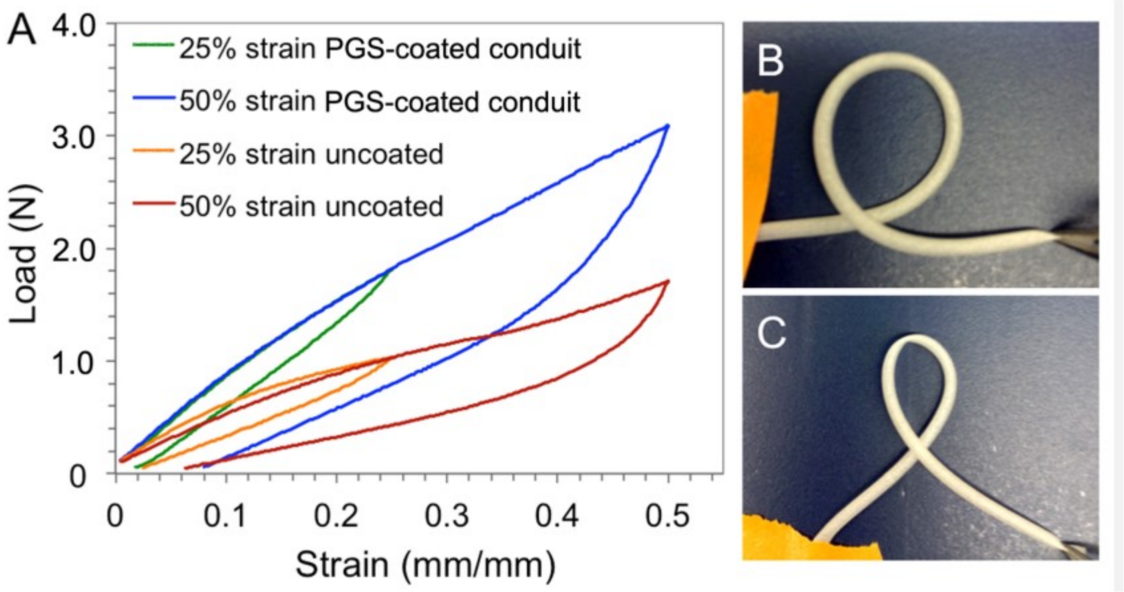

Figure 1-6: Improved mechanical properties of PGA multifilament braided tubes after PGS coating.

Following coating with PGS, PGA braids show improved loading hysteresis (a) and can be bent into a 180° loop (b) where uncoated kink when bent beyond 90°.

1.10 References

1. Webster JP. *Refrigerated Skin Grafts.* in *Ann Surg.* 1944. p. 431–448.
2. Charnley J. The Man and the Hip. 1990.
3. Billingham RE and Medawar PB. *The freezing, drying and storage of mammalian skin.* in *J Exp Biol.* 1952. p. 454–468.
4. Polge C, et al., *Revival of spermatozoa after vitrification and dehydration at low temperatures.* in *Nature*. 1949. p. 666.
5. Chardack WM, et al., *Experimental studies on synthetic substitutes for skin and their use in the treatment of burns.* in *Ann Surg.* 1962. p. 127.
6. Green H, et al., *Growth of cultured human epidermal cells into multiple epithelia suitable for grafting.* in *Cell Biol.* 1979. p. 5665–5668.
7. Viola J, et al., *The Emergence of Tissue Engineering as a Research Field.* in *Natl Sci Found*. 2003;
8. Rey C. *Calcium phosphate biomaterials and bone mineral: Differences in composition, structures, and properties.* in *Biomaterials.* 1990. p. 13–15.
9. Cao Y, et al., *Transplantation of chondrocytes utilizing a polymer-cell construct to produce tissue-engineered cartilage in the shape of a human ear.* in *Plast Reconstr Surg.* 1997. p. 297–302.
10. Mansbridge JN. *Tissue-engineered skin substitutes in regenerative medicine.* in *Curr Opin Biotechnol.* 2009. p. 563–567.
11. Amit M, et al., *Clonally Derived Human Embryonic Stem Cell Lines Maintain Pluripotency and Proliferative Potential for Prolonged Periods of Culture.* in *Dev Biol.* 2000. p. 271–278.
12. Boucard N, et al., *The use of physical hydrogels of chitosan for skin regeneration following third-degree burns.* in *Biomaterials.* 2007. p. 3478–3488.
13. Uematsu K, et al., *Cartilage regeneration using mesenchymal stem cells and a three-dimensional poly-lactic-glycolic acid (PLGA) scaffold.* in *Biomaterials.* 2005. p. 4273–4279.
14. Mauney JR, et al., *Mechanical Stimulation Promotes Osteogenic Differentiation of Human Bone Marrow Stromal Cells on 3-D Partially Demineralized Bone Scaffolds In Vitro.* in *Calcif Tissue Int.* 2004 May;74(5):458–468.
15. Atala A, et al., *Tissue-engineered autologous bladders for patients needing cystoplasty.* in *The Lancet.* 2006. p. 1241–1246.
16. Macchiarini P, et al., *Clinical transplantation of a tissue-engineered airway.* in *The Lancet.* 2008. p. 2023–2030.
17. Stock UA and Vacanti JP. *Tissue engineering: current state and prospects.* in *Annu Rev Med.* 2001. p. 443–451.
18. Yu J, et al., *The use of human mesenchymal stem cells encapsulated in RGD modified alginate microspheres in the repair of myocardial infarction in the rat.* in *Biomaterials.* 2010. p. 7012–7020.

19. Bastings MMC, et al., *A Fast pH-Switchable and Self-Healing Supramolecular Hydrogel Carrier for Guided, Local Catheter Injection in the Infarcted Myocardium.* in *Adv Healthc Mater.* 2014. p. 70–78.
20. Habib M, et al., *A combined cell therapy and in-situ tissue-engineering approach for myocardial repair.* in *Biomaterials.* 2011. p. 7514–7523.
21. Tong X and Yang F. *Engineering interpenetrating network hydrogels as biomimetic cell niche with independently tunable biochemical and mechanical properties.* in *Biomaterials.* 2014. p. 1807–1815.
22. Matricardi P, et al., *Interpenetrating Polymer Networks polysaccharide hydrogels for drug delivery and tissue engineering.* in *Adv Drug Deliv Rev.* 2013. p. 1172–1187.
23. Cascone MG, et al., *Evaluation of poly (vinyl alcohol) hydrogels as a component of hybrid artificial tissues.* in *J Mater Sci Mater Med.* 1995. p. 71–75.
24. Nuttelman C, et al., *Attachment of fibronectin to poly(vinyl alcohol) hydrogel promotes NIH3T3 cell adhesion, proliferation, and migration.* in *J Biomed Mater Res.* 2001. p. 217–223.
25. Gieni RS and Hendzel MJ. *Mechanotransduction from the ECM to the genome: Are the pieces now in place?* in *J Cell Biochem.* 2008. p. 1964–1987.
26. Hinderer S, et al., *Engineering of a bio-functionalized hybrid off-the-shelf heart valve.* in *Biomaterials.* 2014. p. 2130–2139.
27. Baheiraei N, et al., *Synthesis, characterization and antioxidant activity of a novel electroactive and biodegradable polyurethane for cardiac tissue engineering application.* in *Mater Sci Eng C.* 2014. p. 24–37.
28. Schesny MK, et al., *Preserved bioactivity and tunable release of a SDF1-GPVI bi-specific protein using photo-crosslinked PEGda hydrogels.* in *Biomaterials.* 2014. p. 7180–7187.
29. Kidane A, et al., *Accelerated study on lysozyme deposition on poly (HEMA) contact lenses.* in *Biomaterials.* 1998. p. 2051–2055.
30. Kwon OH, et al., *Rapid cell sheet detachment from Poly(N-isopropylacrylamide)-grafted porous cell culture membranes.* in *J Biomed Mater Res A.* 2000. p. 82–89.
31. Sofia S, et al., *Poly(ethylene oxide) Grafted to Silicon Surfaces: Grafting Density and Protein Adsorption.* in *Macromolecules.* 1998. p. 5059–5070.
32. Huh KM and Bae YH. *Synthesis and characterization of poly (ethylene glycol)/poly (L-lactic acid) alternating multiblock copolymers.* in *Polymer.* 1999. p. 6147–6155.
33. Alexandridis P, et al., *Lyotropic liquid crystallinity in amphiphilic block copolymers: temperature effects on phase behavior and structure for poly (ethylene oxide)-b-poly (propylene oxide)-b-poly (ethylene oxide) copolymers of different composition.* in *Langmuir.* 1996. p. 2690–2700.
34. Batrakova EV, et al., *Anthracycline antibiotics non-covalently incorporated into the block copolymer micelles: in vivo evaluation of anti-cancer activity.* in *Br J Cancer.* 1996. p. 1545–1552.
35. West JL and Hubbell JA. *Polymeric Biomaterials with Degradation Sites for Proteases Involved in Cell Migration.* in *Macromolecules.* 1999. p. 241–244.

36. Zhang S, et al., *A self-assembly pathway to aligned monodomain gels.* in *Nat Mater.* 2010. p. 594–601.
37. Ardońa HAM and Tovar JD. *Energy transfer within responsive pi-conjugated coassembled peptide-based nanostructures in aqueous environments.* in *Chem Sci.* 2015. p. 1474–1484.
38. Pratt AB, et al., *Synthetic extracellular matrices for in situ tissue engineering: Synthetic Extracellular Matrices for In situ Tissue Engineering.* in *Biotechnol Bioeng.* 2004. p. 27–36.
39. Tu C, et al., *The fabrication and characterization of poly(lactic acid) scaffolds for tissue engineering by improved solid-liquid phase separation.* in *Polym Adv Technol.* 2003. p. 565–573.
40. Hiraoka Y, et al., *Fabrication and biocompatibility of collagen sponge reinforced with poly (glycolic acid) fiber.* in *Tissue Eng.* 2003. p. 1101–1112.
41. Yu J, et al., *The effect of injected RGD modified alginate on angiogenesis and left ventricular function in a chronic rat infarct model.* in *Biomaterials.* 2009. p. 751–756.
42. Wang H, et al., *Promotion of cardiac differentiation of brown adipose derived stem cells by chitosan hydrogel for repair after myocardial infarction.* in *Biomaterials.* 2014. p. 3986–3998.
43. Pati F, J et al., *Printing three-dimensional tissue analogues with decellularized extracellular matrix bioink.* in *Nat Commun* 2014. p. 3935
44. Fukuda J, et al., *Micropatterned cell co-cultures using layer-by-layer deposition of extracellular matrix components.* in *Biomaterials.* 2006. p. 1479–1486.
45. Kim HJ, et al., *Bone tissue engineering with premineralized silk scaffolds.* in *Bone.* 2008. p. 1226–1234.
46. Um SH, et al., *Enzyme-catalysed assembly of DNA hydrogel.* in Nat Mater. 2006. p. 797–801.
47. Zhu J. *Bioactive modification of poly(ethylene glycol) hydrogels for tissue engineering.* in *Biomaterials.* 2010. p. 4639–4656.
48. Brandl F, et al., A. *Rational design of hydrogels for tissue engineering: Impact of physical factors on cell behavior.* in *Biomaterials.* 2007. p. 134–146.
49. Poel W. *Preparation of Acellular Homogenates From Muscle Samples.* in *Science.* 1948. p. 390–391.
50. Badylak S, et al., *The use of xenogenic small intestinal submucosa as a biomaterial for Achelles tendon repair in a dog model.* in *J Biomed Mater Res.* 1995. p. 977–985.
51. Gonfiotti A, et al., *The first tissue-engineered airway transplantation: 5-year follow-up results.* in *The Lancet.* 2014. p. 238–244.
52. Simon P, et al., *Early failure of the tissue engineered porcine heart valve SYNERGRAFT in pediatric patients.* in *Eur J Cardiothorac Surg.* 2003. p. 1002–1006.

53. Kim S-H, et al., *Extracellular matrix and cell signalling: the dynamic cooperation of integrin, proteoglycan and growth factor receptor.* in *J Endocrinol.* 2011. p. 139–151.
54. Frantz C, et al., *The extracellular matrix at a glance.* in *J Cell Sci.* 2010. p. 4195–4200.
55. Mecham R. *Overview of extracellular matrix.* in *Curr Protoc Cell Biol.* 2001
56. Schaefer L and Schaefer RM. *Proteoglycans: from structural compounds to signaling molecules.* in *Cell Tissue Res.* 2010. p. 237–246.
57. Lee CH, et al., *Biomedical applications of collagen.* in *Int J Pharm.* 2001. p. 1–22.
58. Hulmes DJS. *Building Collagen Molecules, Fibrils, and Suprafibrillar Structures.* in *J Struct Biol.* 2002. p. 2–10.
59. Galbraith CG and Sheetz MP. *Forces on adhesive contacts affect cell function.* in *Curr Opin Cell Biol.* 1998. p. 566–571.
60. Geiger B, et al., *Transmembrane crosstalk between the extracellular matrix and the cytoskeleton.* in *Nat Rev Mol Cell Biol.* 2001. p. 793–805.
61. Ruoslahti E. *Fibronectin and its receptors.* in *Annu Rev Biochem.* 1988. p. 375–413.
62. Colognato H and Yurchenco PD. *Form and function: the laminin family of heterotrimers.* in *Dev Dyn.* 2000. p. 213–234.
63. Brunner G, et al., *An endogenous glycosylphosphatidylinositol-specific phospholipase D releases basic fibroblast growth factor-heparan sulfate proteoglycan complexes from human bone marrow cultures.* in *Blood.* 1994. p. 2115–2125.
64. Manon-Jensen T, et al., *Proteoglycans in health and disease: the multiple roles of syndecan shedding: Syndecan shedding at the cell surface.* in *FEBS J.* 2010. p. 3876–3889.
65. Kjellén L and Lindahl U. *Proteoglycans: structures and interactions.* in *Annu Rev Biochem.* 1991. p. 443–475.
66. Casu B and Lindahl U. *Structure and biological interactions of heparin and heparan sulfate.* in *Adv Carbohydr Chem Biochem.* 2001. p. 159–206.
67. Engler AJ, et al., *Matrix Elasticity Directs Stem Cell Lineage Specification.* in *Cell.* 2006. p. 677–689.
68. Pelham RJ and Wang Y. *Cell locomotion and focal adhesions are regulated by substrate flexibility.* in *Proc Natl Acad Sci.* 1997. p. 13661–13665.
69. Wells RG. *The role of matrix stiffness in regulating cell behavior.* in *Hepatology.* 2008. p. 1394–1400.
70. Ruoslahti E. *RGD and other recognition sequences for integrins.* in *Annu Rev Cell Dev Biol.* 1996. p. 697–715.
71. Alam N, et al., *The integrin—growth factor receptor duet.* in *J Cell Physiol.* 2007. p. 649–653.
72. Hemler ME and Lobb RR. *The leukocyte beta(1) integrins.* in *Curr Opin Hematol.* 1995. p. 61–67.

73. Jiang F, et al., *Assembly of collagen into microribbons: effects of pH and electrolytes.* in *J Struct Biol.* 2004. p. 268–278.
74. Massia SP and Hubbell JA. *An RGD spacing of 440 nm is sufficient for integrin alpha V beta 3-mediated fibroblast spreading and 140 nm for focal contact and stress fiber formation.* in *J Cell Biol.* 1991. p. 1089–1100.
75. Mitra SK, et al., *Focal adhesion kinase: in command and control of cell motility.* in *Nat Rev Mol Cell Biol.* 2005. p. 56–68.
76. Choi CK, et al., *Actin and α-actinin orchestrate the assembly and maturation of nascent adhesions in a myosin II motor-independent manner.* in *Nat Cell Biol.* 2008. p. 1039–1050.
77. Hersel U, et al., *RGD modified polymers: biomaterials for stimulated cell adhesion and beyond.* in *Biomaterials.* 2003. p. 4385–4415.
78. Shin H, et al., *Biomimetic materials for tissue engineering.* in *Biomaterials.* 2003. p. 4353–4364.
79. Kirkpatrick CA, et al., *Spatial regulation of Wingless morphogen distribution and signaling by Dally-like protein.* in *Dev Cell.* 2004. p. 513–523.
80. Kreuger J, et al., *Opposing activities of Dally-like glypican at high and low levels of Wingless morphogen activity.* in *Dev Cell.* 2004. p. 503–512.
81. Brandley BK and Schnaar RL. *Tumor Cell Haptotaxis on Covalently Immobilized Linear and Exponential Gradients of a Cell Adhesion Peptide.* in *Dev Biol.* 1989. p. 74–86.
82. Patel VN, et al., *Heparanase cleavage of perlecan heparan sulfate modulates FGF10 activity during ex vivo submandibular gland branching morphogenesis.* in *Development.* 2007. p. 4177–4186.
83. Ruoslahti E. *Specialization of tumour vasculature.* in *Nat Rev Cancer.* 2002. p. 83–90.
84. Yong VW. *Metalloproteinases: Mediators of Pathology and Regeneration in the CNS.* in *Nat Rev Neurosci.* 2005. p. 931–944.
85. Shiomi T, et al., *Matrix metalloproteinases, a disintegrin and metalloproteinases, and a disintegrin and metalloproteinases with thrombospondin motifs in non-neoplastic diseases: MMP, ADAM and ADAMTS in pathology.* in *Pathol Int.* 2010. p. 477–496.
86. Brew K and Nagase H. *The tissue inhibitors of metalloproteinases (TIMPs): An ancient family with structural and functional diversity.* in *Biochim Biophys Acta BBA - Mol Cell Res.* 2010. p. 55–71.
87. Vlodavsky I, et al., *Mammalian heparanase: gene cloning, expression and function in tumor progression and metastasis.* in *Nat Med.* 1999. p. 793–802.
88. Birk DE, et al., *Characterization of collagen fibril segments from chicken embryo cornea, dermis and tendon.* in *Matrix Biol.* 1996. p. 111–118.
89. Vidal BDC and De Carvalho HF. *Aggregational state and molecular order of tendons as a function of age.* in *Matrix.* 1990. p. 48–57.
90. O'brien FJ. *Biomaterials & scaffolds for tissue engineering.* in *Mater Today.* 2011. p. 88–95.

91. Kissa K and Herbomel P. *Blood stem cells emerge from aortic endothelium by a novel type of cell transition.* in *Nature.* 2010. p. 112–115.
92. Chan-Park M, et al., *Biomimetic control of vascular smooth muscle cell morphology and phenotype for functional tissue-engineered small-diameter blood vessels.* in *J Biomed Mater Res A.* 2009. p. 1104–1121.
93. Duan Y, et al., *Shear-induced reorganization of renal proximal tubule cell actin cytoskeleton and apical junctional complexes.* in *PNAS.* 2008. p. 11418–11423.
94. Curtis A and Wilkinson C. *Topographical control of cells.* in *Biomaterials.* 1997. p. 1573–1583.
95. Valentin A and Humphrey JD. *Modeling Effects of Axial Extension on Arterial Growth and Remodeling.* in *Med Biol Eng Comput.* 2009. p. 979–987.
96. Choi JS, et al., *The influence of electrospun aligned poly(ε-caprolactone)/collagen nanofiber meshes on the formation of self-aligned skeletal muscle myotubes.* in *Biomaterials.* 2008. p. 2899–2906.
97. Wakelam MJ. *The fusion of myoblasts.* in *J Biochem* 1985. p. 1.
98. Chen B, et al., *In vivo tendon engineering with skeletal muscle derived cells in a mouse model.* in *Biomaterials.* 2012. p. 6086–6097.
99. Helm P, et al., *Measuring and Mapping Cardiac Fiber and Laminar Architecture Using Diffusion Tensor MR Imaging.* in *Ann N Y Acad Sci.* 2005. p. 296–307.
100. Lehmkuhl D and Sperelakis N. *Electrotonic spread of current in cultured chick heart cells.* in *J Cell Physiol.* 1965. p. 119–133.
101. Guan J, et al., *The stimulation of the cardiac differentiation of mesenchymal stem cells in tissue constructs that mimic myocardium structure and biomechanics.* in *Biomaterials.* 2011. p. 5568–5580.
102. Black LD, et al., *Cell-induced alignment augments twitch force in fibrin gel-based engineered myocardium via gap junction modification.* in *Tissue Eng Part A.* 2009. p. 3099–3108.
103. Costa KD, et al., *Creating alignment and anisotropy in engineered heart tissue: role of boundary conditions in a model three-dimensional culture system.* in *Tissue Eng.* 2003. p. 567–577.
104. Wu Y, et al., *Interwoven Aligned Conductive Nanofiber Yarn/Hydrogel Composite Scaffolds for Engineered 3D Cardiac Anisotropy.* in *ACS Nano.* 2017. p. 5646–5659.
105. Kingham PJ, et al., *Adipose-derived stem cells differentiate into a Schwann cell phenotype and promote neurite outgrowth in vitro.* in *Exp Neurol.* 2007. p. 267–274.
106. Siemionow M and Brzezicki G. *Chapter 8 Current Techniques and Concepts in Peripheral Nerve Repair.* in I*nt Rev Neurobiol* 2009. p. 141–172
107. Guenard V, et al., *Syngeneic Schwann cells derived from adult nerves seeded in semipermeable guidance channels enhance peripheral nerve regeneration.* in *J Neurosci.* 1992. p. 3310–3320.
108. Motlagh D, et al., *Hemocompatibility evaluation of poly(glycerol-sebacate) in vitro for vascular tissue engineering.* in *Biomaterials.* 2006. p. 4315–4324.

109. Scott JB, et al., *The promotion of axon extension in vitro using polymer-templated fibrin scaffolds.* in *Biomaterials.* 2011. p. 4830–4839.

110. Bozkurt A, et al., *The role of microstructured and interconnected pore channels in a collagen-based nerve guide on axonal regeneration in peripheral nerves.* in *Biomaterials.* 2012. p. 1363–1375.

111. Joddar B, et al., *Spatial gradients of chemotropic factors from immobilized patterns to guide axonal growth and regeneration.* in *Biomaterials.* 2013. p. 9593–9601.

112. Dodla MC and Bellamkonda RV. *Differences between the effect of anisotropic and isotropic laminin and nerve growth factor presenting scaffolds on nerve regeneration across long peripheral nerve gaps.* in *Biomaterials.* 2008. p. 33–46.

113. Tang S, et al., *The effects of gradients of nerve growth factor immobilized PCLA scaffolds on neurite outgrowth in vitro and peripheral nerve regeneration in rats.* in *Biomaterials.* 2013. p. 7086–7096.

114. Paratcha G, et al., *The neural cell adhesion molecule NCAM is an alternative signaling receptor for GDNF family ligands.* in *Cell.* 2003. p. 867–879.

115. Cao X and Shoichet M. *Investigating the synergistic effect of combined neurotrophic factor concentration gradients to guide axonal growth.* in *Neuroscience.* 2003. p. 381–389.

116. Eggers R, et al., *Lentiviral Vector-Mediated Gradients of GDNF in the Injured Peripheral Nerve: Effects on Nerve Coil Formation, Schwann Cell Maturation and Myelination.* in *PLoS ONE.* 2013. p e71076.

117. Tannemaat MR, et al., *Differential effects of lentiviral vector-mediated overexpression of nerve growth factor and glial cell line-derived neurotrophic factor on regenerating sensory and motor axons in the transected peripheral nerve.* in *Eur J Neurosci.* 2008. p. 1467–1479.

118. Blits B, et al., *Rescue and sprouting of motoneurons following ventral root avulsion and reimplantation combined with intraspinal adeno-associated viral vector-mediated expression of glial cell line-derived neurotrophic factor or brain-derived neurotrophic factor.* in *Exp Neurol.* 2004. p. 303–316.

119. Hoyng SA, et al., *A comparative morphological, electrophysiological and functional analysis of axon regeneration through peripheral nerve autografts genetically modified to overexpress BDNF, CNTF, GDNF, NGF, NT3 or VEGF.* in *Exp Neurol.* 2014. p. 578–593.

120. Liu H, et al., *Current sustained delivery strategies for the design of local neurotrophic factors in treatment of neurological disorders.* in *Asian J Pharm Sci.* 2013. p. 269–277.

121. Wood MD, et al., *Affinity-based release of glial-derived neurotrophic factor from fibrin matrices enhances sciatic nerve regeneration.* in *Acta Biomater.* 2009. p. 959–968.

122. Blondet B, et al., *Pleiotrophin cellular localization in nerve regeneration after peripheral nerve injury.* in *J Histochem Cytochem*. 2005. p. 971–977.

123. Mai J, et al., *Axon Initiation and Growth Cone Turning on Bound Protein Gradients.* in *J Neurosci*. 2009. p. 7450–7458.

124. Yu LMY, et al., *The use of immobilized neurotrophins to support neuron survival and guide nerve fiber growth in compartmentalized chambers.* in *Biomaterials.* 2010. p. 6987–6999.

125. Fricke R, et al., *Axon guidance of rat cortical neurons by microcontact printed gradients.* in *Biomaterials.* 2011. p. 2070–2076.

126. Hardy JG, et al., *Biomimetic conducting polymer-based tissue scaffolds.* in *Curr Opin Biotechnol.* 2013. p. 847–854.

127. Gonzalez-Perez F, et al., *Extracellular Matrix Components in Peripheral Nerve Regeneration.* in *Int Rev Neurobiol* 2013. p. 257–275.

128. Jessen KR and Mirsky R. *Control of Schwann cell myelination.* in *Biol Rep.* 2010.

129. Allodi I, et al., *Specificity of peripheral nerve regeneration: Interactions at the axon level.* in *Prog Neurobiol.* 2012. p. 16–37.

130. Belkas JS, et al., *Peripheral nerve regeneration through guidance tubes.* in *Neurol Res.* 2004. p. 151–160.

131. Ribeiro-Resende VT, et al., *Strategies for inducing the formation of bands of Büngner in peripheral nerve regeneration.* in *Biomaterials.* 2009. p. 5251–5259.

132. Birchmeier C and Nave K-A. *Neuregulin-1, a key axonal signal that drives Schwann cell growth and differentiation.* in *Glia.* 2008. p. 1491–1497.

133. Gordon T, et al., *Accelerating axon growth to overcome limitations in functional recovery after peripheral nerve injury*. in *Neurosurgery.* 2009. p. A132–A144.

134. Seddon HJ, et al., *Rate of regeneration of peripheral nerves in man.* in *J Physiol.* 1943. p. 191–215.

135. Gutmann E, et al., *The rate of regeneration of nerve.* in *J Exp Biol.* 1942. p. 14–44.

136. Tinel J. *Les blessures des nerfs; sémiologie des lésions nerveuses périphériques par blessures de guerre.* Paris, Masson et cie; 1916.

137. Ray WZ and Mackinnon SE. *Management of nerve gaps: Autografts, allografts, nerve transfers, and end-to-side neurorrhaphy.* in *Exp Neurol.* 2010. p. 77–85.

138. Zhang S, et al., *Creating polymer hydrogel microfibres with internal alignment via electrical and mechanical stretching.* in *Biomaterials.* 2014. p. 3243–3251.

139. Borschel GH, et al., *Mechanical properties of acellular peripheral nerve.* in *J Surg Res.* 2003. p. 133–139.

Chapter 2 Development and Modification of Fibrin, Collagen, Alginate, and Other Hydrogel Microfibers

2.1 Background

2.1.1 Alginate as a hydrogel material

Alginate fibers form the basis of electrospun hydrogel fiber spinning due to the ease with which the material can rapidly gel through ionic crosslinking and has low cost due to it being a product typically derived from brown seaweed Alginate structure is composed of linear polymer with blocks of two different disaccharides, β-D-mannuronate (M) and α-L-guluronate (G) [1]. The high negative charge from the carboxylic acid groups in these disaccharides forms an ionic crosslinking point with divalent cations. The distribution of alginate M and G blocks are highly dependent on seaweed source from which it is derived [2]. Control of the M to G block ratio and distribution of M and G blocks provide a mechanism to tailor pore size and mechanical properties of alginate hydrogels. Gelation is most frequently through interaction of the G blocks with Ca^{+2} though different divalent cations such as Mg^{+2} or Ba^{+2} can also induce gelation through interaction with M blocks or both M and G repeat units [2]. While not found physiologically, alginates are particularly good for cellular encapsulation and drug delivery [3]. The high hydrophilicity of alginate and lack of adhesive sequences minimizes protein adsorption and makes the material unable to directly interact with cells without conjugation of adhesion ligands. [4]

Mammalian cells do not naturally synthesize alginase to enzymatically break down alginates after implantation, instead, alginates slowly dissolve through a process of monovalent cation exchange with the divalent cations (Ca^{+2}) crosslinking the G blocks in the alginate chain.

2.1.2 Fibrin as a tissue engineering material and physiological role

Fibrin plays a highly critical role in wound healing as part of the blood coagulation cascade. As part of the end phase of the blood coagulation phase, fibrin takes on the job of providing temporary extracellular scaffolding for cellular infiltration that is removed once more permanent extracellular matrix is deposited by fibroblasts and other carekeeper cells of the ECM. As a temporary scaffold, fibrin has the capacity to bind many cytokines that play a role in wound healing. Fibrin has a relatively short biological persistence as a matrix material due to the ease in which is degraded by plasmin and MMPs secreted from cells. Degradation is therefore an important factor to consider in any tissue engineering application where fibrin is used as the material must remain present until cellular infiltration is complete and homeostasis is obtained.

Fibrin gels are easily formable at room temperature upon exposure to thrombin and have excellent clinical biocompatibility due to the ability to extract fibrinogen from a patient's blood [5]. Aprotinin controls the enzymatic degradation of fibrin scaffolds and gels by inhibiting the activity of plasmin secreted as cells migration or during the wound healing process [6]. Fibrin plays a particularly important role in the ECM during wound repair by capturing PDGFs and TGFβs to promote angiogenesis [7]. Due to its ubiquity, fibrin hydrogels have been successfully used in tissue engineering applications involving smooth muscle cells for vascular formation [8] and chrondrocytes for cartilage reconstruction [9].

Following injury to local vasculature, circulating platelets bind to collagen in the surrounding ECM, triggering a signaling cascade leading to the binding of fibrinogen by the platelets. Coagulation of blood in the wound proceeds through either an intrinsic pathway, caused by contact activation in associated with collagen by the platelets or an extrinsic pathway, caused by the rapid release of prothrombin and its activation to thrombin via prothrombin interaction with factors Xa and Va. This generation of thrombin promotes the activation of further downstream coagulation components, ultimately leading to the activation of factor X. Factor X is then activated by either factor VIIa and Ca^{+2} or the tenase complex formed by factor IX and VIII on the platelet surface through the extrinsic and intrinsic pathways respectively.

Activated factor X interacts with the platelet cell membrane and its cofactor, factor V, and Ca^{+2}, to form a prothrombinase complex that converts prothrombin to thrombin. The cleaving of the fibrinogen Aα and Bβ polypeptide regions by thrombin results in a drastic increase in fibrinogen hydrophobicity during its conversion to fibrin, causing precipitation of the protein [10]. As fibrin is formed, it is further stabilized by thrombin activated factor XIIIa which acts as a transglutaminase that chemically crosslinks glutamines within the fibrin amino acid sequence to lysine in other fibrin molecules, increasing its resistance to proteolytic degradation [11].

The biological role of fibrin as a sealant and temporary scaffolding has led to its clinical usage primarily as a hemostatic sealing agent with several FDA approved sealants available such as Tisseel® and Evicel™ by Baxter and Ethicon, respectively. Besides its usage as a fibrin glue, fibrin is also currently being used for tissue engineering applications in the form of hydrogels and microbeads. Due to its ubiquitous nature, fibrin has been used for cardiovascular, muscular, angiogenic, and neuronal tissue engineering applications amongst others.

In particular, fibrin has been used in nerve guides as a luminal filler in short gap studies [12]. Neurites are particularly adept at navigating fibrin due to their ability to enhance fibrinolysis through plasmin secretion at the neurite tip as demonstrated by the reduction of neurite outgrowth of embryonic chicken dorsal root ganglia when aprotinin, a plasmin inhibitor, was added to cell culture media [13, 14]. In the late 1990's, fibrin glues were shown by several groups to successfully reconnect dorsal root stumps to the spinal column [15].

2.1.3 Collagen as a tissue engineering material and physiological role

Collagens have high levels of structural variation with at least 28 types having at least a single triple-helical domain [16]. A triple helical structure is a defining feature of collagen where three procollagen strands aggregate together through a combination of hydrogen and covalent bonds during their biosynthesis [17, 18]. Stabilization occurs through the combination of a glycine residue present every third amino acid in the chain backbone resulting in characteristic ~65 nm banding structures repeat when viewed under TEM [19]; interchain hydrogen bonding caused by the high amounts of proline and hydroxyproline [20]; and electrostatic association between lysine and aspartic acid residues [21]. Collagen mechanical properties can be further enhanced through the addition of chemical crosslinkers [22], physical gelation treatments such as freeze drying [17, 23], and blending with other materials to form composites [24-26], making collagen a remarkably flexible biomaterials engineering material. Physiological collagen can be degraded enzymatically through collagenase secretion by cells, allowing the material to be remodeled after implantation. Collagen applications include use as a tissue culture substrate, in liver [27], skin [28], and nerve repair [29]. Following implantation, secretion MMP-1 by cells will preferentially degrade collagen I while denatured collagens such as gelatin are degraded by MMP-2 [30].

Electrospinning of collagen is not new as several groups have shown the capacity to electrospin the material into nanofiber meshes using organic solvents. Deliberation exists within the literature as to the effect organic solvents have on the collagen during the spinning process. Some groups argue that the use of organic solvents denatures the collagen fibers into gelatin, yielding nanofibers meshes made up of gelatin rather than collagen, reducing some of the bioactivity and reducing the biomimicry of the electrospun collagen nanofibers to the native ECM [31, 32]. Others argue that electrospun collagen nanofibers still maintain good biological properties and that the striated structure of collagen remains even after electrospinning using organic solvents [33].

Denaturation of the triple helical structure of collagen into their individual fibril strands results in the formation of gelatin. Collagen denaturation is most frequently obtained via combined acidic and thermal treatment or exposure to strongly basic solutions. It is simple to make hydrogels through decreases in temperature causing physical entanglement of the gelatin strands although these gels tend to have weak mechanical properties and need to be modified for improved strength [34].

2.1.4 Hyaluronic acid as a tissue engineering material and physiological role

Similar to collagen, hyaluronic acid is particularly prevalent throughout the body and found in most tissues to some degree [35]. HA is a particularly important glycosaminoglycan (GAG) composed of (1-4)-linked β-D-glucuronic acid and N-acetyl-β-D-glucosamine repeats in a linear chain. Physiologically, it plays a role in wound healing, helping to promote hydration of the wound and helps lubricate load bearing joints. Its high level of hydration makes it highly compatible with collagen and alginate hydrogels to form composite materials [22, 36]. Hyaluronic acid hydrogels can be specifically degraded in vivo by hyaluronidase [37]. HA can be used in many applications including bone fracture healing [38] and are excellent for soft tissue reconstruction due to their weak mechanical properties [39].

2.2 Methods

2.2.1 Alginate hydrogel fiber spinning

Alginate fibers form the basis of electrospun hydrogel fiber spinning due to the ease with which they rapidly gel for through ionic crosslinking to form highly aligned fibers. To generate these fibers, seaweed derived alginate (Sigma) or higher purity alginate (Pronova) is dissolved at a concentration ranging from 0.5 wt% to 3 wt% in a solution of 0.2% polyethylene oxide (Mz 4,000,000, Sigma) in DI water. Lack of ions is highly important in the solvent for alginate to not only ensure clean electrospinning but to also prevent premature gelation of the material. Typical usage of the material is at 1.5 wt% alginate as this provides good mechanical properties without running into viscosity issues that may occur at compositions higher than 3.0 wt%. Alginate fibers are best spun into strings and filaments over sheets due to the low interaction between adjacent strings on the collection bath resulting from rapid saturation of the available negative charge site on an individual strand during its formation. Because of this, sheets tend to be difficult to make as the strands will easily slip past one another, preventing sheet formation of reasonable quality.

Due to its rapid crosslinking capability, alginate makes an excellent sacrificial material when blended to form an interpenetrating network fiber with a secondary biomaterial that is crosslinked in a non-ionic manner, such as when alginate is blended with a secondary material like methacrylated gelatin that is crosslinked under UV irradiation when photoinitiator is added. As the ionic gelation of alginate with divalent cations are a reversible form of bonding, a chelating agent such as sodium citrate can be used to strip away the crosslinking ions, allowing alginate to have a lower effective molecular weight and thereby can freely diffuse away from the remaining secondary structure, in this example the UV crosslinked gelatin.

Alginate mechanical properties are primarily determined by the rotation speed of the collection bath and the divalent cation concentration in the bath at a given alginate molecular weight. Increases in collection bath rotation speed generate higher mechanical strain rates during fiber formation to better captures the initial alignment induced by the electric field. An upper limit on the mechanical strain that can be applied to alginate is present due to collector design as a balance must be struck between high alignment features versus risk of jettisoning the collection bath solution due to the centripetal force of the collector rotation. This is a limiting feature of the hydrogel spinning setup and restricts the minimum fiber size to diameters that are higher than the nanometer scales that can be achieved with a traditional dry electrospinning collector setup with its substantially higher collector rotation rates. Cation concentration can, to a minimal extent, affect the mechanical properties. Once minimum cation concentration in the collection bath is established to form stable alginate fibers, increases in cation concentration will result in additional crosslinking up until the point at which the available crosslinking sites are saturated, at which point no further gains in mechanical properties would be expected without secondary covalent crosslinking.

2.2.2 Fibrin hydrogel fiber spinning

Electrospun fibrin hydrogels are primarily spun from a fibrinogen precursor polymer solution that is prepared just prior to spinning by dissolving fibrinogen in 0.2 wt% polyethylene oxide (M_z 4,000,000, Sigma) in DI water and placing the solution in a 37C water bath for a minimum of 15 minutes, using longer times for higher wt% compositions. Typical solution composition ranges from 0.5 wt% fibrinogen up to 3.0 wt%. Normally, fibrinogen solutions are solubilized in a saline solution such as 0.9% NaCl as they are only metastable in DI water and will precipitate over the course of a couple hours. This is a limitation for spinning fibrinogen due to the disruption of the polymer jet formation that occurs as additional charge carriers are added to the precursor solution, in this case Na^+ and Cl^-. Some batch to batch variability exists between different stocks of fibrinogen due to bovine sourcing differences. This manifests itself as differences in precipitation rates depending on fibrinogen batch. Should a batch of fibrinogen precipitate too rapidly, the user must filter the solution with a 0.22 μm filter prior to spinning else the precipitated material will disrupt the jet and/or yield significant amorphous regions within the fibrin hydrogel fiber.

The collection solution used for forming fibrin hydrogel microfibers is based on mimicking the native blood coagulation pathway by using thrombin as a pseudo-crosslinking agent. In the blood coagulation pathway, thrombin acts by enzymatically cleaving end peptides on fibrinogen to drastically increase hydrophobicity of the protein, causing rapid precipitation of the fibrinogen to form a fibrin clot [40]. The speed of this clot formation can be increased as thrombin concentration increases [41, 42], allowing the formation of pure fibrin hydrogel fibers when thrombin concentrations of 10 U/ml or higher are used or blended fibrin-X fibers with thrombin concentrations of 2U/ml or higher. The resultant fibrin fibers have high elasticity and can be relatively rapidly degraded through treatment with plasmin, the native protein that fulfills this role, making it an excellent temporary scaffold material [43]. Degradation lifetime can be improved through treatment with Factor XIII, which stabilizes the structure via covalent crosslinking, without significantly altering the mechanical properties of the material. Crosslinking speed is lower relative to alginate spinning due to a combination of thrombin's higher molecular weight reducing diffusion speed relative to calcium cations and the need enzymatic fibrinogen cleaving process being slower than ion capture.

Fibrin fibers have highest amount of versatility amongst the big three materials used for electrospun hydrogel fiber spinning (alginate, fibrin, and collagen) as its ease of handling and relatively high hydrophobicity promote its use to form strings, sheets, and tubes. Additionally, as no component in the process is synthetic, there is very minimal chance of inducing inflammation processes associated with immunomodulatory cells interacting with chemical sequences they are unfamiliar with, typically a problem when non-zero length crosslinkers are used [44]. Fibrin strings collected can be air dried under strain to yield mm+ diameter fiber with very high alignment features and have been used for forming blood vessels *in vitro* [45]. Shorter spin times can yield fibrin filaments with low diameters in the range of 40 to 120+ μm that can be used as filler within nerve guidance conduits to provide topographical cues for Schwann cell and neuronal infiltration by providing a better physical guiding cue than found in a random fibrin clot. Through use of a linear stage, which rasters the landing position of the fibrinogen jet on the thrombin collection bath, fibrin sheets can be generated. Fibrin sheets, once formed, can be collected as sheets using an end-over-end wrapping technique with a plastic frame, tubes when wrapped around a PTFE coated mandrel during collection, or pulled out of the solution directly with tweezers to yield strings with more ribbon-like characteristics relative compared to non-rastered fibrin string collection.

2.2.3 Collagen hydrogel fiber spinning

Electrospinning of collagen hydrogel fibers provides a biorecognizable substrate with the capacity to be more persistent upon implantation relative to usage of fibrin fibers with their relatively rapid degradation rate. Isolation of the type-specific metalloproteinase enzymes involved in collagen fiber assembly in the extracellular space is more difficult than isolation of thrombin used for the biological pathway mimicking assembling of fibrin. To get around this issue, the carboxylic groups of aspartic and glutamic acids within the collagen primary structure can be rapidly crosslinked to the amine groups of lysine and arginine using 1-ethyl-3-(3-dimethylaminopropyl)carbodiimide hydrochloride (EDC) to form an aligned fiber. A drawback of this process is that a high amount of EDC is needed per spin due to the need to very rapidly crosslink to capture alignment. Additionally, EDC’s short half-life in aqueous conditions limits the collection bath usage time to ~1 hr before exchanging to a fresh collection solution. The short half-life of EDC by itself is usually remediated by addition of sulfo-(N-hydroxysulfosuccinimide) (NHS) which stabilizes the EDC for bioconjugation reactions. Experiments testing NHS addition to EDC for collagen spinning did not yield successful fibers due to the increase in crosslinking reaction time with both EDC and NHS in the collection bath.

To make the fibers, 1.2 ml of a stock of 1.0 wt% calf skin derived collagen solubilized in 0.075 M citrate solution at pH 3.7 with 0.01% NaN_3 (Elastin Products Co.) is aliquoted into 2.0 ml round bottom Eppendorf tubes that have 2.4 mg dry PEO per tube in a biological safety cabinet several days before the day of spinning. Once aliquoted, the Eppendorf tubes are inverted to allow collagen to soak up any PEO powder that was above the solution line. Tubes are then oriented upright and briefly vortexed to ensure mixing of the PEO into the 1.0 wt% collagen solution. This adds bubbles to the solution which would impair spinning so collagen aliquots are placed in a rack and stored at 4°C for several days to remove air bubbles and allow time for the PEO to fully solubilize and mix with the collagen.

A linear stage is setup as in the fibrin cardiac sheet spinning setup if sheets are desired, otherwise collagen fibers can be spun as a bundle. A single syringe pump is set to a flowrate of 3.25 ml/hr in either case, though this flowrate is tailorable to the application. Collagen fibers are spun onto a crosslinking solution consisting of 40 mg/ml EDC. A byproduct of the EDC crosslinking reaction is urea, which can cause a yellow discoloration of the collagen fibers. This tends to be more significant during second or third spins using the same collection solution, where more EDC has been reacted yielding more of the byproduct. Collagen fibers are soaked overnight in DI water to remove the urea before further processing. Collagen fiber sheets will be ready for use in most *in vitro* applications involving cell seeding following the overnight soak unless further drying is required for the downstream application.

2.2.4 Gelatin hydrogel fiber spinning

Gelatin requires conjugation of photo-reactive groups and usage of alginate as a temporary scaffold to spin making it an excellent example of hydrogel fiber made through UV mediated crosslinking. Gelatin was first methacrylated by solubilizing porcine gelatin at a concentration 5g gelatin per 50 ml PBS at 60°C with stirring before reduction of temperature to 50°C and dropwise addition of methacrylic anhydride (Sigma) at 1.6 ml anhydride per 10 ml gelatin solution. The reaction is allowed to proceed for 1 hour to form methacrylated gelatin (GelMA). The GelMA is dialyzed against DI water at minimum overnight before being frozen down in a -80°C freezer and lyophilized for two days. Lyophilized GelMA is placed an Eppendorf round bottom tube before addition of 1.5 wt% AG with 0.2 wt% PEO in the same manner as HA spinning to yield a final GelMA concentration of 1 or 2 wt%. The photo initiator Irgacure 2959 is added to the GelMA + AG solution and collection bath at a final concentration of 1 wt% to eliminate loss of the photoinitiator to diffusion.

Spinning of GelMA is onto a collection bath consisting of 50 mM $CaCl^{+2}$ which has 1.0 wt% Irgacure added to balance out diffusion forces that would otherwise cause the photo initiator in the precursor solution to diffuse away. After the spin is complete, the GelMA-AG fiber is removed and placed on cell culture dish where it is exposed to a UV lamp for approximately 60 seconds at an intensity of 900 mW/cm^2 to crosslink the GelMA. Once crosslinked, the GelMA-AG fiber is soaked in 250 mM sodium citrate overnight to remove alginate, leaving behind the soft gelatin fiber. GelMA is advantageous in that it can easily be mixed with alginate, unlike fibrin, and in a manner similar to the thiolated HA, allowing the three to be potentially used as an AG-HA-Gel system. The crosslinking system is much cheaper for GelMA than HA enabling its use even with the high crosslinker bath solutions. Despite these advantages GelMA was latter supplanted by collagen fibers for cell culture use as the collagen is not denatured, can be spun as a pure material with better mechanical properties, and does not require the additional methacrylation step to enable cross-linking. While not used for a majority of experiments, there still remains potential GelMA use in applications where very soft materials and alignment are needed as the mechanical properties can be tuned by altering the relative proportion of alginate and GelMA mixed together in the precursor solution. It should be noted that due to the lower mechanical properties of gelatin relative to collagen, the EDC crosslinking bath method with collagen does not work with plain gelatin, as any potential gelatin fiber is too weak to handle.

2.2.5 Hyaluronic acid hydrogel fiber spinning

Hyaluronic acid (HA) is not directly spinnable as a pure material like alginate, fibrin, and collagen hydrogel microfibers. Instead, it must be mixed with alginate, which is used as a temporary scaffold while the HA is crosslinked. For our preliminary studies using HA, a thiolated HA was used to enable use of an acrylated poly(ethylene glycol) (PEG) as a crosslinking agent via Michael Addition. Lyophilized thiolated hyaluronic acid is added to a round bottom Eppendorf tube so that there is a final composition of 1 wt% HA when 1.2 ml of 0.75 wt% alginate in 0.2 wt% PEO solution is added. Mixed solution was given at least 4 hours at 37°C to dissolve completely. High levels of negative charge in the repeat units of both alginate and hyaluronic acid enable their excellent mixing in aqueous solutions to form an interpenetrating network hydrogel fiber when exposed to the crosslinking agent without precipitation of the two materials in the precursor solution. The crosslinking bath for the thiolated HA consists of 50 mM Ca^{+2} for rapid crosslinking of alginate with addition of an eight armed acrylated PEG at 1.43 wt% 8 arm PEG. A diacrylated PEG (two armed) was also tested but did not yield mechanically sound HA fibers once the alginate was removed through treatment with 250 mM sodium citrate overnight due to the very soft mechanical properties native to HA hydrogels, even with the mechanical property enhancement that results from the polymer chain alignment during spinning. Unfortunately, the high cost of the acrylated PEG severely limits the use of HA hydrogel fibers due to the high volume of collection bath solutions required (typically 20 to 50 ml). Recycling of the collection bath acrylated PEG reduces this cost somewhat but requires filtering and the solution can still only be used for a few spin sessions per collection bath.

2.2.6 Synthetic 3D microfiber bundle spinning – PLGA

The electrospun hydrogel fiber setup is not limited to biologically derived materials. The spinning method can also be used to generate loosely associated bundles of synthetic polymer microfibers that are normally electrospun onto a dry surface in nanofiber form. A proof of concept for this spinning variation is the generation of PLGA microfiber bundles, where the polymer is soluble in organic solvents such as dichloromethane but not soluble in aqueous solutions. This allows the spinning of 3D PLGA bundles to be done by spinning onto a rotating bath of DI water in much the same manner as the biologically derived materials are spun, though this requires a much higher needle to wheel separation distance due to the higher viscosity of PLGA relative to alginate/collagen/fibrin/etc. The PLGA microfibers form and spread on the DI water surface, which can then be easily bundled upon removal from the wheel. The concept of spinning onto non-solvents is applicable to other synthetic polymers such as for the spinning of PCL onto aqueous media or even biologically derived polymers such as collagens and alginates onto non-aqueous medias like isopropanol if they are quenched in a separate crosslinking bath immediately following collection. To demonstrate this, 10% PLGA was dissolved in dichloromethane and then spun onto a DI water bath to generate 3D microfiber bundles for fiber analysis using SEM.

2.2.7 Mechanical property testing of electrospun hydrogel fibers

Mechanical testing of hydrogel fibers including those based on alginate, gelatin, collagen, fibrin, and hyaluronic acid were primarily done through use a Q800 DMA to measure the tensile properties. Although rheometers are typically used to measure the viscoelastic properties of hydrogels, for these materials it makes more sense to compare the tensile properties as this is the primary engineering advantage of the material and can be correlated to the ease at which cells can deform their local microenvironment and for comparison to the application tissue, whether that is for neural, muscular, or cardiovascular applications. Tensions tests were always performed with the DMA in ramp force mode with increasing force applications of +0.05 N/min for hydrated samples and +0.25 N/min for dried sample. Generally, tests were performed on hydrogel fiber bundles or strings as opposed to sheets, which were more difficult to setup and whose cross-sectional dimensions were more difficult to quantify for engineering stress calculations. Dried fibers were dried at least overnight prior to testing. As the DMA lacked an environmental chamber for hydrated fiber testing, hydrated samples were stored in solution until just prior to testing so they could be loaded into the DMA clamps hydrated and remain so until testing was complete within four minutes of sample loading. All tests were run until failure and no cyclic testing was done due to limited lifetime of hydration of hydrated samples. Use of a custom built bioreactor enabled testing of fiber mechanical properties in fully hydrated conditions for measurements taken characterizing the effect of alginate-fibrin ratio and treatment of alginate-fibrin composite fibers with alginate lyase at 1-2 U/ml for 24 hours to remove alginate [46].

2.2.8 Optical transparency measurements of electrospun hydrogel fiber sheets

The ability to spin collagen and fibrin microfibers into sheet form enables these to be used as a backing for amniotic membranes (AM), which on their own have very weak mechanical properties despite their desirable growth factor capture and extracellular matrix structure. Collagen and fibrin sheets were spun and then the optical transmittance of the two materials were measured using a plate reader (BioTek Synergy 2) at 50 nm wavelength intervals from 200 nm to 800 nm for comparison against water to encompass ultraviolet, visible, and IR wavelength ranges in hydrated conditions using n = 3 samples per fiber type. Following initial testing of transparency of the two materials, selection of the fiber sheet with best transparency was made and used for backing with the AM membrane though EDC/NHS crosslinking and high applied pressure to fuse the two materials together. For the collagen sheet-AM composite membrane, the optical properties were measured at 20 nm intervals from 200 to 800 nm wavelengths to ensure that the composite could enhance the mechanical properties of the AM membrane without reducing optical clarity for corneal patch applications. The effect of collagen fiber sheet thickness was also investigated to determine if there was a reduction in optical clarity as sheet thickness increases.

2.2.9 Graded ethanol drying and lyophilization of fibrin fiber tubes for vascular graft preparation

Fibrin fiber tubes for vascular grafts were dried through use of either lyophilization or a graded ethanol dry. Lyophilization of grafts were performed by freezing fibrin tubes in a -80°C freezer after several hours minimum soak in DI water to remove excess thrombin and salts. Once frozen, fiber tubes were placed in a lyophilizer for approximately one day. Once lyophilized, tubes were removed from the mandrel.

Graded ethanol drying follows the same salt and thrombin removal steps as lyophilization. At this point, fibrin tubes, while still on mandrels, are placed sequentially into increasing concentrations of ethanol for a minimum of 15 minutes at each step going from 0, 25, 50, 70, 80, and 90% EtOH. At 90% EtOH, fibers are soaked overnight to minimize cracking during drying. Once this is complete, fibrin fiber tubes are soaked for a minimum of 15 minutes each in 95% and triple soaked in 100% EtOH. Once the sequence is complete, the dehydrated fibrin tubes are left to dry in open air a laminar flow hood before being removed from the mandrel.

2.3 Results and Discussion

2.3.1 Effect of biological material type on mechanical properties

Comparisons of the mechanical properties of alginate, fibrin, gelatin, and hyaluronic in the dry, hydrated-as-spun, and rehydrated states were made early on during development of the electrospun hydrogel microfiber platform to get an idea of the mechanical property range, and therefore tissue types, that these fibers could be potentially be applied to. Of the materials tested early on, alginate had the highest degree of stiffness in the dry, hydrated, and rehydrated states at stiffnesses of 10^4 MPa, nearly 1 MPa, and 100 MPa respectively (Fig. 2.1). Fibrin had the second highest stiffness of the materials tested in the three conditions followed by gelatin gibers and finally hyaluronic acid fibers which were the softest. The resultant range of stiffness ranged from ~1 kPa to 1 MPa in the hydrated state depending on the material spun. Particularly useful mechanical properties were measured with the rehydrated fibrin fiber group, which had elastic moduli very similar to the native sciatic nerve. The rehydrated mechanical properties for all four materials lie in between the hydrated and dry properties, making it very important to understand what properties are required for the final application of the fibers as the storage, whether staying hydrated or being dried first, will have an impact on the final fiber mechanical properties. It is hypothesized that the fibers do not fully regain their hydrated properties when rehydrated due to the increased Van der Waals interaction between fiber chains after drying limiting infiltration of solution and therefore decreasing cross sectional area when rehydrating, causing engineering stress to increase although the individual fiber mechanical properties on a micro-scale likely remain the same. Further tests could potentially be done use AFM for force analysis to determine if this is true on the micro-scale, regardless the material type and hydration configuration can be used to match the mechanical properties of the target native tissue.

2.3.2 Precursor solution weight % effect on fiber strength

The elastic moduli of fibrin fibers could be easily tuned through alterations in the weight % of fibrinogen solutions spun. Resultant tensile properties increased as fibrin composition increased. 1 wt% fibrin fibers had lowest elastic moduli at 35 kPa which increased to 50 kPa, 62 kPa, and 68 kPa at 2, 3, and 4 wt% fibrin fibers respectively (Fig. 2.2). Decreasing levels of increase with wt% change occurred when moving to higher wt% fibrin fibers as a result of the decreased fibrinogen solution stability, where solutions of increased wt% fibrinogen tended to have reduced stability and more readily precipitate out as amorphous fibrinogen clumps. When spun, these clumps provide less mechanical strength increase compared to the aligned fibrin fibers formed, thereby the increasing proportion of clumps at higher wt% spun reduces incremental mechanical property gain otherwise expected from more material being spun. The tuning of fibrin mechanical properties in this range allows it to match the mechanical properties well of several tissues that are typically in the 10s of kPa range, such as skeletal muscle and cardiac tissue, in both homeostatic and pathological states.

2.3.3 Effect of additional strain on fibrin fiber mechanical properties

While there is significant strain induced during the alignment of the polymeric chains due the combined effects of the electric field and mechanical drawing effect of the collection bath rotation, additional strain can be induced during fiber drying to further enhance the tensile properties of the fibers by substantially increasing internal alignment. To test the effect of additional strain on mechanical properties, 2.0 wt% fibrin fibers were spun and subjected to additional strains of 0%, 33%, and 66% during drying by hanging fibers between wooden posts after applying the target level of strain to the fibers. Results are shown in Figure 2.3 where the 0% strain fibers had elastic modulus measured by the DMA at just under 400 kPa when rehydrated. Additional strain to 33% during drying resulted in rehydrated fibrin fibers with a modulus of 500 kPa. Most substantial increase in stiffness occurred with the 66% strain samples which more than doubled the rehydrated stiffness at 950 kPa. This data demonstrates an easy way to further enhance fibrin mechanical and alignment properties for applications where additional stiffness or higher degrees of topographical guidance cues are needed.

2.3.4 Collector rotation speed effect on resultant dry alginate fiber diameter

Of the various spinning parameters, the rotation speed of the collection bath should also affect the resultant fiber bundle diameter by more efficiently packing together parallel strands of material as the mechanical strain of the collector rotation increases. To test this, 1.5 wt% alginate solutions were spun onto 50 mM $CaCl_2$ solutions are rotational speeds of 30, 48, and 72 RPM for 1 minute before being collected, dried, and diameters characterized under a microscope. The results of Figure 2.4 show that increasing wheel rotational velocity causes a decrease in resultant fiber diameter with these short duration spins when alginate is used. The lowest RPM yielded fibers with 35 µm diameter, increasing RPM to 48 yielded 24 µm diameter fibers, and 72 RPM had the smallest diameter at 19 µm. Fine tuning of the fiber diameter in the dry state can be achieved through manipulation of the wheel RPM although this method is less precise than using time for diameter variation. Although rehydrated diameter values were not measured, the effect of wheel RPM demonstrates that it is important to spin with consistent parameters as variation in RPM could confound the desired effects of spin time and solution composition when targeting a specific fiber diameter for a given application.

2.3.5 Effect of flow rate on diameter of short duration alginate fiber spins

While fiber bundles have many applications for tissue replacement and bulk cell culture, the effects of high radius of curvature on cells when fibers have diameters similar to the cell (~10-20 µm) are important as this will evoke a different response than flatter surfaces and fibers with diameters in this range fill an important niche between fiber bundles and traditional synthetic electrospun nanofibers. To characterize fibers in this size range, diameters of alginate fibers at 1.5 wt% and 0.75 wt% and spun for 15 seconds were measured at several flow rates to determine how finely fiber diameter could be controlled. Figure 2.5 shows the resultant fiber diameters in the dry and hydrated state of the two alginate compositions at different flow rates. As expected, reduction in flow rate yielded lower diameter fibers with the rehydrated diameters reducing from 19 µm to 11 µm for 1.5 wt% alginate as flow rate was reduced from 1 ml/hr to 0.25 ml/hr. Similar decreases were seen with 0.75 wt% alginate dropping from 14 µm to 11 µm as flow rate was reduced from 1 ml/hr to 0.5 ml/hr.

Particularly important is the demonstration with this experiment that relatively tight control of small fiber diameters can be achieved that are distinguishable from each other as separate sizes merely by changing the flow rate of the material being spun. Using flowrate as a tuning parameter helps to reduce the potential size distribution with very short duration spins compared to trying to modulate fiber size using small differences in time spun such as 14s vs 16s, where the high error in timing can obfuscate the effects of time differences when measuring fibers. Highly exciting from this experiment is the ability to generate very small diameter fibers such as the 6 µm drystate fibers when spinning 1.5

wt% alginate at a flowrate of 0.25 ml/hr. While possible to spin fibers of these diameters, the difficulty in handling increases exponentially as size decreases as even normally small effects such as solution surface tension and do much to disrupt the stability of the fiber structure when trying to use these for engineering applications. Additionally, a great difficulty of the sub 10 µm fibers is that unlike traditional electrospinning, it is not easy to prepare mats of fibers in this regime of diameter as the hydrogel nature of the fibers would cause them to merge together into a bundle rather than remaining distinct as in the preparation of PCL electrospun nanofibers meshes. Due to this, any applications using sub 10 µm fibers need to have fibers prepared and handled separately which becomes immensely time consuming to the point of being prohibitive to use. Such an example is the preparation of fiber filaments for nerve guides where the squared term in circular area = πr^2, results in massive increases in the number of fibers required to fill a given area. Going from even as small a difference as 25 µm diameter fibers down to 10 µm requires 6.25 times as many 10 µm fibers as the 25 µm ones to have the same final total cross-sectional area filled!

2.3.6 Effect of PEO and PVA composition on diameter of one-minute alginate fiber spins

PEO is added to all biopolymers that are electrospun as hydrogel fibers and acts as the “secret ingredient” that enables fiber formation to occur by providing the long polymer chains that maintain the jet in string form by avoiding polymer jet breakage. Its primary role is as a viscocifier that is drawn along by the electric field application that uncoils the long PEO chain along with the biopolymer being spun. As PEO can be spun on its own without any additional components, it was of interest to see how variation in the PEO content could be used to alter the fiber diameter of electrospun biopolymers. To test this, increasing amounts of PEO were added to 1 wt% alginate fibers and the resultant hydrated fiber diameter was measured after 1 minute of spinning. The resultant fibers were found to increase in diameter from 24 µm to just above 30 µm as the PEO increased from 0.2 wt% to 0.6 wt% (Fig. 2.6). While this effect was relatively small, the effect leveled off as PEO content was increased to 0.8 to 1.0 wt% where fiber diameters remained in the low 30 µm range.

During the early development phase of the electrospun hydrogel fiber materials protocols, PVA was investigated as an alternative viscosity agent to PEO due to its lower molecular weight potentially increasing its ability to diffuse out of the final hydrogel fiber over time more quickly than PEO, allowing cells earlier and more complete access to integrin binding sites that might otherwise be shielded by the long PEO chains. PVA inclusion to 1% alginate was compared using the same spinning conditions as the experiment with PEO, except where PVA composition ranged from 0.2 to 2.0 wt% of the material being added to alginate due to its lower molecular weight (150 kDa M_w) compared to PEO (4,000,000 M_z). Results of PVA inclusion were less clear (Fig. 2.7) as the resultant fiber diameters ranged from 25 µm to 30 µm with high overlap in standard deviation ranges for all PVA levels tested. As PVA spun materials did not spin as cleanly as PEO precursor solutions and showed less potential for tuning fiber dimension, a conclusion was made to remain with 0.2 wt% PEO and make this standard for all precursor solutions going forward.

2.3.7 Alginate as a porogen: effect on fibrin fiber mechanical properties

Spinning blended mixtures of 2 wt% fibrin with varying amounts of 1.5 wt% alginate can be used as a method to introduce additional porosity into the fibrin fibers following removal of alginate during a post spin soak in 1-2 U/ml alginate lyase or 150 mM sodium citrate solution overnight to 24 hours. Blended mixtures of fibrin with 0 to 50% alginate were sectioned and stained with H&E to quantify overall fiber porosity and correlate this to the resultant fiber stiffness when mechanically tested using a custom developed bioreactor equipped with a force sensor for in situ mechanical testing in hydrated conditions.[46] Unsurprisingly, increases in alginate composition yielded increases in fiber porosity up until a plateau is reached 42% alginate inclusion, above which there was no significant increase in porosity Figure 2.8. Likewise, fiber stiffness decreased from 8 kPa to 4 kPa going from 33% alginate to 42% alginate respectively. Higher porosity values did not further decrease fiber stiffness leading the 6 kPa to be the minimum value using porosity as a variation method with 2% fibrins.

2.3.8 Effect of total spin time on fibrin fiber diameter and swelling

While small fibrin filaments are important for applications as nerve guide fillers, larger scale fibrin fiber bundles have use for applications involving culture of tubular forming vascular cells such as smooth muscle cells (SMCs), endothelial cells, and pericytes that can be seeded on the exterior surface of the fiber bundle. The radius of curvature for such cell culture systems can be important in regard to the cellular response and subsequent cellular alignment, organization, and extracellular matrix deposition. Alterations in the total spin time of fibrinogen can form fibrin fiber bundles of variable diameters when dried and rehydrated due to the buildup of material on the same landing position in the spinning crosslinking collection bath. To demonstrate this, 2.0 wt% fibrinogen was spun for times ranging from 1.0 to 12.5 min and the resultant dry and rehydrated fiber diameters were measured (Fig. 2.9). Fiber landing position was held constant throughout the entire duration of the spin. Increases in spin time were found to generate a nearly linear increase in fiber diameter up to 10 min total spin time, at which point decreases were much smaller for both the dry and rehydrated fiber bundles. The predictable behavior of additional spin time on fiber diameter allows fibrin filaments and fiber bundles to be formed tailored to the target engineering applications, such as luminal fillers in nerve guides or large fiber bundle sizes for skeletal muscle replacement. Higher spin times. The swelling ratio could also be determined by comparing the cross-sectional area of the dry and rehydrated states. The ratio was highest at the 1 min spin at nearly 1000% swelling while the remainder of longer spin times had swell ratios leveled off around 450% cross sectional area when rehydrated. Larger diameter fibrin bundles could be formed by altering the landing position of the fibrinogen jet periodically to ensure thrombin accessibility of later-deposited material was not limited.

2.3.9 Effect of flow rate at constant spin time on fibrin filament diameter

For the preparation of fibrin filaments to be used as part of a nerve guide construct, characterization of the effects of fibrinogen solution composition and flow rate had to be characterized to determine the dry and rehydrated fibrin fiber properties as these would differ from the previous characterization done with short spin time alginate fibers due to the relatively higher hydrophobicity of fibrin fibers relative to the very hydrophilic alginate fibers. To develop a range of small fiber diameters, flow rates of 1.5 ml/hr to 4.5 ml/hr were used in conjunction with either 0.75 wt% fibrinogen or 2.0 wt% fibrinogen and the subsequent dry and rehydrated fiber diameters were measured under an optical microscope after being electrospun for 30 seconds. More variation in fiber diameter with flow rate was found with the 2.0 wt% fibrin fibers compared to the 0.75 wt% (Fig. 2.10). The lower wt% composition ranged from 10 μm dry diameter up to 17 μm with increasing flowrates and a similar trend in rehydrated diameter was seen with the rehydrated fibers increasing from 25 μm to nearly 40 μm in diameter for a range of 15 μm between all three groups when rehydrated. The 2.0 wt% fibrin fibers had much more variation in the rehydrated diameters, jumping from 40 μm rehydrated at 1.5 ml/hr flow to nearly 100 μm rehydrated when flow rate was increased to 4.5 ml/hr. Dry fibers at 2.0 wt% ranged from 15 μm to 25 μm as flow rate increased from 1.5 ml/hr to 4.5 ml/hr. Differences between 0.75 wt% fibrin and 2.0

wt% fibrin are most likely due to differences in the total amount of material being spun, as more material per unit time is deposited during 2.0 wt% fibrin preparation, leading the higher wt% fibrin fibers to be more tunable based on flowrate for a given spin time.

2.3.10 Effect of spin time at constant flow rate on fibrin filament diameter

As an alternative to tuning fiber diameter with variations in flow rate, which requires resetting syringe pump parameters between conditions and potentially changing the drawing behavior of the polymer jet in response to the electric field due to changes in the solution viscosity profile with flow rate, investigation was made into the effect of spin time on dry and overnight rehydrated fiber diameter in DI water while keeping flow rate constant at 3.25 ml/hr. Spin times characterized were 30, 60, and 90 seconds for both 0.75 wt% and 2.0 wt% fibrinogen precursor solutions. The fiber diameters measured in (Fig. 2.11) show relatively small changes in fiber diameters between 30 sec and 60 sec spin time for 0.75 wt% fibers when rehydrated but a larger relative jump in rehydrated fiber diameter is seen going from 60 sec spin to 90 sec where diameter jumps from 30 µm to just over 60 µm. Higher variation rehydrated fiber diameter was seen at longer spin times for 0.75 wt% fibrin fibers although variation remained small for dried fibers, which increased relatively linearly with time. The 2.0 wt% fibrin fibers showed higher rehydrated fiber diameter jump going from 30 sec to 60 sec where diameter increased from 40 µm to nearly 100 µm, more than doubling diameter with a doubling in spin time (Fig. 2.12). Smaller increase was found continuing onto 90 sec spins where the rehydrated diameter only increased to 120 µm. As with the 0.75 wt % fibers, the dry state 2.0 wt% fibers showed a relatively linear increase in diameter with increasing spin time. All rehydrated 2.0 wt% fibrin fibers showed at least +/- 10 µm variation in rehydrated diameter indicating that there is increasing variability in the ability of water to infiltrate between fibrin chains with differences in the total fiber diameter.

2.3.11 Effect of drying method on fibrin tube mechanical properties

Drying of fibrin for the testing done to compare materials type was done through air drying of strings after removal from the collection wheel but there exists other drying methods that can be used for other applications such as graded ethanol drying and lyophilization that have been used for investigation of fibrin tubes for vascular graft applications *in vitro* and *in vivo*. A comparison of the elastic modulus, strain to failure and ultimate tensile strength were made along with diameter measurements of the dry and rehydrated state for graded ethanol. Graded ethanol dried fibrin tubes were stiffer at 20 kPa than the lyophilized fibrin tubes at 7.5 kPa, most likely due to the walls of the tube being denser following drying with the graded ethanol treatment reducing cross sectional area for the engineering stress calculation (Fig. 2.13). UTS followed a similar trend with the ethanol dried tubes having a higher ultimate strength of 180 kPa compared to the lyophilized tubes at 50 kPa. Strain to failure was similar for both drying methods ranging from 120 to 130 % strain. The swelling behavior of the two drying methods actually did differ. Ethanol drying led to the expected swelling in tube diameter of 600 µm dry to 900 µm when rehydrated in DI water overnight. Surprisingly, the lyophilized tubes shrank slightly upon rehydration, going from 1300 µm dry to 1100 µm rehydrated, though the lyophilized results were not statistically significant. A potential reason for this could be the lack of shrinkage during lyophilzation, despite damage to the fiber alignment structure due to ice crystal formation during freezing, allowing water to fill the pores and exert a small pulling force due to the solid liquid interface.

2.3.12 FXIII treatment effect on fibrin tube mechanical properties

As coagulation factor XIII is a known covalent crosslinker of fibrin that imparts increased degradation resistance to the material, investigation was made into its viability as a method of improving the mechanical properties of fibrin based vascular graft tubes. Following normal fibrin tube production, the material was soaked in a solution of 10 mM $CaCl_2$ in 0.9 wt% NaCl containing 20 µg/ml FXIII and 4 U/ml thrombin as a cofactor overnight at 37°C before mechanical properties were tested using the Q800 DMA. FXIII treatment was tested with both graded ethanol dried fibrin tubes and lyophilized tubes and were found to slightly increase the elastic modulus of the tubes from 21 to 24 kPa for ethanol dried samples and 8 to 11 kPa for lyophilized although neither were statistically significant (Fig. 2.14). Strain to failures were relatively unaffected, remaining around 120 to 130% as seen with the previous mechanical property investigation of the two drying methods (Fig. 2.15). UTS for both materials were increased with FXIII treatment compared to the untreated samples, increase the UTS of the ethanol dried fibrin tubes from 180 to

260 kPa and increasing the lyophilized tubes from 50 to 100 kPa (Fig. 2.16). While the mechanical properties of the bulk fibrin tubes were not substantially increased through factor XIII treatment, treatment using the factor has been able to assist in stabilizing fibrin against proteolytic degradation as found by the increased lifetime of fibrin sheets in culture with neuronal cells, where sheets would remain mechanically robust for an additional two or three days compared to fibrin sheets that lacked both FXIII treatment or aprotinin addition to media.

2.3.13 Layering and drying processing effect on fibrin tube stability and cracking

Early in the fibrin tube project, investigations into the best method of drying were made to compare drying via ethanol dehydration and lyophilization. Ethanol drying was found to better preserve fibrin microstructure than lyophilization. Ice crystal formation during the freezing process in -80°C for lyophilization causes disruption to the fiber alignment structure (Fig. 2.17). There is potential to still use freeze drying as a method of drying of fibrin tubes and sheets if a cryoprotectant such as glucose is added at high concentration to reduce ice crystal formation, particularly if a more rapid freezing method is used. While modified lyophilization procedure remain a potential drying option if needed, the current protocol for graded ethanol dry is simpler to run and has proven itself to work for generating implantable fibrin tubes.

The specific drying sequence used for implantable fibrin fiber tubes is a sequential ethanol drying starting at 25% EtOH and progression upward in EtOH concentrations of

50%, 70% and 80% for a minimum of 15 minutes each. At this point fibrin tubes are soaked in a 90% EtOH solution overnight before continuing with additional concentrations of 95%, 100%, 100%, and finally a third 100% EtOH soak for 15 minutes each. Earlier protocols used 15 minutes for all dehydration steps but this led to some inconsistency in drying due to frequent crack formation (Fig. 2.18). Adjustment of the 90% EtOH step to overnight alleviated this problem, likely by allowing more diffusion time of EtOH into the fibrin tube and therefore improving the EtOH exchange deeper into the fibrin layers, causing more uniform drying to occur. While the specific mechanism causing the excessive cracking with 15 min cycles only has not been investigated, the overnight 90% has proven reliable for multiple batches of fibrin tube generation and can be considered standard practice for tube preparation.

2.3.14 Comparison of fibrin fiber diameters holding total mass flow constant

Variations in the resultant fiber geometric properties following spinning are predominantly controlled by three main variables. These are the weight percentage of material being spun, the flow rate, and the total spin time. The three factors can be used together to determine what is herein termed the “mass flow constant” (MFC) as defined by:

$$MFC = (wt\%) * (flow\ rate) * (t)$$

An example of which is given by a fibrin spinning condition that typically yields clean fibers:

$$MFC = (2\ wt\%) * \left(3.25\frac{ml}{hr}\right) * (10\ min) = 65$$

By holding the MFC value constant, other variables can be changed to yield the same total amount of material deposition during a given spin. Say there is need to spin a material with MFC = 65 using a 1.5 wt% fibrinogen solution that has the same total spin time of 10 min as in the previous example. Rearranging the expression yields the required flow rate needed:

$$flow\ rate = \frac{MFC}{(wt\%) * (t)} = \frac{65}{(1.5\ wt\%) * (10\text{min})} = 4.33\ ml/hr$$

Likewise, using the same expression, changes in time to 14 min spin and keeping precursor solution at 1.5 wt% can be made to yield fibers with the same total amount of material in all three example spins using the following flow rate:

$$flow\ rate = \frac{MFC}{(wt\%) * (t)} = \frac{65}{(1.5\ wt\%) * (14\text{min})} = 3.10\ ml/hr$$

This demonstrates that the three variables can be tuned as needed if the MFC is held to a constant value allowing fair comparison of different spinning conditions without having variation in total amount of material.

To test the validity of the MFC, several 2% fibrin fibers with a MFC value of 3.5 were spun altering the flow rate and spin time to compare the resultant dry and rehydrated fiber diameters. (Fig. 2.19) shows that the dry fiber diameters in all cases were very similar at ~28 µm. Rehydrated values were all centered around 80 µm for flow rates up to 3.5 ml/hr. Spins done for 15 seconds at 7.0 ml/hr showed slightly higher diameter when rehydrated at 90 µm, indicating that extreme conditions of very short spin times or high flow rates may deviate from the predictability that the MFC value has. Despite this, the MFC value remains an excellent method to rapidly generate alternative spinning conditions for a given fiber spinning condition. Holding MFC values constant provides a potential method to investigate surface topography differences on cellular organization caused by flow rate effects generating larger or smaller diameter fibers during the spin at higher or lower flow rates.

2.3.15 Swelling ratios of fibrin and collagen fibers during rehydration

The amount of swelling during rehydration is an important material property to characterize for these electrospun materials as hydrogels are known to have high degrees of water uptake and therefore swelling. This is an important design aspect of hydrogel fibers to consider as their manipulation frequently involves a dehydrating step before being rehydrated for application. The volumetric swelling ratios of fibrin, Secant collagen fibers, and EDC crosslinked electrospun hydrogel collagen fibers were measured by comparing their dry and rehydrated diameters after overnight exposure to DI water. Fibrin spin time was varied to determine if the final swelling ratio was significantly impacted by changes in that parameter. (Fig. 2.20) shows the resultant fiber diameters and volumetric swelling ratios after soaking in DI water overnight. Changes in fibrin spin time has minimal impact as these fibers all showed swelling ratios in the high single digits despite increases in fiber diameter causing decrease in surface area to volume ratio. Secant collagen fibers showed similar volumetric swelling ratios to the fibrin fibers. Small diameter EDC crosslinked electrospun hydrogel collagen fibers showed a dramatic increase in swelling with a volumetric swelling ratio just over 40. This is a result of the dramatic increase in fiber diameter to 400 µm from a dry fiber in the 60 µm range, similar to the dry fiber diameters seen with the fibrin and Secant collagen fibers. This result implies that the combined effects of what are likely to be increased crosslink mesh size and the greater hydrophilic properties of electrospun hydrogel collagen fibers relative to fibrin fibers. Surprisingly, the Secant collagen fibers and electrospun hydrogel collagen fibers had vastly different swelling properties, an indication that processing differences can have a massive impact on the resultant swell properties.

2.3.16 Rehydration of alginate, fibrin, and collagen fibers with time

The speed at which the hydrogel fibers swell to their maximum size is an important design consideration for any application where fibers may need to be applied dry such as applications involving injection of fiber filaments or potential blockage applications. Hydrogel fibers composed of 2 wt% fibrin, 1 wt% collagen, and 1.5 wt% alginate were spun and rehydrated in DI water for fibrin and collagen or DI containing 50 mM $CaCl_2$ in the case of alginate. Measurements of the dry mass after overnight air drying were taken before rehydration and then masses of alginate, fibrin, and collagen (n = 6 each type) were taken within 10 minutes immediately after rehydration, at one hour, and after 24 hours. Percent hydration was calculated as the ratio of the hydrated mass to dry fiber mass. All three materials showed relative little difference in hydration with time (Fig. 2.21). Primary differences between materials were the hydration level which is highly dependent on their relative hydrophobicity or hydrophilicity. Being relatively hydrophobic, fibrin only showed hydration levels in the low 80% range. Alginate fibers had higher hydration levels in the high 80%. Collagen fiber hydration level approached 95%, results which are not surprising considering the massive level of swelling seen with the material being highly hydrophilic. Notably all three materials have the high levels of hydration that define a hydrogel material, typically by having 90% or higher hydration levels. Alginate and collagen fibers clearly fit into the typical hydrogel hydration range while fibrin fibers could be defined as quasi-hydrogel fibers due to their relatively high hydrophobicity limiting solution uptake after rehydration. While data is not shown here, as-prepared fibrin fibers contain higher levels of hydration than those that have been air dried. It is hypothesized that the air drying of fibrin enables van der waals forces to play a larger role in the fibrin structure and prevent full rehydration by limiting the ability of solution to infiltrate the fiber core, hence reducing the total amount of solution uptake and fiber swelling, causing a reduction in percent hydration after rehydration.

2.3.17 Degradation of alginate and fibrin fibers

In vitro characterization of the degradation of alginate and fibrin were done by exposing the materials to alginate lyase and plasmin respectively. 1.5 wt% alginate fibers were spun and then exposed to DI water, Schwann cell culture media, PBS, 0.5 U/ml alginate lyase, 1.0 U/ml lyase, and 2.0 U/ml lyase in SC media for up to 72 hours (n = 3 per condition). Mass measurements were taken of the fiber after removal from degradation medium at 12, 24, 48, and 72 hours. Results shown in (Fig. 2.22) indicate that exposure to alginate lyase has the greatest impact on degrading alginate fibers, with all three concentrations tested showing increased degradation at all time points compared to DI water, Schwann cell culture media, and PBS. Degradation in all three lyase groups were similar, showing no increased % mass degraded as lyase concentration increased from 0.5 U/ml to 2.0 U/ml. Degradation for the lyase groups occurred rapidly, all showing approximately 60% mass loss after 12 hours with little change in mass loss at further timepoints. This is similar behavior to that seen with the DI water, media, and PBS groups. Surprisingly, of the three non-lyase groups, DI water showed the highest % mass degraded at > 40% mass loss compared to the 20-35% seen with media and PBS, indicating that some of the Ca^{+2} ions may be driven by diffusion out of the alginate chain and into the DI water, causing some degradation of the material. This indicates that unlike fibrin and collagen fibers, hydrated alginate fiber storage requires addition of Ca^{+2} ions to DI water or there is risk of weakening of the material over time due to degradation.

2 wt% fibrin fibers were spun for comparison of plasmin concentration on degradation when fibers were placed in media. (Fig. 2.23) shows the resultant time to

degradation of fibrin fibers at plasmin concentrations of 0.1, 0.25, 1.0, and 15 CU/ml plasmin. As expected, increases in plasmin concentration resulted in shorter times required for full degradation of the fibrin fibers. Exposure to 0.1 CU/ml plasmin resulted in fiber degradation after 24 hours. Increasing plasmin concentration to 0.25 CU/ml showed fiber degradation after 12 hours; 1.0 CU/ml plasmin exposure degraded fibers within 6 hours. The highest plasmin concentration, 15 CU/ml, degraded fibrin fibers within 1 hour. The rapid degradation of fibrin shows the need to protect fibers from proteolytic degradation during in vitro cell culture studies by addition of aprotinin. (Fig. 2.24) shows the effect of axons on fibrin sheet degradation, where secretion of plasminogen from the axon tips rapidly degrades any fibrin fibers the axons come in contact with as they move outward from a DRG explant.

2.3.18 Effect of landing position of fiber jet during sheet formation

Alterations in the relative landing position of the fiber jet can have significant implications regarding the final sheet quality by changing the width of the resultant sheet. As the linear stage moves a constant distance per pass, the width of the fiber sheet can be tuned by changing to position of the needle tip relative to the collection wheel. Generally, these adjustments can be made between the 9 o'clock and 12 o'clock positions of the wheel when looking down from above. The relative positional differences cause the rastered fiber jet to pass through the collection bath width to differing degrees depending on whether the polymer jet is landing near 12 o'clock or 9 o'clock. The 12 o'clock position causes the fiber jet to cut through the maximum possible width of collection bath during deposition to generate the maximum width sheets possible for a given linear stage raster distance. This can be highly important as the buildup of material can have negative effects if buildup of material is too high on a particular region of the wheel depending on material type and total spin time. Generally, issues are most prominent in long fibrin spins so 12 o'clock positions maximizes the spread of material as the raster moves perpendicular to the direction of fiber alignment at this position.

Fiber sheet width is reduced as one adjusts the landing position of the fibers from 12 o'clock towards 9 o'clock where width reaches a minimum as the raster is moving along parallel with the deposited fiber alignment in this position as illustrated in (Fig. 2.25). To avoid these maximum and minimum sheet width conditions, fiber sheets are most typically spun in the 10 to 11 o'clock range. This region allowed sufficient width of sheet to be formed that is easily wrapped using plastic frames or around mandrels for tube generation while also allowing some room for tuning sheet width as needed based on the amount of collection solution on the wheel and wheel RPM. Wider sheets closer to 12 o'clock can sometimes be a little too thin and the alignment during wrapping may be disrupted by air bubbles entrapped during the flipping of frames. Narrower sheets have more difficulty with stacking sheets over the same position over multiple wraps around a frame and are more difficult to wrap around PTFE coated mandrels during tube generation since fewer rotations of the mandrel can be completed, potentially skewing distribution of the fibers resulting in non-uniform wall thickness.

2.3.19 Optical properties of electrospun hydrogel fibers

The comparative optical properties of collagen, fibrin, and water are shown in (Fig. 2.26). Unsurprisingly, DI water has high transparency along all wavelengths tested. Six-layer collagen hydrogel fiber sheets have excellent transparency on par with DI water in the visible and IR spectrum but had reduced transmittance in the UV range, particularly under 325 nm wavelengths in the UVB region. Six-layer fibrin fiber sheets show reduced transparency at all wavelengths compared to collagen fiber sheets with a maximum transparency of ~60% at the IR region which steadily decreased down to 5% transparency in the UVB region. This result is not surprising as the fibrin fiber sheets have typically always been more visually opaque than the highly transparent collagen sheets. Particularly exciting is the absorbance of collagen sheets of energies in the UVB range as this infers that use of collagen fibers as an AM membrane backing can help protect the internal components of the eye from UV damage caused by exposure to sunlight during the course of repair.

The effects of collagen sheet thickness in (Fig. 2.27) show no significant difference between 7-layer and 12-layer collagen fiber sheets. It is possible that there exists a maximum thickness where the collagen sheets would begin to affect optical properties but it appears that anything under at least 12 layers of collagen will have similar optical properties.

Transparency of fused collagen fiber sheets to the AM membrane were compared against AM membrane alone, PBS, and calcified rabbit cornea (Fig. 2.28). The AM membrane and composite showed similar levels of transmittance in the tested range with a crossover point between the two occurring at 550 nm wavelength, where the lower wavelength ranges show slightly more transmittance of the composite membranes, likely due to the additional solution uptake of the collagen fiber sheet relative to the AM membrane upon rehydration. Calcified rabbit cornea showed the lowest levels of transparency showing that the replacement of calcified structures with AM membrane composites could improve optical clarity directly after implantation while cellular processes take over repair.

2.3.20 Spinning of synthetic PLGA fiber bundles

Despite the differences in equipment setup for generation of electrospun hydrogel fibers, mainly the use of a rotating collection bath, spinning of traditional synthetic electrospun materials such as PLGA can still be done. Spinning onto a non-solvent for the synthetic material allows generation of 3D fiber bundles composed of the synthetic material, such as PLGA spun onto DI water. Figure 2.29a shows the resultant PLGA microfiber bundle. As a Taylor cone is not established in the electrospun hydrogel fiber method, the fiber diameter is larger than those obtained in traditional electrospinning where the whipping instability that forms as solvent evaporates under high electric field drastically draws fibers down to submicron diameters. Escape of the solvent from PLGA fibers into the DI water bath results in the formation a pocked surface morphology (Fig. 2.29c).

2.4 Conclusions

Parameters important to characterize and tune hydrogel fiber physical properties were established to enable many options to specifically engineer hydrogel fibers for many potential tissue engineering applications and to establish standard techniques for fiber production. Mechanical properties can generally be tuned through compositional changes such as the biological polymer that is spun or the amount of material spun, which can affect both the properties and geometry of the material. Other equipment based operational parameters such as the wheel rotational speed or spinning time can be used to further fine tune mechanical properties and geometries. Swelling of hydrogel fibers are consistent with traditional hydrogels and the relative swelling behavior of the various materials spun respond based on the materials hydrophilicity, with fibrin being the least hydrophilic of the primary biological hydrogel fibers spun. Demonstration of enzymatic mechanisms of degradation ensure that hydrogel fibers have the capacity to be remodeled upon implantation and that their production and crosslinking does not prevent degradation. Post-treatment of fibers can have a large impact on both the structure and properties of hydrogel fibers as shown by the effects of drying technique on fiber tube microstructure and post-spin crosslinking of fibrin with factor XIII treatment. Materials selection can even have impact on optical transparency for applications involving ocular patch engineering where more hydrated hydrogel fiber sheets had increased transparency.

2.5 Figures

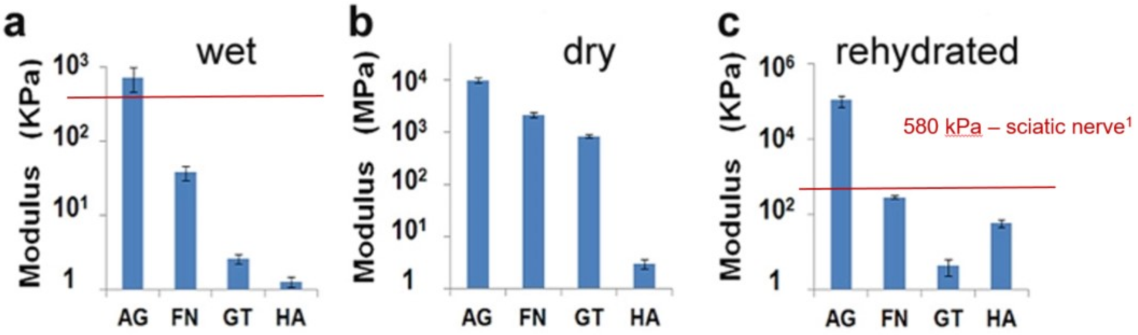

Figure 2-1: Effect of biological material type on mechanical properties.

Elastic modulus, as measured by DMA using a repeat of at least n = 3 for each wet, dry, and rehydrated condition per fiber type shows stiffness is highest with alginate fibers in all three states. Rehydrated stiffness (c) were always at intermediate values between the as spun wet state (a) and dried (b) indicating that once dried, hydrogel fibers do not fully return to their initial swelling state.

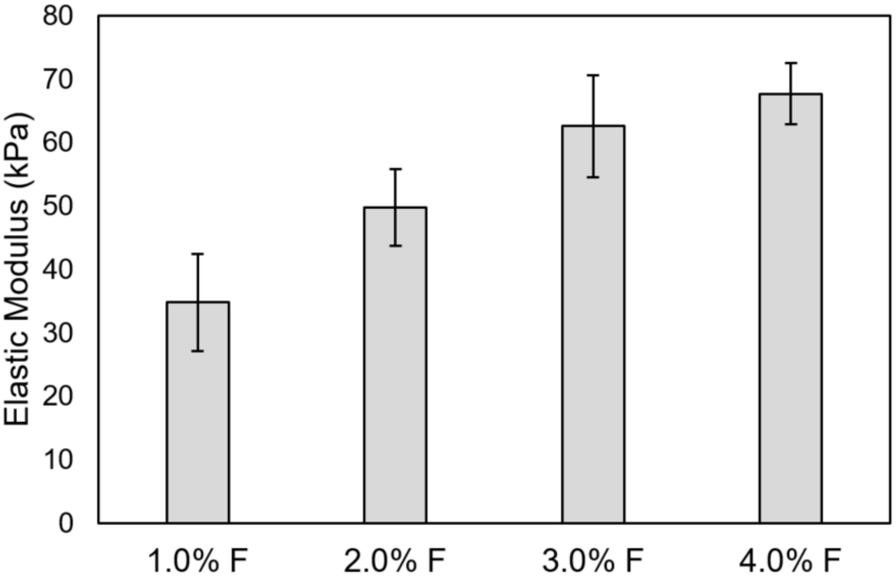

Figure 2-2: Mechanical properties of fibrin fibers increase as wt% of fibrinogen in precursor solution increases.

Hydrated fibrin fibers were mechanically tested using Q800 DMA. Higher wt% spinning solutions trended towards higher mechanical properties with highest gains seen when moving to more concentration solutions from the lower fibrinogen levels.

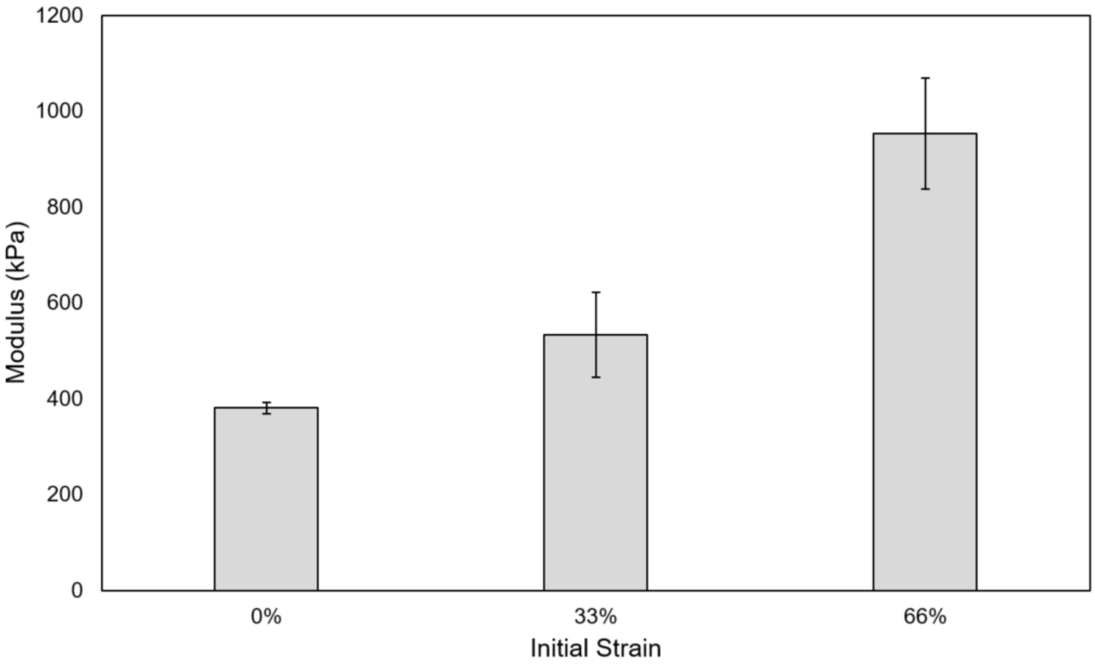

Figure 2-3: Effect of additional strain on fibrin fiber strength.

Hydrated fibrin fibers were mechanically tested using Q800 DMA (n= 3 to 6). Higher strains attained anchoring fiber ends to wooden stakes set to 0, 33% or 66% strain during air drying show large increases in mechanical properties with 66% strain enhancing strength (980 kPa) by more than double compared to 0% strain (390 kPa).

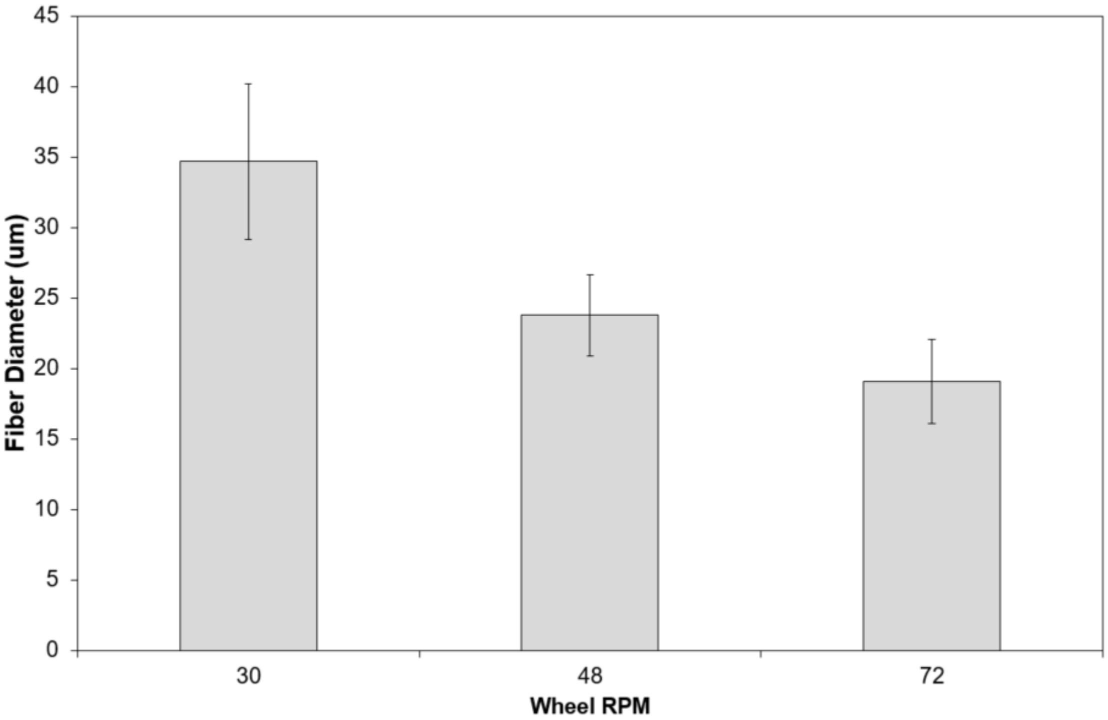

Figure 2-4: Increasing rotation speed of collection wheel reduces dried alginate fiber bundle diameter.

Alginate fibers spun onto 50 mM $CaCl_2$ for one minute with various wheel rotation speeds show over 40% reduction in alginate fiber bundle diameter when collector RPM changes increases from 30 to 72 RPM. Limitations of collection wheel design prevent RPM testing below 30 (motor cannot generate steady rotation) or higher than 72 (collection solution is jettisoned over wheel rim due to centripetal force). Fiber diameters were collected using an optical microscope by measuring least three fibers at three images per fiber and taking ten measurements per image.

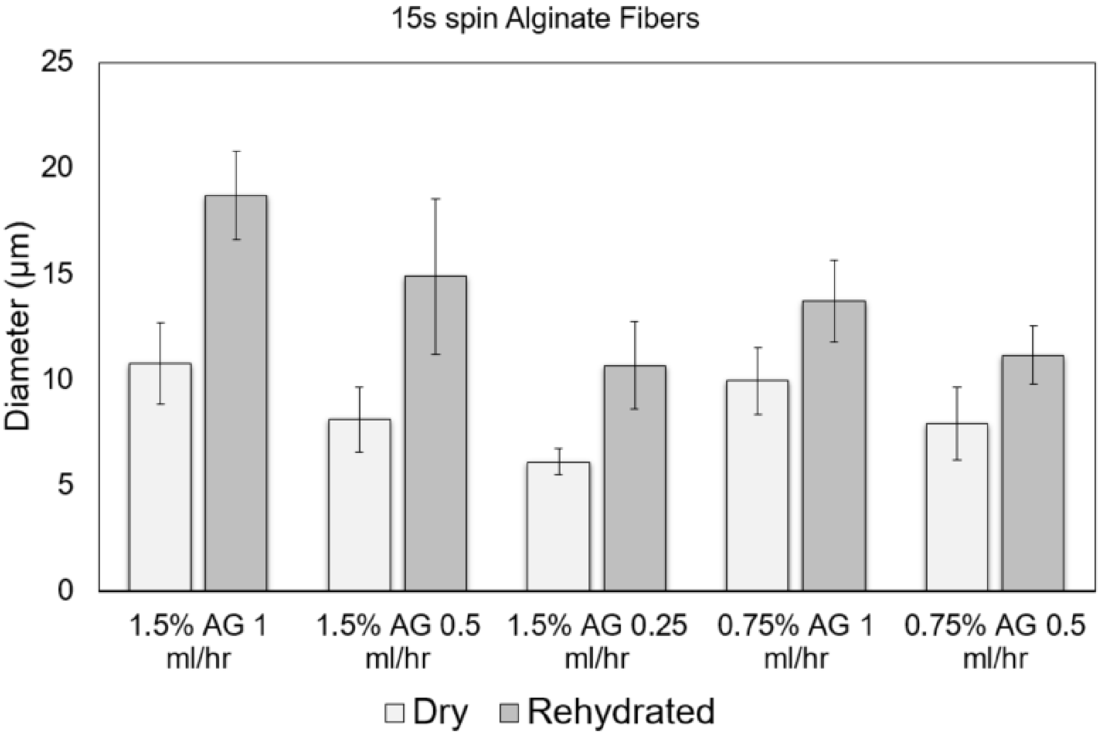

Figure 2-5: 1.5 wt% vs 0.75 wt% alginate fiber diameters after 15s spin time varying flow rate.

Alginate fibers spun onto 50 mM $CaCl_2$ for 15 seconds with flow rates ranging from 0.25 ml/hr up to 1.0 ml/hr. Higher flow rates yielded larger diameter fibers in both the dry and rehydrated states. For matched flow rates, there tended to be no significant difference between fiber diameters when dry but higher wt% alginate had more swelling during dehydration than 0.75 wt%. Fiber diameters were collected using an optical microscope by measuring least three fibers at three images per fiber and taking ten measurements per image.

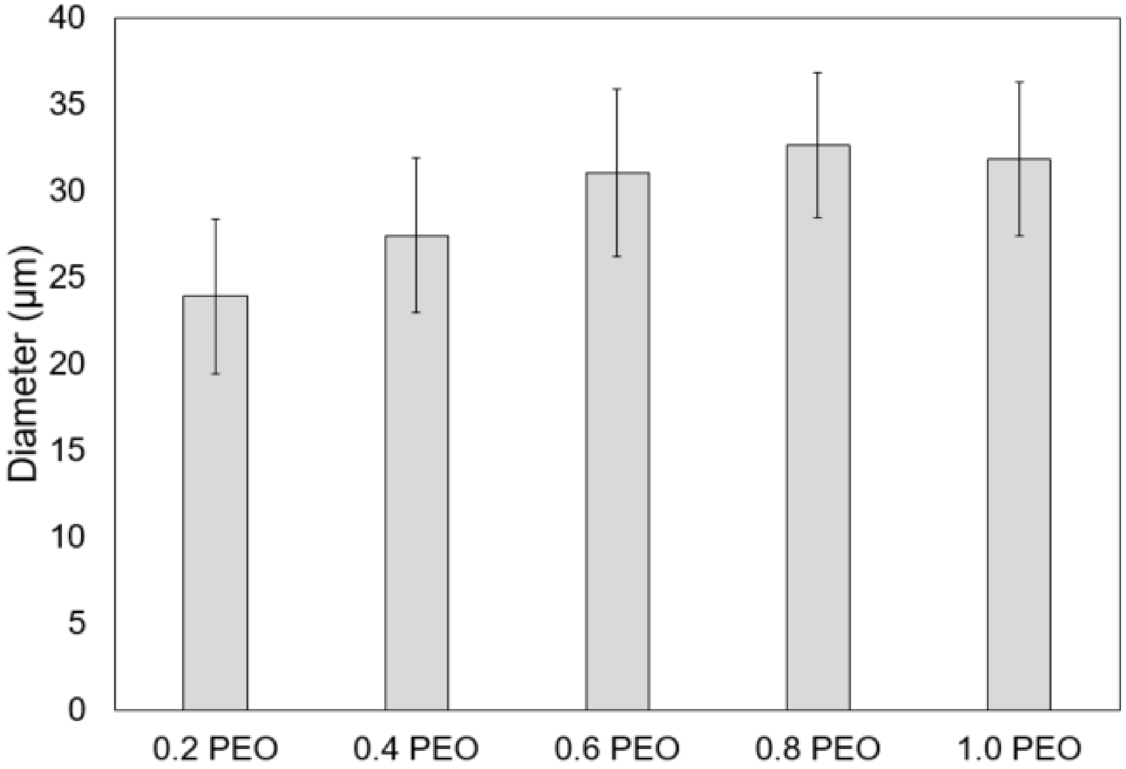

Figure 2-6: Effect of PEO composition on 1 wt% alginate fiber diameters after one-minute spins.

Alginate fibers spun onto 50 mM $CaCl_2$ for 1 minute at 2 ml/hr with increasing amounts of PEO. Higher levels of PEO yielded slightly more swollen alginate fibers up to 0.8 wt % PEO addition. Fiber diameters were collected using an optical microscope by measuring least three fibers at three images per fiber and taking ten measurements per image.

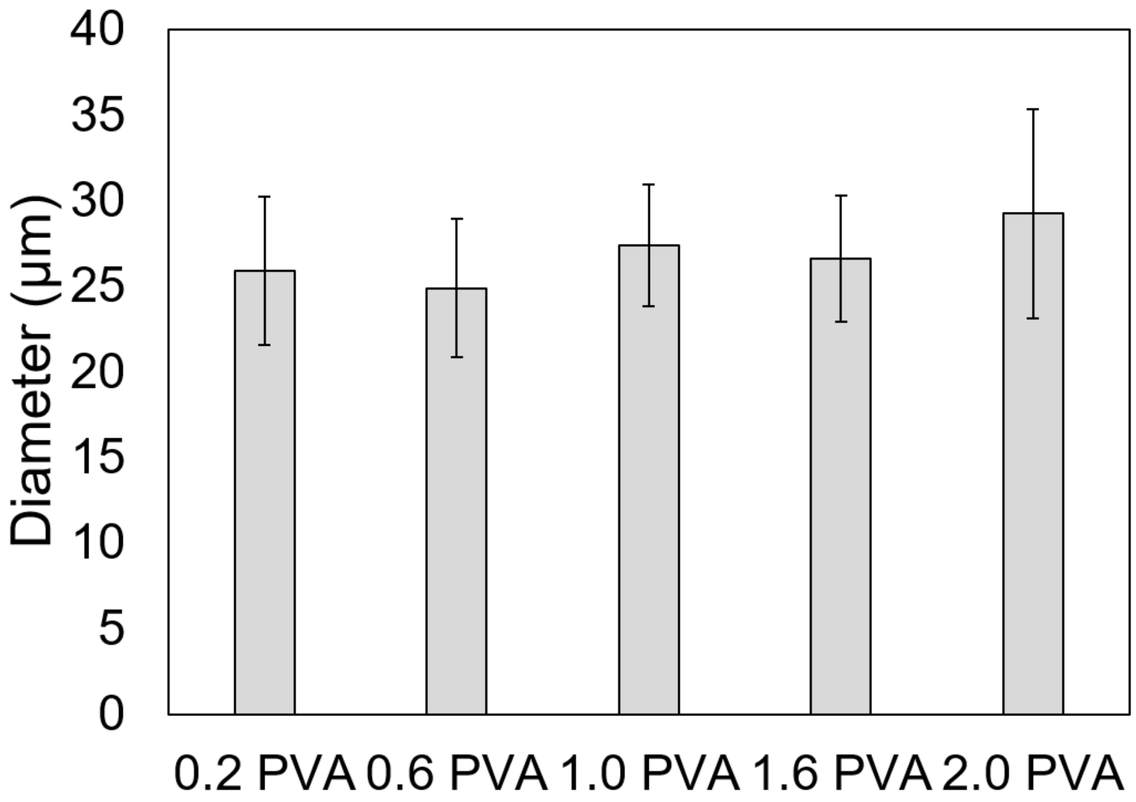

Figure 2-7: Effect of PVA composition on 1 wt% alginate fiber diameters after one-minute spins.

Alginate fibers spun onto 50 mM $CaCl_2$ for 1 minute at 2 ml/hr with increasing amounts of PVA. Different levels of PVA all had similar levels of swelling and showed comparable swelling to 1.0 wt% alginate + 0.2 wt% PEO fibers (Fig. 2.6). Fiber diameters were collected using an optical microscope by measuring least three fibers at three images per fiber and taking ten measurements per image.

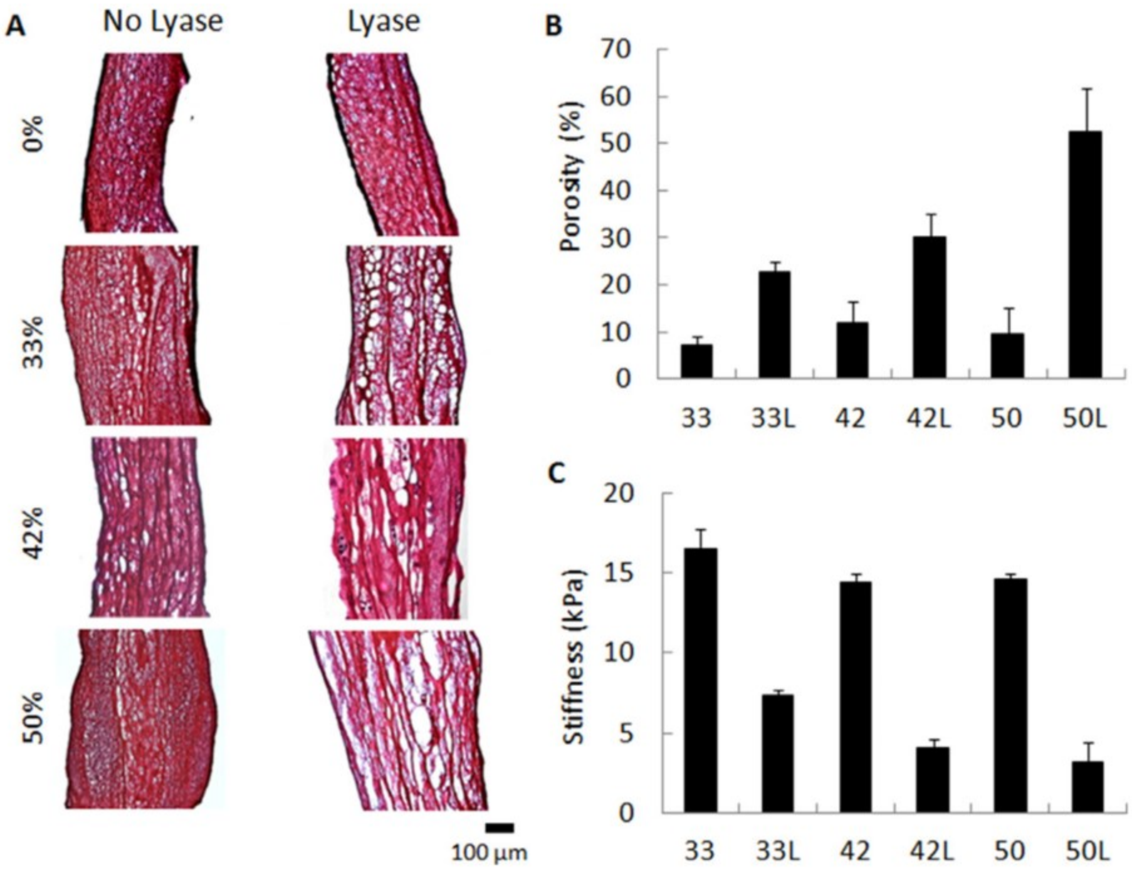

Figure 2-8: Alginate lyase treatment of alginate-fibrin fiber composites increases porosity and reduces elastic modulus.

Alginate-fibrin composite fibers were treated for 24 hours with 1-2 U/ml alginate lyase and then stained with H&E (a) for characterization of porosity (b) and mechanical property measurement in a custom bioreactor (c). Porosity increases reduced fiber stiffness once alginate was removed up to a composition of 42% alginate where further decreases in mechanical properties were not generated with higher porosity. From Cook et. al. [46]

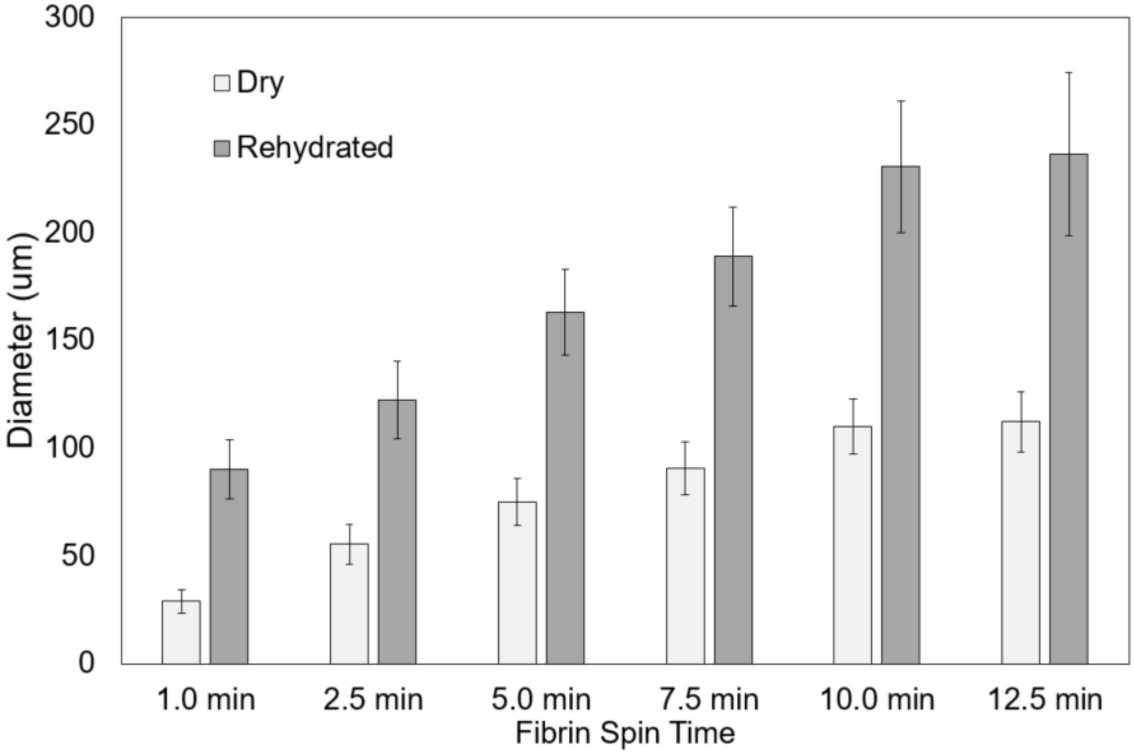

Figure 2-9: Fibrin bundle dry and rehydrated size as a function of spin time.

2.0 wt % fibrin fibers spun onto 50 mM $CaCl_2$ collection bath containing 20 U/ml thrombin for up to 12.5 minutes holding landing position constant. Fiber bundle diameter increases were seen in both dry and rehydrated state for spin times up to 10 minutes. Longer duration spins did not add much to fiber diameter due to lower fibrin aggregation efficiency as buildup of material at longer spin times limits the crosslinking capacity of fibrinogen after 10 minutes of spinning. Fiber diameters were collected using an optical microscope by measuring least three fibers at three images per fiber and taking ten measurements per image.

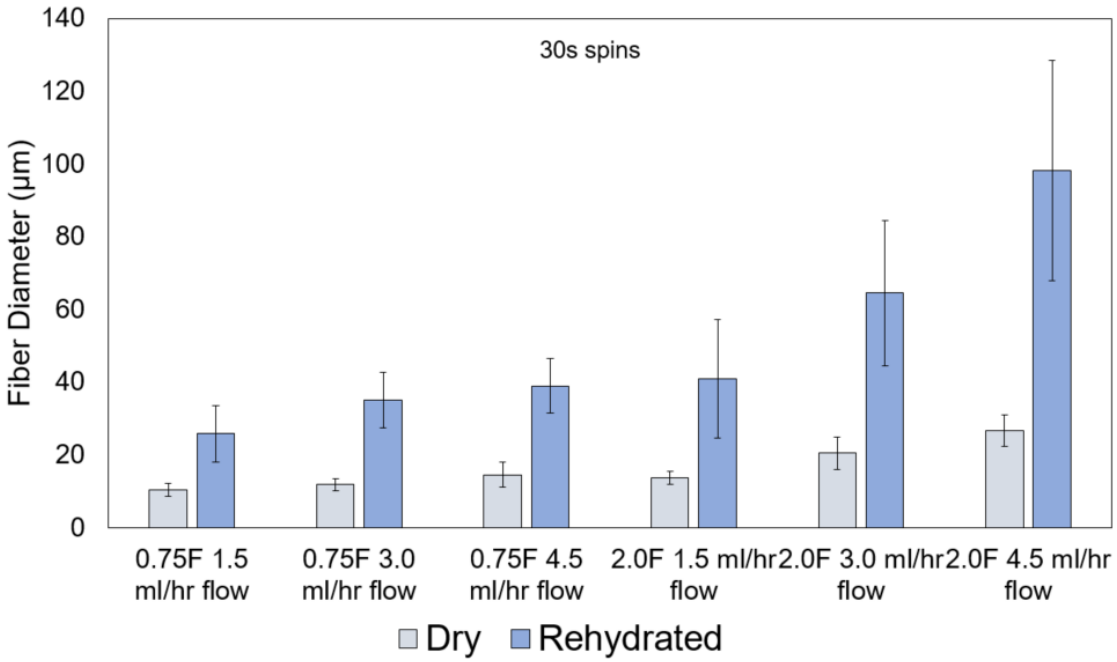

Figure 2-10: Flow rate effects on fibrin filament diameter.

2.0 wt% or 0.75 wt% fibrin fibers spun onto 50 mM $CaCl_2$ collection bath containing 20 U/ml thrombin for up to 30 seconds holding landing position constant. Increases in flow rate did not have substantial effect on the 0.75 wt% fibrin fibers due to the low amount of material deposited per unit time. Flow rate had more noticeable effects on 2.0 wt% fibrin fibers, causing more swelling of fibers at higher flow rates. Fiber diameters were collected using an optical microscope by measuring least three fibers at three images per fiber and taking ten measurements per image.

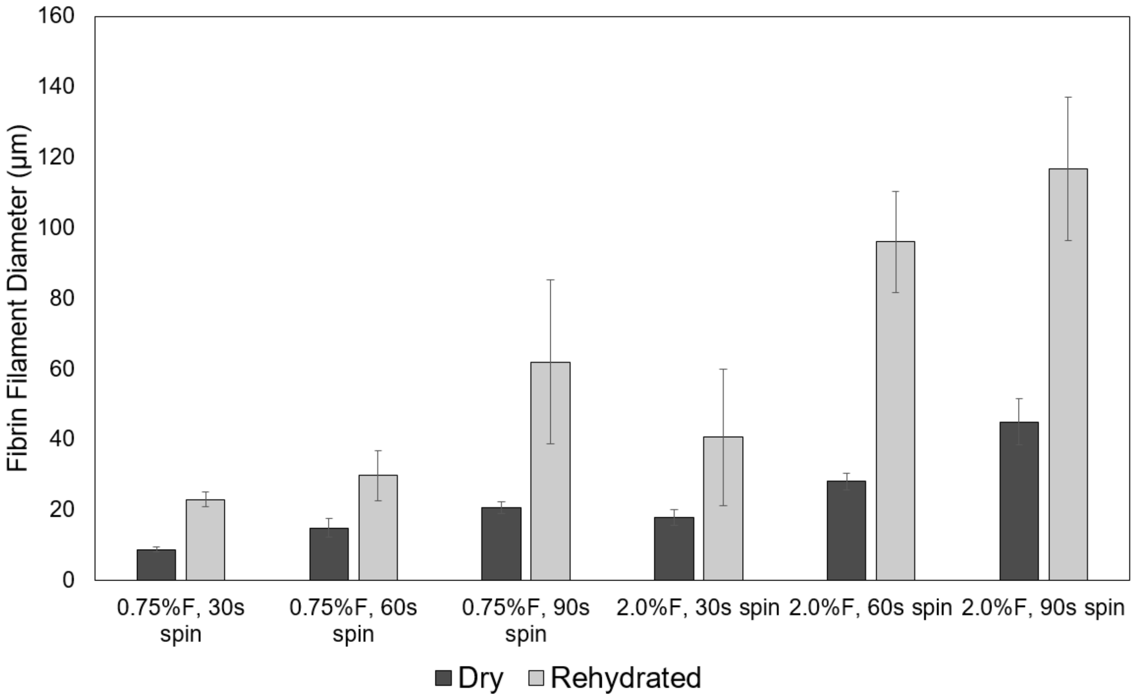

Figure 2-11: Small fibrin filament size as a function of spin time.

2.0 wt % or 0.75 wt % fibrin fibers spun onto 50 mM $CaCl_2$ collection bath containing 20 U/ml thrombin for up to 90 seconds holding landing position constant. Fiber filament diameter increases were seen in both dry and rehydrated state with longer spin time. Fibrin fibers spun from 2.0 wt % fibrinogen showed higher degrees of swelling at a given spin time relative to 0.75 wt% due to the increased quantity of material deposited. Fiber diameters were collected using an optical microscope by measuring least three fibers at three images per fiber and taking ten measurements per image.

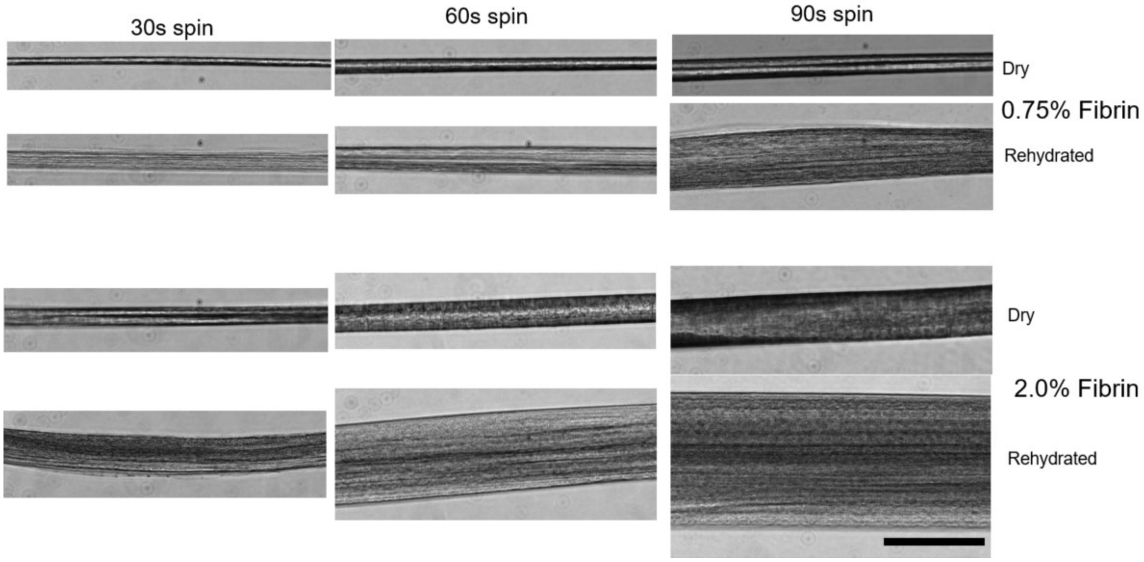

Figure 2-12: Fibrin filament swelling at different spin times.

2.0 wt % or 0.75 wt % fibrin fibers spun onto 50 mM $CaCl_2$ collection bath containing 20 U/ml thrombin for up to 90 seconds holding landing position constant. Swelling of fibers is readily apparent after rehydration overnight. Fiber diameters were collected using an optical microscope by measuring least three fibers at three images per fiber and taking ten measurements per image. Scale bar: 100 µm.

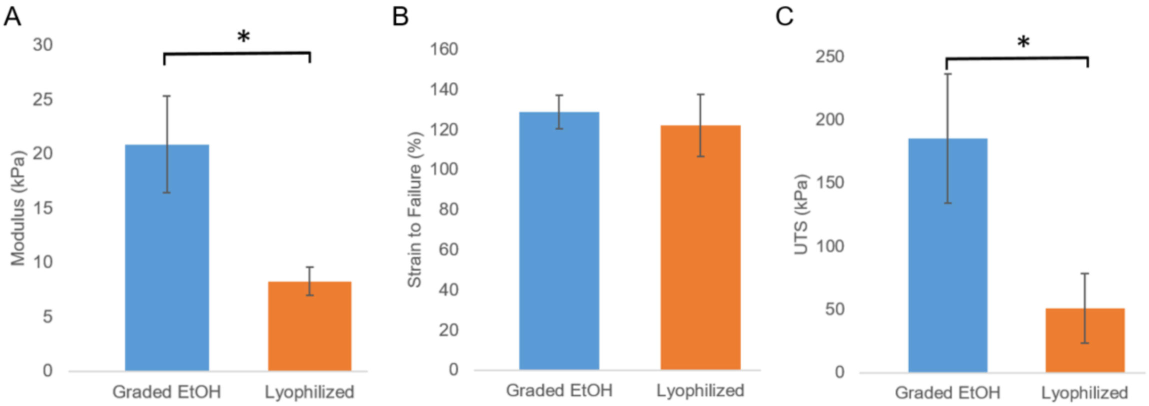

Figure 2-13: Drying treatment effect on fibrin fiber tube stiffness.

Fibrin fiber tubes were dried through graded ethanol drying or lyophilization. Graded EtOH drying yielded higher stiffness when rehydrated (A) and ultimate tensile strength (C) when tested using a Q800 DMA. Strains to failure were similar between the two drying conditions indicating that mechanical property differences are mainly attributed to the reduced cross-sectional area of the EtOH dried tubes.

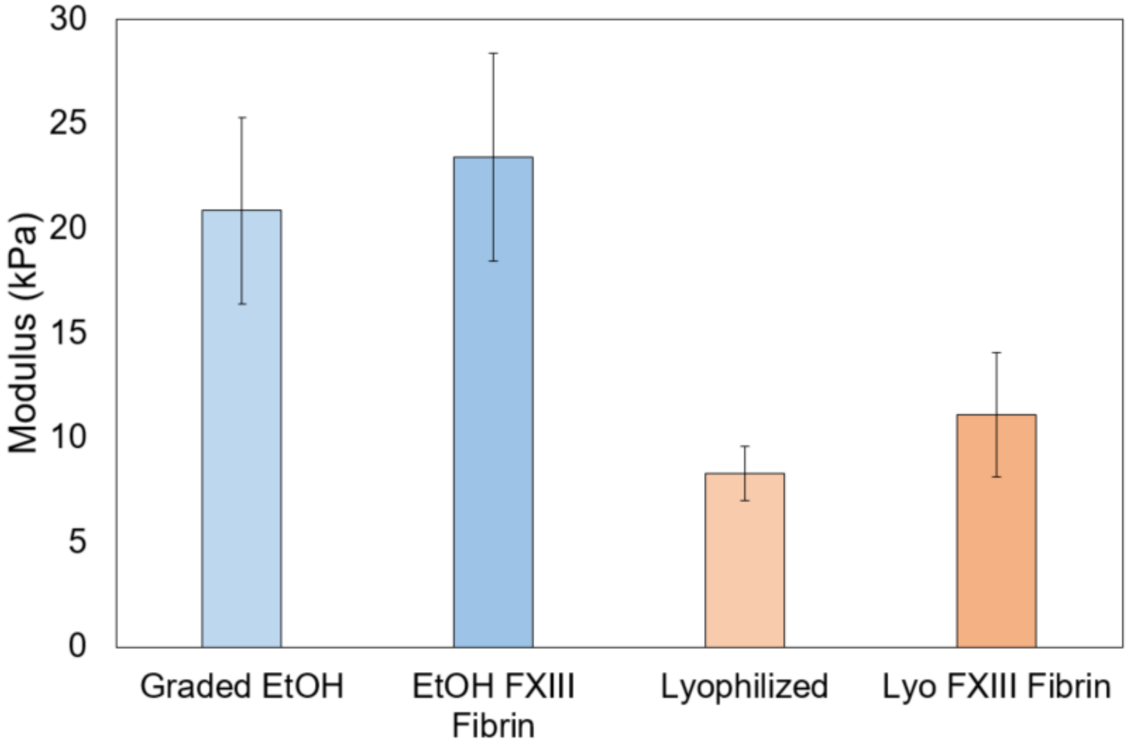

Figure 2-14: Factor XIII effect on fibrin fiber tube stiffness.

Treatment of fibrin tubes after overnight soak in 20 µg/ml FXIII and 4 U/ml thrombin show small, but not significant, gains in stiffness.

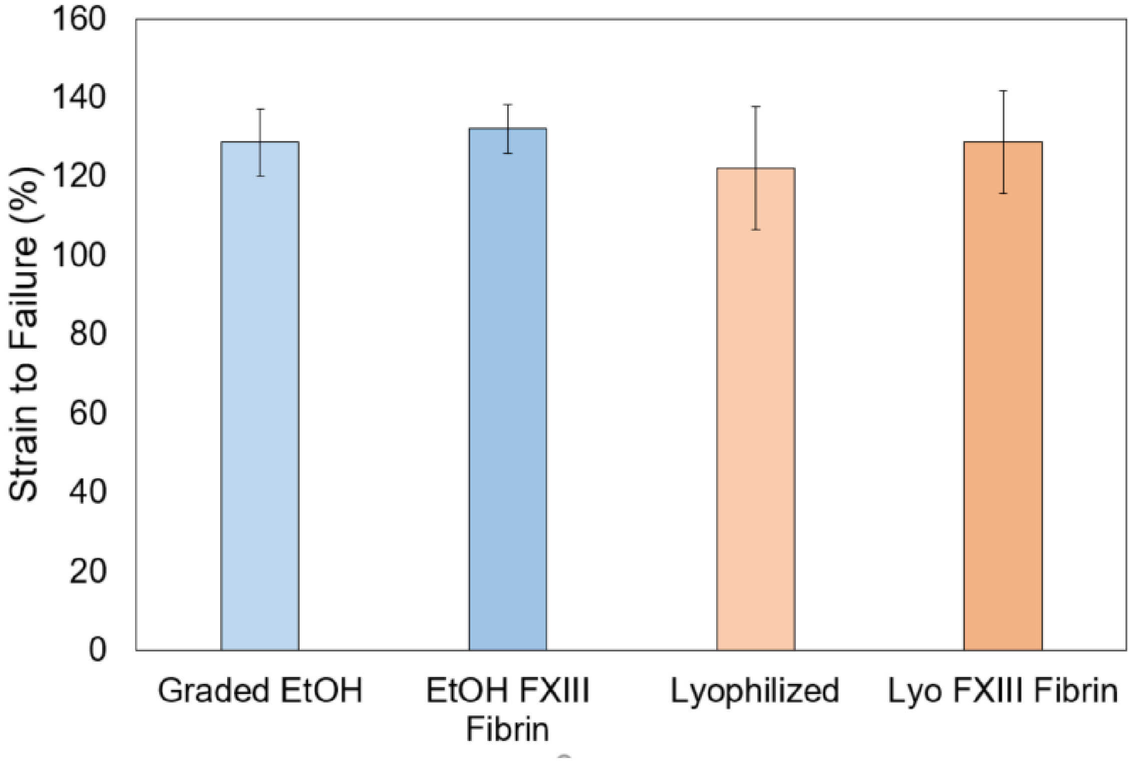

Figure 2-15: Factor XIII effect on fibrin fiber tube strain to failure.

Treatment of fibrin tubes after overnight soak in 20 μg/ml FXIII and 4 U/ml thrombin show no gains in strain to failure after FXIII treatment.

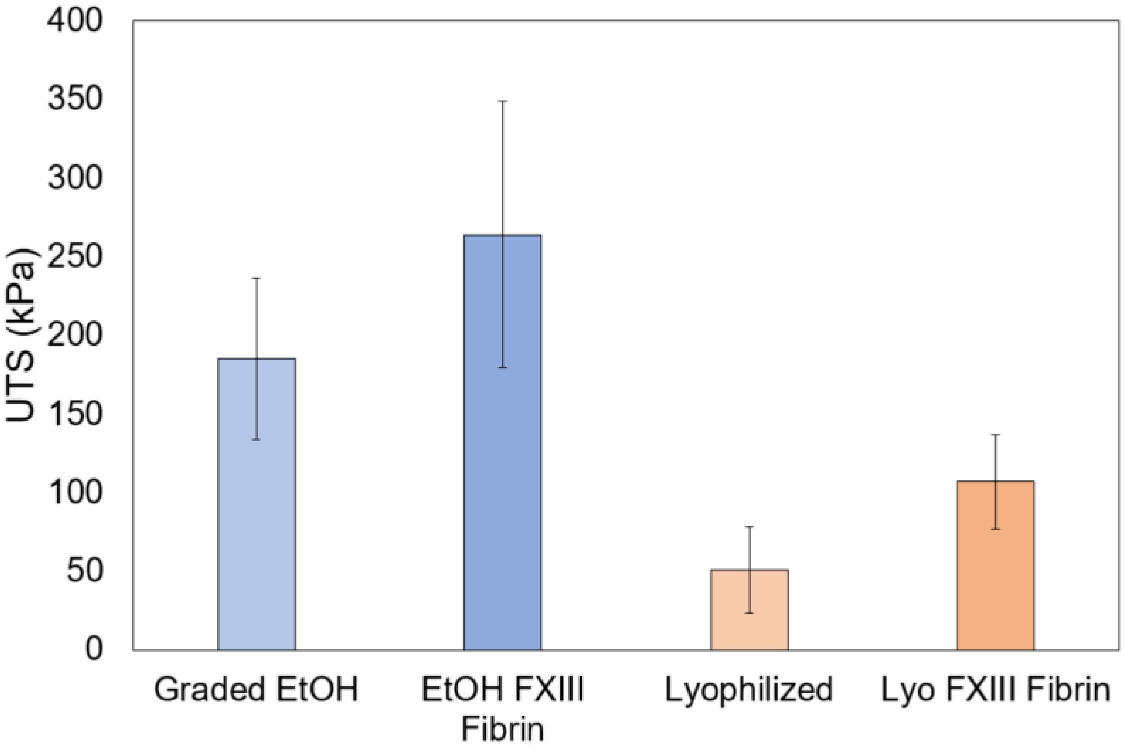

Figure 2-16: Factor XIII effect on fibrin fiber tube ultimate tensile strength.

Treatment of fibrin tubes after overnight soak in 20 µg/ml FXIII and 4 U/ml thrombin show improvement in UTS after FXIII treatment.

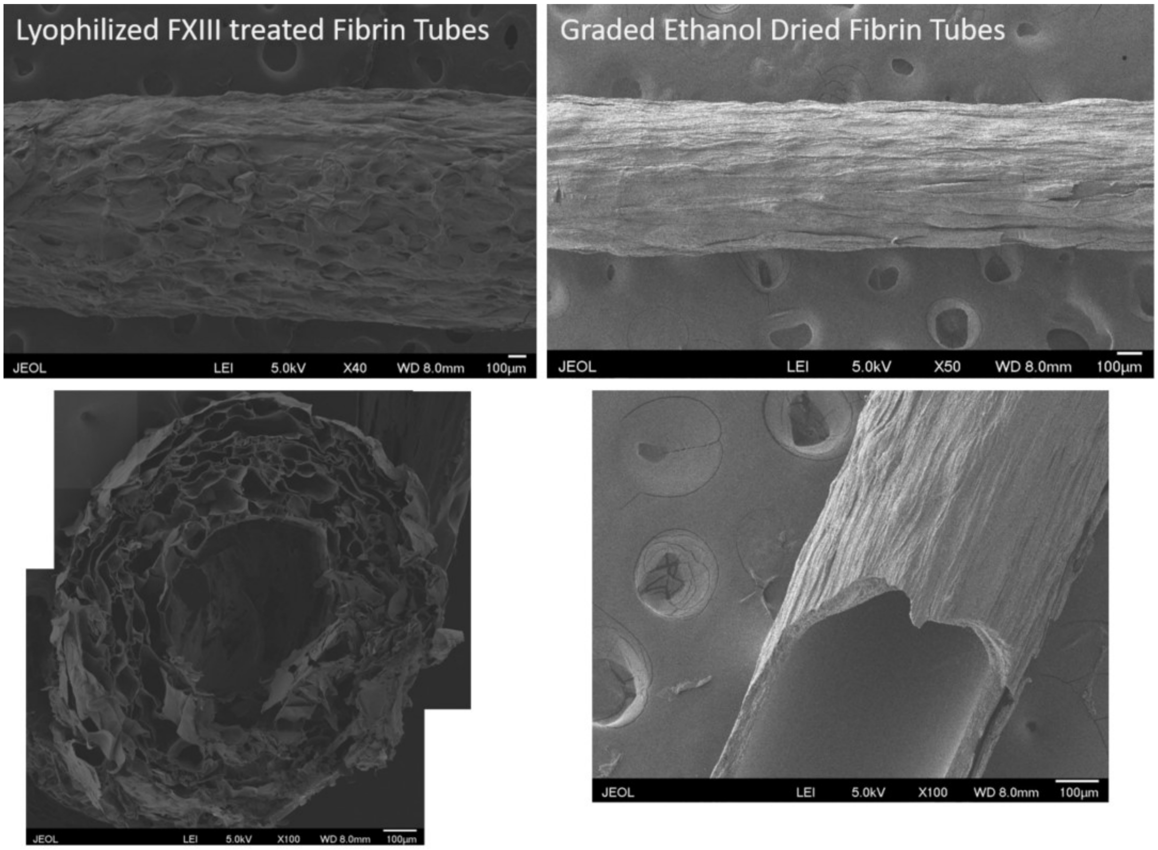

Figure 2-17: Comparison of lyophilization and ethanol drying of fibrin tubes.

Lyophilization does little to preserve the aligned structure of fibrin tubes once the process is complete yielding tubes with a disorganized structure on the surface (top left) and thicker, highly porous walls (bottom left). Graded ethanol drying maintains longitudinal alignment structure (top right) and generates thinner, more dense, walls (bottom right).

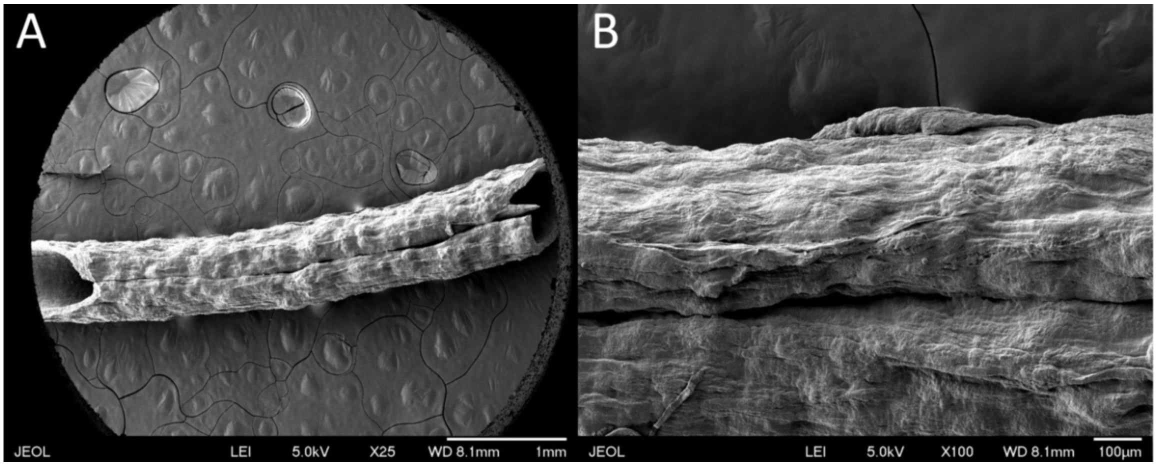

Figure 2-18: Cracking occurring in fibrin tube during drying.

Cracks sometimes run along whole length of fibrin tube vascular graft when ethanol drying treatment is done without overnight soak in 90% ethanol, leading to rapid device failure upon implantation (a). Higher magnification image of crack showing folded-like structure that ruptures upon being implanted or perfused (b).

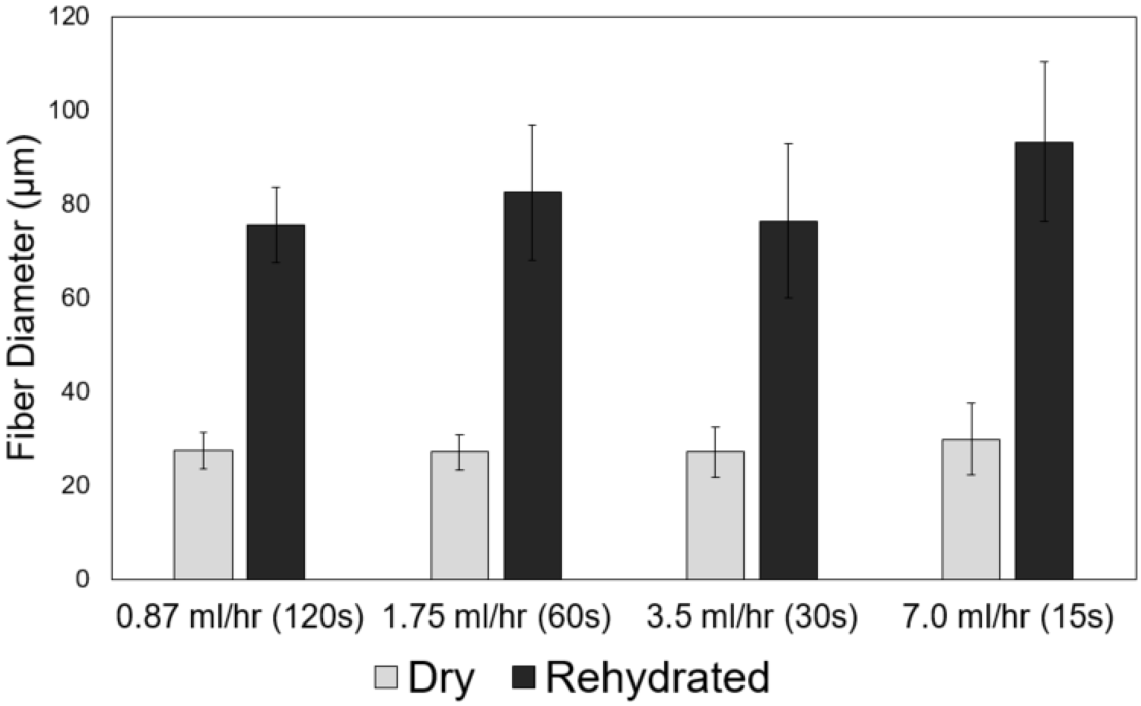

Figure 2-19: Application of mass flow constant to achieve similar fiber diameters with different spin conditions.

Variation of flow rate and spin time when electrospinning 2 wt% fibrin hydrogel fibers show similar fiber dry and rehydrated fiber diameters at Mass Flow Constant (MFC) of 3.5.

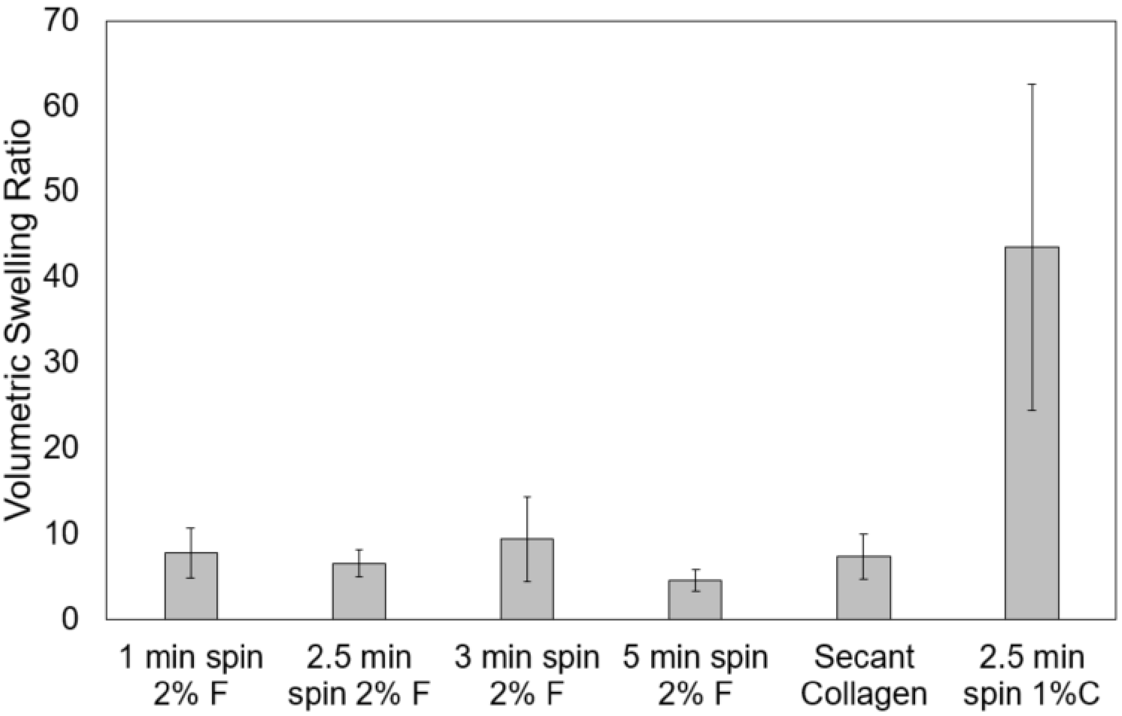

Figure 2-20: Swelling ratios of fibrin and collagen hydrogel fibers.

Fibrins show similar swelling compared to Secant collagen fibers but are at a much lower swelling degree compared to electrospun collagen hydrogel fibers. Electrospun collagen hydrogel fibers are more hydrophilic than fibrin fibers, Secant collagen are very dense leading to reduced water permeability and therefore swelling.

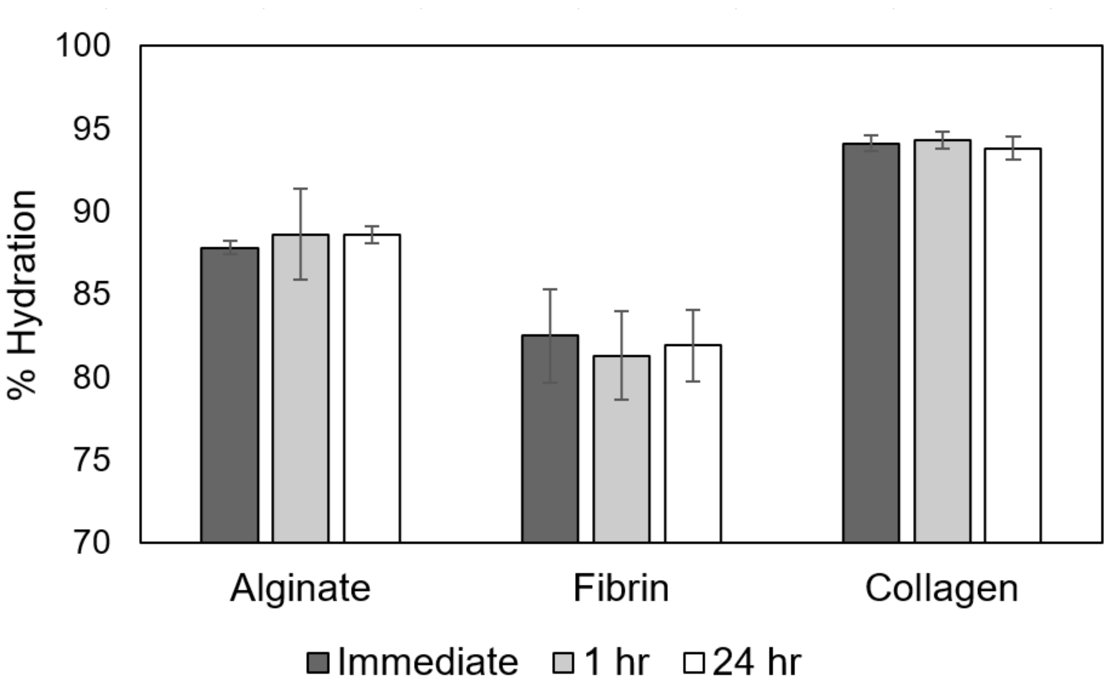

Figure 2-21: Rapid rehydration of alginate, fibrin, and collagen hydrogel fibers.

Measurements of the rehydration of alginate, fibrin, and collagen hydrogel fibers show that rehydration occurs quickly, within 10 minutes, and no significant additional rehydration or swelling occurs after additional time.

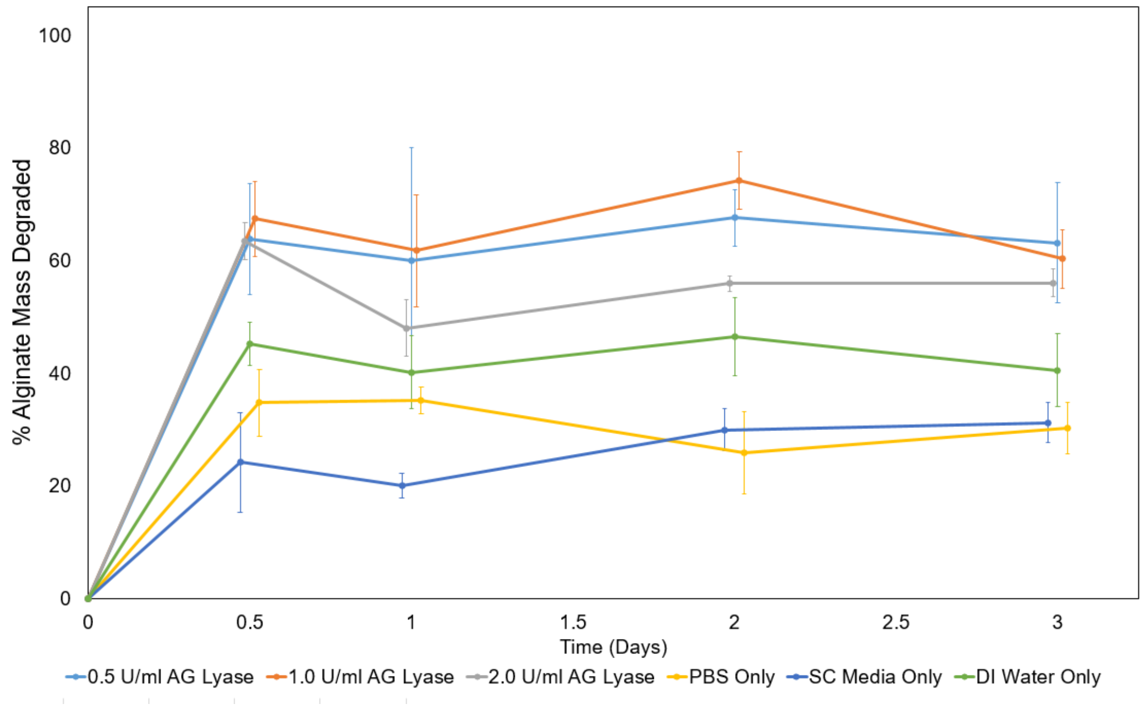

Figure 2-22: Degradation of alginate fibers in alginate lyase, PBS, Schwann cell media, and DI water.

Mass loss of alginate fibers was highest in lyase solutions. Concentration differences in alginate lyase between 0.5 U/ml to 2.0 U/ml did not show significant difference from each other. Degradation was highest during the initial 12 hours. Schwann cell media, PBS, and DI water showed lower degradation than the lyase group with degradation in the lower three being primarily due to Ca^{+2} ion exchange and chelation.

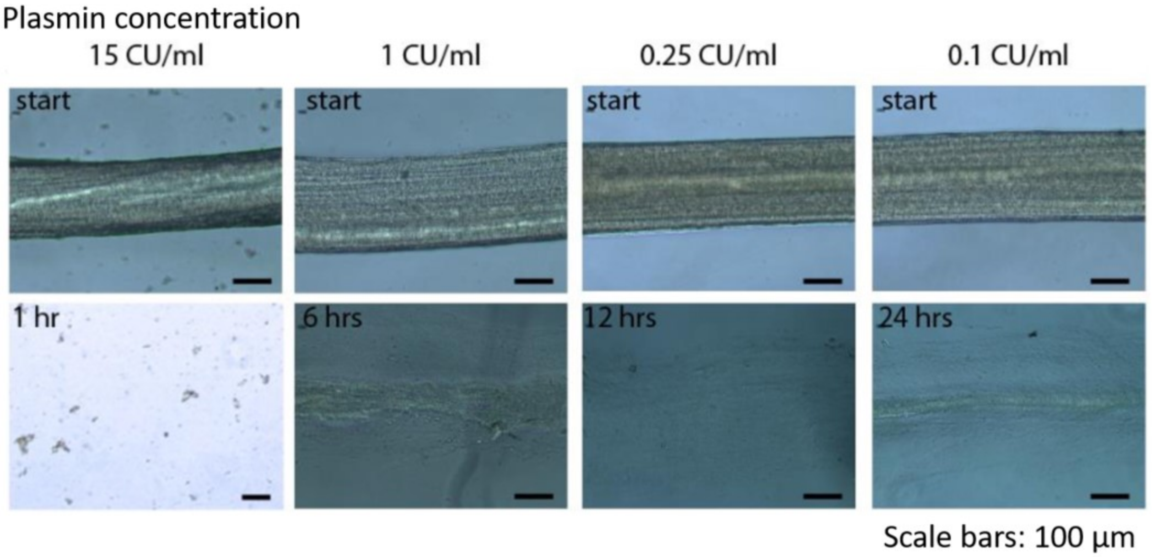

Figure 2-23: Fibrin fiber bundle degradation with plasmin treatment ranging from 0.1 CU/ml to 15 CU/ml.

Plasmin treatment of fibrin fiber bundles show concentration dependent degradation with reduction in complete degradation time down to 1 hour when using high plasmin concentrations of 15 CU/ml. Fiber lifetime was 24 hours at 0.1 CU/ml.

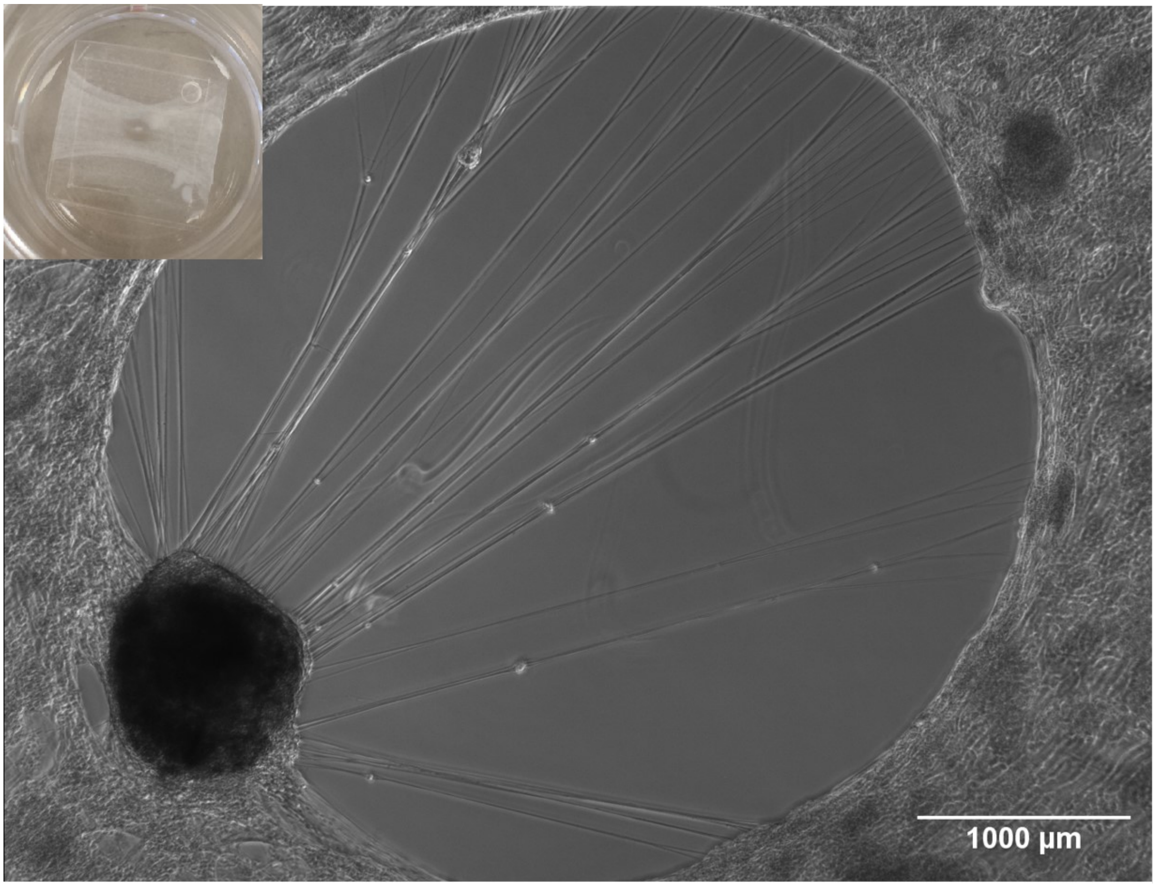

Figure 2-24: Degradation of fibrin fiber sheets by DRG explant without addition of aprotinin.

Lack of aprotinin addition to cell culture media when DRG explants are seeded on fibrin sheets leads to degradation of fibrin sheet as neurites extend away from explant.

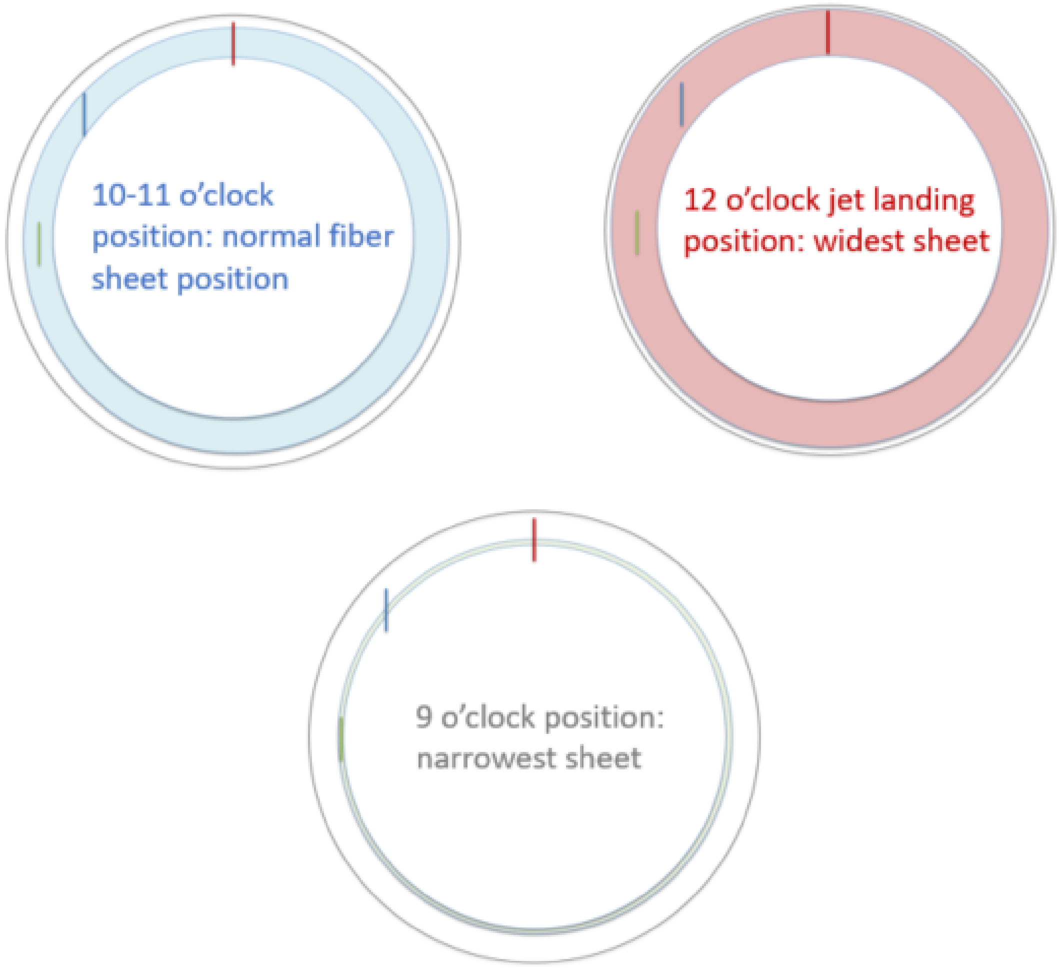

Figure 2-25: Modifying fiber sheet width by changing landing position of fiber jet.

Adjustment of fiber sheet width using constant linear stage raster distance is done by altering the clock landing position of the jet. Positions where the jet is traveling parallel to the tangent of wheel rotation (12 o'clock) will have wider sheet formation due to the jet raster cutting across a maximum width of collection solution when needle is horizontally oriented in the above figure and travels at a constant distance (indicated by green, blue, and red line). Narrower sheets form as landing position moves towards the 9 o'clock minimum, where the jet landing position is perpendicular to the flow and a minimum width of the collection solution band is intersected by the polymer jet.

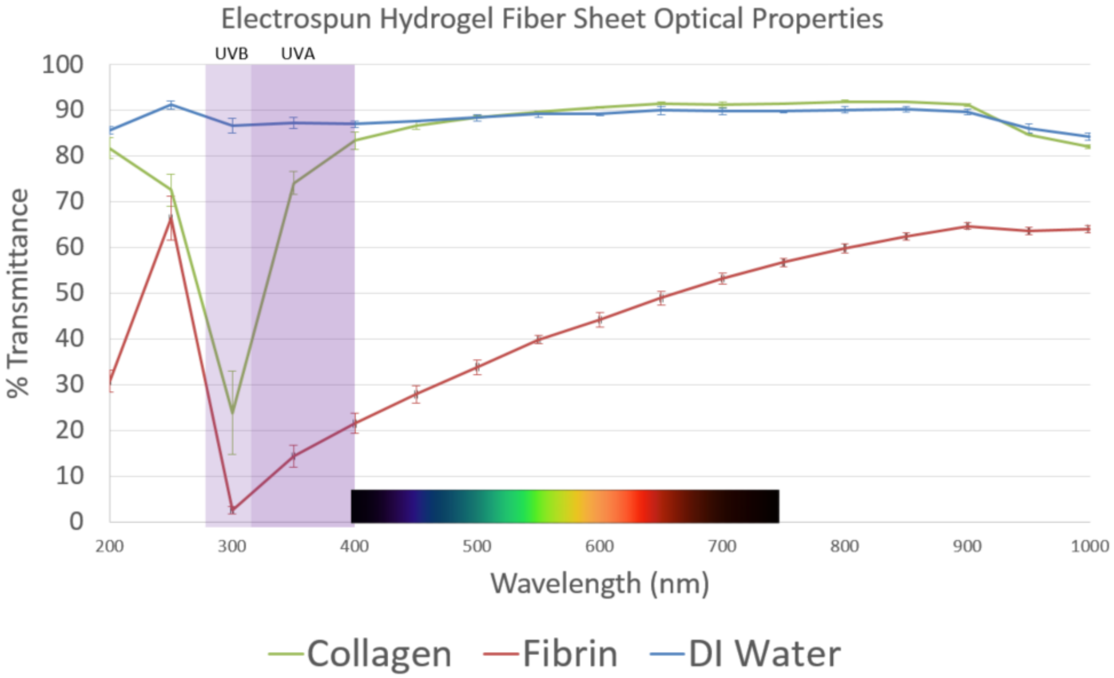

Figure 2-26: Optical transparency properties of collagen and fibrin fiber sheets.

Collagen shows greater transparency in solution throughout visible wavelengths compared to fibrin fiber sheets and has comparable optical properties to water due to the high levels of hydration characteristic of collagen hydrogel fiber sheets. Collagen sheets shows some absorption in the UVB wavelength range, leading these sheets to potentially provide a UV protective effect when used for ocular applications. N = 3 fiber sheets measured per type in wavelength steps of 50 nm.

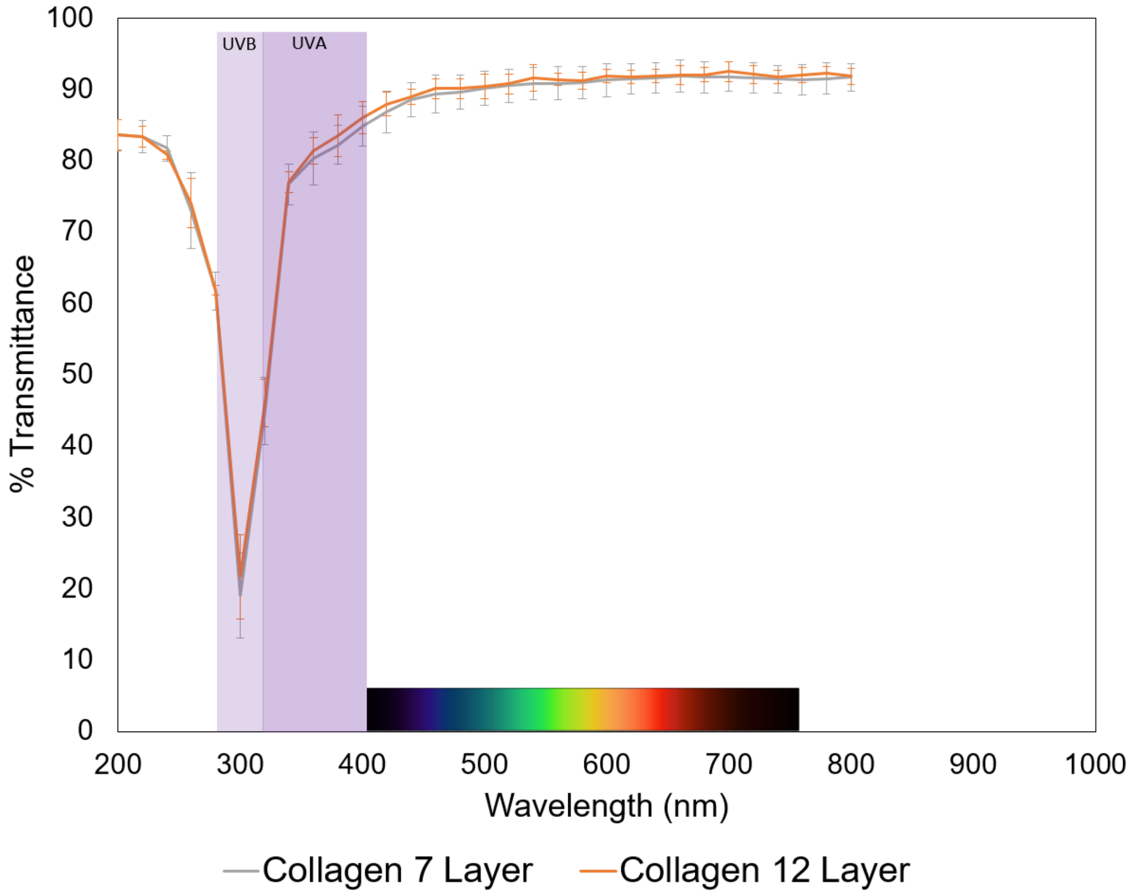

Figure 2-27: Effect of collagen fiber sheet thickness on optical properties.

Effect of collagen fiber sheet thickness on optical properties do not show significant change in transparency properties when comparing EDC crosslinked collagen fiber sheets composed of seven or twelve wrapped layers. N = 3 fiber sheets measured per type in wavelength steps of 20 nm.

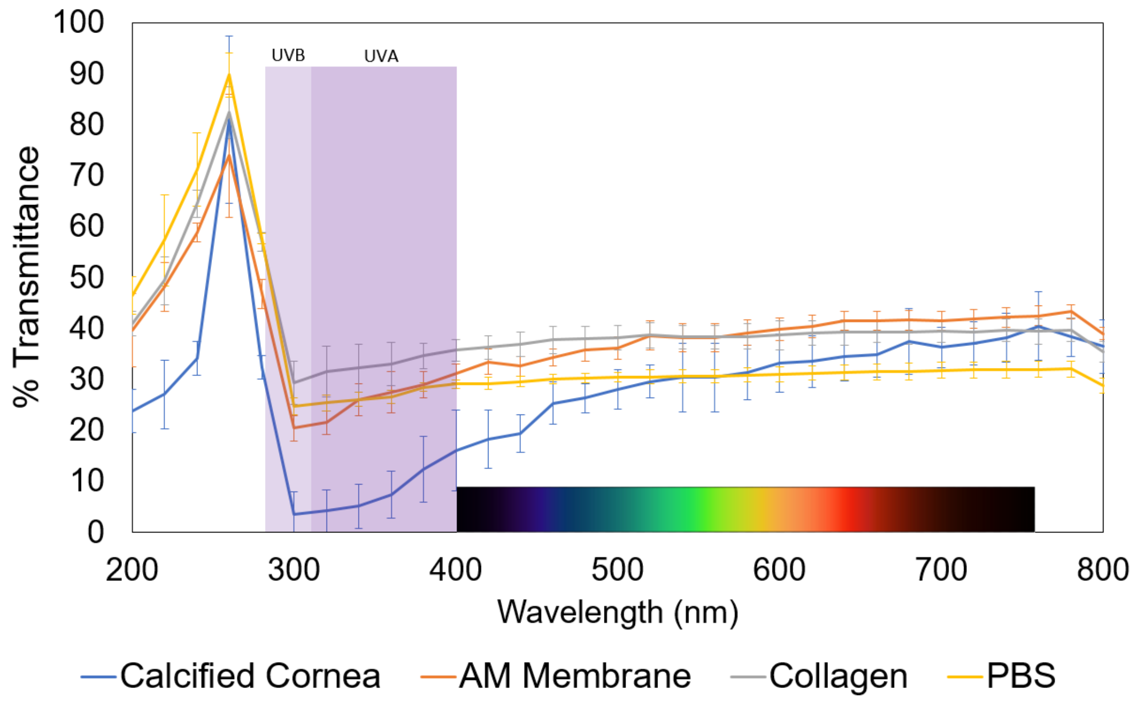

Figure 2-28: Comparison of optical properties of collagen, AM membrane, and calcified cornea.

Collagen fiber sheet transparency was compared with AM membrane for potential use in optical patch applications as a mechanical support of the weak AM membrane. Collagen sheets have similar transparency to the AM membrane in PBS. Reduction in transparency of collagen compared to the previous two figures is predominantly due to the use of PBS as the solution rather than DI water. N = 3 fiber sheets measured per type in wavelength steps of 20 nm.

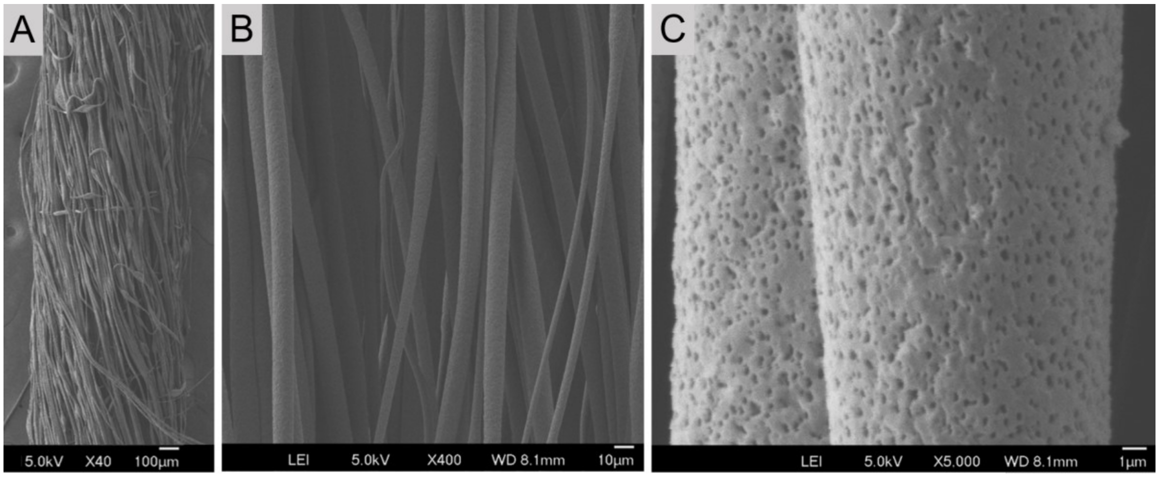

Figure 2-29: 3D PLGA microfiber bundle spinning.

PLGA microfibers spun onto DI water, a non-solvent, precipitates on collection solution and can be collected as a fiber bundle (a). Fibers are several microns and larger due to lack of whipping instability during electrospinning (b). Escape of dichloromethane solvent from PLGA fibers upon contact with water forms pock textured surface (c).

2.6 References

1. Nowacki M, et al., *Are agricultural and natural sources of bio-products important for modern regenerative medicine? A review.* in *Ann Agric Environ Med* 2017.
2. Smidsrod, O, et al.,. *Alginate as immobilization matrix for cells.* in *Trends Biotechnol.* 1990. p. 71–78.
3. R Wayne, et al., *Protein release from alginate matrices.* in *Adv Drug Deliv Rev.* 2012. p. 194–205.
4. Smetana K. *Cell biology of hydrogels.* in *Biomaterials.* 1993. p. 1046–1050.
5. Hantgan RR and Hermans J. *Assembly of Fibrin: A Light Scattering Study.* in *J Biol Chem* 1979. p. 11272–11281.
6. Ye Q, et al., *Fibrin gel as a three dimensional matrix in cardiovascular tissue engineering.* in *Eur J Cardiothorac Surg.* 2000. p. 587–591.
7. Soffer E, et al., *Fibrin sealants and platelet preparations in bone and periodontal healing.* in *Oral Surg Oral Med Oral Pathol Oral Radiol Endodontology*. 2003. p. 521–528.
8. Ikari Y, et al., *Alpha(1)-protease inhibitor, alpha(1)-antichymotrypsin, or alpha(2)-macroglobulin is required for vascular smooth muscle cell spreading in three-dimensional fibrin gel.* in *J Biol Chem.* 2000. p. 12799–12805.
9. Meinhart J, et al., *Stabilization of fibrin-chondrocyte constructs for cartilage reconstruction.* in *Ann Plast Surg.* 1999. p. 673–678.
10. Mosesson MW. *Fibrinogen and fibrin structure and functions.* in *J Thromb Haemost.* 2005. p. 1894–1904.
11. Schense JC and Hubbell JA. *Cross-Linking Exogenous Bifunctional Peptides into Fibrin Gels with Factor XIIIa.* in *Bioconjug Chem.* 1999. p. 75–81.
12. Williams LR, et al., *Spatial-temporal progress of peripheral nerve regeneration within a silicone chamber: Parameters for a bioassay.* in *J Comp Neurol.* 1983. p. 460–470.
13. Herbert CB, et al., *Effects of Fibrinolysis on Neurite Growth From Dorsal Root Ganglia Cultured in Two- and Three-Dimensional Fibrin Gels.* in *J Comp Neurol.* 1996. p. 380–391.
14. Sakiyama-Elbert SE and Hubbell JA. *Development of fibrin derivatives for controlled release of heparin-binding growth factors.* in *J Controlled Release.* 2000. p. 389–402.
15. Cheng L-N, et al., *Transplanted Neural Stem Cells Promote Nerve Regeneration in Acute Peripheral Nerve Traction Injury: Assessment Using MRI.* in *Am J Roentgenol.* 2011. p. 1381–1387.
16. Ricard-Blum S. *The Collagen Family.* in *Cold Spring Harb Perspect Biol.* 2011.
17. Lee CH, et al., *Biomedical applications of collagen.* in *Int J Pharm.* 2001. p. 1–22.
18. Greenspan DS. *Biosynthetic processing of collagen molecules.* in *Top Curr Chem.* 2005. p. 149–183.
19. Bruckner P. *Suprastructures of extracellular matrices: paradigms of functions controlled by aggregates rather than molecules.* in *Cell Tissue Res.* 2010. p. 7–18.

20. Persikov AV, et al., *Electrostatic Interactions Involving Lysine Make Major Contributions to Collagen Triple-Helix Stability*. in *Biochemistry* 2005. p. 1414–1422.
21. Fallas JA, et al., *Solution Structure of an ABC Collagen Heterotrimer Reveals a Single-register Helix Stabilized by Electrostatic Interactions.* in *J Biol Chem.* 2009. p. 26851–26859.
22. Park SN, et al., *Characterization of porous collagen/hyaluronic acid scaffold modified by 1-ethyl-3-(3-dimethylaminopropyl)carbodiimide cross-linking.* in *Biomaterials.* 2002. p. 1205–1212.
23. Schoof H, et al., *Control of pore structure and size in freeze-dried collagen sponges.* in *J Biomed Mater Res A.* 2001. p. 352–357.
24. Chen G, et al., *Development of biodegradable porous scaffolds for tissue engineering.* in *Mater Sci Eng C.* 2001. p. 63–69.
25. Tan W, et al., Evaluation of nanostructured composite collagen-chitosan matrices for tissue engineering. Tissue Eng. 2001;203–210.
26. Huang L, et al., *Engineered collagen-PEO nanofibers and fabrics.* in *J Biomater Sci Polym Ed.* 2001. p. 979–993.
27. Kaufmann PM, et al., *Highly porous polymer matrices as a three-dimensional culture system for hepatocytes.* in *Cell Transpl.* 1997. p. 463–468.
28. Auger FA, et al., *Tissue-engineered human skin substitutes developed from collagen-populated hydrated gels: clinical and fundamental applications.* in *Med Biol Eng Comput.* 1998. p. 801–812.
29. Farole A and Jamal BT. *A Bioabsorbable Collagen Nerve Cuff (NeuraGen) for Repair of Lingual and Inferior Alveolar Nerve Injuries: A Case Series.* in *J Oral Maxillofac Surg.* 2008. p. 2058–2062.
30. Klein T and Bischoff R. *Physiology and pathophysiology of matrix metalloproteases.* in *Amino Acids.* 2011. p. 271–290.
31. Dong B, et al., *Electrospinning of Collagen Nanofiber Scaffolds from Benign Solvents. Macromol Rapid Commun.* 2009. p. 539–542.
32. Elamparithi A, et al., *Electrospun type 1 collagen matrices preserving native ultrastructure using benign binary solvent for cardiac tissue engineering.* in *Artif Cells Nanomedicine Biotechnol.* 2015. p. 1–8.
33. Fiorani A, et al., Comparative performance of collagen nanofibers electrospun from different solvents and stabilized by different crosslinkers. J Mater Sci Mater Med. 2014 Oct;25(10):2313–2321.
34. Kuijpers AJ, et al., *Characterization of the Network Structure of Carbodiimide Cross-Linked Gelatin Gels.* in *Macromolecules.* 1999. p. 3325–3333.
35. Lodish H, et al., Molecular Cell Biology. 6th ed. 2007.
36. Oerther S, et al., *High interaction alginate-hyaluronate associations by hyaluronate deacetylation for the preparation of efficient biomaterials.* in *Biopolymers.* 2000. p. 273–281.
37. Afify AM, et al., *Purification and Characterization of Human Serum Hyaluronidase.* in *Arch Biochem Biophys.* 1993. p. 434–441.

38. Radomsky ML, et al., *Novel formulation of fibroblast growth factor-2 in a hyaluronan gel accelerates fracture healing in nonhuman primates.* in *J Orthop Res.* 1999. p. 607–614.
39. Duranti F, et al., *Injectable hyaluronic acid gel for soft tissue augmentation. A clinical and histological study.* in *Dermatol Surg.* 1998. p. 1317–1325.
40. Chernysh IN, et al., *Fibrin Clots Are Equilibrium Polymers That Can Be Remodeled Without Proteolytic Digestion.* in *Sci Rep.* 2012.
41. Rowe SL, et al., *Influence of thrombin concentration on the mechanical and morphological properties of cell-seeded fibrin hydrogels.* in *Acta Biomater.* 2007. p. 59–67.
42. Duong H, et al., *Modulation of 3D fibrin matrix stiffness by intrinsic fibrinogen–thrombin compositions and by extrinsic cellular activity.* in *Tissue Eng Part A.* 2009. p. 1865–1876.
43. Ariëns RA, et al., *Role of factor XIII in fibrin clot formation and effects of genetic polymorphisms.* in *Blood.* 2002. p. 743–754.
44. Courtman DW, et al., *The role of crosslinking in modification of the immune response elicited against xenogenic vascular acellular matrices.* in *J Biomed Mater Res A.* 2001. p. 576–586.
45. Barreto-Ortiz SF, et al., *A Novel In Vitro Model for Microvasculature Reveals Regulation of Circumferential ECM Organization by Curvature.* in *PLoS ONE.* 2013.
46. Cook CA, et al., *Characterization of a novel bioreactor system for 3D cellular mechanobiology studies.* in *Biotechnol Bioeng.* 2016. p. 1825–1837.

Chapter 3 Cellular Organization and Migratory Effects using Aligned Hydrogel Microfibers and Neurotrophic Cues In Vitro

3.1 Background

3.1.1 Interaction of cells with extracellular matrix

Cellular interaction with the surrounding extracellular matrix is controlled by four primary effects: substrate stiffness, confinement, adhesion, and surface topology [1]. Substrate mechanical properties have a large effect on how integrin binding sites interact with the ECM and can drive differentiation due to the large differences in mechanical properties found in the native ECM of various tissues like adipose and neural (100 Pa) [2], muscle (1 kPa) [3], or bone (tens of GPa) [4]. Actomyosin stress fiber generation during mechanotrasduction of stiff substrates lead to cytoskeletal tension within the cell [5, 6]. When adhesions of the back side of the cell are released, the tension slides the cell body towards the leading edge that is still attached to the substrate, movement that is much in the same manner as that of a hungry caterpillar. Stiff substrates also upregulate the production of proteases such as MMPs to prevent the cells from remaining indefinitely under high tension [7]. Mechanotransduction signaling can additionally provide the cell with information to determine stiffness gradients present in the ECM, leading to the induction of durotaxis [8].

Softer substrates enables high levels of migration for cells through the matrix by enabling them to deform the ECM, opening up migratory pathways. Thus, it is important to consider that both the stiffness of the whole tissue engineered construct and localized stiffness play a role in cellular response as demonstrated by the differences in stem cell differentiation caused by changes in the local mechanical properties of collagen [9]. Cellular migration through soft substrates ultimately is controlled by the deformability and, in the case of hydrogels, the network mesh size formed by crosslinking as the nucleus of the cell can only be deformed to diameters as low as 4 μm [10].

3.1.2 Topographical guidance cues

Electrospinning provides a technique to generate ECM-like nanofiber materials with both synthetic and biologically derived polymers. The flexibility of the platform has led to the generation of ECM-like structures for vascular grafts [11], tendons [12], nerves [13], and others though it is difficult to create truly 3D structures with traditional nanofibers spinning processes.

Topographical cues presented to the cells can be classified as those that provide continuous or discontinuous surfaces. Continuous surfaces would be planar substrates such as TCPS or dense electrospun nanofiber meshes that mimic the basement membrane where cells are able to broadly spread lamellipodia [14]. Discontinuous surfaces are those that have spacing of several hundred nanometers or more between adhesive cues that confine cells and reduce cellular traction [15]. Discontinuous topographical cues cause cells to elongate along the cue direction due to the relatively linear directionality the actin filaments are forced into [16]. Confinement generated by discontinuous substrates necessitates the use of alignment features if migratory speed is an important design consideration as linear directionality will reduce the travel distance required compared to more disorganized discontinuous matrices [17].

3.1.3 Cardiac tissue engineering

The complex shaping, cyclic strain, and underlying structural ECM alignment of the heart presents a challenge to tissue engineers developing materials to treat pathological states like myocardial infarction and congenital defects [18]. An additional challenge is that there is very little cardiac cell replacement each year so acellular tissue engineered constructs will be unlikely to incorporate many native cells [19]. This area of research is particularly important as there are nearly a million deaths each year in the United States to cardiac disease [20]. Structurally, any sort of patch used should match the mechanical properties of the myocardium so that muscle contractility is not impeded [21] and there is no impedance of electrical signaling between cardiomyocytes, which can be affected by scaffold stiffness [22]. The general range of stiffness required for cardiomyocytes to function as they do in healthy tissue is in the range of 10 to 20 kPa. Such a scaffold stiffness range can be met using electrospun hydrogel fiber sheets very easily.

Other considerations to be made with cardiac tissue engineering include the biocompatibility of the material and potential immune response. Should a cardiac patch induce a significant inflammation response, the patch could possibly be degraded more rapidly than expected due to additional macrophage invasion [23]. Several natural materials have been used for cardiac tissue engineering due to their good biocompatibility and immune response properties. These include collagens, alginate, fibrin, and gelatin [24]. Synthetic polymers have also been used for cardiac tissue engineering but due to their very high relative stiffness, are most often used as a support structure for naturally derived materials [25].

3.1.4 Vascular graft engineering

Incorporation of existing vascular (angiogenesis) or development of new vascular networks from cell progenitors (vasculogensis) is of critical importance for tissue engineering products as without adequate nutrient transport and oxygen, many tissue will fail to regenerate or repair [26]. Tissue engineered grafts have to take into consideration not only the mechanical properties of the graft, ideally matching that of the native extracellular matrix, but also to consider the adhesive cues required and the need to mimic the natural presentation levels of vascular signals such as VEGF, FGF, TGF, and other chemical cues to direct neovascularization [27, 28].

Some current vascular grafts in development include hollow tubes composed of cast collagen gels that are very analogous to Integra's NeuraGen nerve guide, in that there is no alignment tube provided and that the main advantage of the device is the native material usage. These collagen tubes have been shown to show stable blood flow through the conduit for 20 minutes [29]. Other techniques for vascular grafting include using patterned PDMS substrates to induce alignment of fibroblasts to secrete aligned ECM over six week, which is then wrapped up into a tube [30] and elastin-PCL hybrid grafts where the composite materials provide the elastic and mechanical strength properties needed for a vascular graft [11],

The ubiquity of fibrin(ogen) in the circulatory system and its intimate relationship with the clotting cascade following damage to blood vessels makes it an excellent material for use in vascular applications. A primary advantage of fibrin usage is its ability to be proteolytically degraded on a relatively rapid timescale compared to more persistent ECM components such as collagen and elastin. The alignment features of the fibrin fibers combined with the degradation properties make them an excellent scaffold material for the culture of pericytes, smooth muscle cells, and other endothelial cell types. The flexibility of the fibrin hydrogel fiber spinning platform enables the generation of scaffold systems with easily variable diameters for *in vitro* cell culture and organization of vascular cells, which later can degrade the luminal fibrin themselves or through addition of plasmin to the culture media. Additionally, fibrin sheets wrapped around Teflon coated mandrels can yield hollow, perfusable scaffolds that can be used as a biomimetic *in vitro* model for vascular tissue engineering or as a suturable implantable construct for vascular repair *in vivo*.

3.1.5 Skeletal muscle tissue engineering

Tissue engineered constructs composed of fibrin hydrogels and skeletal muscle cells have been found to create a highly beneficial microenvironment for skeletal muscle repair [31]. Alginates have also been investigated for use differentiation of skeletal muscle cells after modification with RGD peptides [32]. A general requirement for the underlying structure of skeletal muscle is that the muscle must remain aligned along the entirety of the length of the muscle to ensure maximum contractile forces are possible. Such long-range 3D alignment structures can be generated by electrospun hydrogel fiber bundles.

Scaffolds for skeletal muscle tissue engineering fall into several types. Porous scaffolds with many of the same design parameters as seen with nerve guide design have been used with collagen and synthetics such as PGA [33] to orient skeletal muscle cells along a particular axis. Alignment of skeletal muscle through use of electrospun fiber meshes have also promoted myotube formation on PCL-collagen nanofibers [34].

3.2 Methods

3.2.1 Spreading of primary Schwann cells along fibrin and collagen fiber sheets

Primary Schwann cells were isolated from P2 rat pups and used to form spheroids of approximately 200 µm diameter using 36 sphere molds for 48 hours prior to seeding on electrospun collagen and fibrin fiber sheets. Once seeded, several samples were fixed and stained at days 1, 3, and 6 for S100β (1:200), a marker of Schwann cells, to measure the spreading of the cells. Schwann cells were cultured in Schwann cell maintenance media containing 5% FBS (Invitrogen), 1% penicillin/streptomycin (Invitrogen), 200 µg/ml bovine pituitary extract (Sigma), and 2 µM forskolin (Sigma) without being supplemented with additional growth factors. Media was exchanged every 2nd day.

3.2.2 Neurite extension from DRG explant as function of fiber alignment

As the electrospun fiber sheets do not form discrete fibers distinguishable from one another as can be produced during traditional nanofiber electrospinning, characterization of neurite outgrowth from DRG explants was used to demonstrate that the topographical alignment effects remained intact in a sheet configuration. DRG explants were isolated from postnatal P2-P4 Sprague Dawley rat pups and cultured on random cast collagen gels, aligned collagen microfiber sheets, and aligned collagen fiber sheets that were soaked in matrigel overnight prior to seeding to demonstrated that electrospun collagen fiber sheets maintain cell motility characteristics without the need for additional modification.

Collagen fiber sheets were prepared by electrospinning 1 ml of a 1 wt% collagen solution with 0.2 wt% PEO at a flow rate of 3.25 ml/hr onto a collection solution of 40 mg/ml EDC using a linear stage to raster the landing position over an area of approximately 1.5 cm width. Fiber sheets were collected using a mylar with outer dimensions of 15 mm square an inner centered cutout of 11 mm square. Cast collagen gels with random structural alignment were prepared by neutralizing 800 µl of 1 wt% collagen with 100 µl 7.5 wt%

$NaHCO_3$ and 100 µl 10x PBS. A total of 8 ml collagen was prepared in order to cast 1 ml into each well of a 12 well multiwell plate for DRG explant seeding. Once cast, random collagen was gelled by incubating at 37°C for one hour. A single DRG explant was placed on each of eight random collagen gels, four Matrigel coated aligned collagen microfiber sheets, and four uncoated aligned collagen fiber sheets and cultured in DRG media lacking NGF for 14 days. Samples were fixed in 4% PFA after d14 and neurites stained with 1:200 βIII-tubulin to characterize total outgrowth. Neurite outgrowth was characterized by measuring maximum neurite extension at each 5 degree interval off the axis of fiber alignment from the center point of the explant. The length of the explant itself along each direction was subtracted from the measured outgrowth so as to only count neurite extension.

3.2.3 Outgrowth of neurites from DRG explants on uniformly loaded GDNF collagen fiber sheets

Prior to utilizing loaded electrospun collagen fiber sheets for nerve guide usage, it was necessary to characterize the effect of neurotrophic factor loading on neurite outgrowth to determine the loading level most likely to result in a beneficial outcome on functional recovery once implanted. Collagen fiber sheets were spun using typical parameters of 1ml of 1% collagen spun at 3.25 ml/hr using a collector wheel rotation speed of 45 RPM using a linear stage for sheet formation with 6 layers of material per sheet collected and total sheet area of 1 cm^2. Sheets were loaded with 0, 50, 100, 250, 500, or 1000 ng human GDNF and sheets were then dried under laminar air flow within a biosafety cabinet prior to DRG explant seeding. Heparinized collagen sheets were not tested due to the more rapid GDNF release seen with that configuration. Dorsal root ganglia explants were harvested from P2 Sprague Dawley rat pups and immediately seeded onto the dried collagen sheets. Ten minutes after seeding, 100 µl of DRG media was added to the sheet and then an additional 20 minutes later the remainder of media was added to bring total culture volume to 1 ml. DRGs were cultured for one week to allow neurite extension with media exchange every other day prior to being fixed in 4% PFA and stained for βIII-tubulin (1:200).

Each immunostained image of neurite outgrowth from the DRG explant after seven days were measured as follows. Images were split into two parts by taking the DRG explant and overlaying a vertical line through the midsection of the explant perpendicular to the direction of the alignment. Using this line as a starting point, the maximum neurite outgrowth was measured using ImageJ at 20 µm intervals as seen in Figure 3.1 on both sides of the DRG bisecting line for all samples. Distributions of neurite extension were generated from this data excluding the DRG explant radius and used to determine GDNF loading level usage for collagen fiber sheet loading with the SYSU in vivo nerve guide study.

3.2.4 Consumption of free amines during collagen fiber sheet formation

The rapid crosslinking of collagen fiber sheets requires a high concentration of EDC (210 mM) used in the collection bath. As this crosslinker will conjugate primary amines with carboxylic acid groups, there is the important question of what proportion of free amines remain after sheet formation since these groups are commonly used for bioconjugation reactions such as in applications where growth factors are covalently tethering to a biomaterial surface. To investigate this, the quantity of free amines in the unadulterated collagen stock spinning solution was calculated and then a fluorescamine assay was used in conjunction with a plate reader to characterize the number of moles primary amine remaining both following crosslinking during fiber formation and after conjugation of cell adhesive peptide 945W.

Briefly, each collagen sheet was submerged in 0.9 ml PBS and then 100 µl of 0.3 mg/ml fluorescamine in acetone was added. Acetone was given 10 minutes to evaporate and then solution was vortexed gently for 25 minutes at room temperature. Collagen sheets were then triple washed in PBS and degraded in 1 ml of 1.0 mg/ml collagenase for 45 minutes at 37°C. Once degraded, fluorescence using λ_{ex} = 390 nm and λ_{em} = 475 was measured in a plate reader and compared against ethylene diamine standards using the same procedure. Peptide 945W was conjugated to collagen fibers using SMCC (succinimidyl-4-(*N*-malemidomethyl)cyclohexane-1-carboxylate) to link 945W thiol groups to the remaining collagen primary amines.

3.2.5 Release of GDNF from heparinized collagen fiber sheets

While loading level effects of GDNF were characterized by the DRG neurite outgrowth response, it was also important to determine how tunable the release parameters were by conjugating heparin to collagen fibers during the spin and using heparins affinity to bind soluble GDNF as a method of controlling release. The very high concentration of EDC required limits the capacity of collagen fibers to be post-modified by heparin conjugation using EDC crosslinking of heparin's carboxylic acid groups to the collagen primary amines. To circumvent this, heparin was added directly to the EDC crosslinking bath to be activated and compete with EDC alone for reaction with the collagen primary amines. Heparin was added to the collection bath at several concentrations, characterized by the relative amount of heparin addition to mg of collagen spun as measured by TBO assay for $COOH^-$ (Fig. 3.2). Concentrations tested included a non-heparinized control, 7.6 μg heparin per mg collagen, 17.6 μg hep/mg collagen, and 33.1 μg hep/mg collagen to determine how much heparinization would prolong GDNF release. GDNF was labeled to be fluorescent at 488 nm using a DyLight fluorescent labeling kit and loaded at 250 ng $GDNF_{488}$ per collagen sheet. Collagen sheets were placed into 500 μl PBS for release and full PBS volume was collected and exchanged after 6 hour, 12 hour, d1, d2, d4, d5, d7, and after 12 days. A plate reader was used to compare $GDNF_{488}$ in the collected solution for each timepoint and compared to a known set of $GDNF_{488}$ standards.

3.2.6 Effect of fibrin fiber sheet heparinization on neural stem cell spreading and FITC-lysozyme release

Modification of fibrin fiber sheets with heparin to control growth factor release was investigated. To do this, neural stem cell spheroids were formed from MicroTissue 36 sphere molds seeded with 25k cells per mold for formation overnight and then cultured for seven days on heparinized and non-heparinized fibrin sheets in NSC maintenance media, neuron differentiation media, or GDNF that was preloaded into fiber sheets. Heparinization of fibrin sheets was done as a post-production step by soaking fibrin sheets in a 0.22 µm sterile filtered 0.1 wt% EDC-activated heparin solution in 0.05 M MES for one hour at room temperature while under agitation on an orbital shaker followed by triple washing with sterile DI water prior to cell seeding. GDNF was loaded into the preloaded group were soaked into fiber sheets overnight at a concentration of 10 ng/ml. The same concentration of GDNF was to media in the GDNF soluble group to compare the effects of freely solubilized GDNF with sheets that had GDNF presentation based on release from heparin. Heparinized sheets and non-heparinized sheets were examined after seven days for all four media types after being fixed in 4% paraformaldehyde and stained for βIII-Tubulin, Nestin or GFAP.

3.2.7 Physical loading and release of FITC-lysozyme from fibrin and alginate fibers

As an alternative to controlled release via post loading of heparinized fibers, investigation into direct inclusion of growth factor in situ during fiber formation was investigated using FITC labeled lysozyme. FITC-lysoszyme was added to the precursor solutions for 1.5 wt% alginate and 2.0 wt% fibrin to be captured during the crosslinking of the fibers in the normal 50 mM $CaCl_2$ and thrombin collection baths respectively. Following the spins, fibers were air dried and fluorescence images of the fibers were taken.

Additional images were taken of the fibers after being placed in 50 mM $CaCl_2$ solution for 30 minutes and after days 1, 3, and 10. The relative fluorescence intensity of the fibers at these time points were measured using ImageJ and plotted to generate a relative release profile over 10 days.

3.2.8 In situ spinning of live cells during formation of electrospun hydrogel fibers

A particular advantage of electrospun hydrogel fiber spinning over traditional synthetic polymer nanofiber spinning is the lack of organic solvent usage and the lower wt% of materials that can be spun. To demonstrate this advantage, investigation was made into whether or not live cells could be viable if included in the precursor solution and electrospun. To test this, several types of fibrin and alginate-fibrin composite fibers were investigated with human immortalized Schwann cells added directly to the precursor solution and spun along with additional glucose to maintain solution tonicity. While the primary goal of these experiments were cell survival, the selection of fiber spinning conditions were also aimed at enabling cellular migration through the fiber so some migratory capacity would remain to those cells initially trapped within the matrix created by the electrospun hydrogel fiber. Fibrinogen solutions at the normal 2.0 wt% were expected to be too dense for ASC migration, which tend to only migrate through randomly oriented fibrin structures up to 1 wt% fibrin. As even 1 wt% electrospun fibrin fibers will likely have higher fibril packing efficiency compared to random gels of the same composition, it was desirable to spin the minimum possible fibrinogen composition that could still successfully form a fiber. To this end, 0.4 wt% fibrin fibers were spun with a high cell loading density of 32k human immortalized Schwann cells per µl fibrinogen spun.

An alternative experiment was also conducted utilizing a pair of y-syringe pump setups to spin alginate-fibrin composite fibers where pumps were placed on opposite sides of the collection wheel and spun simultaneously onto the same bath to create distinct regions of fiber containing different cell types. In this case, rather than different cell types, sets of Schwann cells were labeled with different fluorophores and imaged with a fluorescence microscope after seven days culture. Each set of pumps contained human immortalized Schwann cells labeled with either live cell tracker green or live cell tracker far red. Cells were spun at a density of 1000 cells per µl. Fibers containing cells were placed into Schwann cell media directly after spinning. During the first 24 hours, media was supplemented with 0.5 U/ml alginate lyase to remove alginate from the composite to improve motility of cells.

3.2.9 Fibrin cardiac patch spinning

Cardiac patches were formed using two different fibrinogen concentrations to mimic the mechanical properties of native tissue extracellular matrix during homeostasis and the stiffer state that is present following myocardial infarction as these two conditions will impact the contractile response of cardiomyocytes. Fibrin cardiac patch sheets are spun using two compositions of fibrinogen under sterile conditions. Homeostatic-mimicking sheets are spun using a precursor solution of 0.75 wt% fibrinogen in 0.2% PEO while the infarction model sheets are generated using 2.0 wt% fibrinogen. PEO is prepared as a 1.0

wt% stock in DI water that is dissolved over several days at 37°C. Once prepared, the 1.0 wt% PEO stock is further diluted to 0.2 wt% PEO by mixture with additional DI water before use and briefly vortexed to ensure mixing. To prepare at 0.75 wt% fibrinogen precursor solution, ~9 mg of fibrinogen is added to an empty 2 ml round bottom Eppendorf tube (~24 mg added for 2.0 wt% fibrinogen). Once added, the fibrinogen is dissolved by addition of 1.2 ml of 0.2 wt% PEO to the 2 ml Eppendorf tube, which is placed in a 37°C water bath for at minimum 15 minutes to ensure dissolution.

Following dissolution of the fibrinogen, the precursor solutions are transferred to a biological safety cabinet and sterile filtered into autoclaved round bottom Eppendorf 2 ml tubes using a 0.22 µm filter. The filtered fibrinogen is loaded into a 1 cc syringe and large air bubbles are dislodged by gently moving the syringe plunger back and forth while the syringe is facing upwards. The syringe is then loaded onto a syringe pump set to dispense at a rate of 5.0 ml/hr for 0.75 wt% fibrinogen or 3.25 ml/hr for 2.0 wt% fibrinogen. A collection solution of 20 U/ml thrombin in 50 mM $CaCl_2$ is prepared by dissolving 1 ml of a 1000 U/ml thrombin stock solution into 50 ml of sterile filtered 50 mM $CaCl_2$. The DC motor controller is turned on and the power to the collection wheel motor is increased until the wheel is rotating at ~45 RPM, at which point the 50 ml collection solution is added. The linear stage upon which the syringe pump sits is powered on and begins rastering at a rate of ~ 3 cm/min over a distance of 1.5 cm. The syringe pump is set to run and begins dispensing the fibrinogen solution at which point the power supply is turned on and set to 4.5 kV to initiate jet formation.

The solution is electrospun onto the collector for 17 minutes when using 2.0 wt% fibrinogen or 20 minutes total using 0.75 wt% fibrinogen with a pause in spinning after 10 minutes to refill the syringe. Upon completion of the spin time, the fibrin sheets are allowed, at minimum, two additional minutes in the crosslinking solution to ensure fibrinogen deposited later in the spin has had sufficient time to stabilize with the power supply off. A 1 cm x 1 cm plastic frame is then placed onto the resulting fibrin sheet and a cut is made along one side of the fibrin sheet (typically the side of the frame distal to the operator). The frame is flipped end over end towards the operator a total of six times, being careful to ensure entrapped air bubbles do not significantly disrupt alignment. A single spin will normally yield six frames with six fibrin layers. Once collected with the frames, fibrin sheets are placed in DI water to dilute residual thrombin for a minimum of 30 minutes before use. Sheets can be stored in DI at 4°C indefinitely should there be no contamination if sheets are not needed on the day they are spun.

Prior to cell seeding, excess water is wicked away from the fibrin sheets by touching the frame edge against autoclaved kimwipes and then briefly touching the fiber sheet face against the same kimwipes. This has been found to enhance the adhesion of cardiac cells which empirically seem to be more sensitive to fiber hydration conditions compared to neuronal cell types. Once partially dried, sheets should be placed vertically in a 24 well plate and stored at 4°C until use to prevent sheets from drying out. Partially dried fibrin sheets must be used within a couple days or loss of hydration will be substantial enough to start damaging the sheet.

3.2.10 Fibrin fiber sheet alignment effects on microvessel formation and cardiac cell alignment

Fibrin hydrogel microfiber sheets were formed by a modified electrospinning process where fibers were collected on a rotating bath containing a crosslinker bath. Briefly, a 2 wt% fibrinogen (Sigma, St. Louis, MO, USA) was dissolved in 0.2 wt% polyethylene oxide (PEO, 4 million M_z) (Sigma) and loaded into a blunted 27G tip syringe. The loaded syringe was then placed into a syringe pump and extruded at a flowrate 3.25 ml/hr. A positive voltage of 4.5 kV was applied to the syringe tip to propel the fibrinogen-PEO solution jet onto a grounded and rotating collection bath (45 RPM) containing 50 mM $CaCl_2$ (Fisher Scientific, Waltham, MA, USA) and 20 U/ml thrombin (BioPharm Laboratories LLC, Bluffdale, UT, USA) in deionized water to form fibrin hydrogel fibers. Sheets were formed by rastering the landing position back and forth for 17.5 min after placing the syringe pump on a linear stage. Upon completion of the spin, 1 cm^2 sheets were collected by wrapping six layers of sheet from the collection bath onto PET frames. Samples were then soaked in DI water overnight to remove residual thrombin and calcium. To improve cell attachment during seeding, fibrin fiber sheets were partially dried by using sterile Kimwipes to briefly wick away excess water by placing the wipe against the edge of the PET frame. Once partially dried, fibrin sheets are stored at 4°C until seeding to retain moisture and may be stored in such a manner for at least two months. Fibrinogen and crosslinker bath solutions were filtered with 0.22µm filter before use and sheets were spun under sterile conditions in a biosafety cabinet.

The mechanical properties of fibrin fiber sheets are very similar to those of physiological cardiac tissue. For the formation of transplantable cardiac patches to treat regions damaged by myocardial infarction, it is important to not only have a similar stiffness value to native tissue but also induction of the alignment features seen with the cardiomyocytes and their corresponding vasculature to ensure the function of the construct matches as closely as possible with the native tissue. To check this with our fibrin sheets, experiments were done to characterize the alignment of microvessels formed from HUVEC cells and cardiomycytes to see if the resultant structure could be similar to the native pericardium of the heart.

Fiber alignment effects on microvessel formation were characterized from HUVEC cultures on 2 wt% fibrin fiber sheets for one week before being fixed and immunostained for CD31, a blood vessel surface marker, to visualize the spontaneous alignment response of the cells. For trophic support, human adipose derived stem cells were cultured in a 1:1 ratio with HUVECs seeded onto the surface of aligned fibrin fiber sheets at different total cell densities to compare cell number effects on alignment after one week in culture.

3.2.11 Electrospun hydrogel fibrin fiber bundles and tubes for generation of vascular grafts

Early studies demonstrated that fibrin fibers made excellent candidates for culture of vascular cells including endothelial colony forming cells (ECFCs) and smooth muscle cells (SMCs). These studies showed excellent alignment response of the cells to the fiber alignment and were found to promote generation of additional extracellular matrix components such as collagen IV [35, 36]. While these fibrin fibers proved to be highly beneficial for vascular cell culture, the system of culture around a solid fibrin fiber limits such a system to in vitro study. Thus, it was desired to develop a hollow fibrin fiber tube that could be perfusable and implantable as a vascular graft.

There are two primary modes of electrospinning fibrin for vascular applications currently established. The original fibrin string methodology generating dried fiber bundles upon which the outer surface is seeded with endothelial cells. The more recent and advanced configuration is to apply the fibrin sheet spinning methodology in conjunction with Teflon coated mandrels to create hollow fibrin tubes with topographical alignment that can be perfused.

Fibrin strings are generated by mixing alginate (AG) with fibrinogen (F) during the spin followed by stretch drying to enhance topographical alignment features beyond that which can be created from the “off the collection wheel” product. To generate the prepolymer solution for this configuration, 9.1 mg to 24.5 mg fibrinogen are added to 1.5 ml round bottom Eppendorf tubes and then dissolved in a 1.2 ml of 0.2 wt% PEO solution in DI for 15 to 30 min at 37°C just prior to spinning. Alginate is similarly dissolved for several days prior at 37°C in 0.2 wt% PEO as it dissolves more slowly at physiological temperatures than fibrinogen. An additional syringe pump line is added to the standard spinning setup so that both fibrinogen and alginate have separate feeds into a “Y” shaped custom nozzle that mix the two components in line just prior to their jettison at the needle tip connected to the power supply alligator clip. The “Y” syringe consists of two 31 g luer lock needle “inlets” that merge to mix in a 20 g needle that has been cut and polished on both ends. The a 25g “outlet” needle with cut and polished tip is inserted into the 20 g mixing section and then potential leakage sites are sealed with generous wrapping using thin, 1-2 mm diameter, parafilm strips (note that these early gen “Y” syringe needles have been supplanted by improved commercial “Y” syringes in the more recent work done by the lab of Prof. Warren Grayson for skeletal muscle engineering projects at the translational tissue engineering center at Johns Hopkins University using AG-F fibers). The flow rates of the two components can be independently modified to change the relative proportion of alginate and fibrin in the final as-spun fiber, usually characterized by an AG/F ratio.

Fibrin fibers in the earlier study generated by using alginate-fibrin composite spins followed by alginate removal with 150 mM sodium citrate overnight and then stretching of the remaining porous fibrin fibers to strains of 50% during air drying. To generate hollow fibrin tubes, a modification of the fibrin fiber sheet spinning parameters was used. Fibrin fiber sheets were prepared as with the cardiac sheet preparation using 2.0 wt% fibrinogen as the precursor solution. The procedure diverges in the wrapping step. Rather than wrapping sheets around mylar frames, sheets are wrapped around teflon (PTFE) coated stainless steel mandrels (Applied Plastics). Wrapping around the stainless steel mandrel allows alignment of individual layers to be circumferential, perpendicular to the direction of blood flow, or longitudinal, in parallel with the flow of blood. Once wrapping of fibrin tubes are complete, they are stored in sterile DI water overnight to allow residual thrombin captured in the fibrin fibers to diffuse away. Following this, fibers are dehydrated in a series of ethanols up to 100% ethanol and then air dried. Once dried, tubes are able to be removed from PTFE coated mandrels and stored at 4°C dry or rehydrated. Despite not being stretch dried like earlier generation fibrin strings, alignment features remain well aligned on the tube surface.

3.3 Results and Discussion

3.3.1 Spreading of primary Schwann cells on fibrin and collagen fiber sheets

On collagen fiber sheets, Schwann cells showed a high degree of spreading over 6 days with cells migrating up to 1750 μm and showing themselves to be highly responsive to the fiber alignment with a bias in orientation towards the direction of alignment (Fig 3.3). Few Schwann cells migrated out from the spheroids after day 1 with most cell spreading a result of fibroblasts based on the faint non-specific staining seen. By d3, Schwann cells had spread up to 1000 μm away from their initial spheroid position.

Fibrin sheets showed higher initial spreading of Schwann cells after one day culture (Fig. 3.4) with some initial spreading being seen outward from the spheroid. By day three, spreading had continued though not with the same extent of alignment as collagen fiber sheets. Some samples of fibrin sheet showed significant degradation of the sheet by the Schwann cells, leaving large gaps.

3.3.2 Neurite extension from DRG explant as function of fiber alignment

Figure 3.5 shows the resultant extension for the three groups tested. Both aligned collagen fiber conditions clearly show increase in neurite extension along the fiber alignment direction with maximum extensions of nearly 5000 µm after two weeks culture. Little difference was seen comparing the matrigel and uncoated collagen fibers, indicating that the biological integrin binding sites of collagen are maintained during the electrospun hydrogel formation process and that coating with additional cellular adhesive cues such as matrigel, laminin, or fibronectin are not necessarily required to enhance neurite outgrowth on these materials (Fig. 3.6). Substantial difference was seen between the aligned collagen fiber groups and the random cast collagen gel. The random gel showed relatively consistent outgrowth in all directions of 1500-1750 µm. The horizontal axis in each random collagen image were arbitrarily defined as the "fiber alignment axis" for comparing outgrowth from each 5-degree interval. Surprisingly, while the outgrowth distance was much higher for the DRG explant neurites along the aligned fiber axis than the random gel, the outgrowth towards the direction perpendicular to the fiber alignment was actually less than the corresponding outgrowth on random collagen at only 1000 µm. This can be explained from the immunostained images on aligned collagen fiber samples showing some initial axon growth perpendicular to the fiber alignment that soon turns to follow the fiber alignment direction once cleared from the local region surrounding the DRG explant.

3.3.3 Outgrowth of neurites from DRG explants on uniformly loaded GDNF collagen fiber sheets

Lack of GDNF loading yielded the lowest overall neurite outgrowth after seven days (Fig. 3.7). Inclusion of GDNF improved the spreading as illustrated by the shift towards higher neurite outgrowth. 50 ng GDNF shifted the distribution peak from around 1800 μm with no GDNF loading to 2600 μm. Loading of 100 ng GDNF showed similar outgrowth distance from analysis of distribution peaks but the overall spreading was less pronounced at 100 ng compared to 50 ng GNDF due to the increased uniformity in neurite population percentage at a given outgrowth distance. Additionally, both 100 ng and 250 ng showed higher maximum outgrowth higher numbers of neurites present at 4000 μm or higher outgrowth. GDNF levels of 250 ng showed a distribution peak spread more towards the lower end of neurite outgrowth with 15% of neurites extending 1600 μm and an overall distribution peak around 2000 μm. Increasing the GDNF loading to 500 ng showed a shift in peak towards higher outgrowth at 3000 μm while maintaining close to 10% of neurites extending 4000 μm or more. Further increasing GDNF loading to 1000 ng started to show some minor bimodal behavior, with a small peak at 3400 μm but a larger peak also apparent at 2000 μm and another small jump being seen at 1000 μm outgrowth.

The neurite outgrowth distributions show a clear benefit of GDNF inclusion compared to unloaded nerve guides based on the overall shift in distribution peaks towards higher outgrowth after seven days culture and a higher percentage of axons showing high outgrowth over 4000 μm compared to the unloaded collagen sheets that had at highest 3400 μm extension. Less clear is the differences between GDNF groups. Ideally there should be a point of maximal GDNF benefit while minimizing the total amount of growth factor, and therefore cost, required. While 50 ng GDNF distribution data showed a nice skew towards higher outgrowth, there was a relatively small proportion of neurites that grew more than 4000 µmin one week. This is an important subpopulation to consider as better functional recovery would be expected with conditions that more rapidly allow initial reconnection with the distal nerve stump. While the 250 ng GDNF group had good high range spreading, the skew in peak towards lower outgrowth levels eliminated it from contention. The group with best combined high outgrowth performance and distribution skew was the 500 ng per sheet group and so this was the concentration selected for nerve guide inclusion. 1000 ng did not appear to offer significant advantage over 500 ng and while 50 ng showed good performance on an outgrowth per GNDF used metric, the reliability of 500 ng GDNF loading was expected to maintain an effective level of GDNF longer than 50 ng based on release rate studies of GDNF from collagen fiber sheets.

3.3.4 Consumption of free amines during collagen fiber sheet formation

Calculations of theoretical molar concentration of primary amines in 1 ml collagen stock solution yielded around 320 nmol of primary amines potentially available for crosslinking prior to collagen fiber formation. Following fiber formation, the number of free amines were drastically reduced to just 10 nmol, or just over 3% of the original free amines remaining available for bioconjugation through a primary amine pathway (Fig. 3.8). Primary amine levels of collagen following 945W conjugation were even lower, with only 3 nmol or just under 1% of primary amines remaining. While there was a relatively small concentration of primary amines remaining available after fiber formation, it was still possible to do a post-spin modification using amines. Due to only 3% of the original free amines remaining, there exists a limiting cap on the total potential conjugation that can occur and by consequence, a small window of potential concentrations that can be used to investigate effects of peptide conjugation density on cellular response. This currently is a great limiter on the potential tailoring of collagen fiber sheets post-spin. Potential improvements could be made in the bioconjugation capacity of collagen hydrogel fibers by introducing additional conjugation groups such as thiols to the precursor collagen to use other methodologies that do not involve amine groups, such as maleimide crosslinking chemistries.

3.3.5 Release of GDNF from heparinized collagen fiber sheets

Release rates for all four groups tested showed moderate amounts of burst release over the first 6 hours of release (Fig. 3.9) before showing a reduction in release rate after 12 hours to more of a sustained release profile that lasted until experiment endpoint at 12 days. Surprisingly, the addition of heparin sped up release rather than slowing it down as expected. Separating out the % GDNF release into burst release and sustained release categories (Fig. 3.10) shows variation in the burst release up to 6 hours as heparin levels change, with higher release correlating following higher heparin levels. Interestingly, after the burst time period of 6 hours, all four groups had similar overall levels of sustained release between 6 hours and 12 days, with 10% GDNF released over this time period.

The similar sustained release between all groups offers a potential explanation as to why the increased heparin levels unexpectedly cause higher initial release rates of GDNF. As part of its physiological role as a structural component of the extracellular matrix, collagen contains a heparin binding domain that can capture heparin which in turn binds many soluble growth factors and cytokines. It is very possible that rather than the EDC activated heparin being covalently conjugated to collagen fibers during their formation, that instead they are being temporarily electrostatically bound to collagens heparin binding domains due to the smaller EDC molecules having faster diffusivity than EDC-heparin. Heparin bound to the binding domain would still have the capacity to bind growth factors. What is likely happening in this case is that the heparin itself is unbinding from collagen over time, taking growth factor with it.

Higher heparin concentrations added to the collection bath would result in higher levels of electrostatically bound heparin meaning more growth factor would be dislodged along with heparin, causing the higher release rates measured. This sort of behavior is consistent with the relative sustained release being so similar between all groups as after 6 hours as the loosely bound heparin has all cleared itself from collagen. This leaves only GDNF bound directly to collagen for release and with heparin mostly gone, results in the similar % $GDNF_{488}$ sustained release comparing all groups. This is potentially beneficial as conjugation of heparin using other chemistries might improve chance for successful covalent conjugation, allowing a method of delaying growth factor release relative to unmodified collagen fiber sheets. Should more rapid release than unmodified collagen fibers be required, heparin can be added directly to the collection bath to control the initial burst release.

3.3.6 Effect of fibrin fiber sheet heparinization on neural stem cell spreading and FITC-lysozyme release

In all instances of heparinized sheets, cells showed very limited amounts of outgrowth from their initial spheroid seeding positions after 7 days culture (Fig. 3.11). Spreading was seen in all four non-heparinized sheet media and GDNF presentation conditions. Little differences could be qualitatively determined from the non-heparinized fibrin sheets other than the differentiation media group showed minimal spreading compared to the other three conditions, a result that was expected. Fibrin sheets lacking GDNF appear to have higher spreading based on the maintenance media group but this result could be confounded by a higher local NSC spheroid seeding density as seeding density was difficult to control with the spheroids. The primary takeaway from this study was that heparinization of the fibrin sheets can actually inhibit cellular spreading, likely by the high negative charge of heparin shielding integrin binding sites with from the cell surface. While this was not tested, an easy way to avoid this issue could be to have the inner layers of fibrin sheets be heparinized and then later on additional outer non-heparinized sheets be wrapped over these. In such a scenario, growth factor binding and controlled release from heparin would still occur but the cells seeded on the outer non-heparinized layers would not have their attachment capabilities compromised, allowing enhanced spreading and migration from the cytokine release from underneath.

Release rates from heparinized fibrin sheets were tested over one week using fibrin sheets heparinized by soaking in 0.1 wt% EDC-activated heparin for comparison against non-heparinized sheets. FITC labeled lysozyme was used as the model growth factor due to its similar molecular weight to GDNF at 15 kDa. Heparinization was found to slow the release profile of FITC-lysozyme from fibrin sheets unlike with collagen fiber sheet release of GDNF due to the easier heparin corporation into fibrin fibers (Fig. 3.12).

3.3.7 Physical loading and release of FITC-lysozyme from fibrin and alginate fibers

Alginate showed the highest level of release of FITC-lysozyme, with as much as 80% drop in fluorescence intensity after 30 minutes compared to the initial hydrated state (Fig. 3.13). A further 10% drop was seen between days 1 and 3. By day 10, alginate fibers themselves were difficult to distinguish from background levels of fluorescence, which had shown significant increase compared to the early time points. Release of FITC-lysozyme from fibrin was much slower compared to alginate. Very little loss of fluorescence was seen after 30 minutes and only 10% loss seen after one day. Relative rate of release remained similar between days 0 and 1 compared with 1 and 3, resulting in just over 40% loss in fluorescence intensity by day 3. At day 10, nearly 30% of the original fluorescence intensity remained.

These results are consistent with the expected release behavior based on the differences in hydrophobicity and wt% of material spun. Alginate, being relatively hydrophilic, will swell to a higher degree than fibrin as it absorbs more water, as seen from swelling ratio data comparing the two materials. This swelling leads to an increase in the number diffusive pathways for FITC-lysozyme release in alginate compared to fibrin and its lower degree of swelling. This results in the prolonged release of FITC-lysozyme. Larger proteins or particles would be expected to have even better capture in situ. A prime example of this was the addition of fluorescent beads into fibrin fibers in collaboration with Pinar Huri and Colin Cook to track microscale changes in the fibrin structure during mechanical stretch in a custom designed bioreactor [37]. This relative behavior with release rate being dependent on fiber hydrophilicity would likely be maintained across different biomaterials spun. Fibrin is a unique case as it is relatively more hydrophobic than other hydrogel fibers spun so it would be expected that fibers made of hyaluronic acid, collagen, or gelatin would have similar release profiles. Synthetic fibers spun with the electrospun hydrogel platform, such as PLGA, would very likely have slower release profiles compared to fibrin due to their higher hydrophobicity and density although synthetic materials such as these have not been tested for release profiles in this system.

3.3.8 In situ spinning of live cells during formation of electrospun hydrogel fibers

Figure 3.14a shows the resulting fiber and cell loading after 4 days culture using live cell tracker to visualize fibers. Cells remained viable though the fibrin density still remains high enough at 0.4 wt% to minimize spreading of the cells, particularly in the interior.

Results after seven days show that Schwann cells minimally, if at all, migrated away from their home fibers as indicated high degree of segregation between the far red labeled and green immortalized Schwann cells (Fig. 3.14b). It is possible that while cells survived, their function was compromised as a result of in situ encapsulation within the hydrogel fibers. More testing would need to be done looking at functional assays or tracking metabolic activity to get a better idea if cells were damaged during spinning.

Factors to consider for this sort of application are the osmotic pressure, electric field strength, and ionic concentration of the collection bath. Electric field strength can have amongst the highest potential impact on cellular viability. Exposure to the electric field in effect can temporarily cause electroporation of the cellular membrane during its travel along the polymer jet [38]. Due to the electric field strengths involved, it is very likely that the porosity in the cell membrane induced by the electric field will not have had a chance to recover by the time the cells and fiber make contact with the collection bath. This can lead an inrush of the collection bath, particularly the Ca^{+2} ions, into the cytoplasm of the cell, causing massive damage to normal cellular function. As even a small amount of Ca^{+2} imbalance within the cell can cause mass dysfunction in cellular machinery [39], the high 50 mM Ca^{+2} in the bath has a large diffusive driving force to rush into the cell if there is any electroporation remaining. Due to the ion imbalance between the cytosol and collection bath, it is important to minimize the overall electric field strength in order to reduce the magnitude of electroporation that occurs and improve the recovery time of the cell membrane. Additionally, it is important to minimize concentration of ions used in the collection bath to minimize the diffusive driving force of the collection solution into the cell.

For the two in situ cells experiments, cells were spun onto isotonic solutions by balancing solution ion levels with glucose. Another potential avenue of improving the reliability of cellular encapsulation is by increasing the tonicity of both the collection solution and precursor solution to hypertonic levels. Tonicity levels have been shown in studies by other labs [40] to affect the electroporation of the cell membrane upon exposure to the electric field. By making a hypertonic solution, cells in the precursor solution will exclude water from the cytosol to balance their internal tonicity with the exterior environment, causing a reduction in size of the cell. This has the effect of improving resistance to electroporation, which could potentially minimize the infiltration of collection solution and reduce recovery time of the cell membrane after exposure to the electric field. Future investigation into cellular encapsulation would likely include having a precursor solution that is somewhat hypertonic being spun with cells onto a collection bath that is even more hypertonic to minimize damage caused by the electric field.

3.3.9 Fibrin fiber sheet alignment effects on microvessel formation and cardiac cell alignment

Fibrin sheets wrapped end over end to generate 6 layers were seeded with various amounts of vascular and cardiac cells (Fig. 3.15). Figure 3.16 shows the alignment of HUVECS at densities of 100k, 200k, 400k, and 600k cells/cm^2 on 1 cm^2 fibrin fiber sheets after seven days. Vessels showed good alignment in all four seeding conditions with particularly prominent alignment being seen at the 100k and 200k cells/cm^2 densities. Higher cell seeding density still maintained good alignment but had much higher levels of interconnectivity between microvessels. To confirm that alignment induction would occur with other vascular cell types, human endothelial cell forming cells (ECFCs) were also cultured in a 1:1 ratio with ASCs on the surface of fibrin fibers. ECFCs showed a high degree of alignment even at a very high cell seeding density (Fig. 3.17). Comparison of HUVEC alignment was made with random fibrin gels (Fig. 3.18) showing the superior alignment induction of by the fibrin fiber sheets compared to the random structure seen with the random gel after one week culture.

Rat ventricular cardiomyocytes were also cultured on fibrin hydrogel microfiber sheets and showed strong response to topographical alignment cues. Particularly exciting is the presence of α-actinin filament striation, indicating that not only are the cardiomyocytes aligning with the fibers, but are also showing features of mature phenotyping *in vitro* after seven days culture (Fig. 3.19).

3.3.10 Electrospun hydrogel fibrin fiber bundles and tubes for engineered vascular grafts

Organization of endothelial cells and their ECM deposition on large diameter fibrin strings 200-250 μm are shown in (Fig. 3.20). As can be seen in the images, there is a high degree of cellular organization along the direction of fibrin fiber alignment from the directionality of the actin filaments within the cells and elongation of the nuclei in the direction of alignment. The topographical alignment cues are not only limited to the cellular structure but also the deposition of extracellular matrix components by endothelial colony forming cells including collagens I, III, and IV, fibronectin, and laminin along the direction of fiber alignment. All of these extracellular matrix components were found to be upregulated at least 3 fold on the three dimensional fibrin fiber surface compared to a two dimensional fibrin gel substrate [35].

Most commonly, 1.5 wt% AG is used with 2.0 wt% F at flow rates of 2 ml/hr and 1 ml/hr respectively yielding an AG/F ratio of 1.5. Fibers are spun for ~15 to 35 minutes onto a collection solution containing 10 U/ml to 20 U/ml thrombin in 50 mM $CaCl_2$ at a wheel speed of 30 – 45 RPM without rastering at an applied voltage of ~ 4kV and separation distance of 3 cm to yield an AG-F string. A maximum spin time of 10 to 15 minutes can be achieved without rastering without the presence of ‘bulbing’, where fibrinogen deposited at later time points does not crosslink as rapidly as that deposited earlier in the run, causing small amorphous blobs to form on the fiber surface. Once spun, AG-F fibers are cut into 1/3rd and soaked in a 250 mM sodium citrate solution for five hours to overnight. The citrate acts as a chelating agent for the Ca^{+2} that form the ionic crosslinks in alginate, removal of which causes the alginate to dissipate into solution leaving behind a fibrin fiber. This fibrin fiber is rinsed several times in DI water and then dried in air strained to 150% of its initial length by anchoring the two fiber ends during dry to enhance the alignment properties further beyond those achieved with the mechanical rotation of the collection bath and electrically induced alignment. Prior to cell seeding, fibers are soaked in 75% EtOH for 10 minutes then dried again.

The second, more advanced, configuration for fibrin fiber usage in vascular applications is as a perfusable fibrin tube that has alignment features on the outer surface and in the lumen of the tubes (Fig. 3.21). Preparation is identical to the 2.0 wt% fibrinogen spinning for sheet formation used with cardiac patch applications before diverging in the method of collection. To collect the fibrin tubes, the sheets are wrapped with 0.5 mm ID or 0.6 mm ID teflon coated stainless steel mandrels. The orientation of the mandrel relative to the sheet can be used to control whether the alignment at the surface or lumen are circumferential or longitudinal, thereby allowing mimicry of the native vessel ECM alignment.

Two different measurements terms are used for defining the amount of material wrapped depending on if the wrap is longitudinal or circumferential. Circumferential uses fractional ‘wheels’ to define the amount of sheet wrapped where the ‘wheels’ are defined as the fraction of sheet taken up relative to the collection dish. As an example, typical circumferential wraps will consist of 1/6th of a wheel, which corresponds to 1/6th of the sheet collected. ‘Layers’ are used for longitudinal wrapping where each ‘layer’ is defined by the uptake of fiber sheet with length equal to the Teflon coated mandrel at one position when the mandrel position is parallel with the aligned fiber direction. As a general rule, to obtain stable longitudinally aligned fibrin tubes, there needs to be a minimum of one ‘layer’ wrapped for every 0.1 mm ID of Teflon coated mandrel. Wrapping using either method yields a highly swollen tube on the mandrel that must be dried to reduce tube wall thickness and improve mechanical properties.

The drying process used is a graded ethanol dry which begins with soaking the collected tubes on mandrels in steps of 25%, 50%, 70%, 80% EtOH for a minimum of 15 minutes each, followed by an overnight soak in 90% EtOH, then finally soaks in 95%, 100%, 100%, and 100% EtOH for a minimum of 15 minutes each step. It has been found that the overnight soak in 90% EtOH helps to reduce the incidence of cracking during drying that occurs with some batches of fibrinogen due to batch-to-batch variability and bovine sourcing. Once the ethanol drying is complete, tubes are dried in air overnight, yielding a dry fibrin tube with reduced diameter compared to the as-collected state. The compression due to drying makes it difficult to remove the fibrin tubes from the Teflon coated mandrels. The work around to this is soaking the fibrin tubes briefly in 100% EtOH to act as a lubricant for tube removal. Once removed, dried fibrin tubes can be stored at 4°C until use, making them an excellent potential off the shelf product. Such fibrin tubes have been successfully implanted in a rat aortic vessel replacement model with survival of animals up to 10 days (Fig. 3.22).

3.4 Conclusions

Electrospun hydrogel fibers were demonstrated to be compatible with many cell types as could be expected with the use of biologically derived materials. In addition, methods for modification of the hydrogel fibers for use as a therapeutic agent delivery mechanism was assessed through physical loading of FITC-lysozyme or heparinization to modulate GDNF release. While heparinization showed some success with fibrin fibers, the common crosslinking-conjugation chemistries used for collagen fiber formation and heparin conjugation made it difficult to incorporate heparin covalently. Instead, it is likely that heparin electrostatically interacts with collagen and release growth factor is mediated more by the dissociation of heparin from collagen rather than the factor from heparin. While this was an unexpected result, it does offer a methodology to increase release rate compared to the native fibers and more importantly, loaded heparin that dissociates is likely to form interaction elsewhere in the ECM so it is likely that growth factors would stay near the tissue target of interest. The varieties of applications, loading methods, and other fiber manipulations of this chapter offer potential avenues to further engineer hydrogel fiber materials for specific future applications as everything present is at least feasible with some additional investigation. In particular, most future work will ideally be aimed at conjugation of factors to the fiber surface to further modulate cellular interaction and research more highly focused on specific methods of factor release from the fibers as the variety of methods presented provide a roadmap of most likely paths to factor delivery success.

3.5 Figures

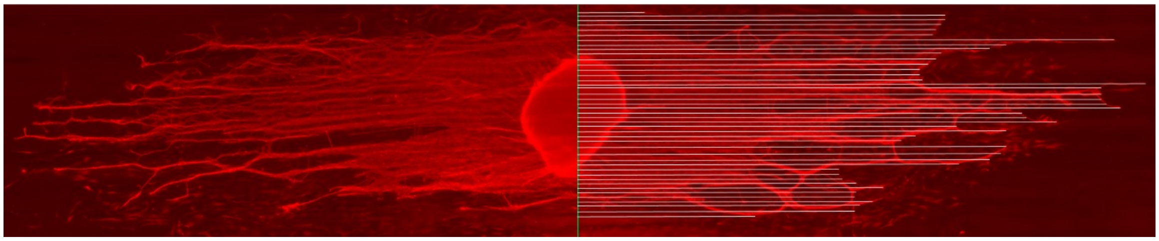

Figure 3-1: Measurement method of neurite outgrowth from DRG explant.

Outgrowth of DRG explant neurites (red) was through using bisecting line (green) which then had lines extending outward along the fiber alignment direction at 20 µm intervals (white lines). Maximum neurite along each white line was used to generate outgrowth distributions and data. Main body of the DRG explant was excluded from neurite extension measurement.

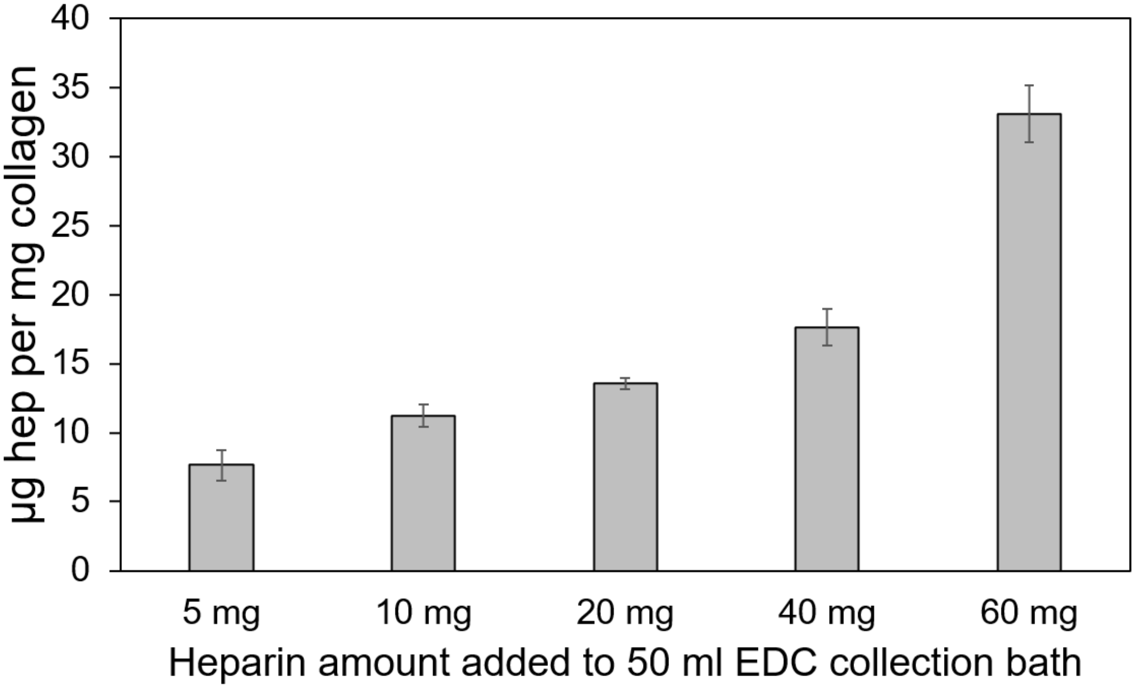

Figure 3-2: Capture of heparin in collagen fibers during spin. Heparin was added directly to the EDC crosslinking solution at several concentrations to become activated and compete with EDC for access to the free primary amines of collagen. Mass of heparin, measured by TBO assay, captured in collagen fibers increase as more heparin is added to EDC collection bath.

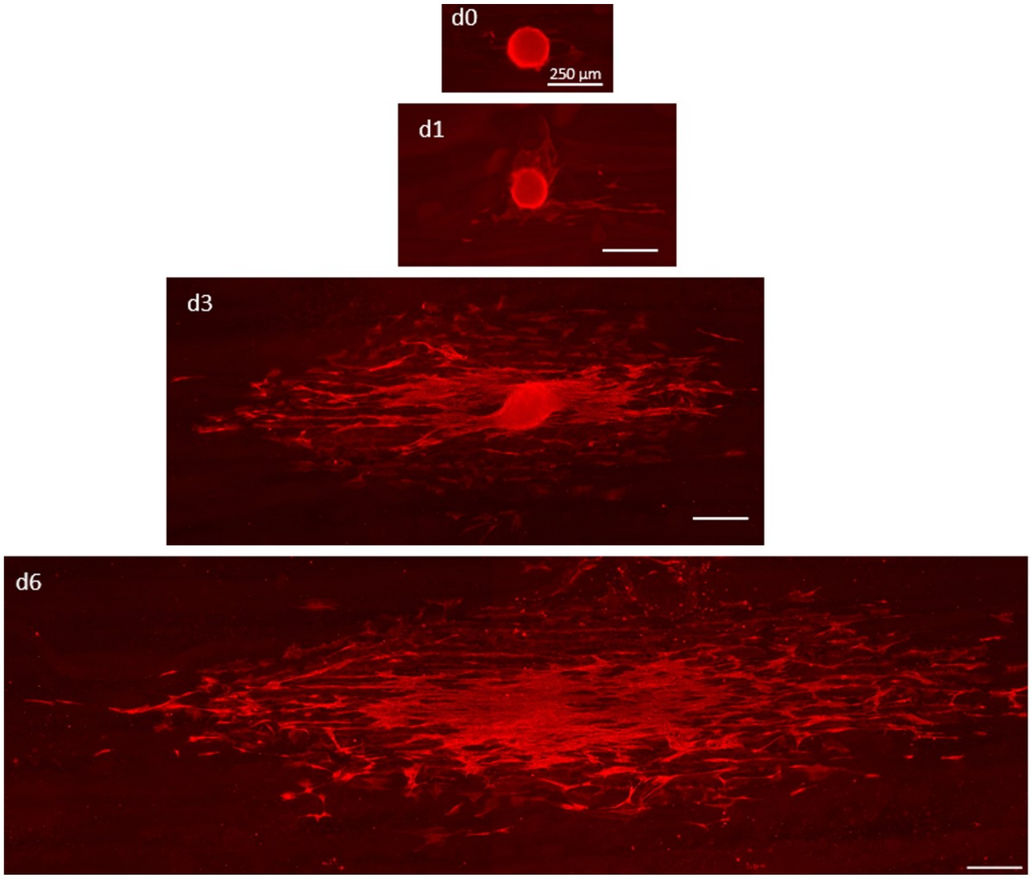

Figure 3-3: Spreading of primary Schwann cells from spheroid over 6 days on electrospun collagen fiber sheets. Primary Schwann cells seeded on collagen fiber sheets were fixed and stained for S100 (red) after one, three, and six days to characterize cell spreading. Cells were shown to migrate up to 1750 µm over six days. Scale bar: 250 µm.

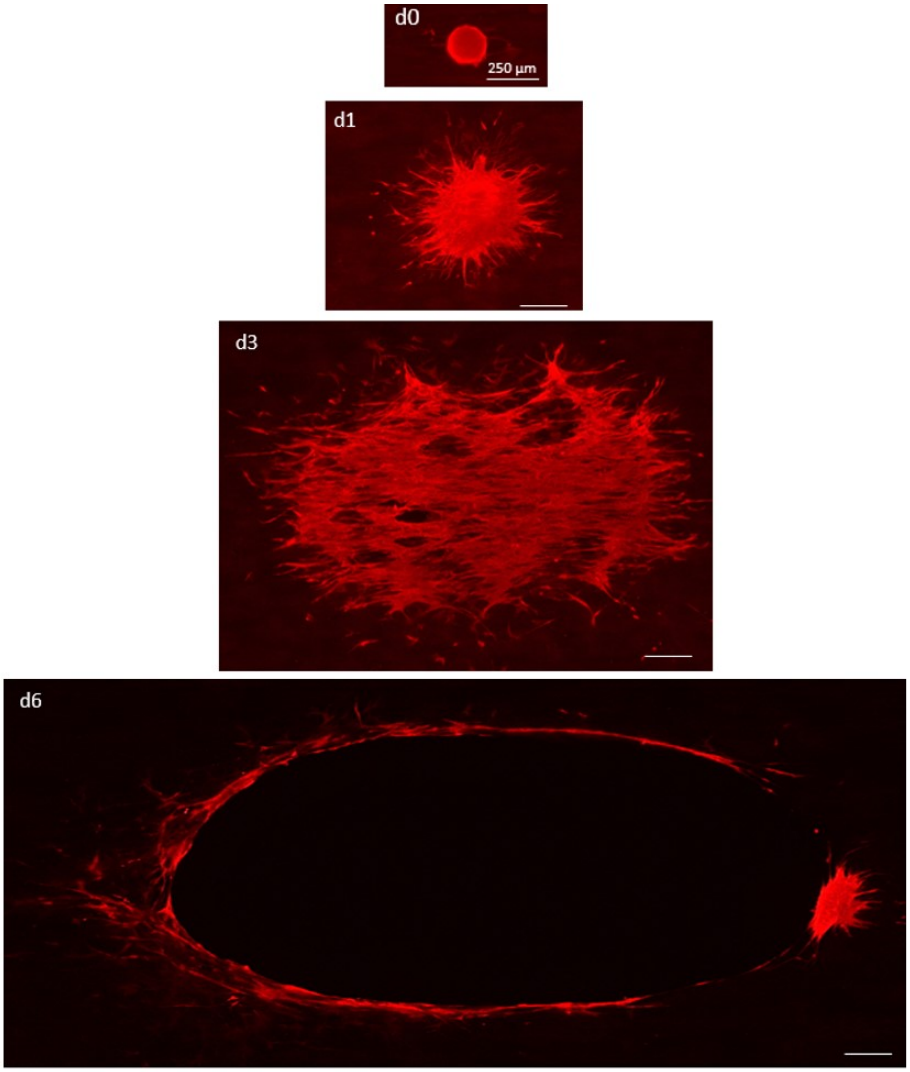

Figure 3-4: Spreading of primary Schwann cells from spheroid over 6 days on electrospun fibrin fiber sheets. Primary Schwann cells seeded on fibrin fiber sheets were fixed and stained for S100 (red) after one, three, and six days to characterize cell spreading. Cells were shown to migrate rapidly from the spheroid over the first three days but with less evidence of topographical guidance effect compared to collagen fiber sheets. Schwann cells in some instances were able to degrade fibrin sheets to high enough extent by 6 days that holes would appear in the sheet. Scale bar: 250 µm.

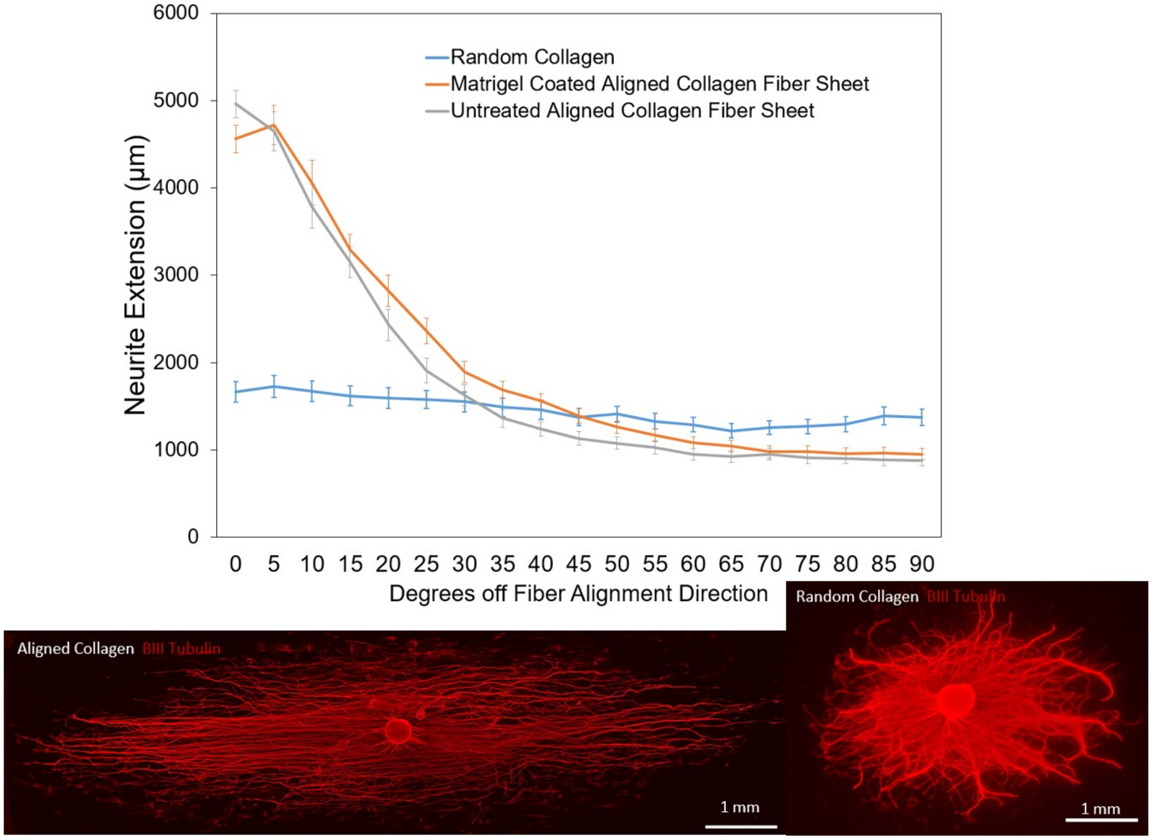

Figure 3-5: Extension of neurites from DRG explants as function of fiber alignment.

DRG explants seeded on Matrigel coated (n = 4), uncoated (n = 4) collagen fiber sheets or cast collagen gels (n = 8) were fixed and stained for βIII-tubulin (red) after 14 days to characterize neurite outgrowth as a function of alignment. Neurites clearly following alignment direction of aligned collagen fiber sheets while random collagen hydrogel shows relatively uniform extension of neurites in all direction. Scale bar: 1 mm.

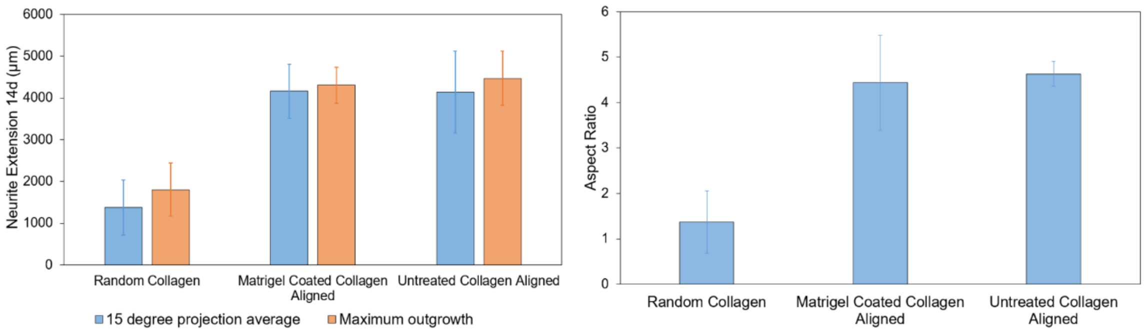

Figure 3-6: Maximum neurite outgrowth and aspect ratio of outgrowth show Matrigel coating does not enhance untreated collagen fiber sheets. Fiber alignment promotes more extensive maximum outgrowth of neurites from DRGs after 14 days compared to random collagen gels (left). Aspect ratio and maximum extension are similar between Matrigel coated collagen and unmodified collagen fiber sheets (left and right).

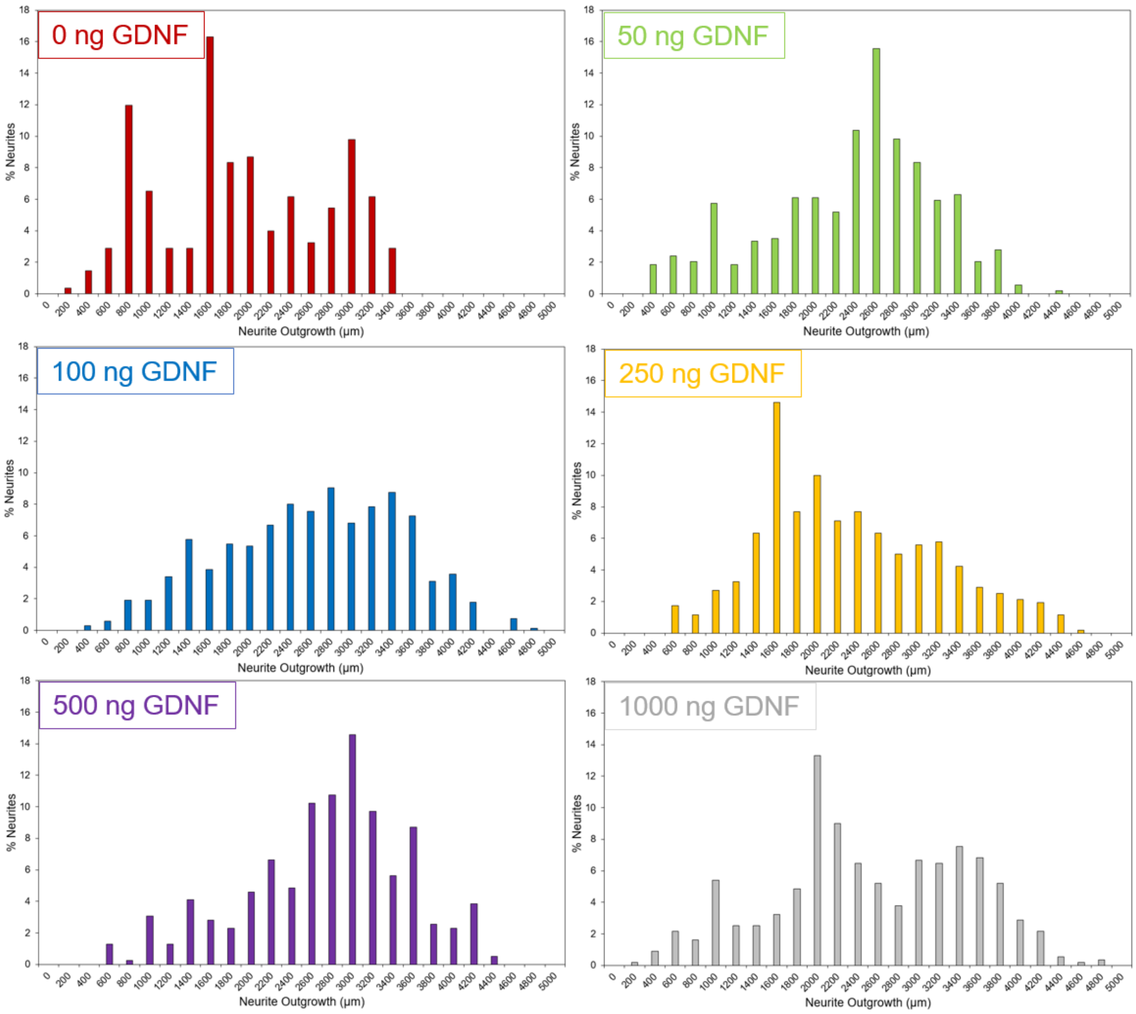
0 ng GDNF

50 ng GDNF

100 ng GDNF

250 ng GDNF

500 ng GDNF

1000 ng GDNF

Figure 3-7: Distribution of neurite outgrowth as a function of GDNF loading level on aligned collagen fiber sheets after seven days. Collagen fiber sheets lacking GDNF had neurite outgrowth most skewed towards shorter distances. Addition of GDNF enhanced neurite outgrowth with bias towards high outgrowth most seen with 50 ng GDNF and 500 ng GDNF. Other GDNF concentrations, 100 ng, 250 ng, and 1000 ng showed more centralized distributions of neurite outgrowth.

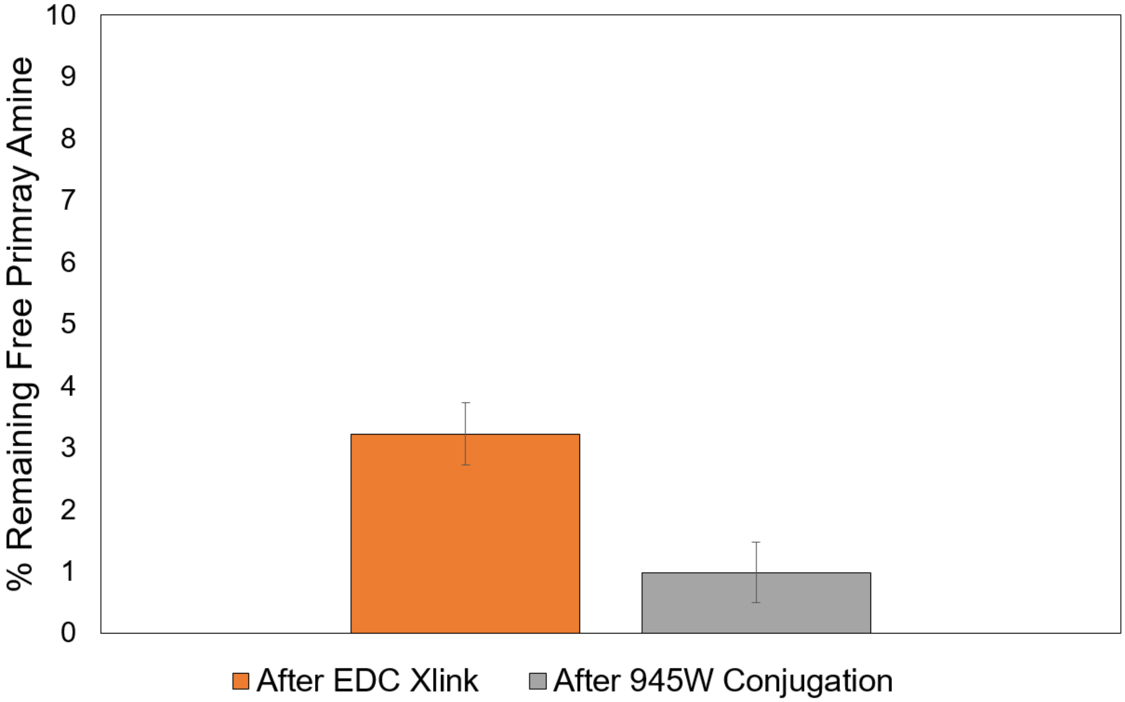

Figure 3-8: Quantity of collagen free amines drastically depleted following electrospinning onto EDC-based crosslinking bath solution. Following collagen fiber formation, fluorescamine assay determined that only 3% of amines remained, leaving only a narrow range for conjugation of other molecules such as cell adhesive peptide 945W.

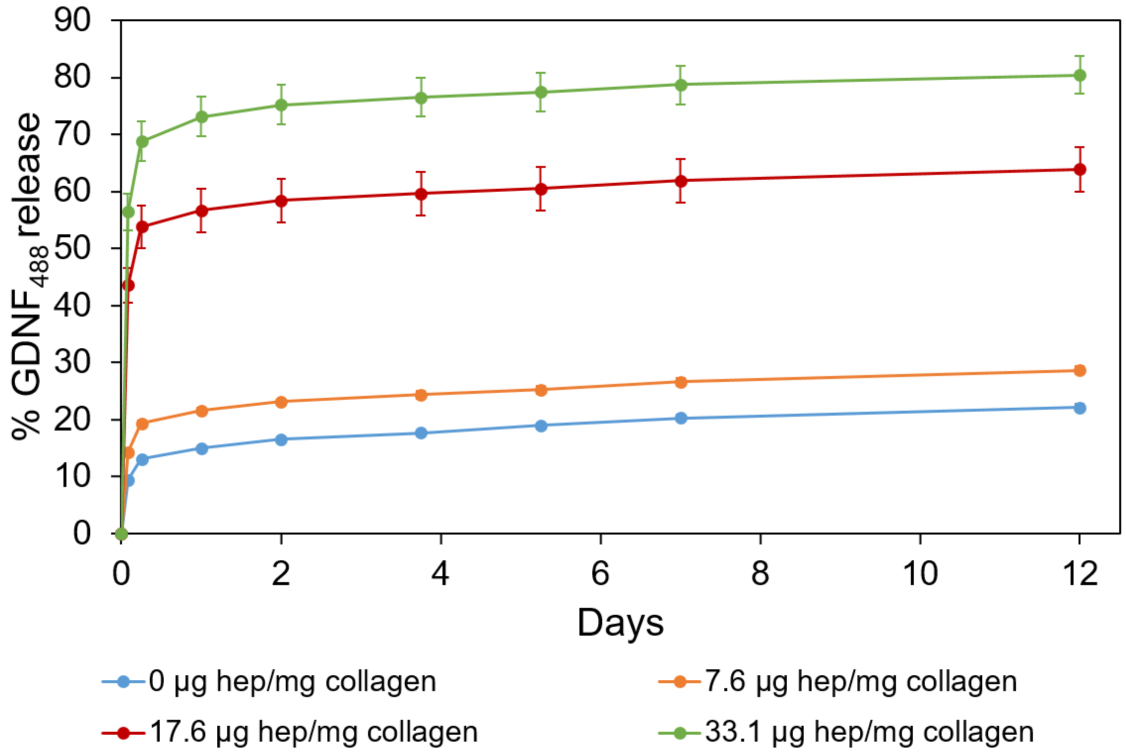

Figure 3-9: Release profiles of GDNF$_{488}$ from collagen hydrogel fiber sheets at different heparin levels. Surprisingly, addition of higher heparin to collagen fibers resulted in more GDNF release at a given time point compared to collagen fiber sheets lacking heparin. This is likely due to EDC activated heparin being unable to compete successfully with EDC for access to collagen primary amines. It is likely instead that heparin is electrostatically bound to the heparin binding domains of collagen and release rates measured are representative of heparin molecules releasing from collagen, taking GDNF with them rather than purely GDNF release.

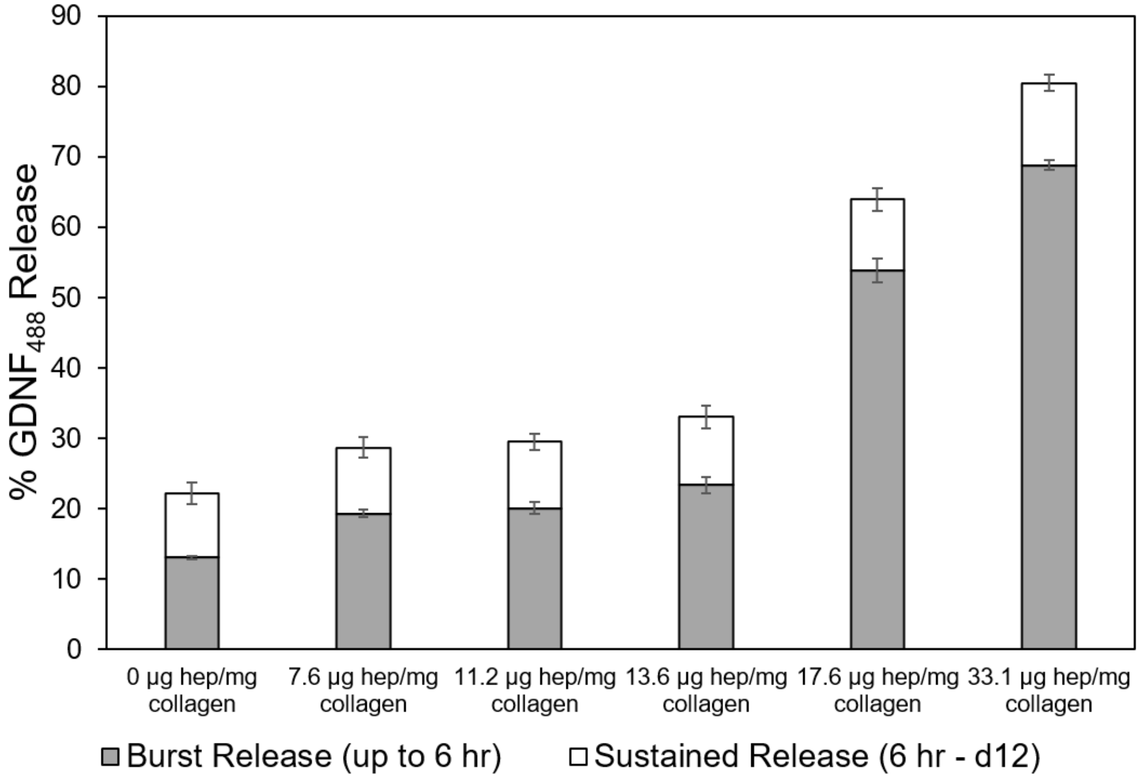

Figure 3-10: Burst and sustained release of $GDNF_{488}$ from collagen hydrogel fiber sheets at different heparin levels. Cumulative sustained release from 6 hours to 12 days for all conditions remain similar with main variation in release rate occurring with differences in burst release likely due to heparin unbinding from collagen fibers taking much captured $GDNF_{488}$ with it.

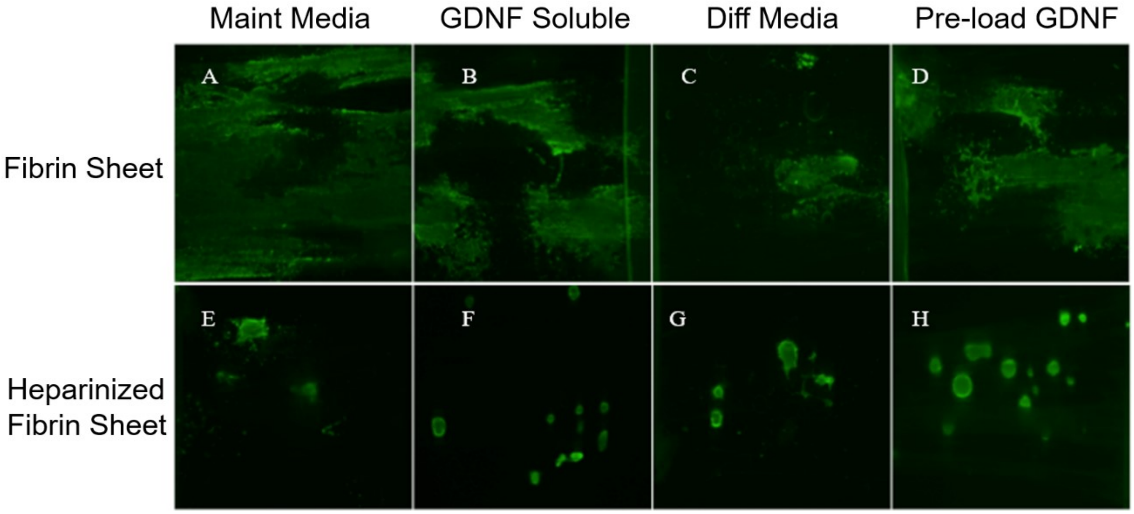

Figure 3-11: Outgrowth of NSC spheroids on fibrin and heparinized fibrin sheets after seven days. In all cases, heparinization leads to inhibited outgrowth of cells when conjugated to the surface of fibrin fiber sheets.

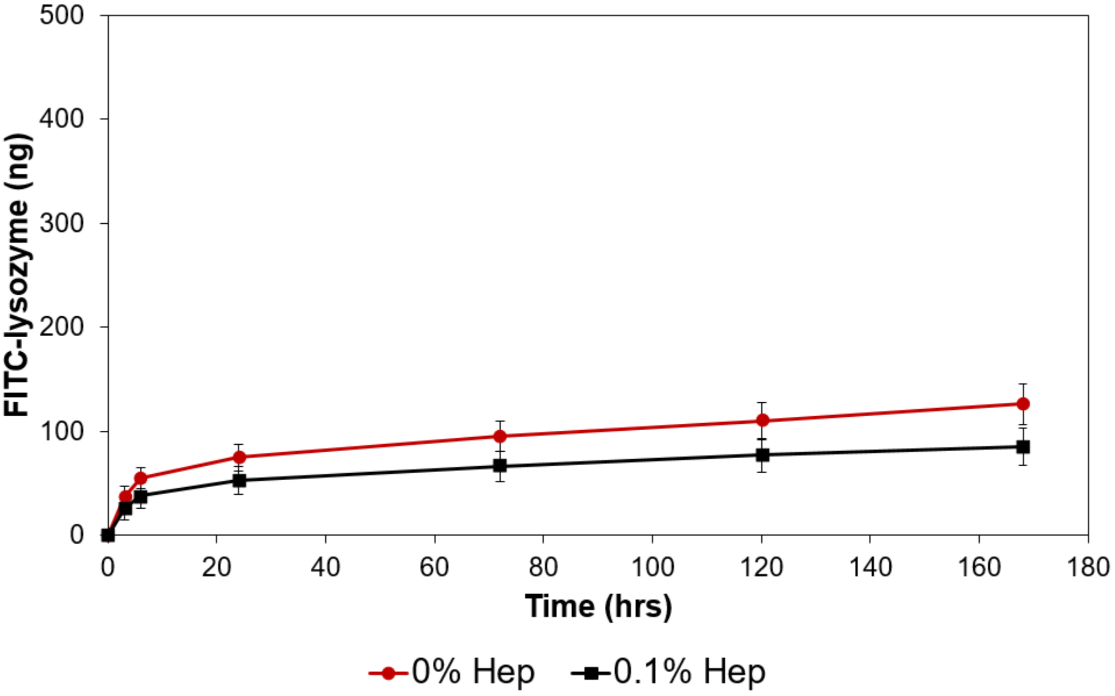

Figure 3-12: Conjugation of EDC activated 0.1 wt % heparin solution to fibrin fiber sheet surface reduces release rate of FITC-lysozyme. Burst and sustained release of FITC-lysozyme is reduced upon heparinization of fibrin fiber surface.

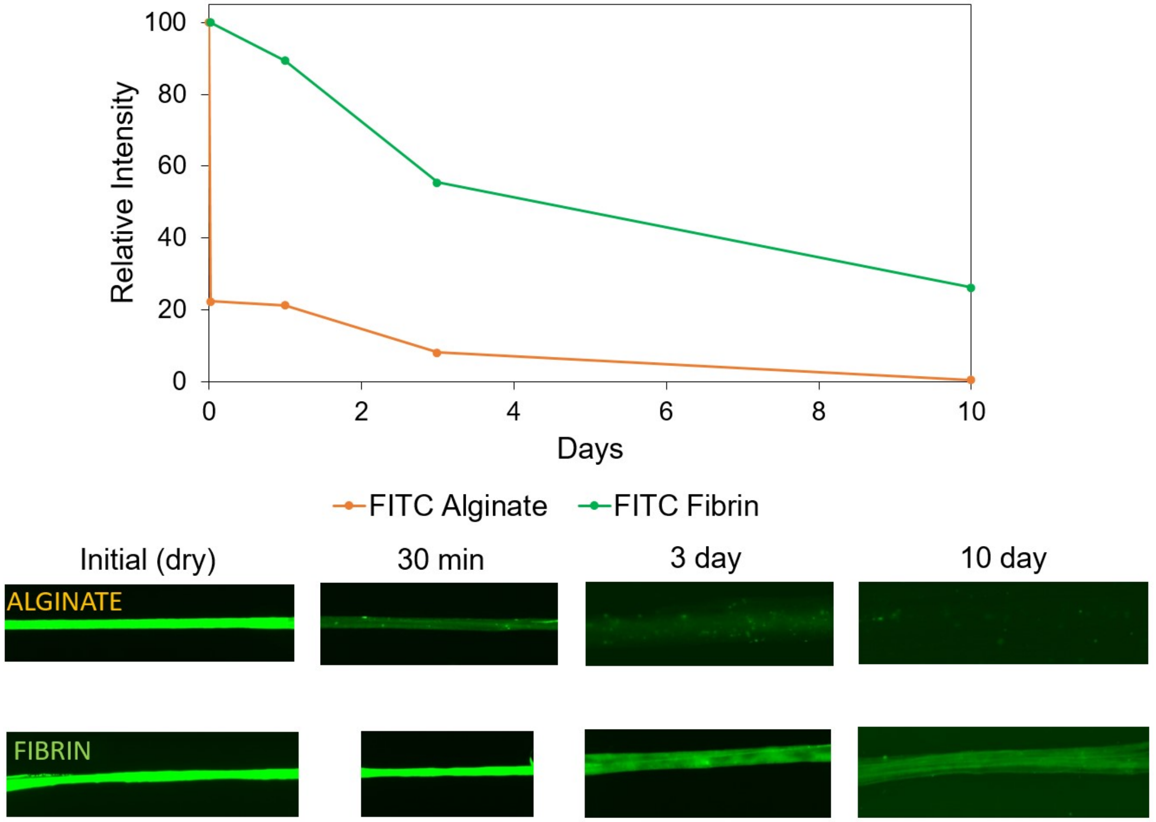

Figure 3-13: Physical loading of FITC-lysozyme *in situ* during alginate and fibrin fiber formation. Alginate shows higher release over 10 days of physically entrapped FITC-lysozyme as a result of having higher hydrophilicity relative to fibrin fibers. Burst release of fibrin fibers is much lower than that of alginate.

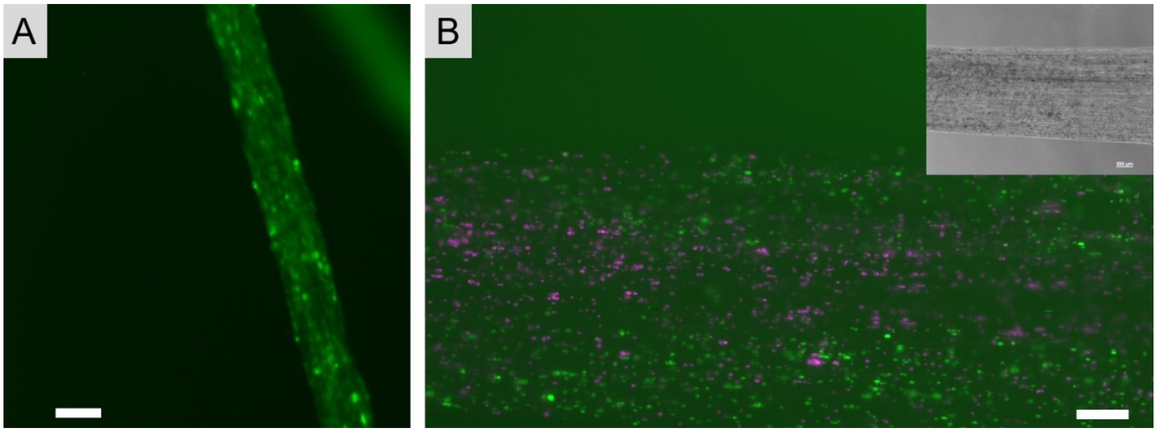

Figure 3-14: ASCs spun *in situ* during 0.4 wt% fibrin fibers are viable after four days culture. Schwann cells show minimal migration between fiber regions after one week. ASC spun in fibrin fibers at a concentration of 32k cells/µl remain viable at day 4 but show minimal spreading within fibrin fiber (a). Two distinctly labeled Schwann cell populations (green and purple) spun into AG/F 0.75 from separate syringes onto the same collection solution show minimal migration out of their host fibers (b). Scale bars: 100 µm (a), 200 µm (b).

Figure 3-15: Preparation of 6-layer fibrin fiber sheets for cardiac tissue engineering applications. Fibrin sheets are spun as described in chapter 2 for seeding of ASCs, HUVECs, ECFCs, and cardiomyocytes. Care must be taken in wrapping sheet onto plastic frame (progression from left to right) to ensure alignment of fiber sheets (outlined yellow dash) is maintained or contractile properties could be compromised.

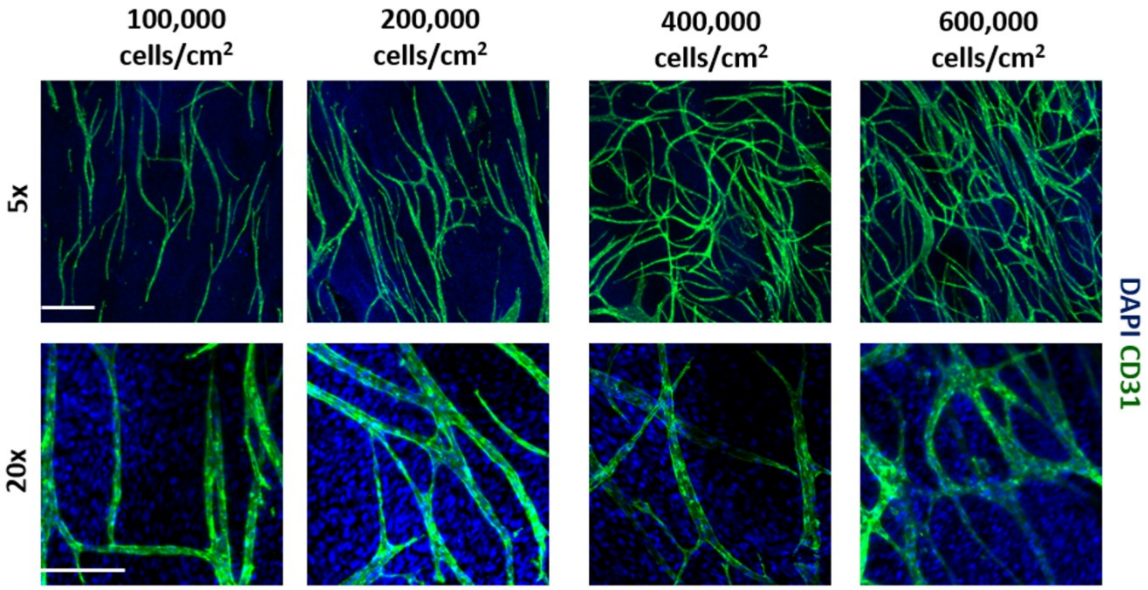

Figure 3-16: Alignment of vasculature formed from different concentrations of HUVEC's co-cultured with ASCs on fibrin fiber sheets. HUVECs seeded on 1 cm^2 fibrin fiber sheets at 100k, 200k, 400k, and 600k cells in 1:1 ratio with ASCs show alignment with fibrin fiber orientation (vertical) with good interconnectivity at higher seeding concentrations. Scale bars: 200 µm (top), 40 µm (bottom).

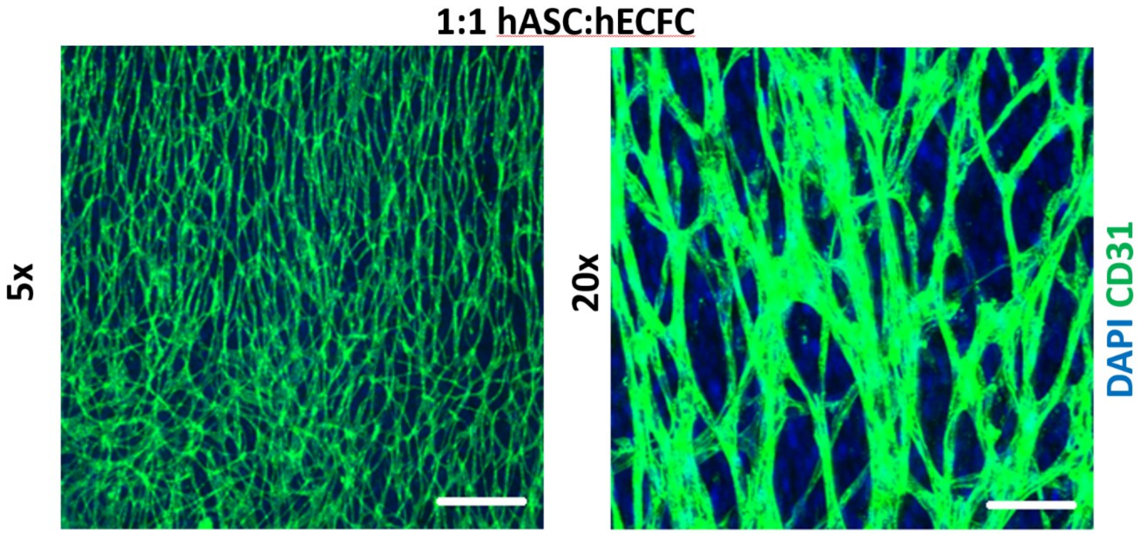

Figure 3-17: Vasculature formed from ECFCs co-cultured with ASCs on fibrin fiber sheets show high alignment and interconnectivity. Like with HUVECs, ECFCs were also able to generate vasculature on fibrin fiber sheets with high interconnectivity. Scale bars: 200 µm (left), 50 µm (right).

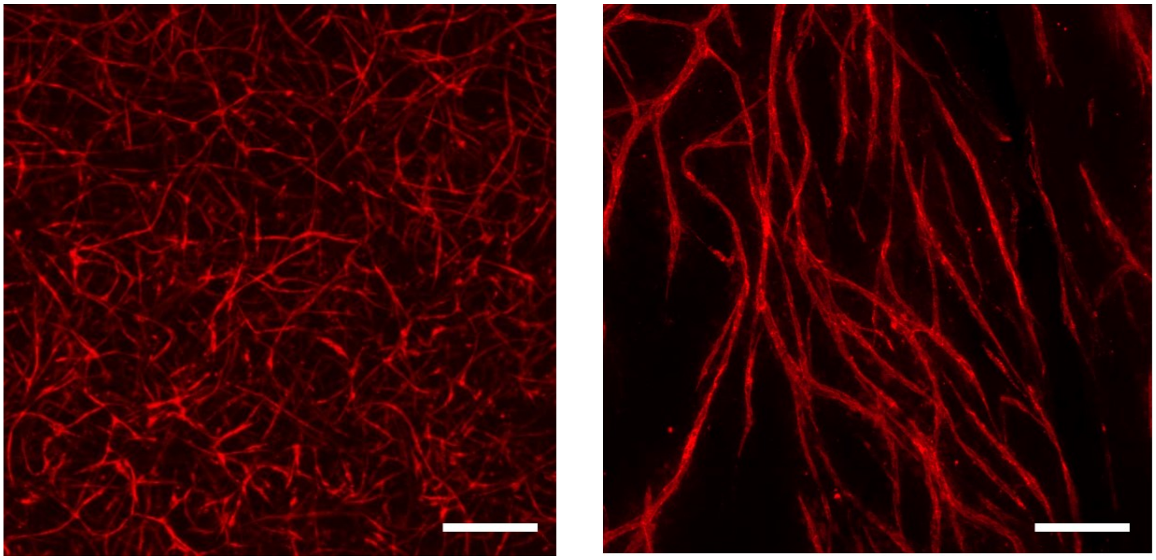

Figure 3-18: Vessel organizational differences on random fibrin gels and aligned fibrin hydrogel microfiber sheets. 100 k : 100 k ASCs and HUVECs (CD31, red) show clear differences in alignment on random fibrin gels (left) and aligned fibrin hydrogel sheets (right). Scale bars: 200 µm.

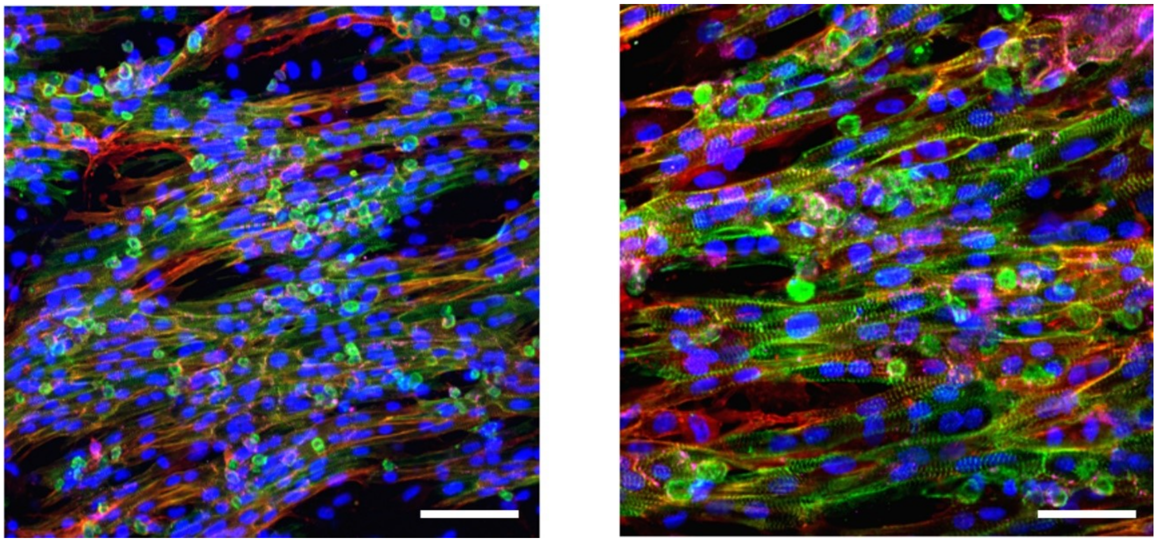

Figure 3-19: Cardiomyocyte cultured on aligned fibrin fibers show striations indicating maturity is promoted by fiber sheets. Cardiomyocytes show striations in α-Actinin (green) organization in cells positive for the cardiac marker αSMA (red) with successful gap junction formation detected (Connexin 43) after seven days culture and organization along fiber alignment direction (horizontal). Scale bars: 50 µm (left), 25 µm (right).

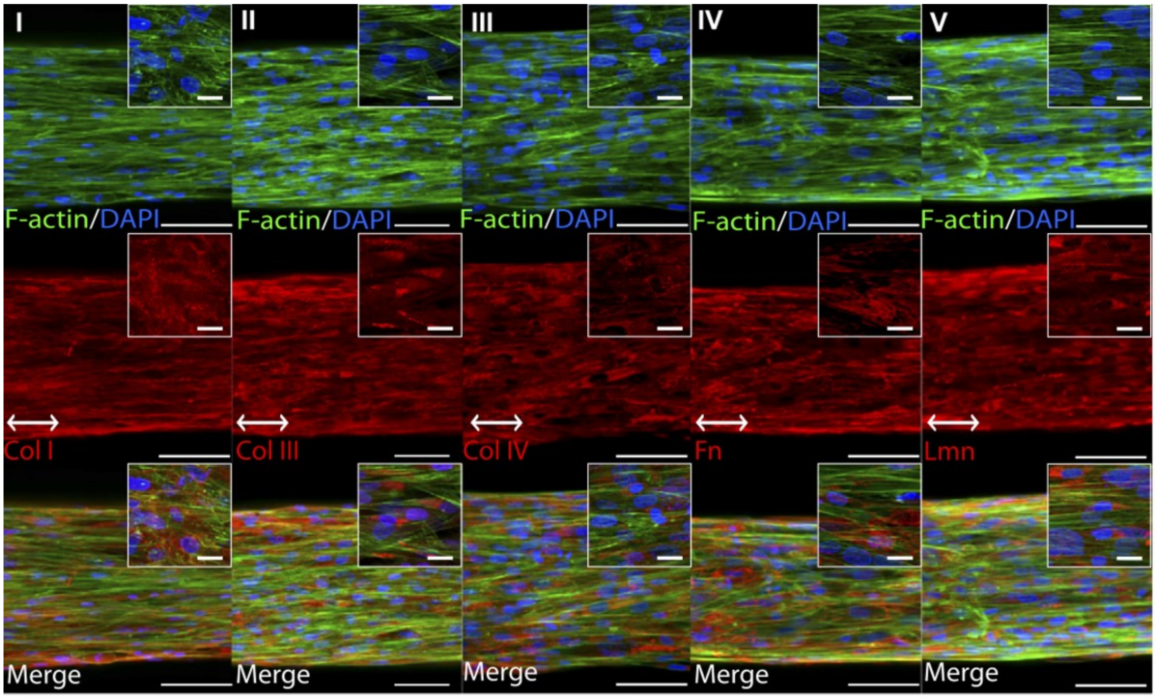

Figure 3-20: Pericytes secrete several cell adhesive molecules and collagens along direction of alignment of 200+ µm diameter fibrin bundles after 5 d culture. Pericytes secrete collagens I, III, IV, laminin, and fibronectin along direction of fibrin fiber bundle alignment. Scale bars: 100 µm, inset: 25 µm**.**

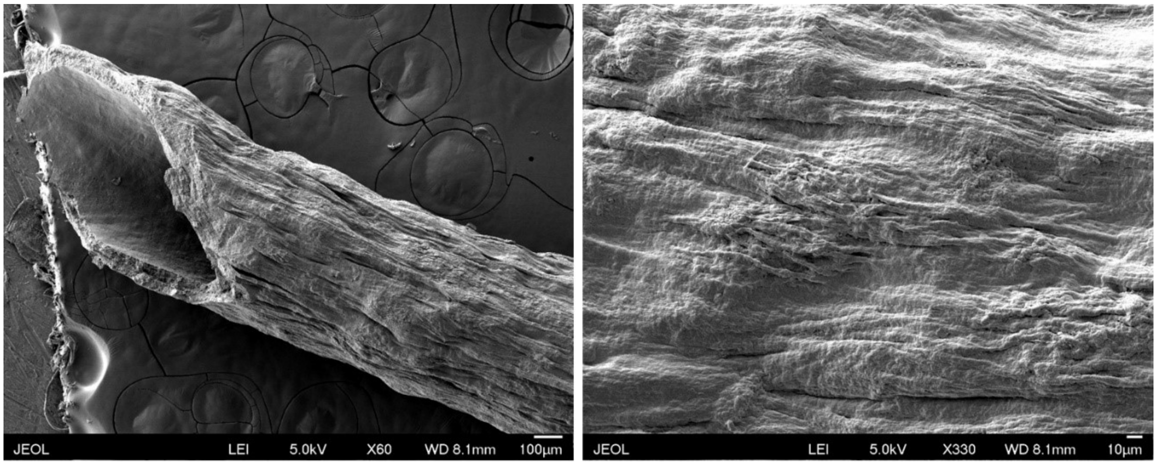

Figure 3-21: Hollow vascular graft tubes made from aligned fibrin fiber hydrogel sheets. Fibrin fiber sheets are formed into hollow, perfusable tubes by wrapping around PTFE coated stainless steel mandrels and then drying (left). Drying is through a graded ethanol process involving soaks for minimum of 15 minutes in 25%, 50%, 70%, 80% EtOH followed by overnight in 90% EtOH followed by 95% for 15 minutes and finally a triple 15 minute soak in 100% EtOH. Once fully dehydrated, tubes are air dried to yield highly aligned surface structures (right).

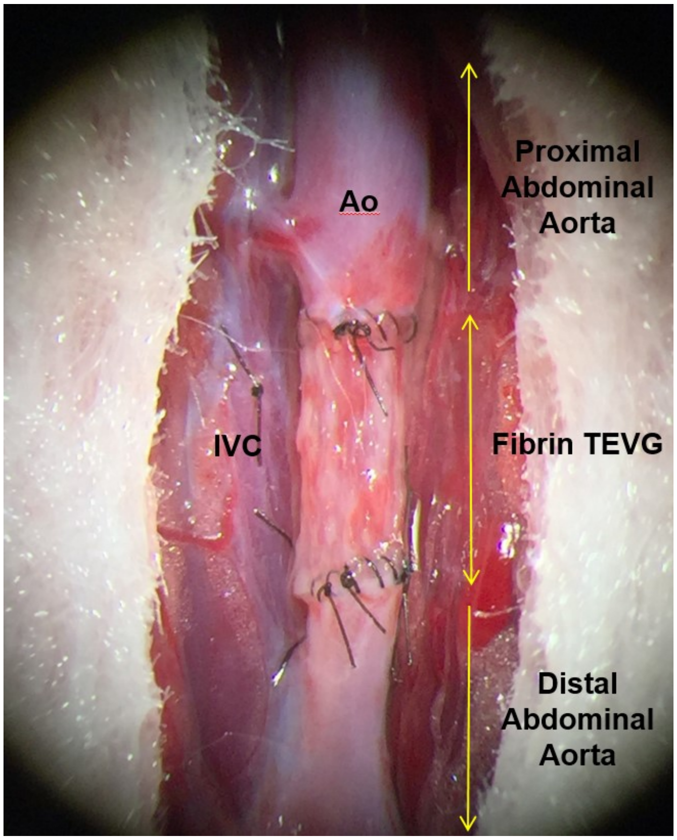

Figure 3-22: Perfusable hollow fibrin fiber tube with longitudinal alignment as vascular graft in rat aortic replacement model. 5 mm length fibrin tubes implanted as aortic vessel replacement has been able to maintain animal viability for up to 10 days post implantation before rupture and have sufficient strength to be directly sutured with aortic stumps without tearing.

3.6 References

1. Charras G and Sahai E. *Physical influences of the extracellular environment on cell migration.* in *Nat Rev Mol Cell Biol.* 2014. p. 813–824.
2. Alkhouli N, et al., *The mechanical properties of human adipose tissues and their relationships to the structure and composition of the extracellular matrix*. in *AJP Endocrinol Metab.* 2013. p. E1427–E1435.
3. Akhtar R, et al., *Characterizing the elastic properties of tissues*. in *Mater Today*. 2011. p. 96–105.
4. Rho JY, et al., *Young's modulus of trabecular and cortical bone material: ultrasonic and microtensile measurements.* in *J Biomech.* 1993. p. 111–119.
5. Trichet L, et al., *Evidence of a large-scale mechanosensing mechanism for cellular adaptation to substrate stiffness.* in *Proc Natl Acad Sci.* 2012. p. 6933–6938.
6. Schwarz US and Gardel ML. *United we stand? integrating the actin cytoskeleton and cell-matrix adhesions in cellular mechanotransduction*. in *J Cell Sci.* 2012. p. 3051–3060.
7. Wu X, et al., *FAK-Mediated Src Phosphorylation of Endophilin A2 Inhibits Endocytosis of MT1-MMP and Promotes ECM Degradation.* in *Dev Cell.* 2005. p. 185–196.
8. Ghassemi S, et al., *Cells test substrate rigidity by local contractions on submicrometer pillars.* in *Proc Natl Acad Sci.* 2012. p. 5328–5333.
9. Trappmann B, et al., *Extracellular-matrix tethering regulates stem-cell fate.* in *Nat Mater.* 2012. p. 642–649.
10. Wolf K, et al., *Physical limits of cell migration: Control by ECM space and nuclear deformation and tuning by proteolysis and traction force.* in *J Cell Biol.* 2013. p. 1069–1084.
11. Wise SG, et al., *A multilayered synthetic human elastin/polycaprolactone hybrid vascular graft with tailored mechanical properties.* in *Acta Biomater.* 2011. p. 295–303.
12. Xu Y, et al., *Fabrication of Electrospun Poly(L-Lactide-co-?-Caprolactone)/Collagen Nanoyarn Network as a Novel, Three-Dimensional, Macroporous, Aligned Scaffold for Tendon Tissue Engineering.* in *Tissue Eng Part C Methods.* 2013. p. 925–936.
13. Wen X, et al., *Cauda Equina-Derived Extracellular Matrix for Fabrication of Nanostructured Hybrid Scaffolds Applied to Neural Tissue Engineering.* in *Tissue Eng Part A.* 2015. p. 1095–1105.
14. Small JV, et al,. *The lamellipodium: where motility begins.* in *Trends Cell Biol.* 2002. p. 112–120.
15. Tozluolu M, et al., *Matrix geometry determines optimal cancer cell migration strategy and modulates response to interventions.* in *Nat Cell Biol.* 2013. p. 751–762.

16. Kim D-H, et al., *Matrix nanotopography as a regulator of cell function.* in *J Cell Biol.* 2012. p. 351–360.
17. Provenzano PP, et al., *Collagen reorganization at the tumor-stromal interface facilitates local invasion.* in *BMC Med.* 2006.
18. Kaiser NJ and Coulombe KLK. *Physiologically inspired cardiac scaffolds for tailored in vivo function and heart regeneration.* in *Biomed Mater.* 2015. p. 034003.
19. Bergmann O, et al., *Evidence for Cardiomyocyte Renewal in Humans.* in *Science.* 2009. p. 98–102.
20. Xu J, et al., *Deaths: Final data for 2013.* in *Natl Vital Stat Rep.* 2016. p. ;1–119.
21. Stienen GJM. *Pathomechanisms in heart failure: the contractile connection.* in *J Muscle Res Cell Motil.* 2015. p. 47–60.
22. Jacot JG, et al., *Substrate Stiffness Affects the Functional Maturation of Neonatal Rat Ventricular Myocytes.* in *Biophys J.* 2008. p. 3479–3487.
23. Freytes DO, et al., *Optimizing Dynamic Interactions between a Cardiac Patch and Inflammatory Host Cells.* in *Cells Tissues Organs.* 2012. p. 171–182.
24. Silvestri A, et al., *Biomimetic Materials and Scaffolds for Myocardial Tissue Regeneration: Materials and Scaffolds for Cardiac Regeneration.* in *Macromol Biosci.* 2013. p. 984–1019.
25. Hiraoka Y, et al., *Fabrication and biocompatibility of collagen sponge reinforced with poly (glycolic acid) fiber.* in *Tissue Eng.* 2003. p. 1101–1112.
26. Ennett AB and Mooney DJ. *Tissue engineering strategies for in vivo neovascularisation.* in *Expert Opin Biol Ther.* 2002. p. 805–818.
27. Carmeliet P. *Manipulating angiogenesis in medicine.* in *J Intern Med.* 2004. p. 538–561.
28. Ehrbar M. *Cell-Demanded Liberation of VEGF121 From Fibrin Implants Induces Local and Controlled Blood Vessel Growth.* in *Circ Res.* 2004. p. 1124–1132.
29. Li X, et al., *Generation, Endothelialization, and Microsurgical Suture Anastomosis of Strong 1-mm-Diameter Collagen Tubes.* in *Tissue Eng Part A.* 2017. p. 335–344.
30. Xing Q, et al., *Aligned Nanofibrous Cell-Derived Extracellular Matrix for Anisotropic Vascular Graft Construction.* in *Adv Healthc Mater.* 2017. p. 1601333.
31. Ye Q, et al., *Fibrin gel as a three dimensional matrix in cardiovascular tissue engineering.* in *Eur J Cardiothorac Surg.* 2000. p. 587–591.
32. Rowley JA, et al., *Alginate hydrogels as synthetic extracellular matrix materials.* in *Biomaterials.* 1999. p. 45–53.
33. Kamelger F, et al., *A comparative study of three different biomaterials in the engineering of skeletal muscle using a rat animal model.* in *Biomaterials.* 2004. p. 1649–1655.
34. Choi JS, et al., *The influence of electrospun aligned poly(ε-caprolactone)/collagen nanofiber meshes on the formation of self-aligned skeletal muscle myotubes.* in *Biomaterials.* 2008. p. 2899–2906.
35. Barreto-Ortiz SF, et al., *Fabrication of 3-dimensional multicellular microvascular structures.* in *FASEB J.* 2015. p. 3302–3314.

36. Barreto-Ortiz SF, et al., *A Novel In Vitro Model for Microvasculature Reveals Regulation of Circumferential ECM Organization by Curvature.* in *PLoS ONE.* 2013. p. e81061.
37. Cook CA, et al., *Characterization of a novel bioreactor system for 3D cellular mechanobiology studies.* in *Biotechnol Bioeng.* 2016. p. 1825–1837.
38. Tsong TY. *Electroporation of cell membranes.* in *Biophys J.* 1991. p. 297–306.
39. Starke PE, et al., *Calcium-dependent and calcium-independent mechanisms of irreversible cell injury in cultured hepatocytes.* in *J Biol Chem.* 1986. p. 3006–3012.
40. Abidor IG, et al., *Studies of cell pellets: II. Osmotic properties, electroporation, and related phenomena: membrane interactions.* in *Biophys J.* 1994. p. 427–435.

Chapter 4 Poly(glycerol sebacate) (PGS) Coated Braided Poly(glycolic acid) (PGA) Nerve Guides

4.1 Background

4.1.1 Academic nerve guide designs

Regeneration of peripheral nerves following injury are currently limited primarily to use of the autologous nerve graft as a repair method of best prognosis despite advances in the materials used for synthetic nerve guides. Many strategies exist for generating nerve guidance to enhance axon outgrowth in the peripheral and central nervous system based on providing topographical guidance cues including interconnected collagen pores[1], orienting collagen gels by magnetic alignment [2], using conductive [3] or nonconductive synthetic nanofibers [4].

Besides providing a protective environment, the nerve guide can contain other engineered features to enhance regenerative outcome such as inclusion of growth factors such as GDNF [5, 6], NGF [7], BDNF and NRG1 [8] to induce more rapid migration of Schwann cells or improve survival of neural subpopulations. Introduction of stem cells into the nerve guide can also provide a powerful technique to control the local microenvironment through secretion or over-expression of chemotrophic cues and other cytokines [9-11]. Stem cells can be used in conjunction engineering of substrate properties within the nerve guide to control differentiation [12-14]. Selection of materials to be used within the nerve guide can provide a major impact on resultant regenerative outcome such as the inhibition of myelination in the presence of fibrin [15, 16] or regulating survival of engrafted cells as seen with improvements in viability of neural stem cells in hyaluronic acid [17].

4.1.2 PGS coatings

The Secant Group, LLC, a biomedical textiles company has developed a braided biodegradable conduit using poly(glycolic acid) (PGA) microfibers, and coated it with biodegradable poly(glycerol sebacate) (PGS), a crosslinked elastomer, previously developed by R. Langer and Y. Wang. [18, 19] In collaboration with Secant, we have engineered a configuration for use as a nerve guidance conduit (NGC). The relatively fast degradation of PGS, approximately 30% mass loss over 9 days *in vitro* [20], enables generation of increased porosity after the initial inflammatory period, is advantageous in promoting nutrient transport to the regenerating nerve within the NGC. While degradation is relatively rapid, PGS is degraded through surface erosion rather than bulk so mechanical properties are maintained for much of the lifetime of the coating [21] and is degraded into metabolically resorbable glycerol and sebacic acid. PGS has been shown to have excellent cellular biocompatibility through improved SC mitotic activity and reduced apoptotic activity when comparing cell culture on PGS sheets relative to PLGA sheets and reduction in inflammatory response compared to uncoated PLGA [18]. The elastic property of PGS renders the braided PGA conduit more kink-resistant, while the underlying braid provides a superior suture anchor point. Polypropylene suture pullout tests using ISO 7198 yielded suture failure before the braid up through 3.0 size sutures. Uncoated PGA braids failed at 18.6 N load compared to 20.2 N loading with PGS coated braids when 2.0 size sutures were used (Fig. 4.1).

4.1.3 Role of macrophages in nerve regeneration

The presence of macrophage has an increasingly appreciated role in nerve regeneration, playing many support roles to promote regeneration. Such roles include inducing the growth of new blood vessels to act as natural guidance cues for Schwann cell migration [22] and contributing to the late Wallerian degeneration by assisting Schwann cells in clearing myelin debris [23]. Recent studies have concluded that not only do macrophages play an important role in clearing debris following injury, but that reduction in accumulation of macrophages in slow Wallerian degeneration mice resulted in a reduction in neurite outgrowth [24]. Sciatic nerve transection neuropathy studies have demonstrated that the transection triggers a downregulation of IL-10 production, improving macrophage M2 polarization [25]. Additionally, during the first several days after injury, M1 macrophages begin the process of polarization to the M2 phenotype with a subsequent increase in the expression levels of ARG1 and CD206 [26].

4.2 Methods

4.2.1 Macrophage isolation and culture for PGS contact effect on differentiation

Mouse bone marrow derived macrophages (BMDM) were isolated from 6 to 8 week old C57BL/6J mice for seeding on TCPS or PGS coated coverslips at 50,000 cells/well in either M0 medium (LPS: 0 ng/ml, IFNγ: 0 ng/ml), low concentration M1 induction media (LPS: 10 ng/ml, IFNγ: 2 ng/ml), or high concentration M1 induction media (LPS: 100 ng/ml, IFNγ: 20 ng/ml) to determine PGS coating effect on M1 vs M2 differentiation of M0 macrophages after two days culture. Phenotyping was characterized through use of Q-PCR using primers for IL1b, IL6, TNFα, and iNOS as M1 genetic markers with CD206 and ARG1 expression for M2 phenotype. BMDM derived M0 macrophages were seeded at a density of 100k/well for PGS samples and 50k/well on TCPS, both in 24 well plates.

4.2.2 Effect of PGS degradation product on macrophage phenotype

BMDMs were additionally cultured on TCPS in the presence of PGS degradation product (DP) at increasing concentrations for 48 hours in the presence of M1 or M2 stimulation media to distinguish the immunomodulatory effect of soluble PGS leachables from direct contact with PGS coating. Q-PCR primers for M1 (IL1b, iNOS, and TNFα) and M2 markers (CD206, ARG1, and FIZZ1) were used to characterize macrophage differentiation under media with differing strengths of M1 bias (0, 10, and 100 ng/ml LPS) and M2 bias (0, 2, and 20 ng/ml IL-4). The effect of degradation product on cell viability was assayed fluorescently through incubation with alamar blue assay for three hours and monitoring medium pH.

4.2.3 Preparation of PGS coated braided PGA conduits and glass coverslips

Poly(glycerol sebacate) coating of braided poly(glycolic acid) tubes were provided by Secant Biomedical (Telford, PA) as part of their role as a collaborator in the investigation of the potential of PGS coated PGA braids as nerve guidance materials. The preparation process is roughly as follows as the precise preparation methodology is proprietary of Secant Biomedical and shall not be disclosed here. Briefly, multifilament PGA threads are braided together around a mandrel at a braid angle of 130 degrees using an industrial braiding machine to form a 1.5 mm ID tube. The braided tube is then dipcoated into a PGS 10-20% w/w solution in ethyl acetate in such a way that the lumen remains open and unclogged (Fig. 4.2). Curing of the PGS is done at elevated temperatures of around 120°C for times of approximately 36 hours under a low vacuum of 10 torr. The degree of polymerization can be tuned by altering the curing temperature and/or time of cure to yield PGS coatings with varying degrees of tackiness. Lower curing times and temperatures results in increased tackiness as a lower amount of PGS fully polymerizes to in these conditions. Following preparation, coated braids were sterilized using gamma irradiation (STERIS Isomedix Services) at 25-40 kGy dosing using a Nordion Cobalt-60

Irradiator for seven hours. After sterilization, coated braids were stored at 4°C until use. Coverslips used for *in vitro* cell culture studies investigating the effect of PGS coating on cellular adhesion and macrophage response were prepared using the same methodology as the nerve guides regarding coating and sterilization.

4.2.4 Nerve guide preparation

Poly(glycolic acid) multifilament braids were manufactured and coated with poly(glycerol sebacate) to a thickness of several μm by The Secant Group, LLC (Telford, PA) with a 130 degree braiding angle and cut to a length of 17 mm per nerve guide. Prior to implantation, PGS coated PGA braided tubes were sterilized using γ-radiation. Dehydrated collagen fibers were loaded into the NGC lumen for one experimental group at a level such that ~25% of the interior would be filled with fiber upon rehydration to ensure adequate porosity remained for cellular infiltration (Fig. 4.3). Uncoated PGA braids were used as negative control and functional recovery assays were compared against the sciatic nerves of the non-operative legs as a positive control.

4.2.5 Outgrowth of neural stem cells as function of fiber filler density and luminal filler preparation for nerve guide usage

To characterize the level of collagen fiber filler to be contained within PGS nerve guides, bundles of Secant collagen fibers were formed for in vitro cell culture of neural stem cells to ensure outgrowth could occur all along the fiber bundle in confined space. Secant collagen fiber bundles were formed by wraping collagen fiber from a spool lengthwise around a 1.5 cm by 3.0 cm mylar frame 25, 50, or 100 times to correspond with 25%, 50%, and 100% fiber loading within a 1.5 mm ID PGS braided tube nerve guide after swelling from rehydration from a dry state (Fig. 4.4). After wrapping around the mylar frame, the ends of the collagen fiber bundle were tied with 7-0 nylon suture and the bundle was cut free from the frame. Samples were sterilized for 30 minutes in 70% ethanol and dried prior to cell seeding. To ease imaging, rather than PGS braided tubes, troughs were made of 1% agarose gel prepared in 0.9 wt% NaCl using 1.5 mm ID stainless steel mandrels cut to 1.5 cm length for culturing NSCs with the Secant collagen fiber bundles in each well of a 6 well plate. Particularly advantageous of the Secant collagen fibers were their production from four parallel needles depositing material into an acetone bath for precipitation resulting in the aggregation of fibers with a cloverlike cross section (Fig. 4.5). This provides additional grooving as a topographical guidance cue for migrating Schwann cells and neurite outgrowth. Higher magnification SEM images show the surface features of the collagen fibers to have a particularly nice aligned texture on a cellular scale, providing excellent anchor points for filopodia during progression of the growth cone into the nerve guide.

Neural stem cell spheroids were prepared by seeding 50 µl of NSC cell pellets diluted to 5,000 NSC/ul for a total of 250k cells per 35 spheroid mold (Microtissues, Inc) to yield spheroids ~ 250 - 300 µm in diameter. Culture plates containing molds were placed on an orbital shaker operating at low RPM inside a cell culture incubator for 72 hours to allow NSCs to form spheroids. Following spheroid formation, molds were inverted and briefly centrifuged down at 200 g to dislodge spheroids, which were then transferred to 50 ml tubes. Tubes were centrifuged down at 200 g and supernatant was aspirated before collected spheroids were diluted down to a concentration of approximately 1 spheroid per µl.

Prior to seeding, the dried Secant collagen fiber bundles were transferred to the agarose troughs. Once placed, 10 µl of NSC spheroids were seeded on one end of the collagen bundles and were left in a 37°C incubator for 30 min for spheroids to attach. Following attachment, a small volume, 100 µl, of media was added to each bundle to maintain hydration for the second set of 30 minutes in the incubator, following which 4 ml of maintenance media was added to each well of the 6 well plate. After 48 hr in NSC maintenance media containing 20 ng/ml bFGF and 20 ng/ml EGF, media was switched to differentiation media lacking bFGF and EGF. Culture was continued for three more additional weeks. After culture, samples were fixed for 10 minutes in 4% paraformaldehyde and stained with DAPI (1:1000, Roche) and rabbit anti-βIII-Tubulin (1:200, Sigma) to visualize neuronal spreading.

4.2.6 In vivo sciatic nerve critical gap defect animal model

A total of 32 adult male Sprague-Dawley rats were used in this study with surgeries and functional assessment being done in accordance with protocols approved by Johns Hopkins Institutional Animal Care and Use Committee and internal review board. Animals were sacrificed after seven days for inflammatory studies or three months for assessment of functional recovery. Nerve guide groups include: (1) uncoated PGA multifilament braids as a comparison to (2) PGS coated PGA multifilament braids with empty lumen and (3) PGS coated PGA multifilament braids containing collagen fibers in the lumen, all for comparison against (4) the gold standard autograft, prepared by cutting out a portion of sciatic nerve and inverting the proximal and distal ends before suturing back to the nerve stumps.

4.2.7 Presence of autophagy in nerve guide groups

Irritation in the transected nerve can cause Sprague Dawley rates to exhibit signs of autophagy, where they will chew at the digits of or even whole foot distal to the injury site. Precautions were taken to minimize this by daily application of bitter nail polish (Mavala Stop) during the first month post-op. The presence of autophagy was compared between groups after 12 weeks prior to sacrifice. Autophagy positive animals in this study were considered to be those that showed one or more digit chewed off or significant signs of wounding on the bulk of the foot itself.

4.2.8 Foot angle of inclination and characterization of atrophy

To confirm the results of the atrophy data, we made measurements of the foot angle of inclination, or bending movement, prior to animal sacrifice. As the muscles of the soleus and gastrocnemius atrophy, a seizing of the foot becomes present, preventing full range of motion as muscular atrophy proceeds. Measurement of the angle of inclination is made by using photos of the maximum forward bending range of the foot from the ankle and drawing straight lines parallel to the foot and the tibia using ImageJ where the angle is measured. Data was collected from all 8 animals in each group on the operative side and 8 randomly selected positive control side legs from all groups. Additionally, the gastrocnemius and soleus muscles were weighed for all animals and compared to the non-operative control side to determine the level of muscular atrophy after three months.

4.2.9 Electrophysiological assessment of functional recovery using Secant PGS nerve guide

Electrophysiological analysis of functional recovery was made of the uncoated PGA braid, PGS coated braid, PGS coated braid containing collagen fibers, and autograft groups after 12 weeks implantation for comparison against the non-operative leg opposite the defect leg by measuring compound muscle action potentials (CMAP) using LabChart 8 Reader software (AD Instruments). Electrical probes were placed proximal to the nerve guide along the sciatic nerve with the downstream probe places into either the ankle or foot for signal propagation characterization with a probe separation averaging 7.5 cm. Characterization included measurements of action potential duration, peak latency, action potential amplitude, and signal onset latency were made for both the operative and non-operative control legs of each animal included in the study.

4.2.10 Histological analysis of axon and myelination characteristics

The axons in the median section of the nerve guides were characterized from histological cross-sectional slices using a minimum of three higher magnification images per animal that had 150 to 200 axons per image. Images were analyzed using an inverted microscope (Nikon) using magnifications of 10× for gross cross section imaging and 63× for characterizing axon calibers and myelin thickness.

4.2.11 Immunofluorescence imaging

Longitudinal sections of all study groups were imaged using either a LSM 510 confocal microscope (Zeiss) or epifluorescence microscope. Macrophages were stained for cell membrane surface markers using mouse anti-CD68 (1:200, Abcam), goat anti-CD86 (1:200, Abcam), rabbit anti-CD206 (1:200, Santa Cruz) using donkey anti-mouse Alexa Fluor-555 (1:500, Invitrogen), donkey anti-goat Alexa Fluor-488 (1:500, Invitrogen), and Cy5 AffiniPure donkey anti-rabbit IgG (H+L) (1:500, Jackson).

4.2.12 In vivo inflammatory response

The inflammation profile present following seven days implantation was characterized through analysis of histological sections, qPCR analysis of the proximal and distal stumps, and ELISA for determining inflammatory cytokine levels present in the proximal and distal tissues. General analysis combines both the proximal and distal data for clearer elucidation of the coating effect while secondary analysis maintains separate proximal and distal subgroups within each nerve guide type to examine the spatial differences in inflammatory response.

The macrophage population was characterized via counting of CD68 (general macrophage marker) positive cells and making comparison to the number of cells that were co-positive for CD86 (M1) or CD206 (M2). Total macrophage population fraction was determined comparing CD68$^+$ cells with DAPI stained nuclei that were CD68$^-$.

Three animals from each group were sacrificed after one week for characterization of the immune response to the various nerve guide configurations. Tissue homogenates from the proximal and distal ends of the nerve guide were collected and analyzed by qPCR for RNA expression of M1 markers using Taqman primers (Invitrogen) for iNOS, TNFα, CD86, and IL-1b. Analysis of M2 markers included primers for: ARG1, PPARG, IL-10, and CD206. Both M1 and M2 macrophage gene expression was compared to the uncoated PGA braid and autograft. ELISA was used to confirm qPCR results by analyzing cytokine levels of iNOS, IL-6, and ARG1 (R&D Systems) in the proximal and distal tissue.

4.3 Results and Discussion

4.3.1 Attachment of BMDM to PGS

BMDMs cultured on PGS showed rounded morphology with no significant spreading and low attachment strength as indicated by higher frequency of detached cells found floating in the culture media (data not shown) for the PGS coverslip groups (Fig. 4.6) where cells showed an abnormal morphology even on the TCPS adjacent to the coated PGS coverslip. This provides indication that some combination of soluble cue and poor attachment are both affecting BMDM morphology and health. Culture of BMDMs on TCPS that did not contain PGS in any form showed normal cell morphologies after 2 days culture in either maintenance, M1, or M2 differentiation media with expected upregulation of M1 or M2 genetic markers in the matched differentiation media (Fig. 4.7).

4.3.2 PGS coating effect on BMDMs in M1 differentiation media

QPCR analysis of RNA expression of BMDMs cultured on TCPS and PGS in the presence of increasing differentiation bias are shown in Figure 4.8. In M1 differentiation media, PGS coating shows resistance to differentiation compared to TCPS as indicated by lower levels of expression of M1 markers at 0, 10, and 100 ng/ml LPS M1 differentiation media. This result was consistent amongst the four M1 markers characterized: IL-1b, IL6, TNFα, and iNOS. M2 markers CD206 and ARG1 showed more variable response to the PGS coating with additional reduction in CD206 found at 10 ng/ml LPS despite less reduction being seen compared to TCPS with CD206 at 100 ng/ml LPS (Fig. 4.9). ARG1 expression also showed variable expression levels on PGS relative to TCPS with higher ARG1 expression present with the PGS coating group at 10 ng/ml LPS compared to the reduction in expression seen at 0 and 100 ng/ml LPS.

4.3.3 Effect of PGS degradation product on macrophage differentiation and viability in vitro

BMDMs cultured on TCPS in the presence of increasing concentrations of PGS degradation product (DP) show reduction in attachment of BMDMs after 48 hours as degradation product levels increased (Fig. 4.10). The buffering capacity of the culture media was surpassed at DP concentrations higher than 1.0 mg/ml with acidity increasing to pH 6.8 with higher DP concentrations. A subsequent decrease in BMDM viability followed with increasing media acidity as measured by relative fluorescence using an alamar blue assay toe measure cellular mitotic activity against BMDMs cultured on TCPS at 0 mg/ml PGS degradation product (Fig. 4.11).

When cultured in a combination of M1 differentiation media and various levels of DP, iNOS expression was upregulated when cultured with 10 // 2 ng/ml and 100 // 20 ng/ml

LPS // IFNγ and DP concentrations up to 2.0 mg/ml (Fig. 4.11a). M0 media with 0 ng/ml LPS // IFNγ showed minimal effects of degradation product until 2.0 mg/ml DP. In all instances, DP concentrations of 4 mg/ml showed reduction in iNOS expression. IL-1b expression was reduced in M0 media except at 0.8 mg/ml DP (Fig. 4.11b). Expression at 10 // 2 ng/ml and 100 // 20 ng/ml LPS // IFNγ M1 media showed increases in IL-1b at 0.1 mg/ml DP and further reduction as PGS DP increases. Trends were similar for TNFα where LPS groups show mRNA expression increases at low DP levels relative to unbiased media with a similar decreasing trend in expression as DP concentration increases to 4 mg/ml. Response was more variable in unbiased media where only 0.1 and 2.0 mg/ml showed increases in TNFα expression relative to the control (Fig. 4.11c).

Addition of PGS DP to M2 differentiation media showed minimal differences in ARG1 expression with addition of up to 2.0 mg/ml DP compared to 0 mg/ml DP (Fig. 4.13a). In unbiased media, 4.0 mg/ml DP increased ARG1 expression while there was significant downregulation in 2 ng/ml and 20 ng/ml IL-4 M2 biasing media. CD206 was downregulated in all media at 4.0 mg/ml DP but did not show significant difference at other DP levels compared to 0 mg/ml DP (Fig. 4.13b). Unlike expression of ARG1 and CD206, expression of FIZZ1 decreased with more sensitivity as DP levels increased (Fig. 4.13c).

4.3.4 Outgrowth of neural stem cells as function of Secant collagen fiber density

Figure 4.14 shows the neurite spreading from differentiated neural stem cells after three weeks of culture. Spreading was most prominent in the 25% collagen fiber fill group where high levels of βIII-Tubulin (red) can be seen throughout the whole length of the Secant collagen fiber bundle. Neurons are highly present on the surface layers of the collagen fiber bundle as there was no chemotactic driving force for them to further infiltrate into the center of the collagen fiber bundles. 50% collagen fiber fill shows a moderate amount of spreading of neurons along collagen fibers but most spreading was localized towards the end of the fiber bundle where seeding had occurred, unlike the 25% collagen fiber fill density group. The 100% collagen fiber fill group also showed some spreading near the seeding site, although this had the least total spreading of all groups visible. This led to the conclusion that a fill density around 25% would be best in vivo usage as a nerve guide fill density to maximize the potential cellular infiltration and axonal extension along the Secant collagen fibers.

4.3.5 Presence of autophagy in nerve guide groups

Significant autophagy was seen in 7 of the 8 uncoated PGA braided nerve guide groups. PGS coating dramatically reduced the presence of autophagy to 1 out of 8 animals in the PGS coating only group while addition of the collagen fibers increased incidence of autophagy to 2 of 8 animals (Fig. 4.15). The autograft did not show any signs of autophagy after 12 weeks. The large difference in autophagy seen comparing the coated and uncoated nerve guides implies that the PGS coating helps to reduce irritation in the surrounding tissue due to the potential immunomodulatory effects of the PGS coating.

4.3.6 Foot angle of inclination and characterization of atrophy

Inclination data in Figure 4.16 shows low ranges of mobility with all three nerve guide groups where the angle of inclination average was around 120 ± 15 to 20 degrees. The autograft showed improved range of motion relative to the nerve guide groups with an average angle of inclination of 138 ± 8 degrees. Control sides showed maximum range of motion of the ankle joint at 160 ± 5 degrees. These results are consistent with that seen from the gastrocnemius and soleus muscle atrophy data, where weakening of the muscles will drastically reduce mobility of the ankle joint, limiting the foot range of motion (Fig. 4.17).

4.3.7 Onset latency measurements

Latencies were taken at both the foot and ankle n = 8 rats per group prior to sacrifice. Due to the potential issue with autophagy of the rat digits, and in extreme cases whole foot, potentially impacting foot data relative to ankle, higher weight is given towards the ankle CMAP data results. Onsets in all cases were higher along the foot than the ankle due to the increased signal propagation distance required for the foot compared to the ankle. For the foot, signal onset latency was highest in the PGS coated group at 8.0 ms with the addition of collagen fibers only reducing the latency by a small amount to just over 7.0 ms (Fig. 4.18). Surprisingly, the PGA braid alone had an average onset latency in the foot that was comparable with the autograft at ~5.5 ms although the PGA braid had a high degree of variance in data due to the autophagy seen within the group. The positive control group had lowest onset latency in the foot at 3.0 ms.

Ankle onset latency data shows a differing trend that the PGS coating is highly beneficial. Onset latency was lower in the ankle of both PGS coated groups at 1.5 ms compared to 1.9 ms seen with the positive control indicating the quality of axons regenerating across the defect are good and that they are successfully bridging with the distal nerve stump. The autograft did slightly worse than the positive control at around 2.3 ms latency while the uncoated PGA braid did the worst at 2.6 ms, though both the autograft and uncoated braid showed a high variance in onset latency.

4.3.8 Peak latency measurements

While the onset latency helps to characterize the speed at which the fastest neurons fire, the peak latency gives a better idea of the propagation speed of the action potential. Like the onset latency, peak latencies were higher in the foot than the ankle due to being more distal to the probe placed proximal relative to the sciatic nerve defect site. The same overall trends were seen with the peak latencies (Fig. 4.19). The autograft and uncoated PGA braid had lower latencies in the foot at around 6.0 to 7.0 ms compared to the PGS coated nerve guides with their latencies of 8.0 ms and 9.0 ms for collagen fiber containing ones and empty respectively. All four groups unsurprisingly fared poorer than the positive control leg at just under 4.0 ms.

Ankle peak latencies were faster than foot and showed similar relative behavior to the onset latencies. In this case, the peak latencies of both PGS coated nerve guide groups were around 2.8 ms, the same speed at which the positive control peak latency was measured. Both the uncoated PGA braid and autograft were around 4.5 ms peak latency with high variation in results seen again with the uncoated braid.

4.3.9 Action potential amplitudes

The amplitude of the action potential peaks gives an indication of the total number axons that form an electrical connection with the distal nerve stump after crossing the nerve guide and are analogous the other overall strength of signal conduction. Foot and ankle amplitudes for the positive control leg were measured to be an average of 6.0 mV with some variability from animal to animal. In all cases for both the foot and ankle amplitudes, the values measured were substantially lower for all nerve guide groups and the autograft compared to the positive control leg due to the significant damage in the defect model used for the study. To better compare the action potential amplitude between groups, comparisons were made as a percentage relative to the positive control leg.

The foot amplitude data shows the lowest conduction strength with the uncoated PGA braid at around 3% of the positive control value, which is much lower than both PGS coated groups, which were at 7% of the positive control. Best action potential performance was seen with the autograft, coming in at 16% of the positive control amplitude after 12 weeks (Fig. 4.20).

Amplitude data for the ankle showed similar poor values relative to the positive control. Uncoated PGA braid was around 4% of the positive control, similar to relative value seen with the foot data for this group. The two PGS groups had relatively lower performance measured at the ankle than the foot at 2% for the PGS coated group and 4% of the positive control amplitude for the collagen fiber containing PGS coated group. The autograft also showed poor conduction amplitude relative to the positive control at 9%. The poor signal conduction amplitude of all three nerve guide groups and autograft relative to the positive control show how poorly even the gold standard autograft is and perfectly illustrates the strong clinical need for nerve guide designs that not only match, but can surpass the performance seen with the autograft.

4.3.10 Histological analysis of axon and myelination characteristics

Counts of the axons per total nerve cross section from mid-graft toluidine blue stained cross sections (Fig. 4.21) show the lowest counts in the uncoated braided PGA nerve guide group at just over 4000 axons per cross section (Fig. 4.22). Improvements were seen in axon count with the PGS coating groups, with the unfilled lumen having higher axon count at over 7000 per cross section. Addition of collagen fibers reduced the average axon counter per cross section of that group to 6000, likely due to the large proportion of fiber remaining after three months implantation taking up space in the lumen. Autograft had the highest degree of axons per cross section at just under 8000. Higher magnification images show the presence of capillary formation inside collagen fibers (Fig. 4.23) along with some fibroblast infiltration and axon outgrowth along the edge of the fibers. Capillaries containing red blood cells are particularly noticeable at the lumen wall near the PGA braid.

Cross sections of the individual regenerating axons were measured and compared (Fig. 4.24). Due to the oblong shape of many regenerating axons, axon caliber and myelin thickness measurements were made by measuring along both the long axis and axis orthogonal to this. Average values of these two measurement directions were taken as the caliber of an individual axon and at least three high magnification images per nerve guide were measured using a minimum of 150 axons per image for characterization. Similar average cross-sectional areas were seen between all nerve guide groups where average values ranged from 8.0 μm^2 for the collagen fiber group to 10.0 μm^2 in the autograft. Axon calibers were typically around 2 to 3 μm average diameter with average myelin thickness in the 500 nm range for all three nerve guide groups (Fig. 4.25). Autograft had slightly higher myelin thickness at approximately 900 nm (Fig. 4.26).

Axon diameter distributions are shown in Figure 4.27. Axon diameter distributions were highly similar for all three of the nerve guide groups and were skewed towards smaller caliber axons with highest clustering in the 1.0 to 2.5 μm range. Autograft showed a higher spread in axon diameters with a largest population of axons with diameters of 4 μm or greater at 24.6%. Nerve guide groups only had populations of 4 μm+ axons at 17%, 18.6%, and 14.9% for uncoated PGA, PGS coated, and PGS coated groups containing collagen respectively. Larger caliber axons tend to be motor neurons so this could be a secondary explanation along with the higher axon count per nerve as to why the action potential amplitudes were higher in the autograft than other nerve guide groups.

Myelination quality was determined by the average g-ratio values, defined as the ratio of axon diameter to axon + myelin sheath diameter. Average values were relatively similar between nerve guide groups with the average g-ratio values being around 0.65 (Fig. 4.28). Autograft showed the lowest g-ratio at 0.59 due to the thicker myelin seen in the histological preparations for the group. There were no statistically significant differences between groups for the average g-ratio despite these small differences. This can be explained by looking at the distributions of axons diameter to g-ratio (Fig. 4.29). Distributions are highly similar between all three nerve guide groups with most clustering of data ranging towards the 0.5 to 0.8 g-ratio range between 1.5 and 4.0 μm. G-ratios for these groups begin to level off around 7.5 at axon diameters greater than 4 μm. The autograft group shows more spread in the data both in terms of g-ratio and the measured axon diameters, matching the data analysis from the axon distribution plots. Fitting the distribution data to logarithmic fits shows tight clustering the overall behavior of the three nerve guide groups with a noticeable decrease and separation of the autograft from the other groups, particularly as axon diameter increases (Fig. 4.30).

4.3.11 Secant PGS braided tube in vivo macrophage response

The highest overall macrophage levels were found to be present in the uncoated PGA braid group with a 50% fraction of macrophage compared to total cells present (Fig. 4.31). PGS coating reduced the relative macrophage population to 35%; and the inclusion of collagen fibers slightly increased the population fraction to 40%, but was not found to differ in a statistically significant manner relative to the PGS coating alone. The autograft group exhibited the lowest macrophage population fraction at 25%.

PGA alone showed little difference in total macrophage population fraction when comparing distal to relative ends, as both were around 50% (Fig. 4.31). Both PGS coated groups and autograft showed higher proportion of macrophages relative to other cells in the distal end compared with the proximal region. The highest difference occurring with the PGS coating alone group which jumped from 25% macrophage fraction in the proximal end to nearly 50% in the distal. Inclusion of collagen showed similar distal macrophage fractions to as the PGS alone but had higher fractions in the proximal region at just over 30% macrophage fraction. Distribution of M1 and M2 macrophages are shown in Figure 4.32.

With the exception of uncoated PGA braids, the aggregate cellular infiltration in the proximal regions were higher than the distal regions with only small drop-offs in infiltration occurring in the distal portion of the PGS coated groups compared to the autograft which had a much larger decrease in cellular infiltration relative to its proximal end (600 vs. 300) (Fig. 4.33). Distal end infiltration was similar amongst all four groups, which ranged from 300 to 400 cells. Total macrophage counts tended to be higher in the distal nerve stumps in the nerve guide groups but similar between proximal and distal for the autograft (Fig. 4.34).

4.3.12 Pro-inflammatory M1 macrophage population

The M1 population amongst the macrophages present, as indicated by those macrophages positive for both CD86 and CD68, showed similar levels across groups (Fig. 4.35) ranging from 50 to 60% with no significant differences between groups. PGS coating with luminally loaded collagen fibers were at the higher end of the range with the PGS and autograft showing nearly identical M1 population fraction at the lower end of the range. In all four groups, the M1 population fraction was higher in the proximal end compared to the distal end (Fig. 4.35) with proximal M1 ranging from 55 to 70% and distal from 45 to 50%.

Primers for iNOS, TNFα, CD86, and IL1β were used to characterize the expression of M1 related markers in the proximal and distal regions of three nerve guides per group after being explanted. The levels of iNOS were highly upregulated in all three nerve guide groups relative to the autograft, showing around 100-fold increases in iNOS expression (Fig. 4.36) and consistent with the histological analysis, the proximal regions show upregulation of iNOS relative to the distal in all four groups (Fig. 4.37). Quantification of iNOS cytokine levels from tissue homogenate collected from the distal and proximal regions via ELISA were consistent with the PCR data collected (Fig. 4.38). The ELISA data shows similar levels of iNOS present in the PGS coated groups and autograft while the PGA alone had elevated levels of the cytokine by comparison. Additionally, the quantification of iNOS levels in the non-operative control leg sciatic nerve had significantly lower levels present at 20 pg iNOS per mg tissue compared with the nerve guide and autograft groups, which had iNOS levels ranging from 80 to 110 pg per mg tissue. While there is some discrepancy in the PCR data relative to the ELISA, this is likely due to the fact that there will be accumulation of iNOS at the wound site over the initial seven days of implantation and the gene expression for iNOS could be more rapidly be downregulated in the autograft compared to the nerve guide groups at day seven. This behavior could be better characterized in potential future studies where earlier and later time points were examined for inflammatory profile to better determine the temporal effects the different nerve guide configurations have on the level of local inflammation. In the case of the ELISA iNOS data, the differences between proximal and distal were less prominent as there were small increases in the proximal region cytokine level compared to distal for the PGA braid and PGS group that included collagen fiber fillers.

TNFα, CD86, and IL1β showed less dramatic fold difference relative to the autograft though differences were still present between groups. Comparing groups, PGA had the highest relative TNFα mRNA expression difference at 8- to 5-fold compared to the autograft (Fig. 4.39). PGS and the collagen fiber containing groups showed less TNFα expression compared to the uncoated braid, with the collagen fiber group surprisingly showing the lower expression at 3- to 5-fold than the PGS only group at 6-fold despite having similar M1 macrophage population profiles, iNOS expression, and cytokine levels between the two PGS groups. Proximal versus distal differences were nearly non-existent for the PGA and PGS with collagen fiber groups (Fig. 4.40). A small decrease in TNFα expression at the distal nerve stump was seen with the PGS alone while the autograft had a small increase in expression at the distal relative to the proximal. CD86 expression was less clear cut than that for TNFα. Expression of CD86 was most elevated in the PGA braid alone with similar expression levels seen with the PGS only and autograft groups. Addition of collagen very slightly elevated CD86 expression compared to the autograft and PGS coating alone. Similar levels of CD86 expression were seen comparing proximal and distal regions with only PGA showing elevation in the distal end. In all cases for CD86, the fold difference was very small (< 2-fold difference) leading this particular dataset to be inconclusive. IL1β unlike TNFα, showed increased expression in the PGS coated groups compared to the uncoated PGA braid. All three nerve guide groups had at least 5-fold expression increase for IL1β compared to the autograft. In this case, inclusion of collagen fibers increased mRNA expression relative to the PGS coated braid by itself. For all four experimental conditions, the proximal region had higher expression levels of IL1β with the highest difference between regions being seen in the PGS with collagen fiber group. Distal expression of IL1β was similar amongst all three nerve guide groups with variation primarily in the proximal region.

4.3.13 Pro-regenerative M2 macrophage population

The M2 macrophage subpopulation was more responsive to changes in nerve guide configuration compared to the responsiveness of M1. Of total macrophages, the M2 population subfraction from isolating cells positive for both CD86 and CD206 were lowest in the uncoated PGA braided tube nerve guide at 20% of the macrophage population (Fig. 4.41). Coating with PGS increased the M2 population to 30% and addition of collagen fibers increased this further to 40% of the macrophage population. The autograft demonstrated highest M2 population at 60% after seven days of implantation. Distal regions in all groups had higher M2 population fractions. Similar proportional levels of M2 macrophages were found in the distal region for both PGS nerve guide groups, the primary difference between these two being the proximal portion of the PGS collagen fiber group having higher M2 population than the PGS group lacking fibers (30% vs 10%). The PGA braid and PGS coating only groups had similar M2 population fractions (10%) with the differences between these two groups being a result of the higher M2 fraction in the distal end of the PGS coating group.

Primers for ARG1, CD206, IL10, and PPARγ were used to characterize the expression of M2 related markers in the proximal and distal regions of three nerve guides per group after being explanted. ARG1 mRNA expression was increased in all three nerve guides relative to the autograft (Fig. 4.42). Interestingly, the PGA braid by itself had higher ARG1 expression than the PGS coating by itself at 9.5-fold expression increase and 4-fold increase respectively compared to the autograft. Highest ARG1 expression was seen with the PGS coating group containing collagen fibers at 12-fold increase relative to the autograft indicating that collagen fiber inclusion is potentially beneficial to the local inflammatory environment. In addition to PCR analysis, ELISA was used to determine ARG1 cytokine levels in the same manner as iNOS. Results of this assay were mixed as similar levels of ARG1 were detected ranging from 80 ng ARG1 per mg tissue for the PGS group and autograft compared to PGA braid and PGS with collagen fiber groups that showed 100 ng ARG1 per mg tissue and 140 ng ARG1 per mg tissue (Fig. 4.43). Despite small differences, there were no significant differences between nerve guide groups and the autograft and all four groups had at least 8-fold increase in ARG1 cytokine levels compared to the nonoperative control.

As with the M1 markers assayed with PCR, there were substantially lower fold differences for M2 markers CD206, IL10, and PPARγ compared to the differences seen with ARG1 analysis. CD206 expressions were similar across all groups with PGS only and PGA showing a 0.4-fold decrease in expression relative to the autograft (Fig. 4.44). The proximal and distal regions for PGA and PGS were similar while the proximal had higher relative CD206 expression in the collagen fiber containing group and autograft. IL10 expression was slightly increased in the PGA group relative to the autograft with the two PGS groups showing highest expression at around 3-fold increase relative to autograft. Again, proximal regions for the PGS containing groups showed a relative increase in expression levels compared to their distal regions although the difference is not significant in the PGS group containing collagen (Fig. 4.45). Very slight increase in IL10 expression was found in the autograft group. Unlike CD206 and IL10, PPARγ expression was found to decrease in the nerve guide groups relative to the autograft although the fold difference was small with the PGS braid group having the largest difference at 0.5-fold expression relative to the autograft. Also unlike CD206 and IL10 expression, higher mRNA expression levels of PPARγ were found in the distal regions for both the PGA braid, PGS containing collagen fibers, and autograft.

4.3.14 Comparative M1 and M2 macrophage populations

The relative proportion of the M1 and M2 macrophage populations could be calculated from the M2/M1 ratio. Figure 4.46 shows the M2/M1 subpopulation ratios to give an indication of the overall pro-inflammatory (M1 type) and pro-healing (M2 type) environment in the proximal and distal regions. The overall environment of the autograft was the most pro-healing being the only condition that had a M2/M1 ratio > 1. Uncoated PGA braid was the most pro-inflammatory environment with an M2/M1 ratio around 0.5, which is consistent with the high levels of M1 marker and cytokine expression seen with this group. Both PGS groups were pro-inflammatory but to a lesser extent relative to the uncoated PGA braid based on their M2/M1 ratios around 0.7. The most pro-healing region based on the M2/M1 criteria occurred with the autograft distal region where the ratio took on a value of 2 to counteract the pro-inflammatory environment in the autograft proximal region with a ratio value of 0.7. In general, distal regions were more pro-healing inclined compared to the matching proximal nerve stumps with distal regions for both PGS coating groups being near or slightly above a M2/M1 ratio of 1. Proximal regions in all groups were found to be pro-inflammatory based on M2/M1 ratio which is consistent with the PCR results for iNOS, IL1β, and to a lesser extent TNFα which were all elevated in the proximal region compared to the distal.

4.4 Conclusions

Axon count differences between the coated and uncoated PGS nerve guide groups can be attributed to the differences in compression amongst the groups. The PGS coating provides additional mechanical reinforcement to the underlying PGA braided structure that help it to resist compressive forces that can reduce the available cross section available for axonal outgrowth from the proximal nerve stump. This can be seen where the total nerve cross sectional area of the PGA braid alone is reduced relative to the PGS coated braid and even the autograft. As a consequence of this, the reduction in axon number crossing the gap results in lower action potential amplitude and therefore strength. This leads to much lower functional recovery and more pronounced negative secondary effects such as increases degree of muscular atrophy.

The uncoated PGA braid also appears to have a higher level of connective tissue formation compared to other groups as indicated by the regions lacking axon ingrowth. This is likely due to the increased permeability of inflammatory cells and fibroblasts through the gaps in the PGA braid that are not filled by the PGS in the other nerve guide groups and the lack of immunomodulatory PGS coating. Some connective tissue is still present in the two PGS coated groups but not to the extent seen in the uncoated as these groups have cellular infiltration origins limited to the proximal and distal nerve stumps.

Differences between the PGS coated groups are likely a result of the persistence of collagen fibers after 12 weeks implantation. Infiltration of axons into the collagen fibers was much lower than that seen in the interstitial space between fibers, leading to a lower effective available cross-sectional space for infiltration of the axonal growth cone. Higher magnification images of the nerve cross sections show that the space between collagen fibers shows similar density of axons in the two PGS coated nerve guide groups per unit area. Higher magnitude images also show more prominent myelin sheath thickness in the autograft compared to all three nerve guide groups, although all groups had g-ratios close to the often cited value of 0.6 in healthy nerve tissue [27]. The autograft had a distribution of axon calibers skewed towards larger relative sizes, further providing evidence into the factors responsible for the improved regenerative response seen with the autograft leading to the conclusion that increased axon count per nerve is a critical factor that nerve guides need to be designed to maximize through creating a microenvironment that minimizes connective tissue formation and maximizes the infiltration of the axonal growth cone.

Interestingly, the PGS coating appears to have a beneficial effect on the formation of new vasculature. This is particularly prominent along the region directly interior to the PGA braid in the PGS coated groups, where large capillaries can be seen to form that have significant presence of red blood cells. High magnification views of collagen fibers show some presence capillary formation within the collagen fibers after 12 weeks implantation. Collagen fibers also show infiltration of fibroblasts (dark spots) through the core structure of the fiber and myelinated axons along the periphery of the fibers.

4.5 Figures

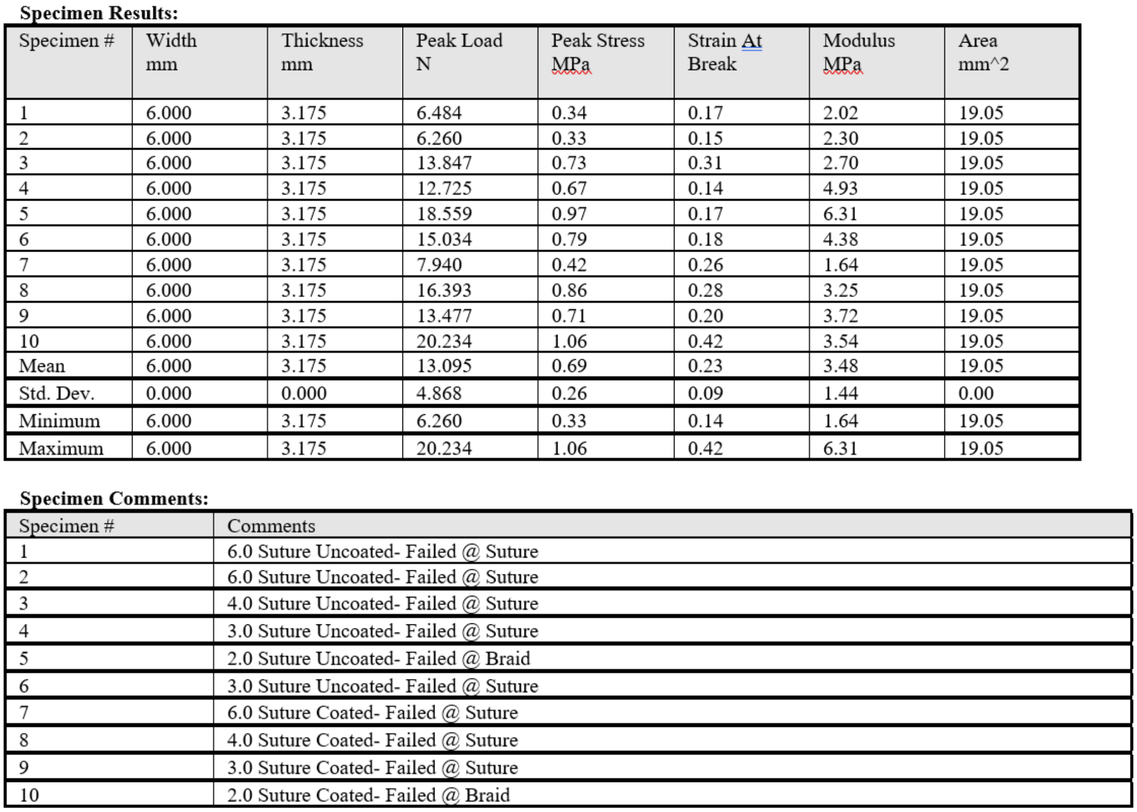

Specimen Results:

Specimen #	Width mm	Thickness mm	Peak Load N	Peak Stress MPa	Strain At Break	Modulus MPa	Area mm^2
1	6.000	3.175	6.484	0.34	0.17	2.02	19.05
2	6.000	3.175	6.260	0.33	0.15	2.30	19.05
3	6.000	3.175	13.847	0.73	0.31	2.70	19.05
4	6.000	3.175	12.725	0.67	0.14	4.93	19.05
5	6.000	3.175	18.559	0.97	0.17	6.31	19.05
6	6.000	3.175	15.034	0.79	0.18	4.38	19.05
7	6.000	3.175	7.940	0.42	0.26	1.64	19.05
8	6.000	3.175	16.393	0.86	0.28	3.25	19.05
9	6.000	3.175	13.477	0.71	0.20	3.72	19.05
10	6.000	3.175	20.234	1.06	0.42	3.54	19.05
Mean	6.000	3.175	13.095	0.69	0.23	3.48	19.05
Std. Dev.	0.000	0.000	4.868	0.26	0.09	1.44	0.00
Minimum	6.000	3.175	6.260	0.33	0.14	1.64	19.05
Maximum	6.000	3.175	20.234	1.06	0.42	6.31	19.05

Specimen Comments:

Specimen #	Comments
1	6.0 Suture Uncoated- Failed @ Suture
2	6.0 Suture Uncoated- Failed @ Suture
3	4.0 Suture Uncoated- Failed @ Suture
4	3.0 Suture Uncoated- Failed @ Suture
5	2.0 Suture Uncoated- Failed @ Braid
6	3.0 Suture Uncoated- Failed @ Suture
7	6.0 Suture Coated- Failed @ Suture
8	4.0 Suture Coated- Failed @ Suture
9	3.0 Suture Coated- Failed @ Suture
10	2.0 Suture Coated- Failed @ Braid

Figure 4-1: Suture retention test for PGS coated and uncoated PGA multifilament braided tubes. Load to failure of PGS coated and uncoated braids, given by peak load force following ISO 7198 standards show PGS coating enhances retention strength, requiring 20.2 N load force to tear braid compared to 18.6 N for uncoated braids. Polypropylene sutures smaller diameter than 2.0 size failed at the suture before the braid.

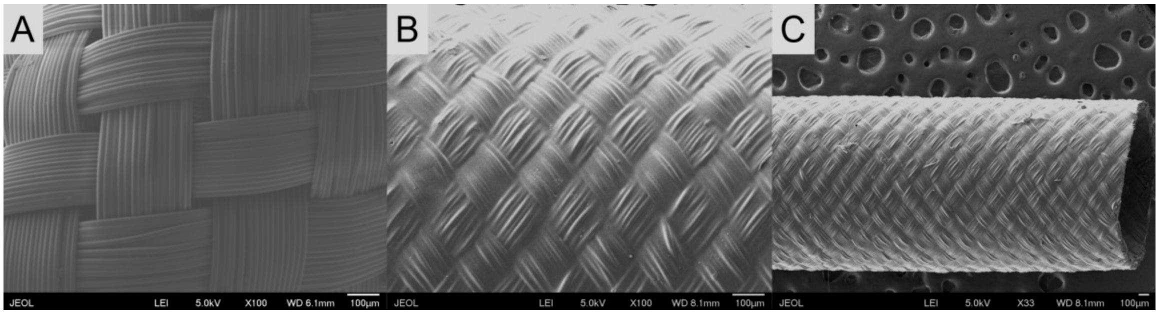

Figure 4-2: Coating of multifilament poly(glycolic acid) (PGA) braided tubes with poly(glycerol sebacate) (PGS). Multifilament PGA fibers are braided into a tubular shape by the Secant Group, LLC (a) and then coated with PGS (b), filling in porous gaps between PGA filaments and improving mechanical properties of the tubes (c).

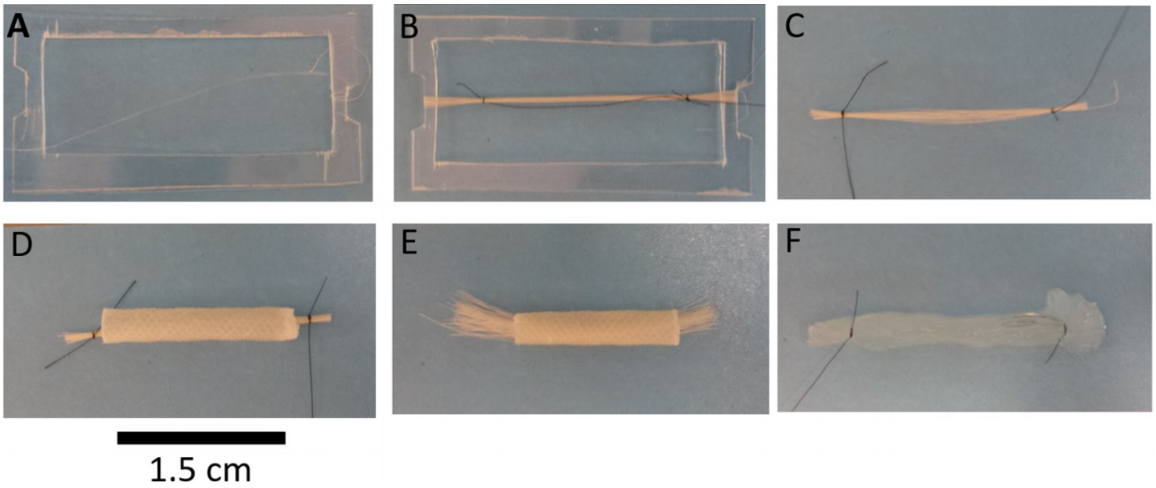

Figure 4-3: Collagen fiber loading into PGS coated PGA braided tubes. Nerve guide preparation. A strand of collagen fiber is tied to the end of a plastic frame (a) and then wound around until total filament count in the bundle is at a count of 25, 50, or 100 (b), which corresponds to the approximate percentage of luminal space taken up by the collagen fibers upon rehydration. Ends are tied off with suture (b) and the bundle is then cut free from the frame (c), loaded into the braided nerve guide conduit (d). Dry fiber bundle expands to fill the lumen of the NGC when released from the suture tie (e). Upon rehydration, fiber bundle takes on gel-like characteristics and fills the conduit (removed for this panel) (f).

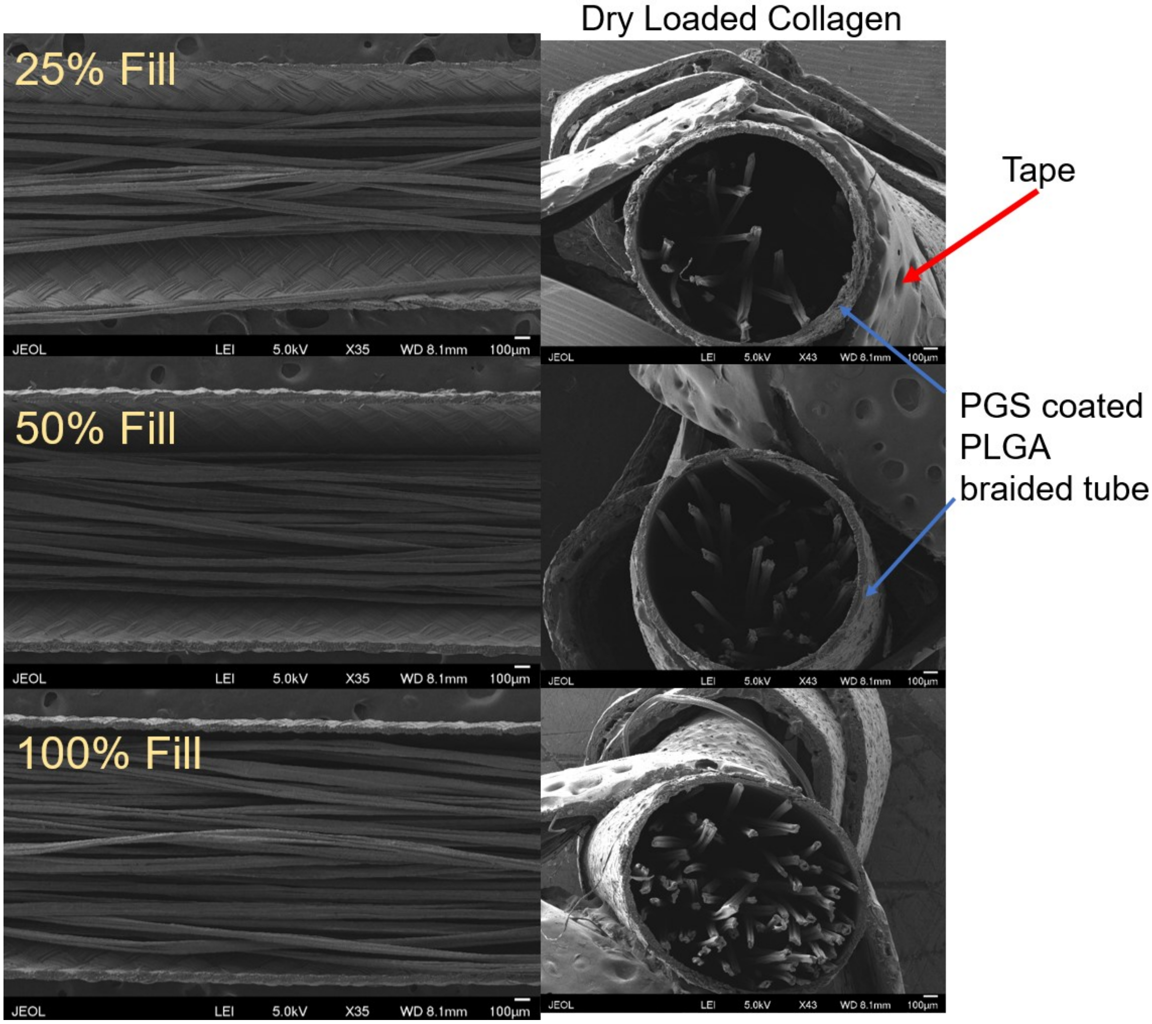

Figure 4-4: 25, 50, and 100% Secant collagen filament fill density within PGS coated nerve guide conduit. Loading of Secant dry collagen fibers within coated nerve guide clearly show difference in loading density moving from 25% to 100% rehydrated fill density, corresponding to approximately 25 and 100 collagen filaments respectively. Relatively high initial dry collagen filament diameter of ~ 90 µm and degree of swelling limits fill amount to relatively few discrete sources of topographical guidance relative to nanofiber based strategies.

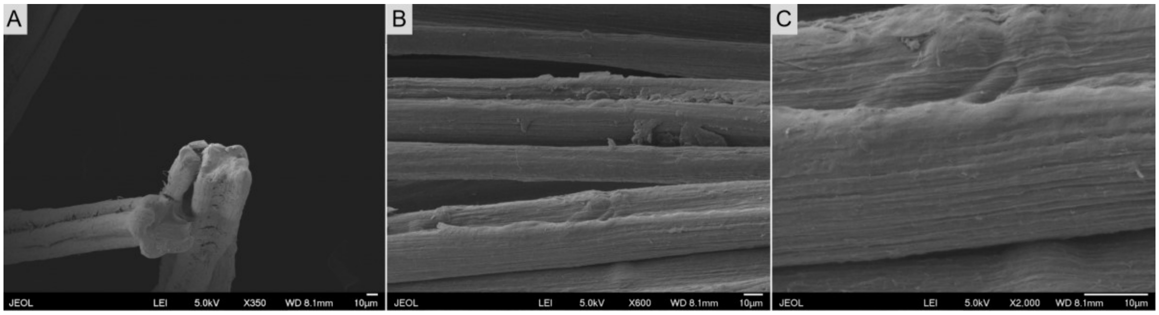

Figure 4-5: Topographical guidance features of Secant collagen filaments. Secant collagen fibers show clover-like aggregate shape (a) due to four outlets dispensing collagen precursor solution into an acetone bath. This results in micron scale topography that is complimented by the aligned nanotopographical features of the filament surface (b, c).

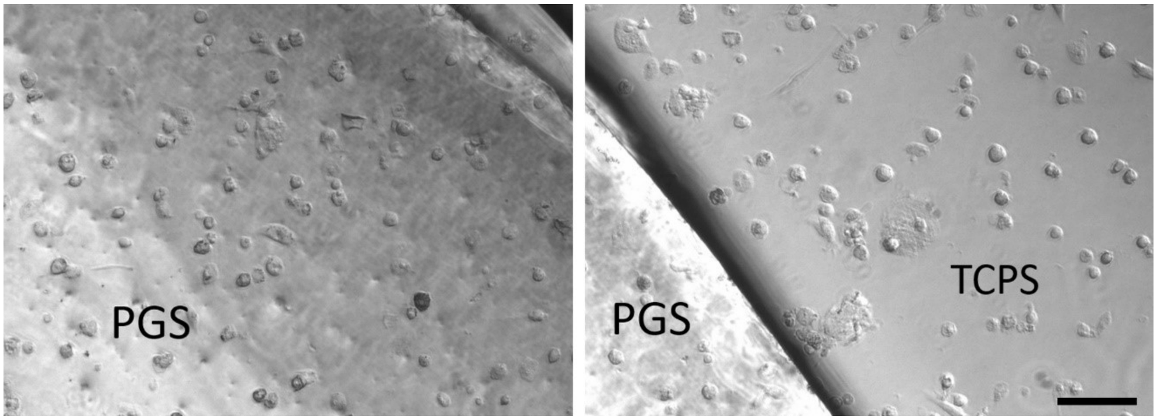

Figure 4-6: Poor attachment of BMDMs on PGS coated coverslips. BMDMs cultured on or near TCPS show poor attachment and unhealthy morphology. Scale bar: 100 µm.

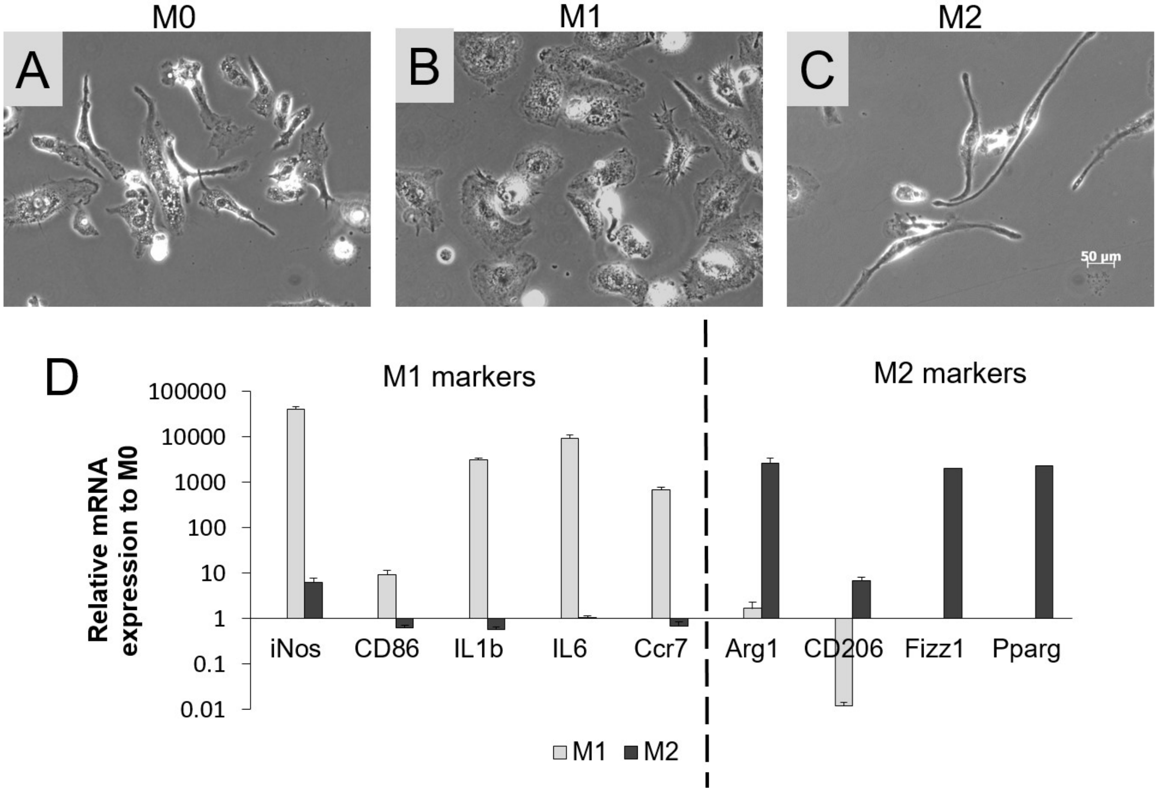

Figure 4-7: Healthy attachment of BMDMs and successful differentiation in absence of PGS coating. BMDMs cultured in maintenance (a), M1 macrophage (b), or M2 macrophage differentiation media (c) show expected healthy cellular morphology in the absence of PGS with more rounded and spindle-like morphologies seen as expected for M1 and M2 macrophages respectively. PCR analysis shows that M1 markers are highly upregulated in the presence of M1 differentiation media and that M2 markers show themselves to be similarly affected by M2 differentiation media (d).

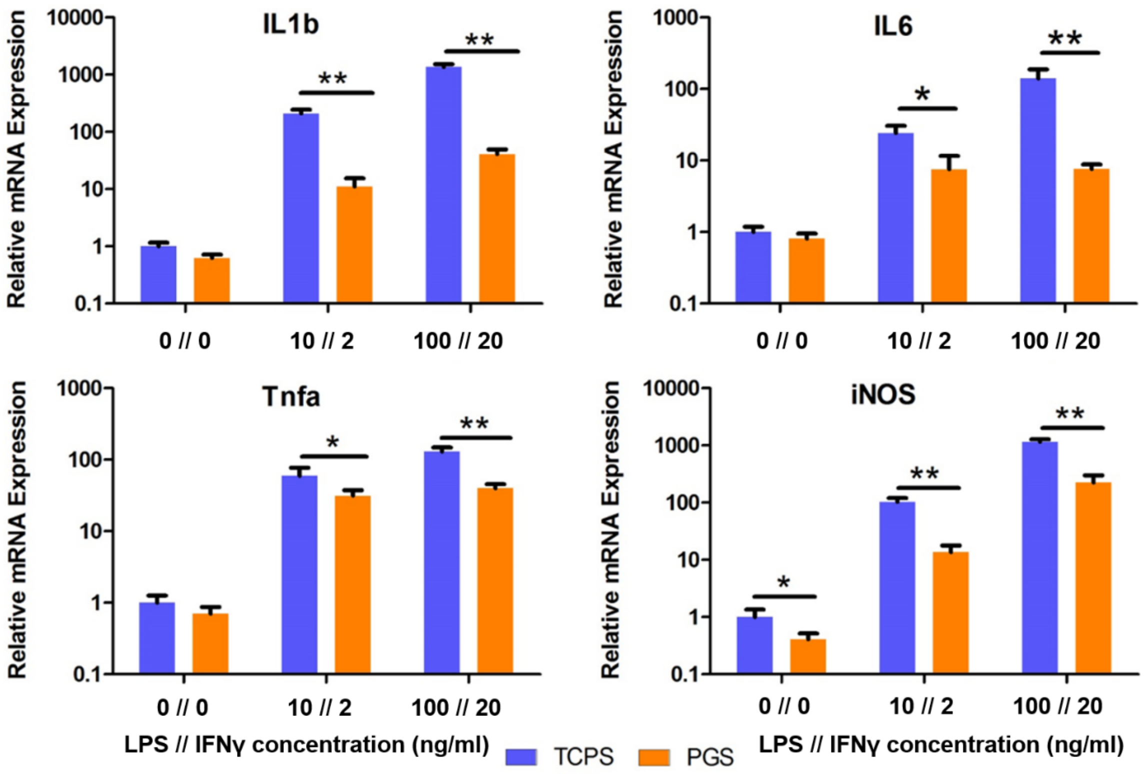

Figure 4-8: Effect of PGS coating on M1 differentiation of BMDMs in vitro using different levels of M1 differentiation cytokines LPS and IFNγ. Expression of M1 markers were quantified using qPCR with increasing levels of LPS and IFNγ added to differentiation media to determine PGS coatings ability to resist BMDM differentiation into M1 phenotype. For all four M1 markers, PGS coating resulted in decreased expression relative to TCPS at all concentrations of LPS and IFNγ. Increases in LPS and IFNγ concentration increased the fold difference in all M1 markers relative to the unbiased 0 ng/ml LPS // IFNγ control though the fold difference was much higher on TCPS compared to macrophages cultured on PGS as concentration increased.

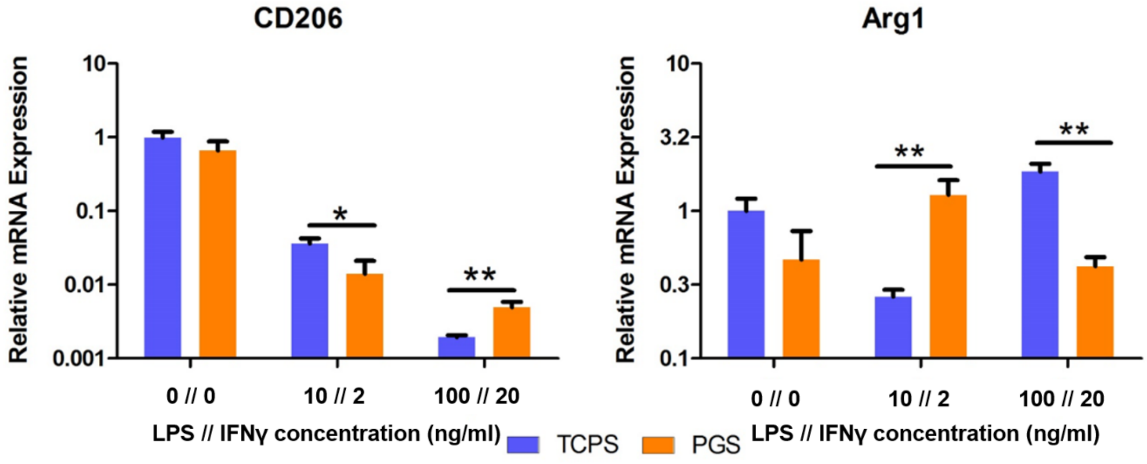

Figure 4-9: Effect of PGS coating on M2 differentiation of BMDMs in vitro using different levels of M1 differentiation cytokines LPS and IFNγ. Expression of M2 markers were quantified using qPCR with increasing levels of LPS and IFNγ added to M1 differentiation media to characterize promotion of differentiation towards the M2 phenotype. For both M2 markers, PGS coating resulted in decreased expression relative to TCPS at all concentrations of LPS and IFNγ except for the ARG1 expression increase seen with PGS at "10 // 2 ng/ml LPS // IFNγ".

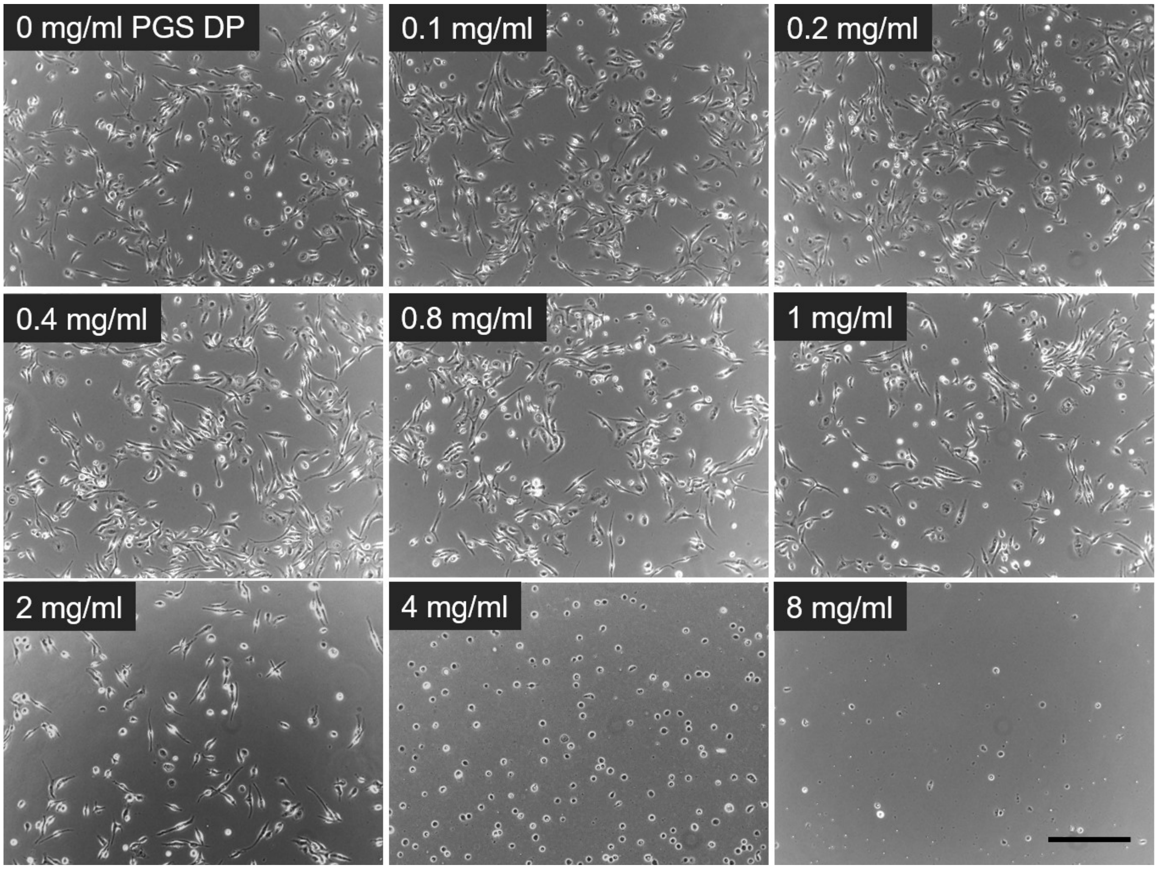

Figure 4-10: PGS degradation product (DP) interferes with normal cell morphology and attachment on TCPS as concentration increases.

PGS degradation product was added differentiation media at various concentrations for 48 hours to determine effect of PGS DP on cell viability. Attachment and morphology of cells did not begin to be noticeably impacted until concentration exceeded 1 mg/ml where increasing numbers of cells had a rounded morphology. At the maximum concentration of PGS DP tested of 8 mg/ml, few cells remained attached. Scale bar: 300 μm.

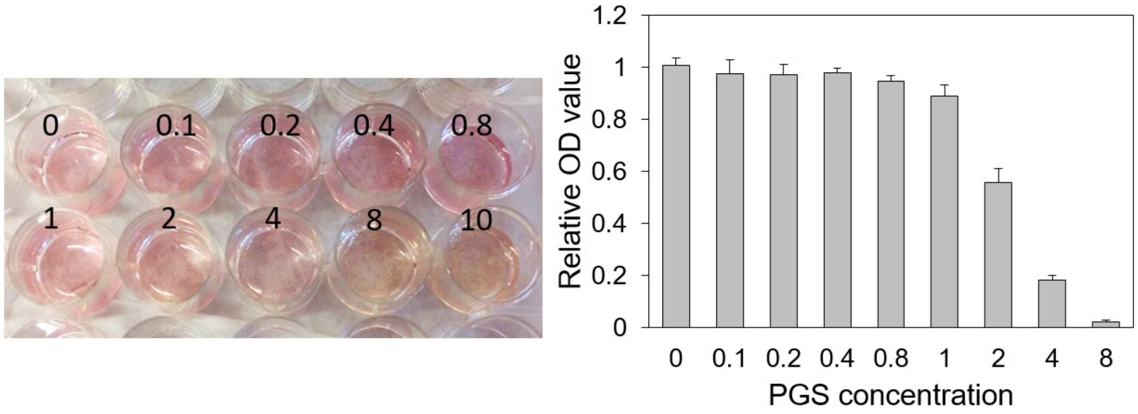

PGS DP (mg/ml)	0	0.1	0.2	0.4	0.8	1	2	4	8
pH	7.58	7.57	7.56	7.54	7.53	7.38	7.36	7.3	6.8

Figure 4-11: PGS degradation product (DP) reduces BMDM viability due to increased media acidity. Culture of BMDMs in differentiation media for 48 hours shows the acidity of PGS DP surpassing the buffering capacity of the culture media as DP concentration exceeds 1 mg/ml. Beyond this point, rapid decrease in cellular mitotic activity was detected as pH dropped when comparing the relative fluorescence of Alamar blue assay against TCPS controls lacking PGS degradation product.

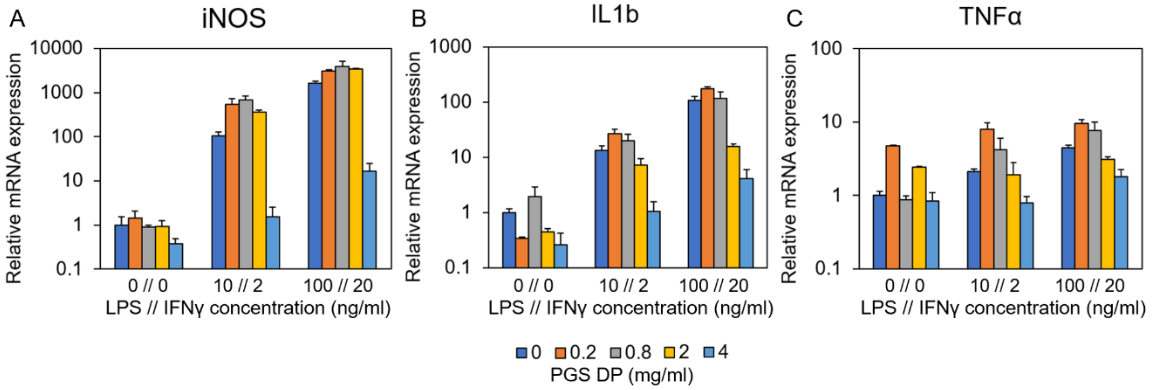

Figure 4-12: Relative mRNA expression of M1 markers when BMDMs are exposed to PGS degradation product and M1 differentiation media. Exposure to both M1 differentiation and PGS degradation product had an affected mRNA expression most prominently at higher DP concentrations above 0.8 where cell viability and morphology were compromised. This relative drop in mRNA expression occurred only at the highest tested DP concentrations for iNOS (a) while IL1b and TNFα showed reduction in their respective expression above 0.2 mg/ml DP (b, c) with even larger expression drops occurring above 0.8 mg/ml DP.

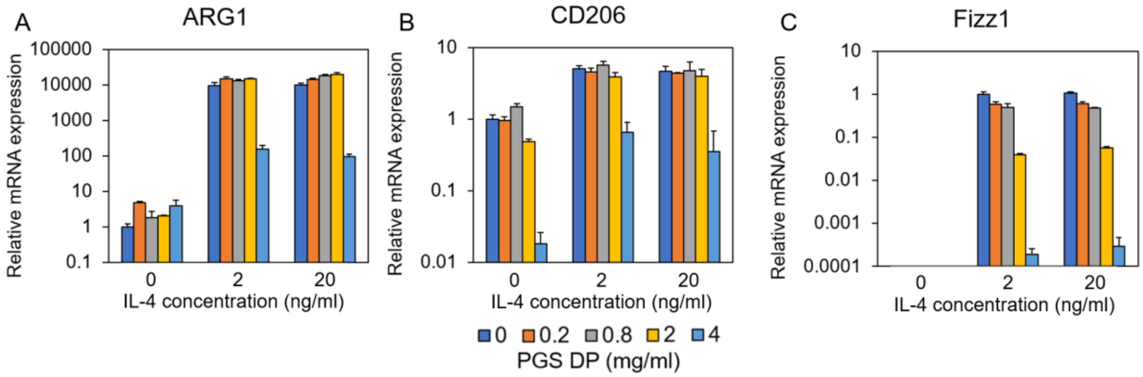

Figure 4-13: Relative mRNA expression of M2 markers when BMDMs are exposed to PGS degradation product and M2 differentiation media. Degradation product concentrations had little effect on CD206 and ARG1 mRNA expression until degradation product levels reached 4 mg/ml and cell viability was affected (a, b). Fizz1 expression showed higher sensitivity to DP concentration, showing a small decrease in expression at 0.2 mg/ml DP with the first large noticeable expression drop occurring at 2 mg/ml DP (c).

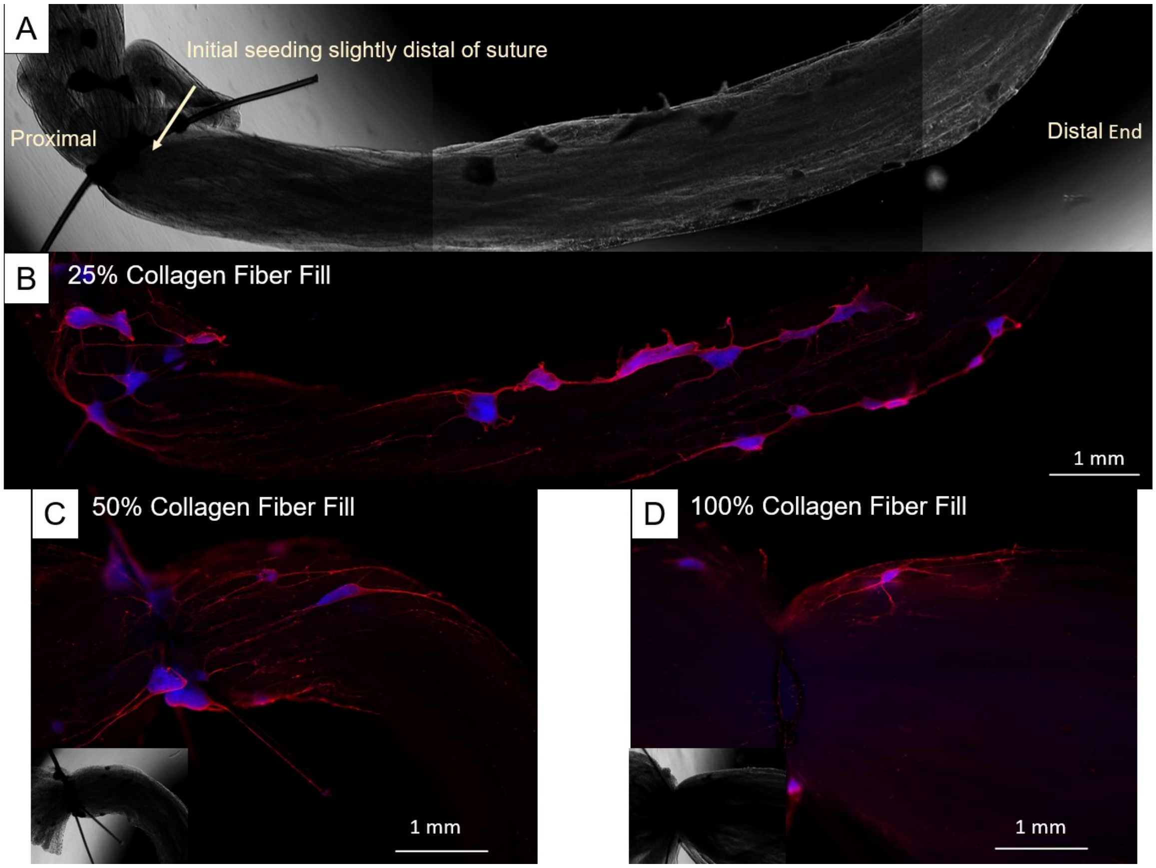

Figure 4-14: Differentiated neural stem cells show higher outgrowth as collagen fiber fill density decreases. Differentiated neural stem cells (βIII-Tubulin, red) show highest degrees of outgrowth along less densely filled 1.5 mm diameter agarose troughs (a-d). Nucleus dense NSC spheroids (DAPI, blue) were mostly found near seeding site on left side of collagen fiber bundle and along fiber bundle surface if carried by media during seeding (b). Less pronounced neurite spreading was seen with denser fiber fill (c,d) with neurites primarily found near collagen fiber bundle surfaces rather than maneuvering through the core of the bundle.

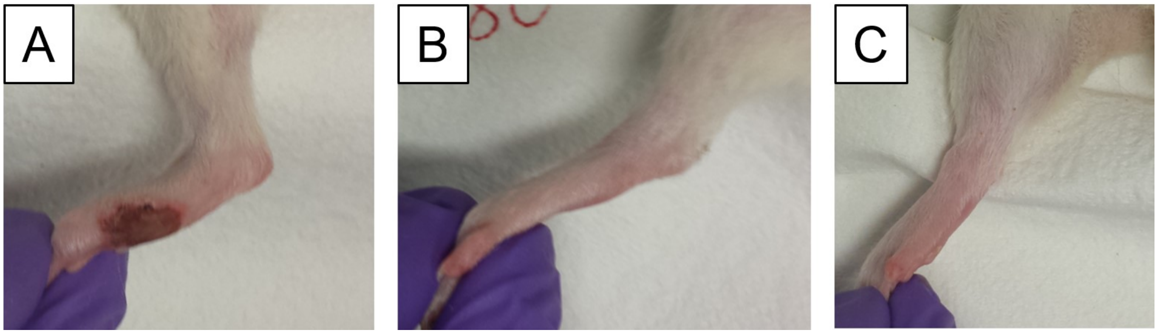

Figure 4-15: Increased incidence of autophagy in uncoated PGA braided nerve guides after implantation using rat sciatic nerve defect model. Wounds resulting from autophagy of the foot and/or toes was present in 7 of 8 animals in uncoated PGA braided nerve guide groups (a). Addition of PGS coating showed significant autophagy in only 1 of 8 PGS coating only animals and in 2 of 8 animals when collagen fibers were included in the lumen of PGS coated braids with most animals in the two PGS groups showing only light wounding if any (b). None of the autograft animals showed signs of autophagy (c).

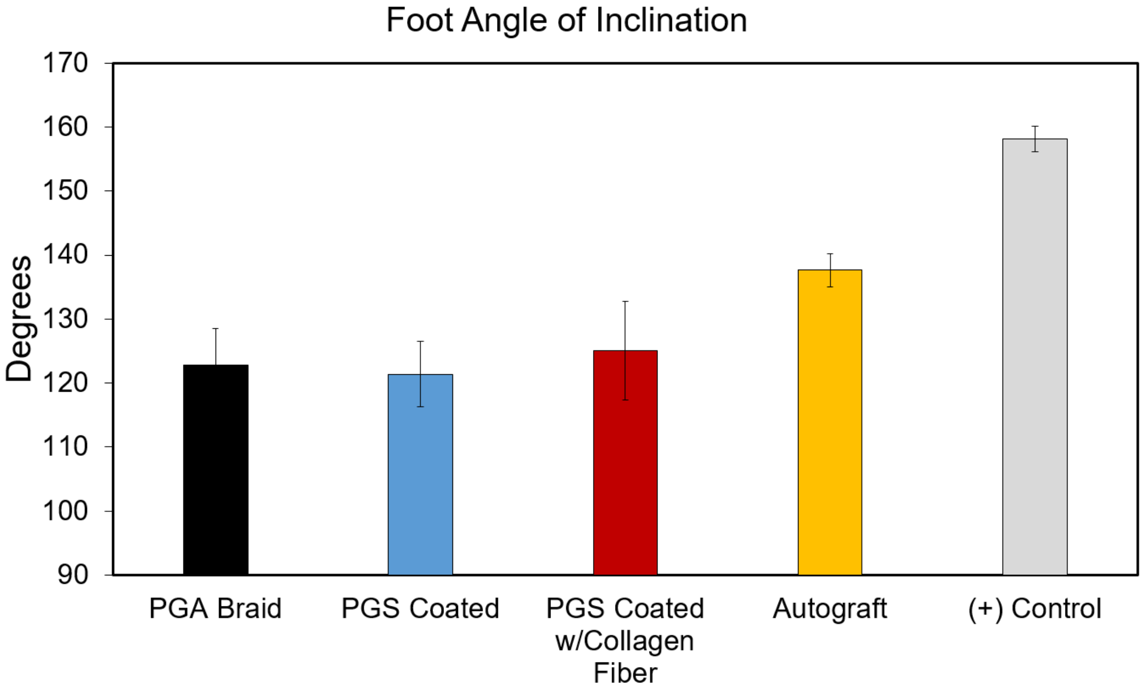

Figure 4-16: Nerve guide groups show reduced mobility of ankle joint after three months compared to autograft and positive controls. All three nerve guide conduit groups showed similar levels ankle joint mobility three months post-implantation. Autograft showed some improvement but this was still well short of the non-operative positive control ankles that had foot inclination values closing in on 160 degrees.

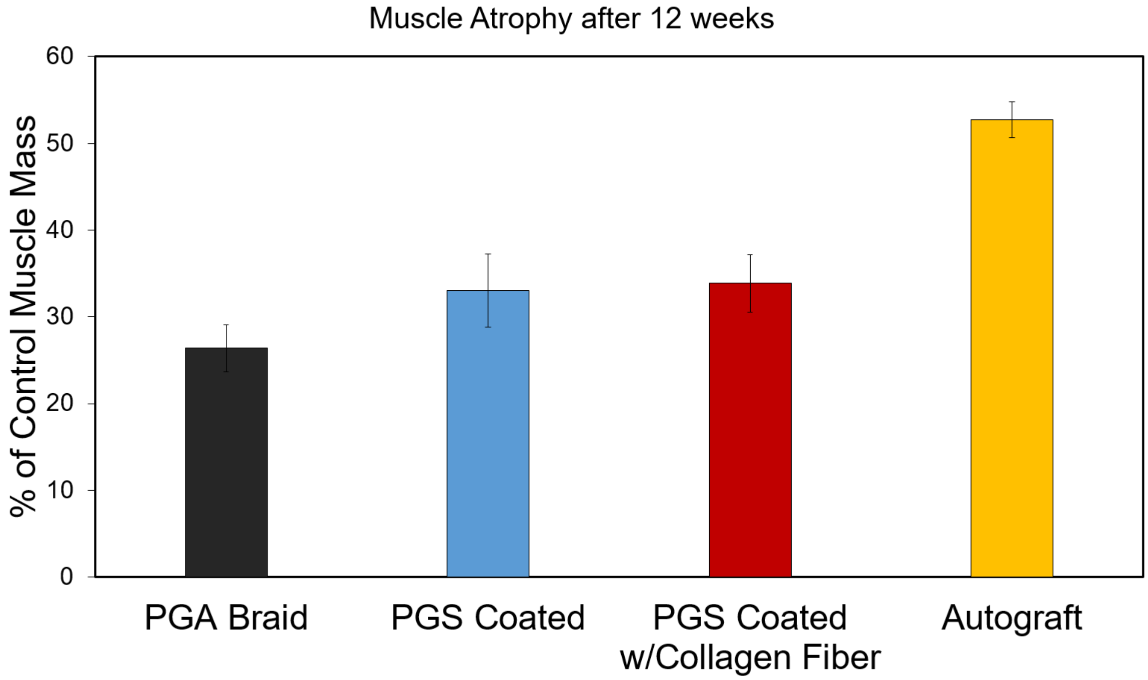

Figure 4-17: Combined atrophy of gastrocnemius and soleus muscle is highest in uncoated PGA braid nerve guidance conduits. Atrophy was highest in the uncoated PGA braid at only 26% of the muscle mass remaining after three months implantation though the PGS coated braids were not statistically significantly better at 33% of the control side muscle mass. Results are consistent with the trends seen with foot angle of inclination data where nerve guide groups yielded similar results that were less positive relative to the autograft.

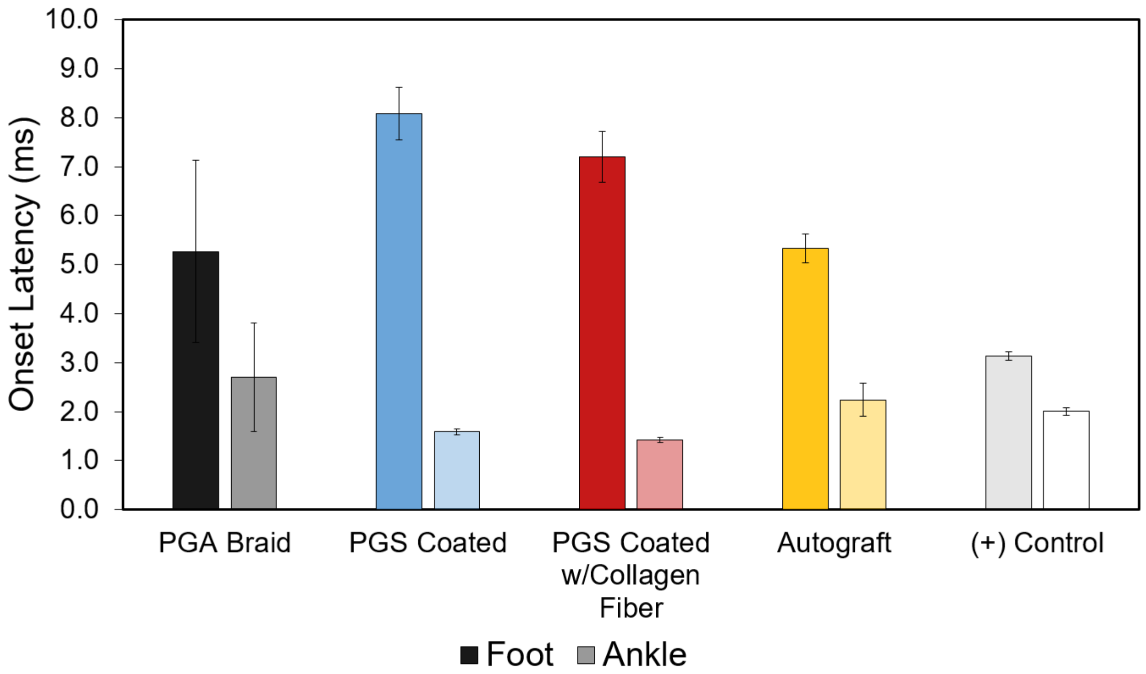

Figure 4-18: Onset latency measurements of foot and ankle for all nerve guide groups after 12 weeks implantation in rat model. CMAP measurements of onset latency show higher latency in foot compared to ankle due to the increased travel distance between electrodes placed proximal to the sciatic nerve defect site and the foot compared to ankle. Higher weight should be placed on ankle data as the foot measurements can be disrupted by autophagy, particularly seen by the large deviations seen in the uncoated braid group. Surprisingly, ankle onset speed was actually more rapid in both PGS groups, averaging 1.59 ms and 1.42 ms for the unfilled and collagen filled PGS respectively, compared to the autograft and positive controls having an average of 2.24 ms and 2.01 ms respectively, indicating high quality axons are successfully bridging the nerve guides.

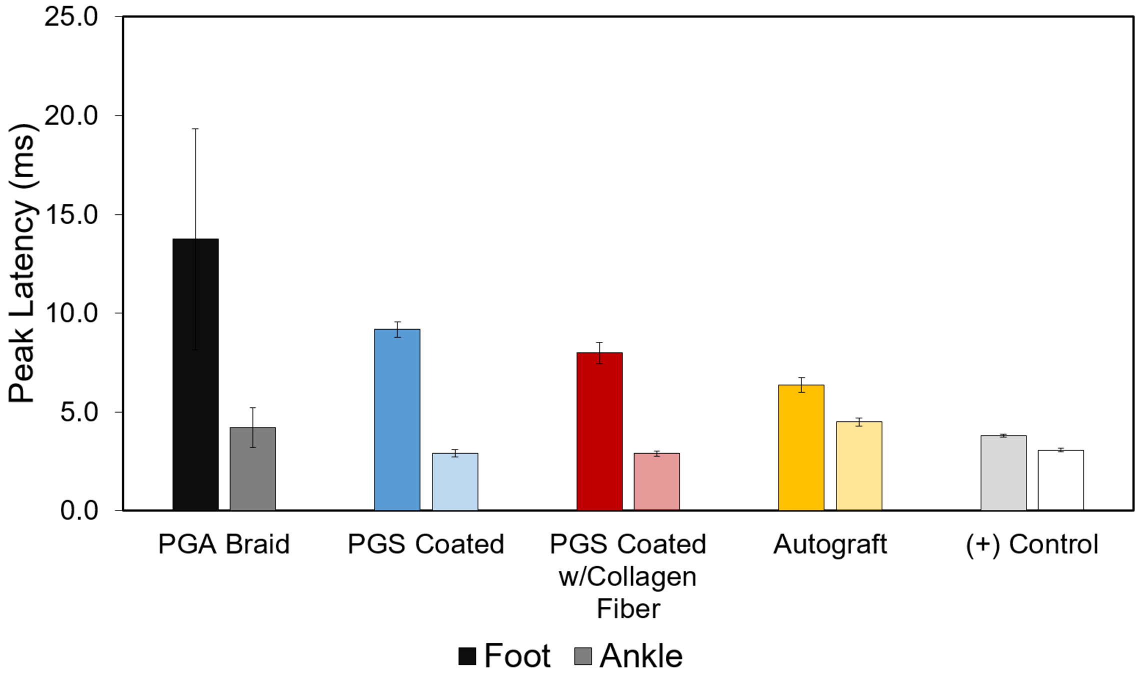

Figure 4-19: Peak latency measurements of foot and ankle for all nerve guide groups after 12 weeks implantation in rat model. The propagation speed of the action potential, characterized by the peak latency, shows slower signal propagation in the foot, matching the onset latency data trends relative to the ankle. Similar onset latency speeds were seen in the PGS coated group ankle measurements around 2.9 ms for both unfilled and collagen fiber filled and these were very similar to the average value of 3.07 ms measured in the positive control. Autograft and the positive control had the lowest differences between foot and ankle measurements, consistent with the average level of autophagy in these groups compared to others.

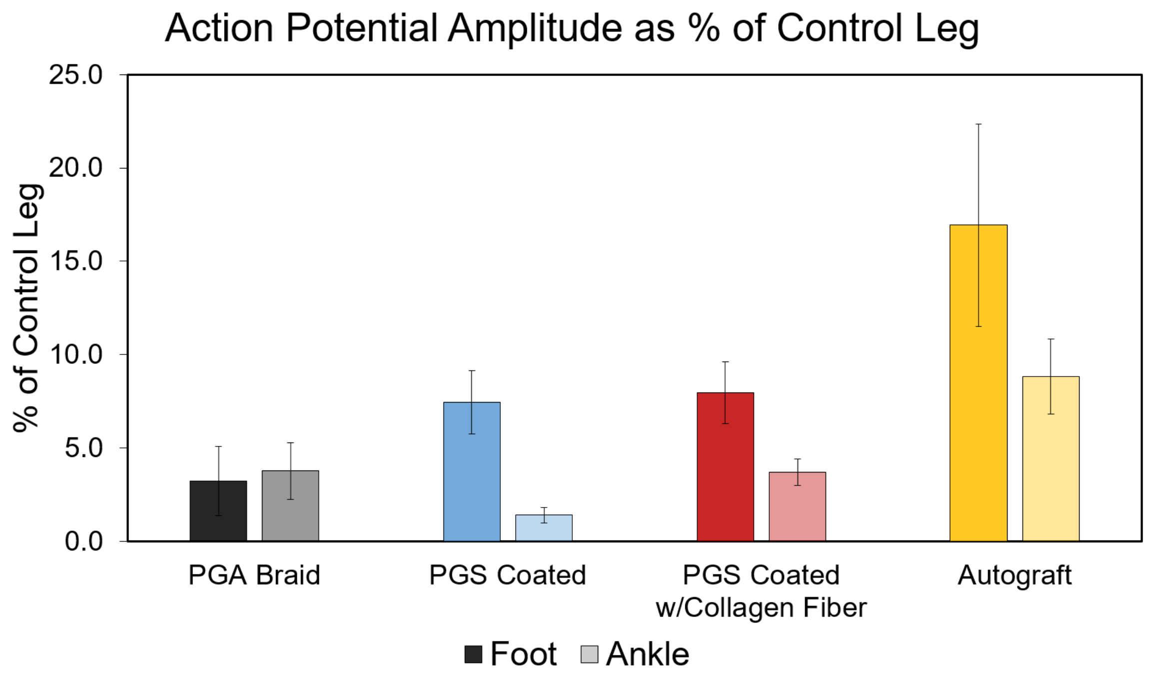

Figure 4-20: Action potential amplitudes of foot and ankle as % of control leg for all nerve guide groups after 12 weeks implantation in rat model. Action potential amplitudes provide one of the best measurements of functional recovery due to the requirement of robust regeneration with many axons bridging the defect to occur for high signal amplitude. Even autograft results are relatively poor at only 8.8% of the amplitude measured in the control ankle, illustrating the need to not only meet, but surpass the autograft with nerve guide strategies. Collagen fiber filling in PGS coated PGA braids provided better signal amplitude in the ankle compared to the empty PGS coated nerve guide. Surprisingly the PGA braid (3.77%) had similar signal amplitude measurements to the collagen fiber group (3.71%). These best performing nerve guide groups were still only 42% as effective as the autograft when ankle amplitudes were compared.

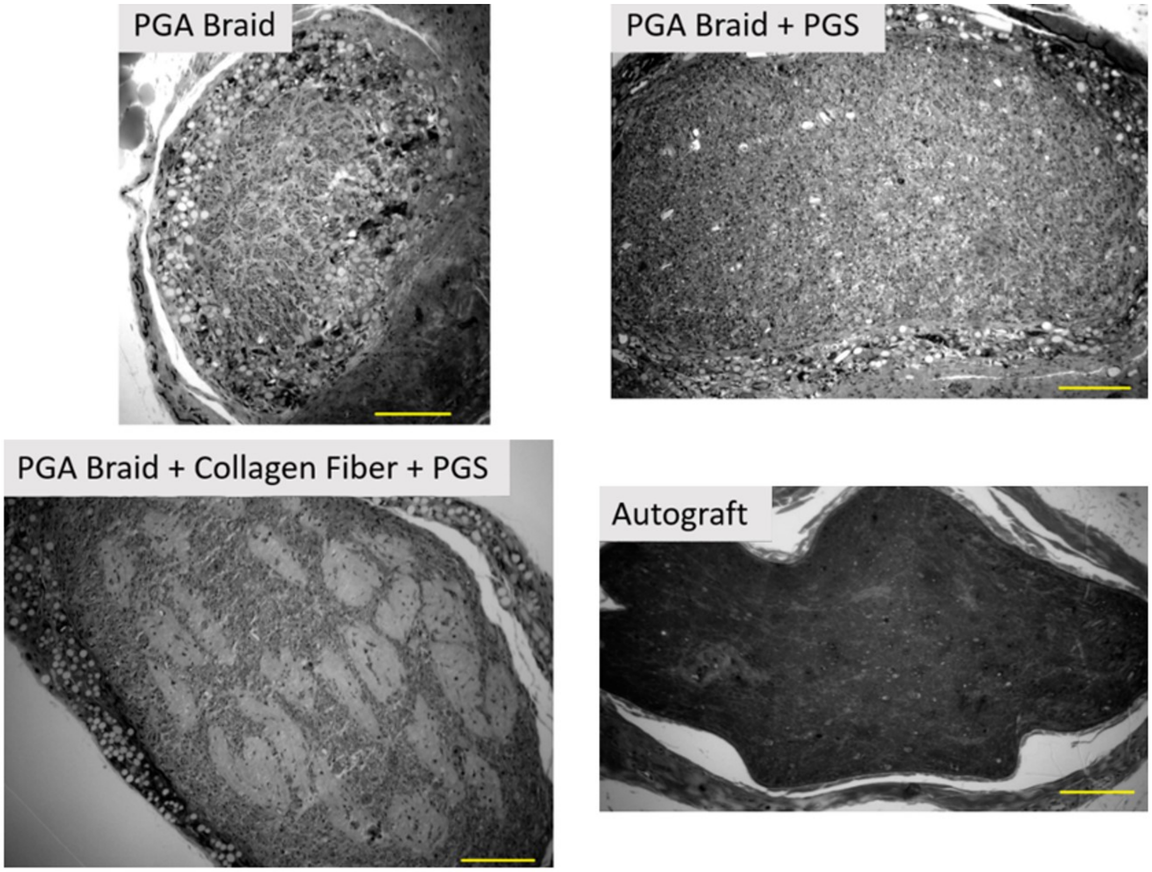

Figure 4-21: Representative mid-graft cross sections of nerve guide explants after three months. PGA braid remains visible to provide mechanical support to the nerve guide as nerve continues to regenerate in all three groups. Some compression of nerve guide seen in uncoated braid (top left) leading to a reduction in nerve cross sectional areas compared to PGS coated braids (top right, bottom left). Collagen fibers remain present even after three months, reducing some of the potential area available for axonal outgrowth (bottom left). Autograft shows darker staining due to more maturation in myelin formation (bottom right) and shows similar total nerve cross sectional area to the PGS coated groups. Scale bars: 100 μm.

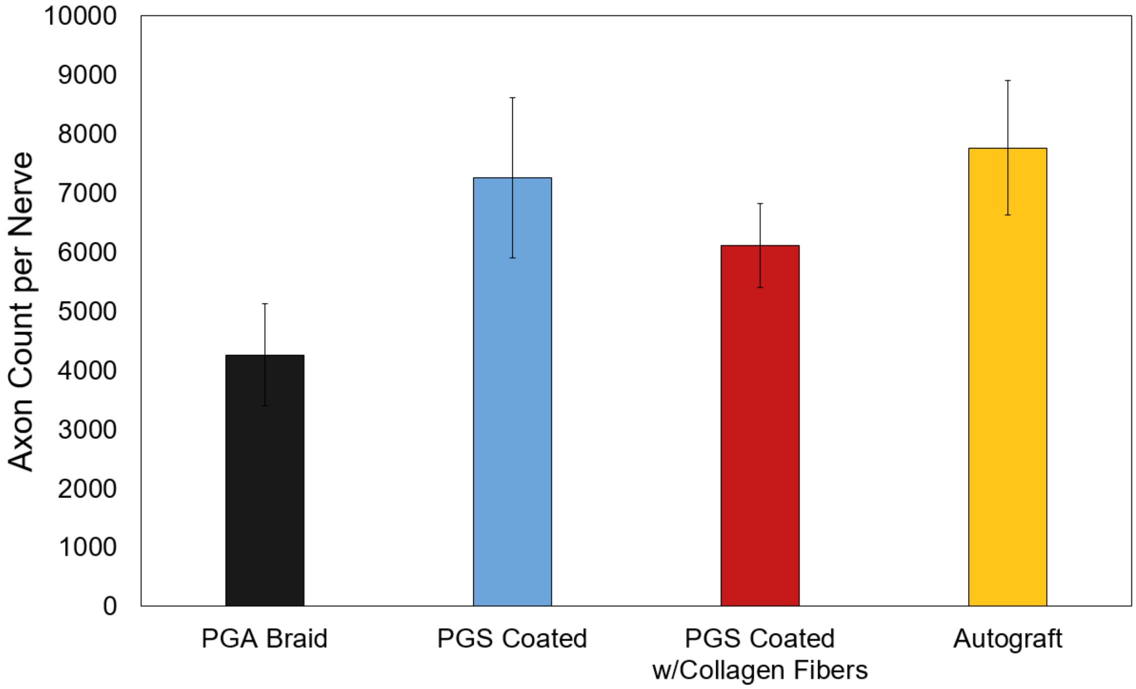

Figure 4-22: Axon count per whole nerve cross-section. Higher axon count per nerve was seen in the two PGS coated groups (averages of 7263 axons unfilled lumen, 6117 axons in collagen fiber filled) relative to the uncoated (4260 axons) due to the compression seen in the uncoated nerve guides. Coating with PGS provided similar axon count levels compared to the autograft (7766 axon average) but addition of collagen fibers slightly reduced axon count levels due to the space taken up by the fibers limiting axonal outgrowth through the fibers. N = 5 to 8.

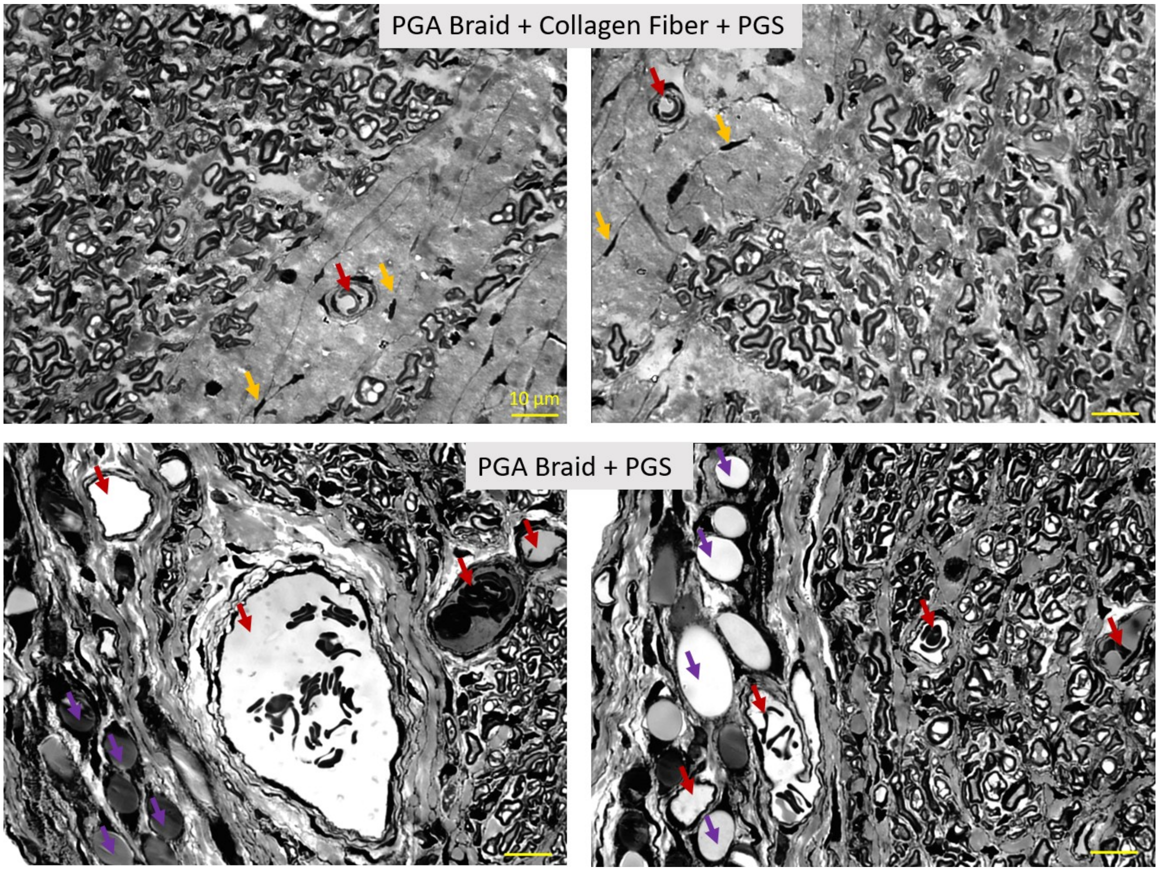

Figure 4-23: Higher magnification images showing capillary formation within collagen fiber and vessel formation near PGA braid. Capillary infiltration seen within Secant collagen fibers (top row, red arrows) and also by fibroblasts (yellow arrows). Surface of collagen fibers have myelinated axons present implying that some axons are following the alignment cues provided by the fibers. Blood vessel formation was seen near the PGA braid (bottom row, purple arrows – PGA braid, red arrows – capillaries) leading to the possibility that PGS is promoting angiogenesis and the PGA braid alignment is guiding vessel growth. Scale bar: 10 µm.

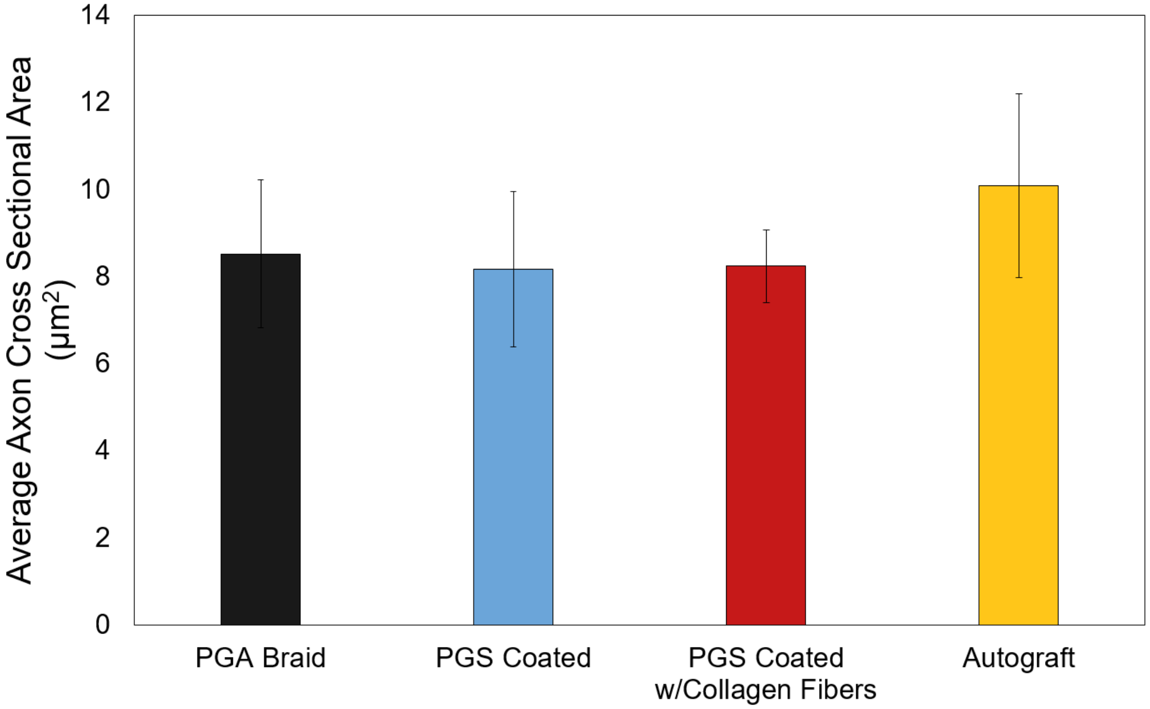

Figure 4-24: Average axon cross sectional area in nerve guide conduit and autograft after three months of nerve regeneration. The average individual axon cross sectional area for all three nerve guide groups were very similar at 8.52, 8.17, 8.24 μm^2 for the uncoated, PGS coated, and collagen fiber filled nerve guides. These were all lower than the autograft axon average area of 10.09 μm^2.

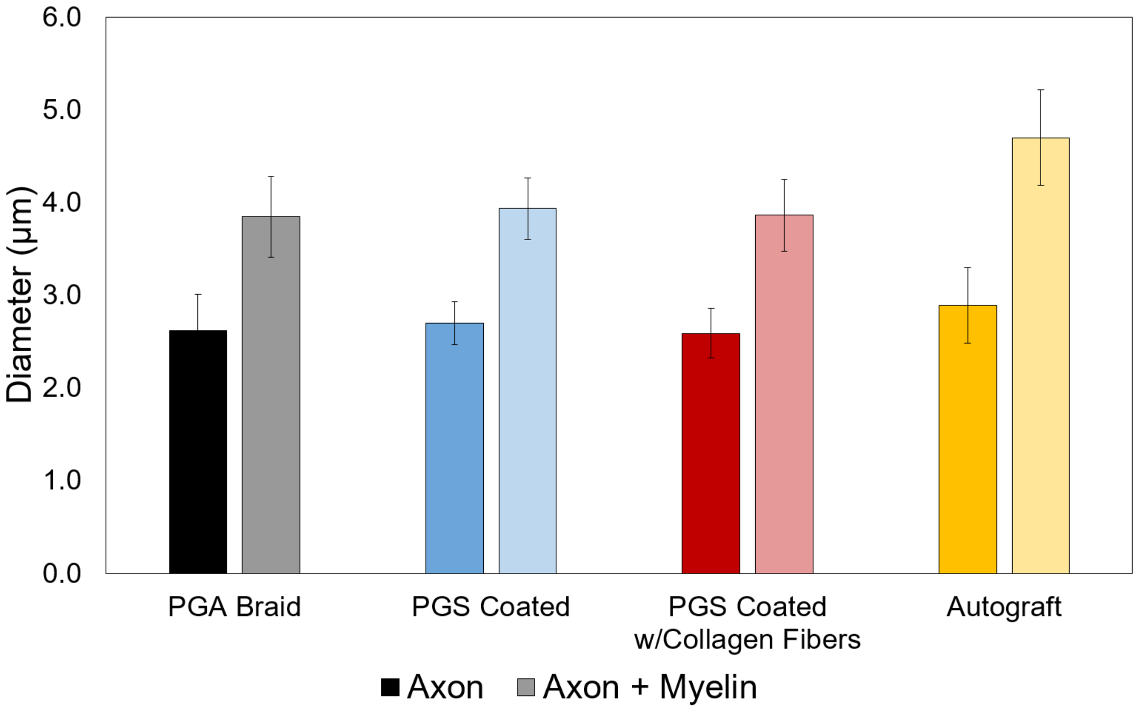

Figure 4-25: Calibers of axons with and without myelin layer inclusion for nerve guide groups and autograft. Axon diameters were very similar amongst all nerve guide groups with autograft being slightly higher as expected from the axon cross section area data. Myelin thickness for nerve guide groups were similar at 0.61 to 0.64 µm which were lower than the myelin thickness of autograft groups that averaged 0.90 µm.

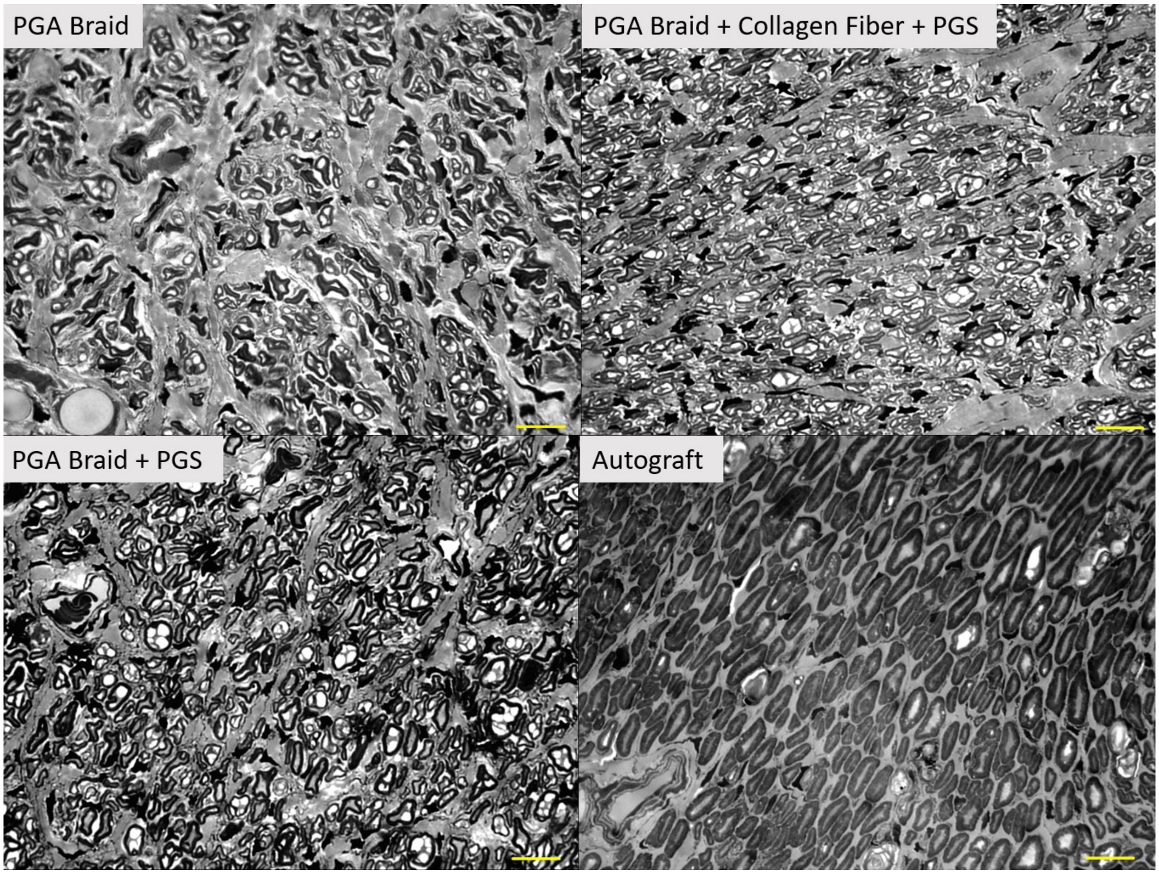

Figure 4-26: Higher magnitude histology of nerve guide groups and myelin. Representative images showing myelin sheath more prominent in the autograft group with little scar tissue formation. Minimal scar tissue was seen in the two PGS coated groups but there did appear to be more scar tissue formation in the PGA braid. Scale bar: 10 µm.

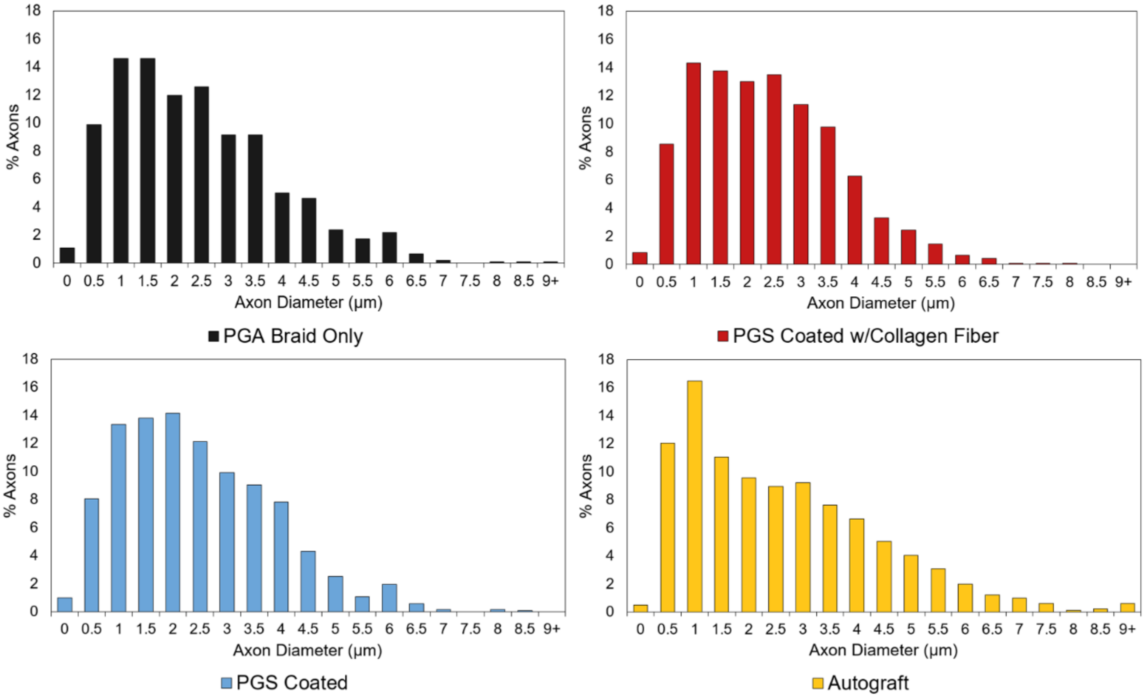

Figure 4-27: Distribution of axon diameters for nerve guide groups and autograft. Higher spread of axon diameters was seen in the autograft relative to the nerve guide group with the autograft having the highest population of axons with diameters of 4 µm or larger with 24.6% of the axons having diameters in this range. Nerve guide groups only had at maximum 18.6%, in the PGS coated nerve guide group, of axons 4 µm or larger.

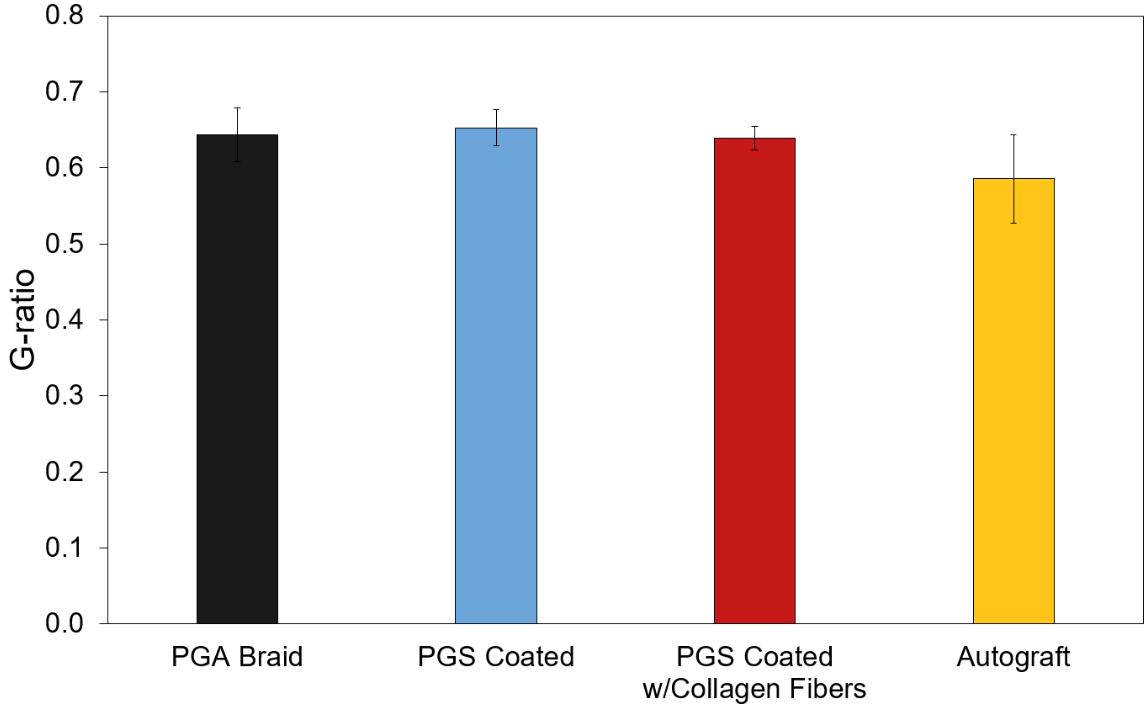

Figure 4-28: Myelin sheath g-ratio measurements. The ratio of axon diameter to axon + myelin layer diameters, or g-ratio, highly consistent in the nerve guide groups at values of 0.64, 0.65, and 0.64 for uncoated, PGS coating, and PGS coating with collagen fiber filling the lumen respectively. The autograft g-ratio was lower at 0.59 due to the overly thick myelin visible in the histological sections. All groups were similar to the typical healthy nerve g-ratio of 0.6.

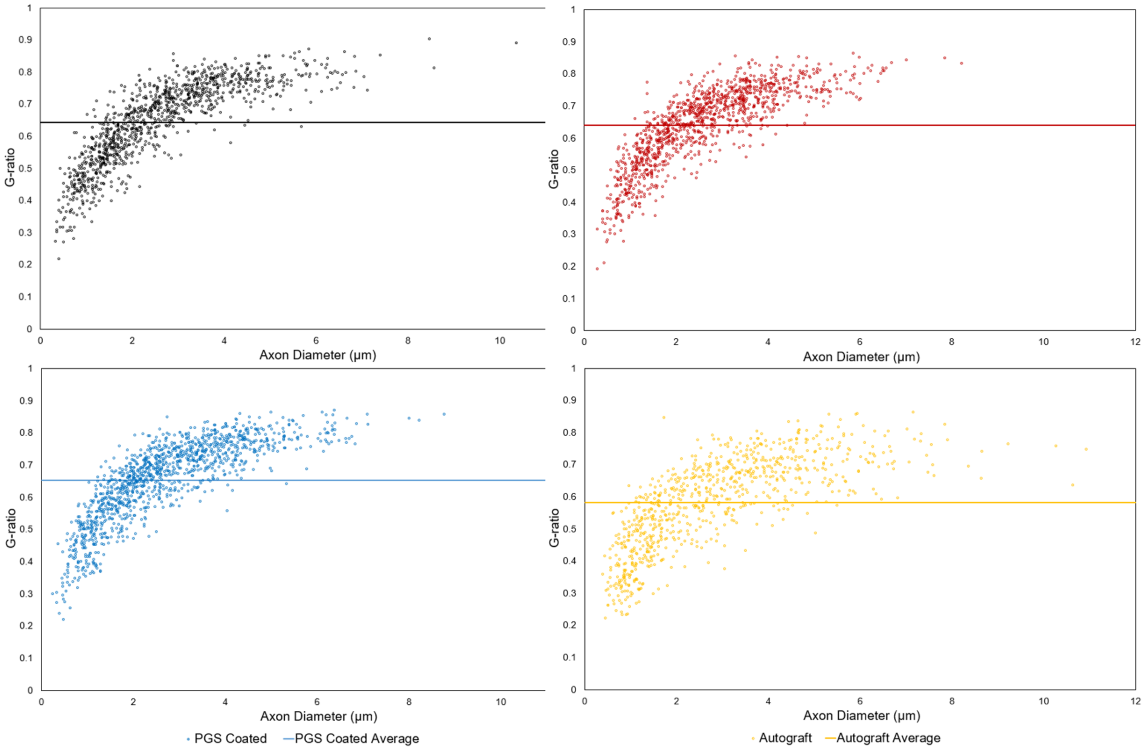

Figure 4-29: Distribution of g-ratios and axon diameters. Thinner myelin sheaths were found as axon diameter increased for all groups as indicated by the increase in g-ratio (top left: uncoated, top right: PGS coating w/collagen fibers, bottom left: PGS coating only, bottom right: autograft). Data spread of the distribution was similar in the three nerve guide groups while much more variation and spread was seen in the autograft distribution, lowering the average g-ratio for the autograft.

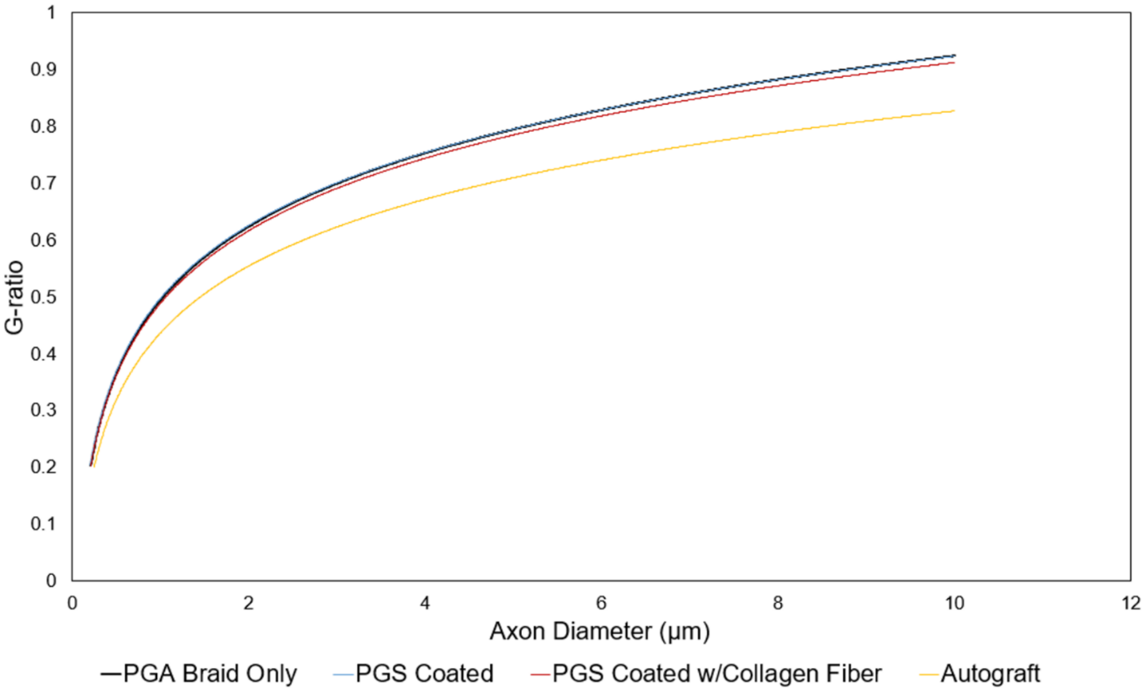

Figure 4-30: Logarithmic fit of G-ratio - axon diameter distribution. Curve fits of the distribution from Figure 4.29 shows clear separation of the autograft distribution profile from the nerve guide groups.

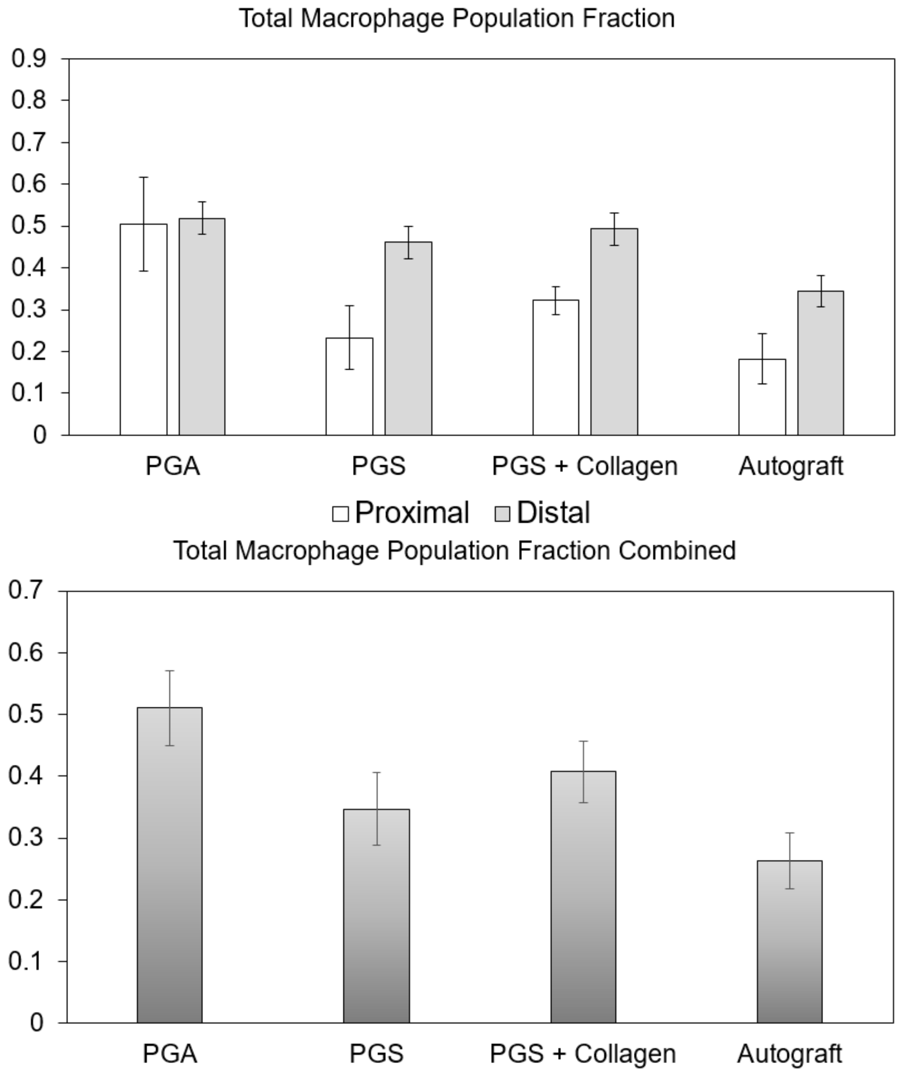

Figure 4-31: Total macrophage population in proximal and distal sections of nerve guide groups. The number of CD68$^+$ cells co-stained with DAPI were compared against the total number of cells in proximal and distal sections of explanted proximal and distal nerve stumps after seven days implantation. In all cases but the uncoated braid, which had the highest overall macrophage activity, the distal regions showed elevated macrophage activity relative to the proximal region.

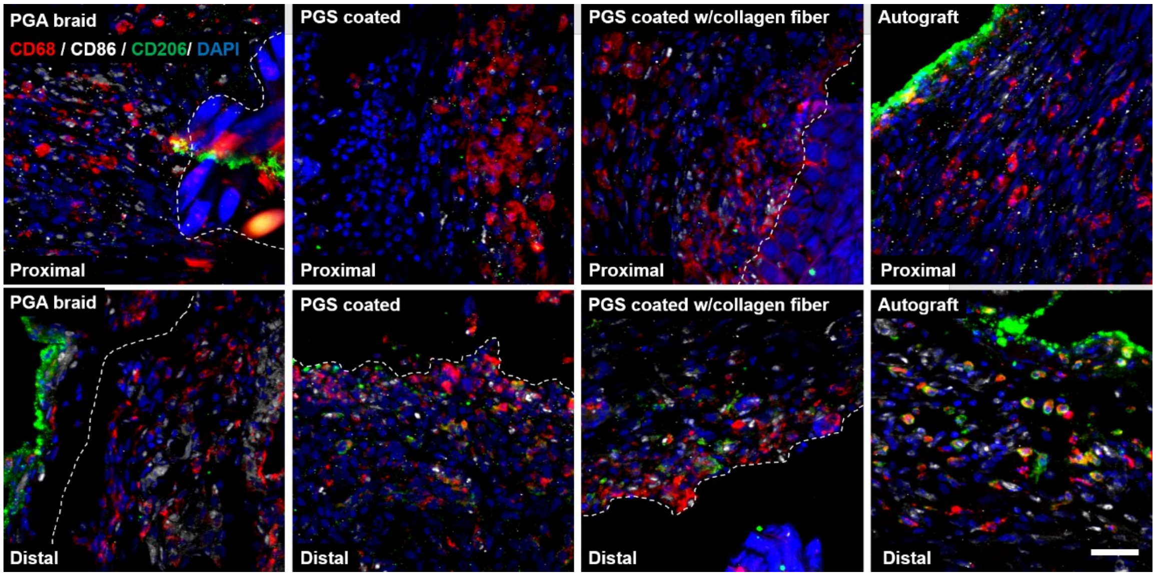

Figure 4-32: Immunostaining of representative proximal and distal cross section slices after 7d. Macrophages (CD68) in proximal and distal sections for all implanted groups after seven days shows highest presence of M2 macrophages (CD206) most localized at the surface of the grafts, particularly with the autograft. M1 macrophages (CD86) more uniformly spread throughout nerve tissue. Scale bar: 30 µm.

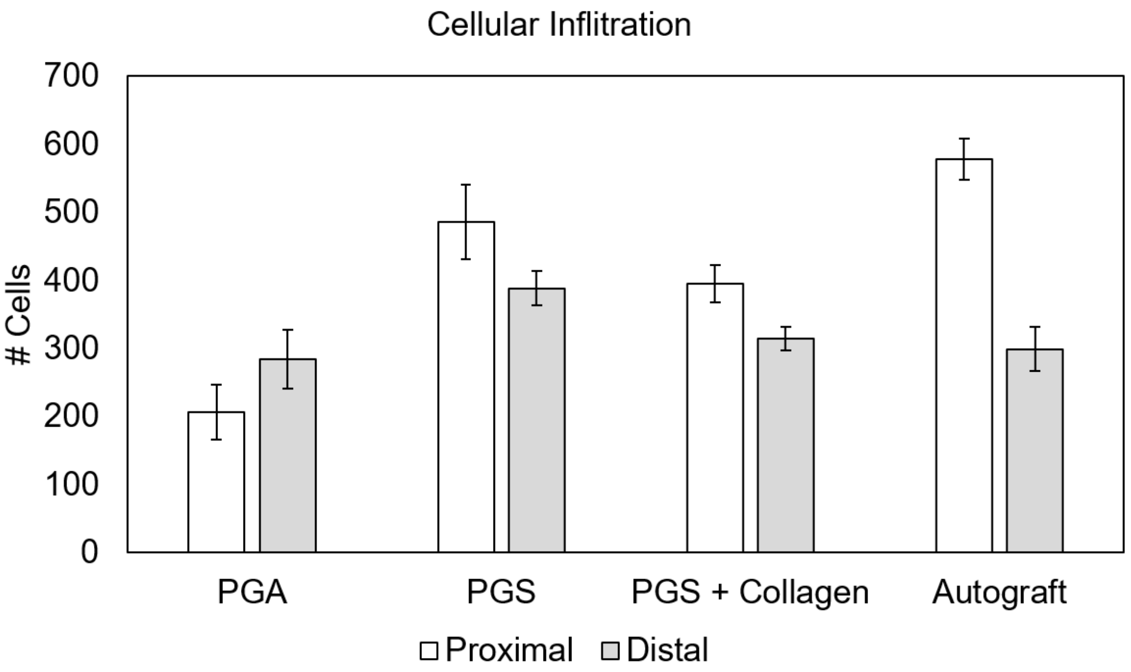

Figure 4-33: Aggregate cellular infiltration into proximal and distal nerve stump regions. Cellular infiltration trended towards being slightly higher in the proximal region, particularly in the case of the autograft. The only exception to this trend was the uncoated PGA braid. This datum is important to correlate with the total macrophage population data graphs of Fig. 4.31 for the autograft because while there were a higher proportion of macrophages infiltrating the distal regions, the total number of cells were lower so similar absolute macrophage population numbers would be present in both the proximal and distal end. With smaller differences in cell population in distal vs proximal nerve stumps for the nerve guide groups, the distal regions still have higher absolute macrophage counts (Fig. 4.33).

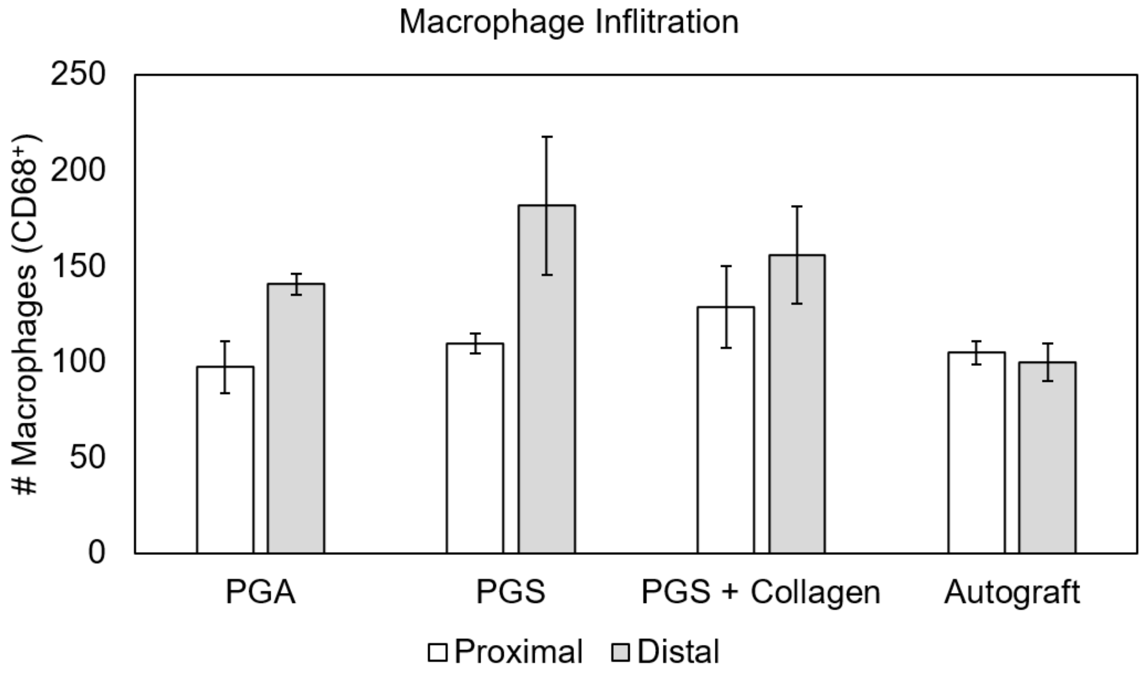

Figure 4-34: Absolute macrophage infiltration into proximal and distal stumps. Autograft shows similar levels of macrophage at either stump. All nerve guide groups show higher levels of macrophage in the distal regions.

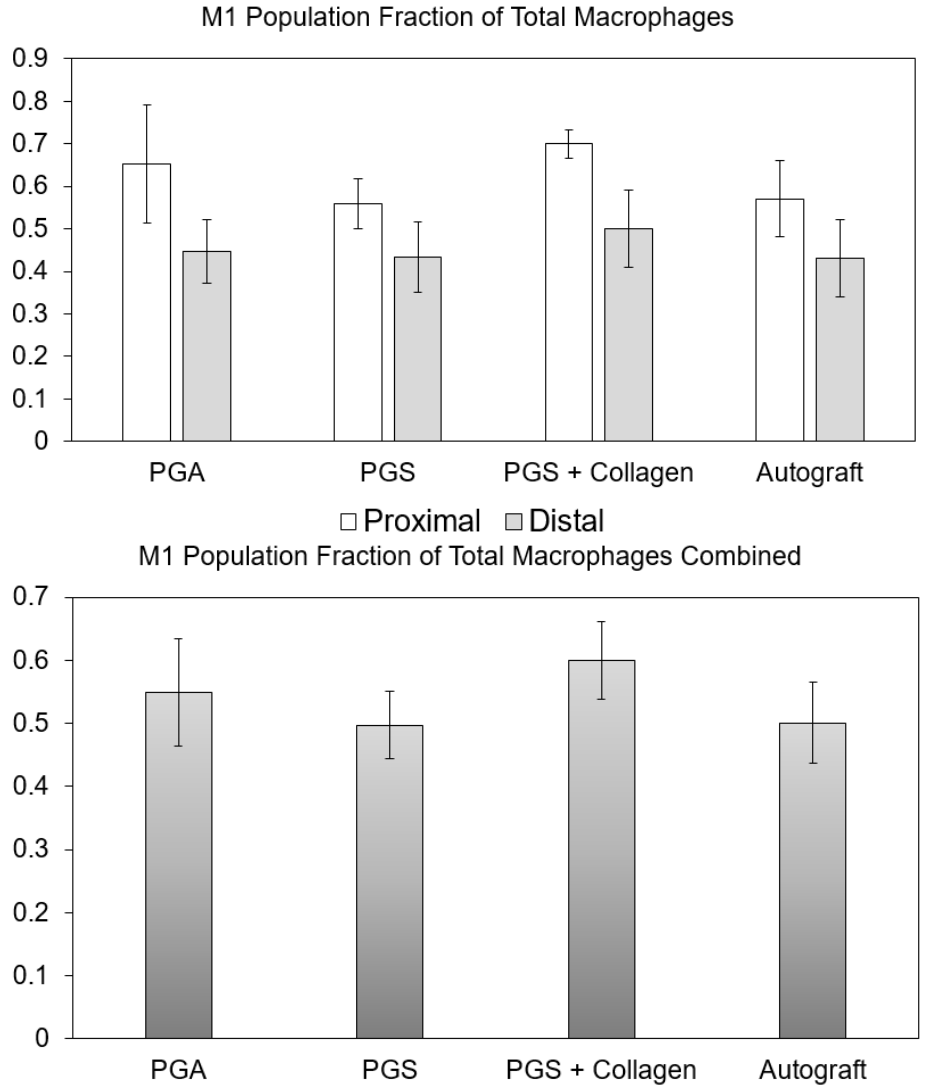

Figure 4-35: M1 subpopulation of macrophages in proximal and distal regions. Proximal regions showed higher proportions of pro-inflammatory macrophages compared to distal nerve stumps (top). When combining proximal and distal data, similar overall proportions of M1 subpopulation macrophages were seen in the PGS coated group and autograft while the uncoated group and collagen fiber group had slightly elevated M1 proportions (bottom).

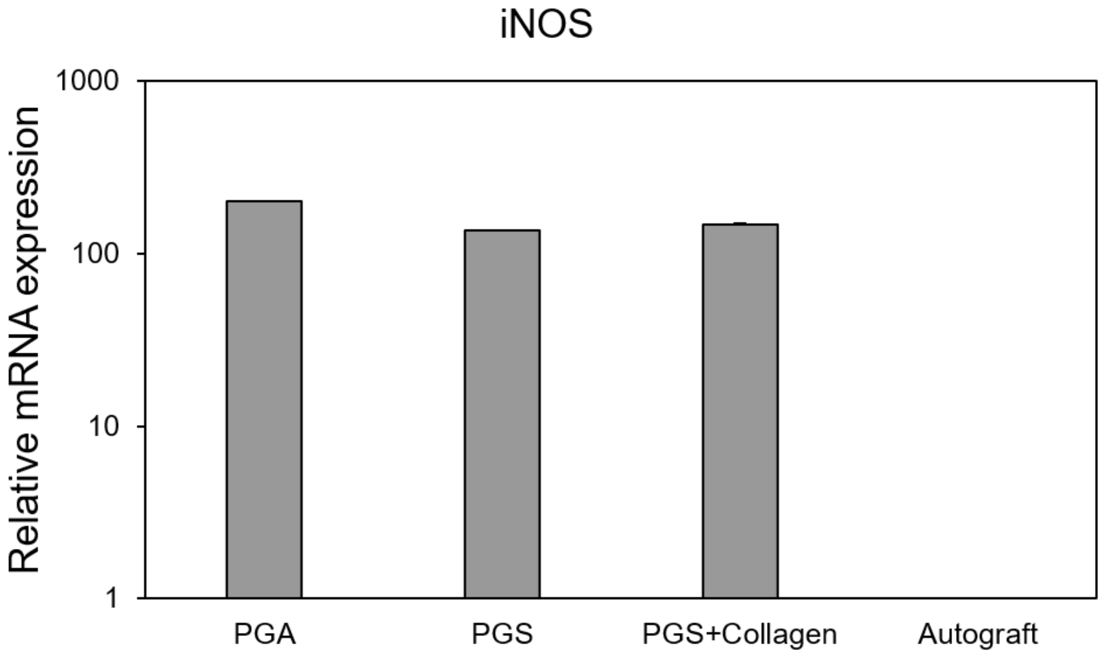

Figure 4-36: Expression increase of iNOS after seven days in nerve guide groups. All three nerve guide groups show at least 100-fold increases in iNOS expression compared to the autograft.

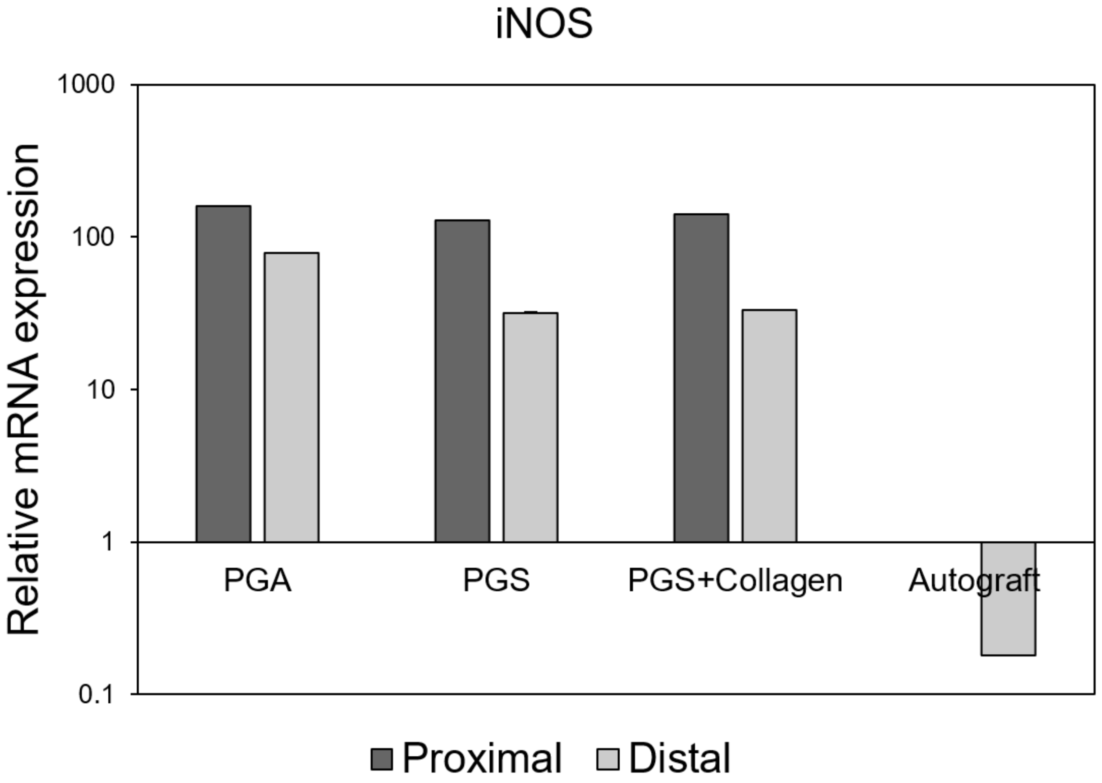

Figure 4-37: Increase of iNOS expression in proximal regions after seven days. All four groups show increases in iNOS expression in proximal nerve stumps compared to the distal.

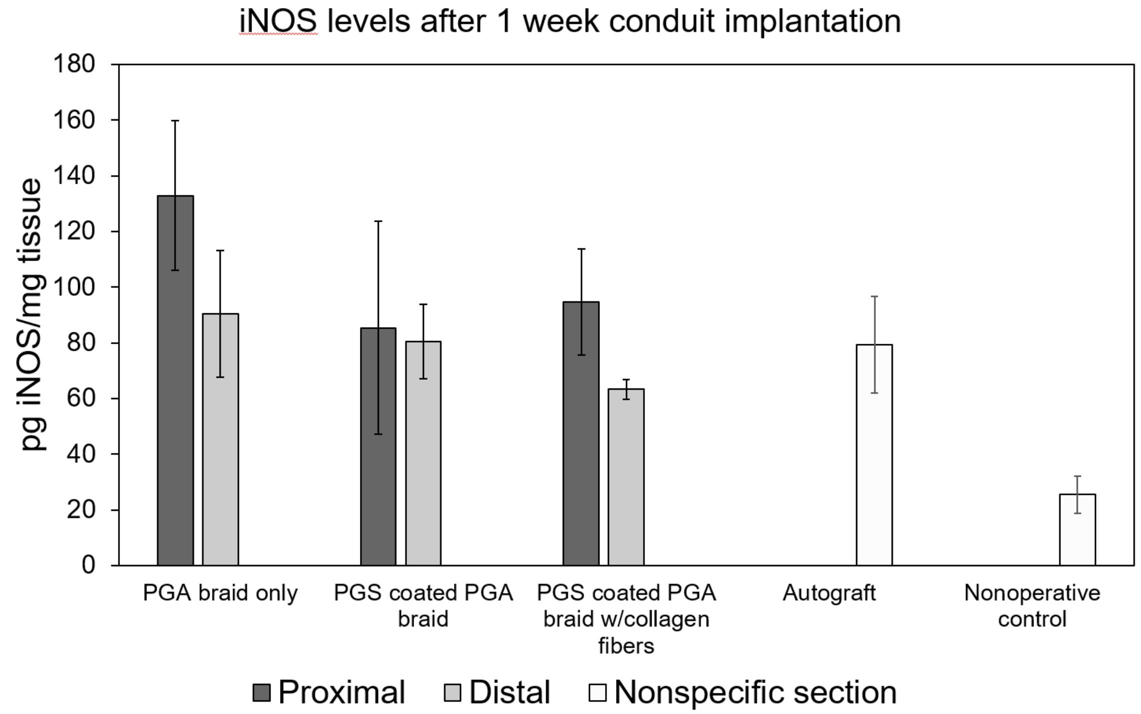

Figure 4-38: ELISA of tissue homogenate to measure iNOS levels in proximal and distal nerve stumps. Quantification of iNOS levels via ELISA match the results seen with the PCR analysis of mRNA expression in regard to the comparative behavior between groups and their proximal vs distal behavior. The non-operative control shows background levels of iNOS much lower than the nerve guide groups and autograft.

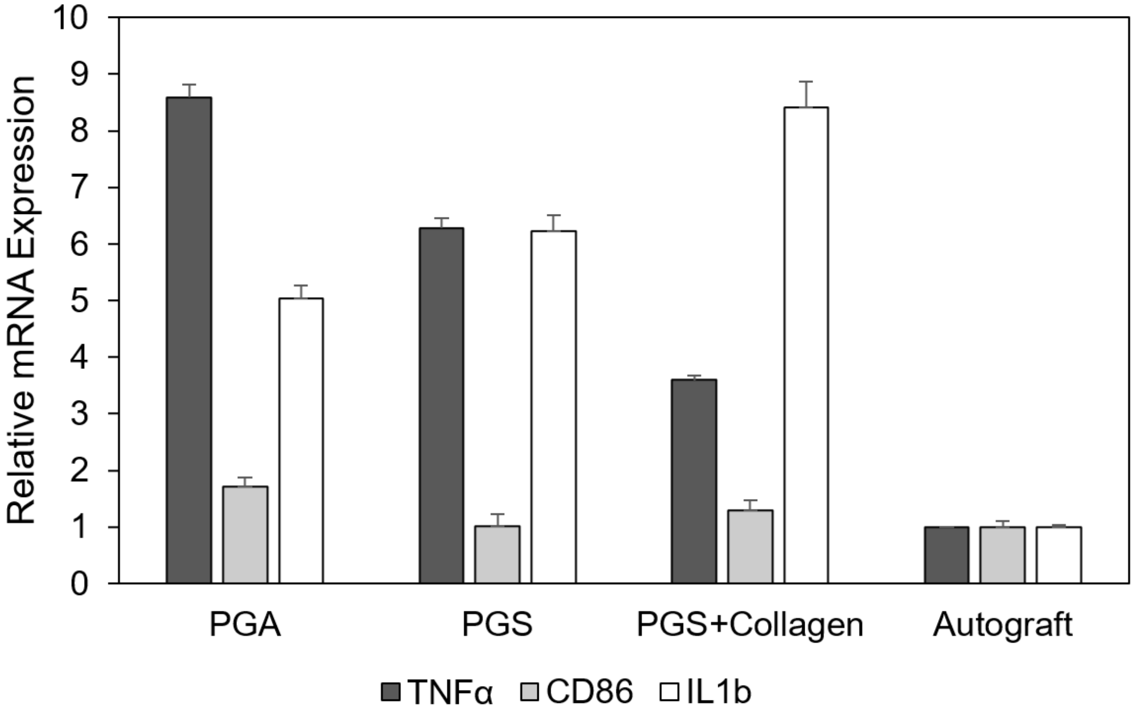

Figure 4-39: M1 macrophage marker mRNA expression of TNFα, CD86, and IL-1b after seven days. PGS coating resulted in reduced expression of TNFα but increased expression of IL-1b. CD86 expression as relatively low in all nerve guide groups, showing very small fold difference from the mRNA expression in the autograft.

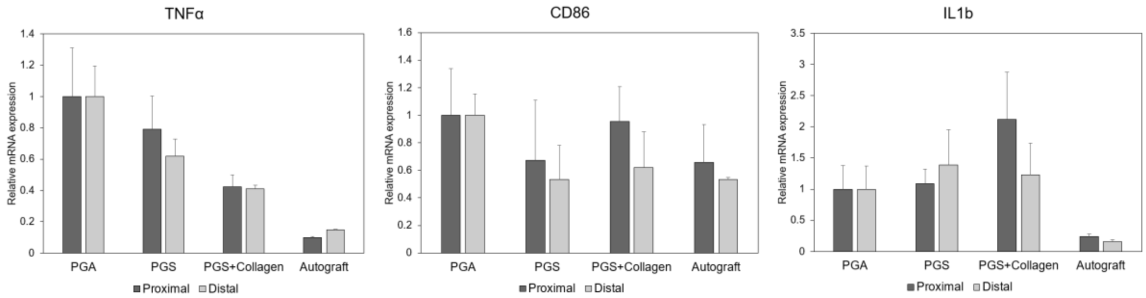

Figure 4-40: Proximal and distal M1 macrophage marker mRNA expression for TNFα, CD86, and IL-1β. Little difference was seen comparing the proximal and distal nerve stump mRNA expression for TNFα, CD86, or IL-1β due to the low fold differences measured with qPCR.

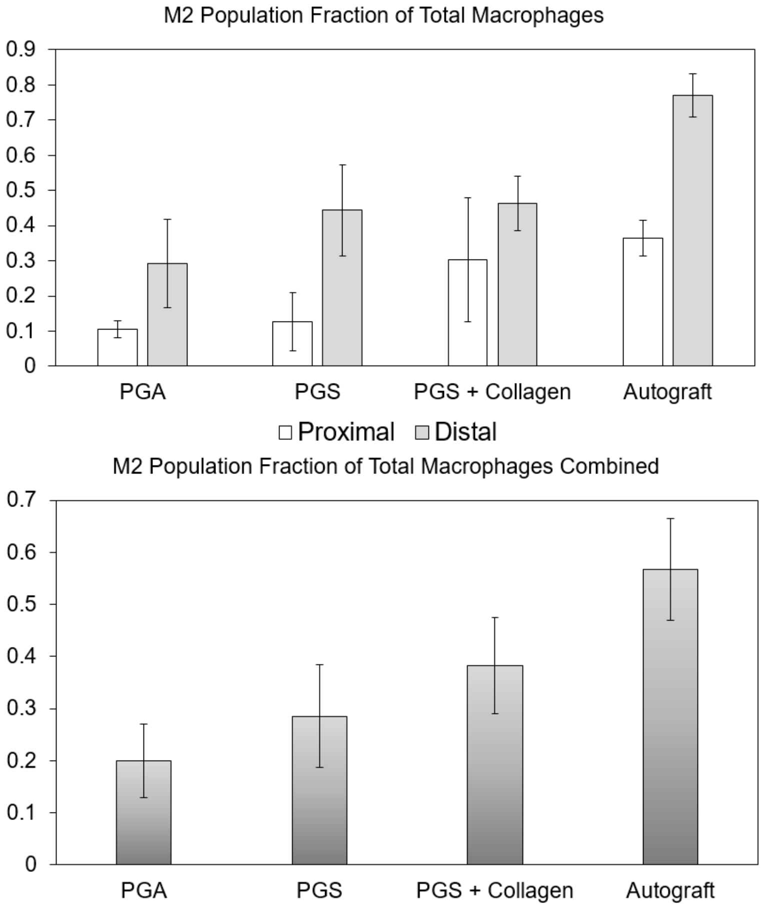

Figure 4-41: Increased M2 subpopulation present in PGS coated nerve guide groups compared to uncoated NGCs. All study groups showed a noticeable increase in pro-healing M2 macrophage subpopulation fractions in the distal region when compared to the proximal (top). Increases in relative M2 populations were seen with PGS coated nerve guide groups (bottom) although these still fell short of the autograft.

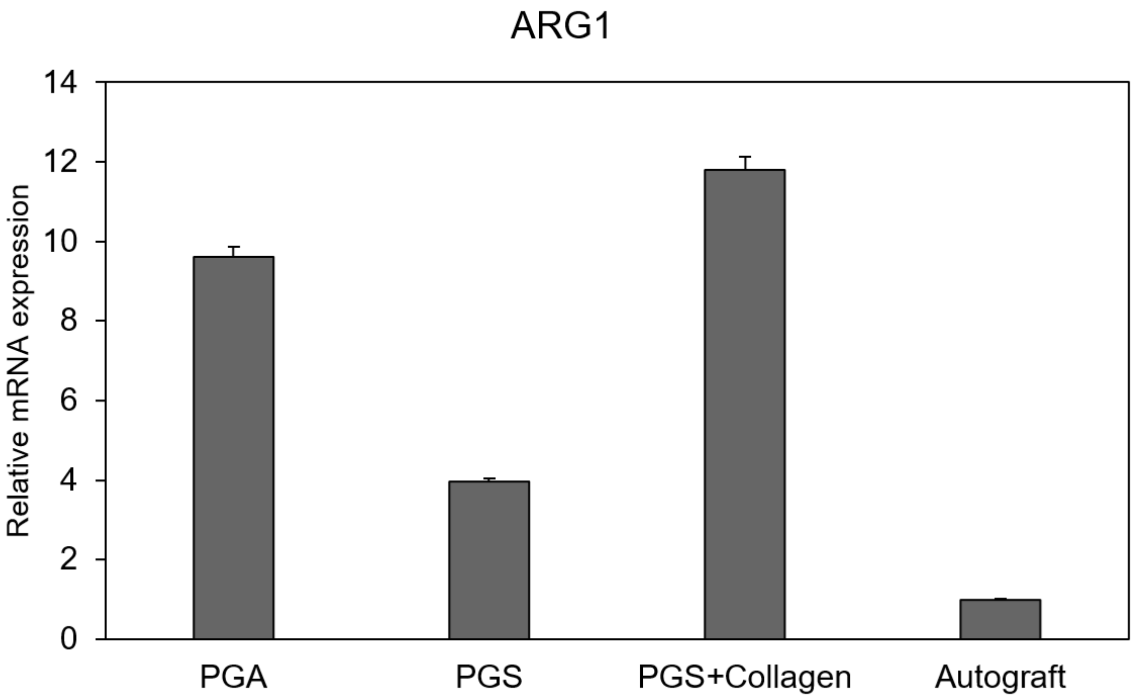

Figure 4-42: Higher levels of ARG1 expressed in PGS coated nerve guides containing collagen fibers as measured by qPCR. All three nerve guides showed higher expression levels of ARG1 after seven days implantation relative to the autograft.

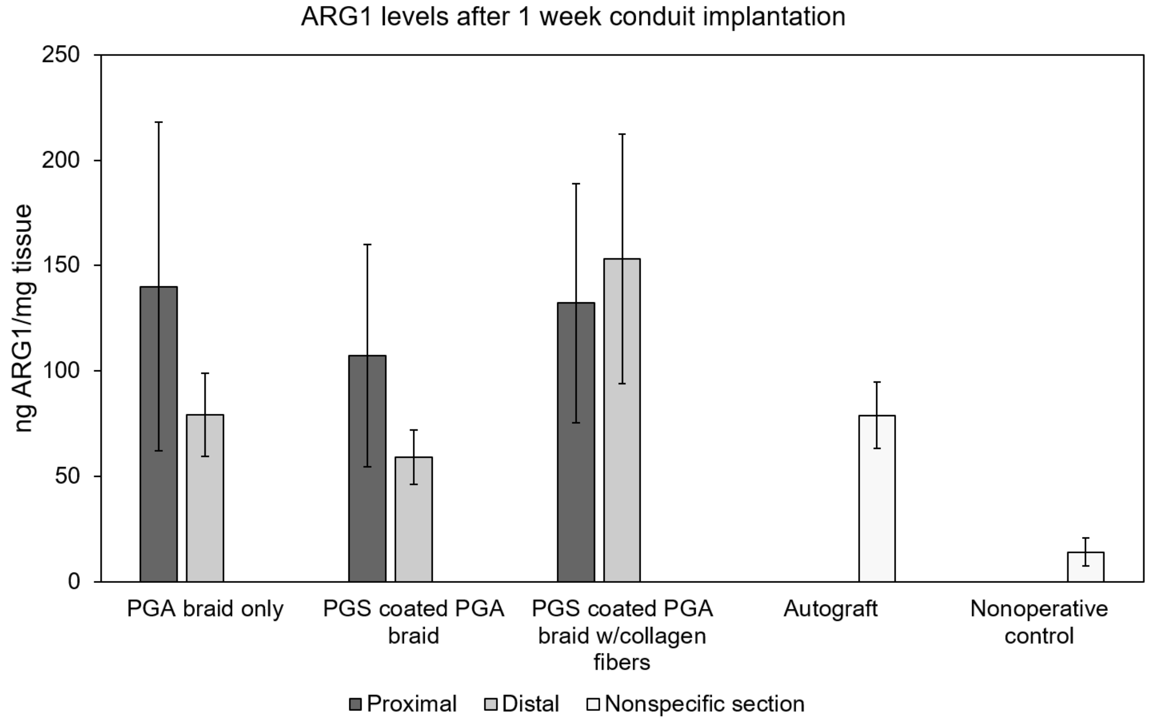

Figure 4-43: ELISA of tissue homogenate to measure ARG1 levels in proximal and distal nerve stumps. Quantification of ARG1 levels via ELISA show mixed results where only small differences were seen between groups due to the large variation present in the proximal cytokine levels of ARG1 detected. While it is difficult to determine differences between nerve guide groups on ARG1 expression, all three nerve guides and autograft show significant increases in ARG1 levels compared to the non-operative control.

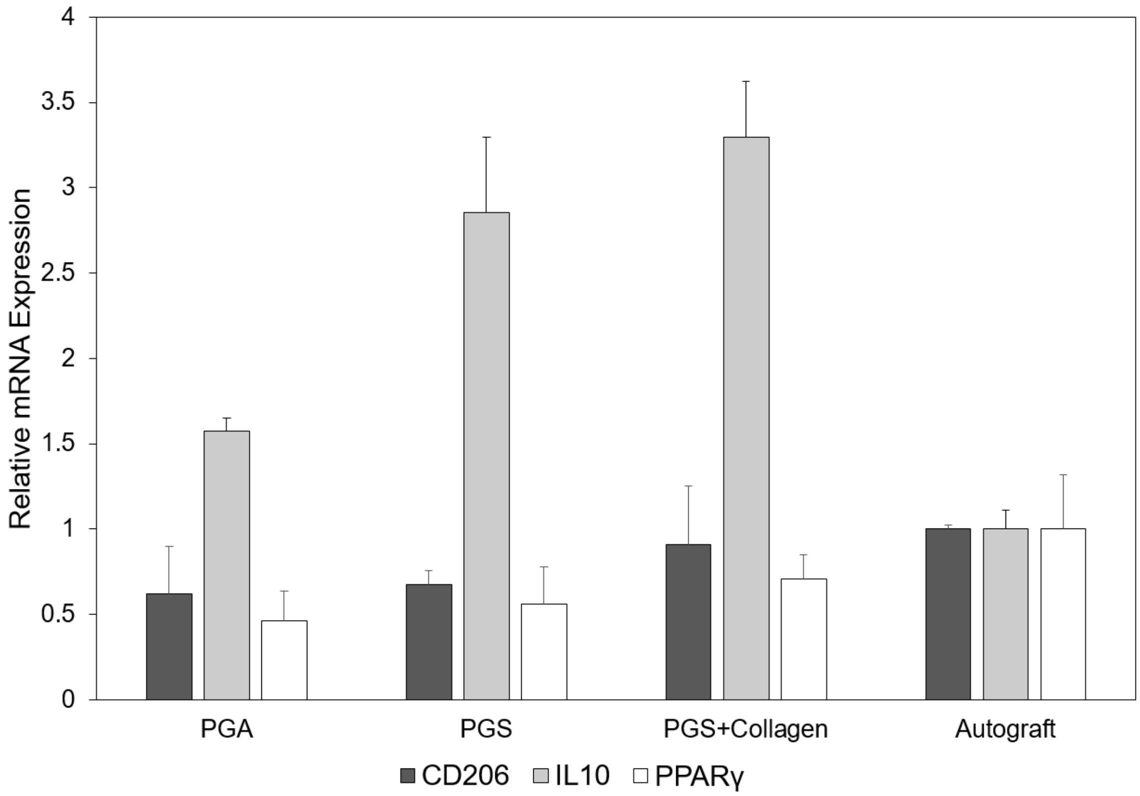

Figure 4-44: M2 macrophage marker mRNA expression of CD206, IL-10, and PPARγ after seven days. Expression of CD206 was similar amongst all groups with very low fold differences seen. Highest variation in mRNA expression occurred with IL-10 expression, where PGS coated groups upregulated expression of the cytokine by several-fold. Like CD206, PPARγ expression was similar throughout all nerve guide designs implanted and the autograft.

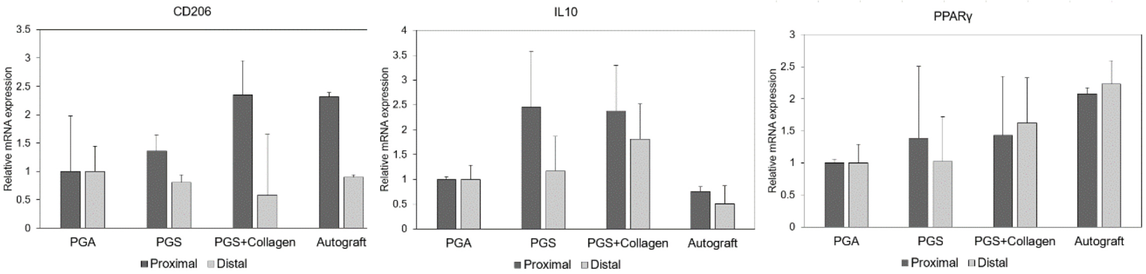

Figure 4-45: Proximal and distal M2 macrophage marker mRNA expression for CD206, IL-10, and PPARγ. Expression of M2 markers were generally decreased at the distal end relative to proximal for CD206 and IL-10. PPARγ expression had high variation in PGS coated nerve guides and had similar levels in both the proximal and distal nerve stumps.

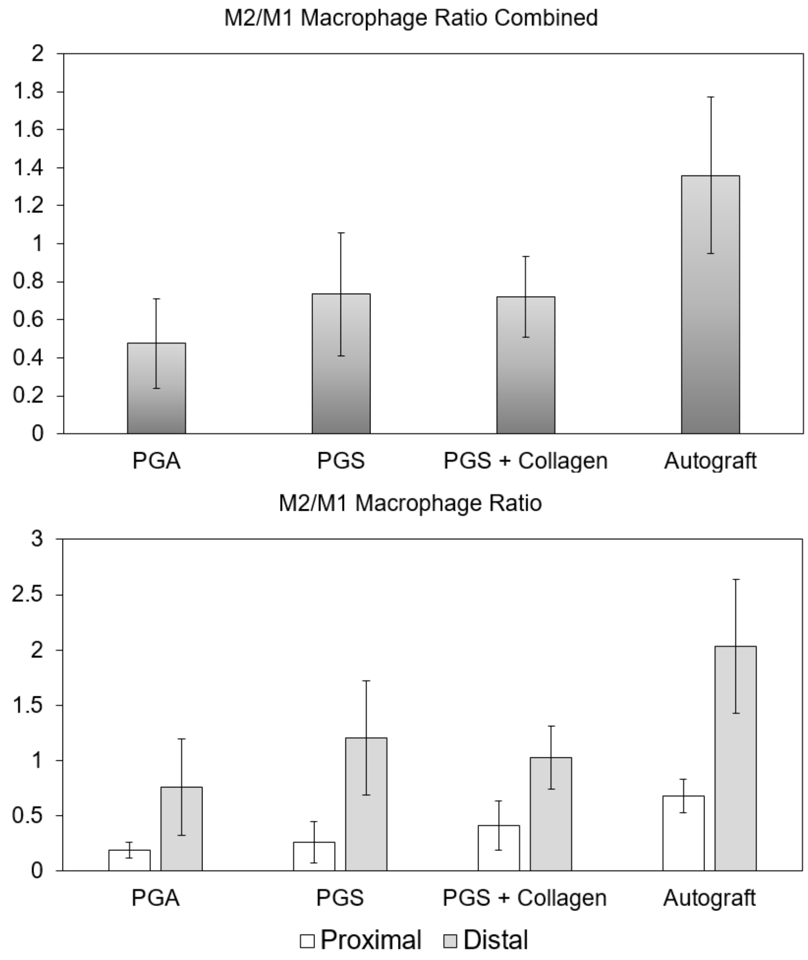

Figure 4-46: Relative inflammatory environment of NGCs given by M2/M1 ratio. PGS coating provided a similar M2/M1 ratio environment that was biased towards M1 macrophage phenotype with an M2/M1 ratio value of 0.73 without collagen fibers and 0.72 with. The lack of PGS coating further biased the macrophage phenotype towards M1 with an M2/M1 ratio of 0.47 for that group. Only the autograft was highly biased towards M2 with a ratio of 1.36 (top). Distal nerve stumps in all cases were biased more towards M2 than the proximal sides.

4.6 References

1. Bozkurt A, et al., *The role of microstructured and interconnected pore channels in a collagen-based nerve guide on axonal regeneration in peripheral nerves.,* in *Biomaterials*. 2012. p. 1363–1375.
2. Dubey N, et al., *Guided neurite elongation and Schwann cell invasion into magnetically aligned collagen in simulated peripheral nerve regeneration.,* in *Exp Neurol.,* 1999. p. 338–350.
3. Song J, et al., *Polymerizing Pyrrole Coated Poly (l-lactic acid-co-ε-caprolactone) (PLCL) Conductive Nanofibrous Conduit Combined with Electric Stimulation for Long-Range Peripheral Nerve Regeneration*., in *Front Mol Neurosci.,* 2016. p. 9.
4. Panahi-Joo Y, et al., *Design and fabrication of a nanofibrous polycaprolactone tubular nerve guide for peripheral nerve tissue engineering using a two-pole electrospinning system.,* in *Biomed Mater.,* 2016.
5. Boyd J. *Glial cell line-derived neurotrophic factor and brain-derived neurotrophic factor sustain the axonal regeneration of chronically axotomized motoneurons in vivo., in Exp Neurol.* 2003. p. 610–619.
6. Wood MD, et al., *Fibrin gels containing GDNF microspheres increase axonal regeneration after delayed peripheral nerve repair.*, in *Regen Med.* 2013. p. 27–37.
7. de Boer R, et al., *Short- and long-term peripheral nerve regeneration using a poly-lactic-co-glycolic-acid scaffold containing nerve growth factor and glial cell line-derived neurotrophic factor releasing microspheres.,* in *J Biomed Mater Res A.,* 2012. p. 2139–2146.
8. Ma Z, et al., *Critical Period of Axoglial Signaling between Neuregulin-1 and Brain-Derived Neurotrophic Factor Required for Early Schwann Cell Survival and Differentiation.*, in *J Neurosci*. 2011. p. 9630–9640.
9. Kempton LB, et al., *Assessment of Axonal Growth into Collagen Nerve Guides Containing VEGF-Transfected Stem Cells in Matrigel.,* in *Anat Rec Adv Integr Anat Evol Biol.* 2009. p. 214–224.
10. Georgiou M, et al., *Engineered neural tissue with aligned, differentiated adipose-derived stem cells promotes peripheral nerve regeneration across a critical sized defect in rat sciatic nerve.,* in *Biomaterials.* 2015. p. 242–251.
11. Heine W, Conant K, Griffin J, Hoke A. *Transplanted neural stem cells promote axonal regeneration through chronically denervated peripheral nerves.,* in *Exp Neurol.* 2004. p. 231–240.
12. Leipzig ND, Shoichet MS. *The effect of substrate stiffness on adult neural stem cell behavior.,* in *Biomaterials.* 2009. p. 6867–6878.
13. Christopherson GT, Song H, Mao H-Q. *The influence of fiber diameter of electrospun substrates on neural stem cell differentiation and proliferation.,* in *Biomaterials.* 2009. p. 556–564.

14. Leong WS, et al., *Cyclic tensile loading regulates human mesenchymal stem cell differentiation into neuron-like phenotype.,* in *J Tissue Eng Regen Med.* 2012. p. s68–s79.
15. Akassoglou K, et al., *Fibrin inhibits peripheral nerve remyelination by regulating Schwann cell differentiation.,* in *Neuron.* 2002. p. 861–875.
16. Akassoglou K, et al., *Fibrin is a regulator of Schwann cell migration after sciatic nerve injury in mice.,* in *Neurosci Lett.* 2003. p. 185–188.
17. Liang Y, Walczak P, Bulte JWM. *The survival of engrafted neural stem cells within hyaluronic acid hydrogels.*, in *Biomaterials.* 2013. p. 5521–5529.
18. Sundback C, et al., *Biocompatibility analysis of poly(glycerol sebacate) as a nerve guide material.* in *Biomaterials.,* 2005. p. 5454–5464.
19. Wang Y, et al., *A tough biodegradable elastomer.,* in *Nat Biotechnol.* 2002. p. 602–606.
20. Kim MJ, et al., *Biodegradable and Elastomeric Poly(glycerol sebacate) as a Coating Material for Nitinol Bare Stent.*, in *BioMed Res Int.* 2014. p. 1–7.
21. Pomerantseva I, et al., *Degradation behavior of poly(glycerol sebacate).,* in *J Biomed Mater Res A.* 2009. p. 1038–1047.
22. Cattin A-L, et al., *Macrophage-Induced Blood Vessels Guide Schwann Cell-Mediated Regeneration of Peripheral Nerves.,* in *Cell.* 2015. p. 1127–1139.
23. Dubový P. *Wallerian degeneration and peripheral nerve conditions for both axonal regeneration and neuropathic pain induction.,* in *Ann Anat - Anat Anz.* 2011. p. 267–275.
24. Niemi JP, et al., *A Critical Role for Macrophages Near Axotomized Neuronal Cell Bodies in Stimulating Nerve Regeneration.,* in *J Neurosci.* 2013. p. 16236–16248.
25. Ydens E, et al., *Acute injury in the peripheral nervous system triggers an alternative macrophage response.,* in *J Neuroinflammation.* 2012. p. 176.
26. Mokarram N, et al., *Effect of modulating macrophage phenotype on peripheral nerve repair. Biomaterials.,* 2012. p. 8793–8801.
27. Rushton WAH. *A theory of the effects of fibre size in medullated nerve.,* in *J Physiol.* 1951. p. 101–122.

Chapter 5 In Vivo Study of Fibrin-Collagen Hydrogel Fiber Based Nerve Guides to Promote Peripheral Nerve Regeneration

5.1 Background

5.1.1 Use of fibrin and collagen in nerve guide design

Fibrin and collagen hydrogel fibers loaded in the luminal space of the NGCs provide physical guidance for infiltrating SCs instead of the disorganized fibrin clot that forms within commercially available hollow NGCs following implantation. The relatively rapid proteolytic degradation of fibrin *in vivo* is advantageous by generating additional porosity as the bulk of the growth cone advances through the conduit. Collagen promotes cellular attachment as it makes up the bulk of the nerve basal lamina but is less rapidly degraded *in vivo*, resulting in a more persistent material choice for neurotrophic factor loading [1]. By using these two fiber types, the duration of the contact guidance and temporal porosity present to the cells can be modulated for short- and long-term effects. Specific integrin based signaling effects will be triggered using naturally derived collagen and fibrin that are not possible with synthetic fibers such as poly(caprolactone) or poly(lactide-co-glycolide). The ability to induce phosphorylation of ERK1/2 by fibrin thus enabling SC to re-enter the cell cycle and proliferate are added advantage of choosing such materials as these for luminal fillers [2, 3].

Fibrin has frequently been used for nerve regeneration in a variety of ways including use as a 3D gel for endometrial stem cell derived neurons [4], a depot for GDNF containing microspheres [5], as a conduit itself [6]. Fibrin is frequently used as a surgical glue and even this version of the material has been used for enhancing peripheral nerve regeneration [7-9]. Collagen has been investigated for peripheral nerve regeneration including as a platform for containing VEGF transfected stem cells [10], along a long gap using laminin coated collagen fibers and filaments within a PGA-collagen tube [11, 12], and as a composite with chitosan [13]. Collagen has been used as a protective outer conduit with clinical success [14, 15]. The structure of collagen has been engineered to contain oriented longitudinal pores [16] or to release GDNF and NGF [17].

5.1.2 Gradient platform modification and development

Preparation of gradients were developed using a modified version of the diffusible gradient platform developed by Kellin Krick as presented in his dissertation (May 2016, Johns Hopkins University Department of Biomedical Engineering) which were based on concepts developed in collaboration with the Khademhosseini lab [18, 19]. Gradient developments in the previous work were based on using cast random collagen gels of thinner widths (3-5 mm) than the electrospun collagen fiber sheets (10 mm) but similar lengths of material at ~10 mm. The original system consisted of a PDMS channel with a single source inlet and single sink inlet. While a single inlet worked well for the narrow collagen gels used in the process development, attempts at using single pairs of source and sinks led to poor gradient quality due to the lateral diffusion that occurred from the central position of the inlets. To alleviate this, two additional inlets were added to each of the source and sink sides so that gradients could be prepared using, in essence, a triplet set of gradient channels.

5.2 Methods

5.2.1 Rat sciatic nerve defect repair model and study overview using electrospun hydrogel microfibers

As the investigation of PGS coated PGA braids as a nerve guide showed beneficial effects in the studies of Chapter 4, we were determined investigate the potential addition of electrospun hydrogel fibers as a technique to further enhance nerve repair. To do this, a collaboration was formed with SYSU in Guangzhou, China to investigate PGS nerve guides containing combinations of fibrin filaments, collagen fiber sheets, and growth factor loading in a 17 mm Sprague Dawley rat critical gap sciatic nerve defect model. Specifically, nerve guide groups consisted of: 1) Empty PGS coated braids for comparison and confirmation of results from the previous *in vivo* study, 2) unloaded 8 layer collagen sheet only, 3) unloaded collagen sheet with 100 µm hydrated diameter fibrin filaments, 4) collagen sheet containing 500 ng GDNF with fibrin filaments, 5) collagen sheet containing a shallow gradient of 2500 ng/ml/cm steepness with fibrin filaments and 6) collagen sheet containing a steeper gradient of 16,666 ng/ml/cm steepness with fibrin filaments. All six of these groups were compared against the autograft after 2, 4, 8, and 12 weeks post implantation for cellular infiltration and functional recovery (Fig. 5.1). All groups containing fibrin filaments were filled with 60 filaments. This is a higher filament count than the 20 collagen filaments used in the previous Secant in vivo study in order to provide increased surface area for topographical alignment as that initial study showed such few filaments having small impact on regenerative outcome.

5.2.2 Preparation and growth factor loading of fibrin-collagen composite nerve guides

Electrospun fibrin filaments were prepared as described in Chapter 2 to a dry diameter of 30 µm so that upon loading into the PGS coated PGA braid (Fig. 5.2), the swelling degree would fill approximately 95% of the luminal cross sectional area once implanted when the fibrin filaments hydrate to 100 µm diameters (Fig. 5.3). Collagen fiber sheets were also prepared as described in Chapter 2 for the purpose of providing to a platform for loading and release of GDNF and as a secondary source of topographical guidance cues for infiltrating neuronal cells. Collagen sheet dry thickness of 60 µm was prepared by wrapping 8 layers of EDC crosslinked collagen fiber sheets followed by drying in a laminar flow hood after an overnight soak in DI water to remove residual urea from the EDC reaction. Collagen sheets were loaded with GDNF via two differing methods based on whether gradient or uniform loading was needed. Uniform GDNF loading of 500 ng sheet was done by taking the dried collagen sheets and applying 500 ng of GDNF in 30 µl DI and allowing the sheet to rehydrated with this solution and dry again within the laminar hood. GDNF was freshly prepared from lyophilized stock before usage so no stabilizers such as bovine serum albumin.

Gradients of GDNF were loaded into the collagen fiber sheets at both a shallow and steep gradient steepness while maintaining a total loading of 500 ng GDNF per sheet. Initial preparation for both gradient steepness included initial rehydration of the collagen fiber sheets within the PDMS mold chamber by adding 10 μl DI water into each of the three source wells and three sink wells for a total rehydration volume of 60 μl. This is to ensure that the gradient is formed in a controlled manner via diffusion rather than being soaked up by the collagen sheets during rehydration. The shallow gradients with a steepness of 2500 ng/ml/cm were then prepared by adding 10 μl of 7.0 μg/ml GDNF in each of the three sink wells followed by addition of 10 μl of 9.5 μg/ml GDNF in each of the three source wells. Steep gradients were prepared to a steepness of 16,666 ng/ml/cm by loading each of the three sink wells with 10 μl of DI water and each of the three source wells with 10 μl of 16.7 μg/ml GDNF. The plastic frames used for collagen fiber sheet collection were marked with a dot on the high concentration end of the frame prior to sheet collection to keep track of gradient orientation in the sheet during later manipulation to load sheets into the PGS coated PGA braid. Gradients were allowed to form over four hours before the collagen sheets were removed from the PDMS mold and air dried under laminar flow.

5.2.3 Hydrogel fiber loading into PGS coated nerve guide luminal space

Dried collagen fiber sheets were loaded into the PGS nerve guides in the following manner. First, collagen sheets were carefully cut free from the plastic frames using a razor blade, taking particular care with the gradient loaded sheets to keep track of the gradient orientation. Sheets were then carefully folded in half and placed over the top of three taped down 7-0 nylon or 6-0 plain gut sutures. The folding of collagen fiber sheet is an important step for loading into the nerve guide as this “twins” the sheet layers providing additional surface area for topographical guidance and eases the loading of the collagen sheet into the nerve guidance conduit relative to an unfolded sheet. The collagen sheet is then gently and loosely tied along all three suture positions to form an initial tube-like structure with the sheet. It is important to not completely tie the sutures during this step as their purpose is to better control the tie of the suture in the next part of preparation and will need to be later removed (Fig. 5.4a). Once the loose tube is formed, one end of the collagen sheet is tightly tied with the suture, leaving several cm extra length of suture available for pulling through the PGS nerve guide. This extra length of suture is threaded through a small bore sewing needle and tied. As the PGS has some residual tackiness even after curing, there is sometimes risk of the collagen sheet sticking to the walls of the nerve guide midway through being loaded. To alleviate this, the collagen tube can be briefly dipped into 70% EtOH, which acts as a lubricant to improve loading efficiency of the collagen sheet. The needle is drawn through the PGS braid until the tied collagen sheet is just about to enter the nerve guide. At this point, corrections to alignment can be made with a pair of sharp point tweezers and the initial mm or so of the tied end of the collagen sheet can be manually loaded into the nerve guide. Once all alignments and initial partial load are complete, the needle can be carefully pulled until the collagen sheet is completely pulled through the nerve guide. At this point, the needle is cut free along with any residual suture ties (Fig. 5.4b). Centrally located sutures are difficult to reach without disrupting the collagen sheet, so in these cases, the plain gut sutures must be used as they will rapidly degrade upon implantation. The EtOH in the tube is allowed to evaporate and then the completed nerve guides are stored at 4°C until use.

A small variation in conduit preparation must be made when fibrin filaments are to be used as a secondary source of topographical alignment. In this instance, fibrin filaments are placed on top of the folded collagen sheets when those sheets are positioned on top of the tie sutures. When positioned in this way, the fibrin filaments are removed from their collection frames so they are spread across the collagen sheet. When sufficient fibrin filaments are positioned, ~60 filaments in this study, the fibrin sheets are bundled together inside the collagen sheet as it is tied. This combined collagen-fibrin construct can then be loaded into the PGS braided tubes using the same procedures as with the collagen sheets alone.

5.2.4 Examination of implanted nerve guides following 8 weeks implantation

Gross histological examination of nerve guides was made after 8 and 12 weeks implantation in order to visualize the overall structure of regenerating nerve tissue and qualitatively assess the stability of the PGS coated PGA braided tubes containing electrospun hydrogel microfiber materials.

5.2.5 Functional recovery assessment

Assays to characterize regenerative potential include electrophysiological characterization of compound muscle action potential (CMAP) measurements of the signal conduction through the nerve guide. Measurements of functional recovery included muscular atrophy, electrophysiological CAMP measurements, along with histological analysis of axon caliber, myelin thickness, g-ratio, and cellular infiltration. Gait analysis was also conducted using SFI scale.

5.2.6 Gait analysis using Sciatic Functional Index (SFI) after 8 weeks implantation

Functional recovery of the rat sciatic nerve was assessed after 8 weeks using Sciatic Functional Index (SFI) measurements of foot spreading along a walking track for all nerve guide groups for comparison with the autograft at prior to surgery and at 1, 4, 6, and 8 weeks for four animals per group. SFI values were calculated as follows:

$$SFI = (-38.3 * PLF) + (109.5 * TSF) + (13.3 * ITF) - 8.8$$

where PLF is the print-length factor, TSF is toe-spread factor, and ITF is intermediary toe-spread factor.

5.2.7 Histological analysis of implanted nerve guides after 8 weeks implantation

Longitudinal sections of nerve guide region tissue were collected after 8 weeks for histological analysis of the cellular infiltration. Sections were stained using Masson's trichrome to visualize collagenous connective tissue (blue), cell cytoplasm (pink) and nuclei (dark red). Myelination properties were characterized using standard staining of mid-graft nerve cross sections with toluidine blue to stain the myelin for characterization of myelin thickness and for assistance in counting myelinated axon density.

5.3 Results and Discussion

5.3.1 Gradient formation in collagen hydrogel fiber sheets

Establishment of gradients in aligned collagen fiber sheets (Fig. 5.5) were tested by making steep and shallow FITC-lysozyme gradients over 6 hours. Fluorescence microscopy shows that this process was able to successfully generate gradients with different properties when source and sink wells were loaded with differing concentrations of FITC-lysozyme (Fig. 5.6). As the testing of gradient formation using a modification of the original Krick diffusible system was successful, gradients were prepared using GDNF for implantation in nerve guides.

5.3.2 Examination of explanted nerve guides following 8 and 12 weeks implantation

Fibrin fiber containing groups showed a high degree of variability in tissue thickness along the nerve guide (Fig. 5.7). Some regions were particularly narrow to the point of pinching off the potential avenue for cellular migration across the gap. In these cases, little sign of the PGS braided tube still remains after 8 weeks. This is surprising as there were no issues with catastrophic degradation in the earlier preliminary study using PGS braided tubes in chapter 4. It is possible that a higher magnitude inflammatory response caused by contamination of fibrin fiber containing groups accelerated the degradation of the PGS coating and PGA braided tube due to increased hydrolysis of the ester linkage in the PGS backbone caused by an decrease in the local microenvironment pH due to the increased inflammatory response allowing the PGA to be more readily degradable. While there were several regions of very narrow tissue, others were swollen much beyond the expected nerve diameter seen in other groups. In these cases, there was prominent incidence of yellow discoloration throughout the vicinity of the nerve guide with particularly high amounts in the lumen region of the NGC. This severely inhibited the ingrowth of neuronal cells through the nerve guide, resulting in no successful functional recovery being detected by electrophysiological analysis and severe levels of atrophy seen of the gastrocnemius muscle compared to the non-operative positive control side in all fibrin fiber containing groups.

Based on the extra swelling seen in the fibrin containing nerve guide groups and the extensive yellow discoloration, it appears that the groups were contaminated at some point prior to implantation. To test this, a repeat of fibrin containing groups was run for 8 weeks after additional sterilization using Co60. Unfortunately, these results will not be completed prior to submission of this dissertation. Once results are known, it should be better clarified if the issue had been due to contamination causing infection or if the discoloration is due massive fibrosis caused by fibrin fibers degrading too slowly and inducing a large fibrotic graft versus host response that blocks the pathway to the distal nerve stump. This swelling response and discoloration was seen in all groups containing fibrin filaments regardless of the GDNF loading conditions.

Gross examination of the PGS groups lacking fibrin filaments appear to be much better. Tissue structure is more uniform in diameter, particularly in the region of the PGS braided tube. There is some buildup of connective tissue at the distal nerve stump which is consistent with what was seen in the previous nerve guide study of Chapter 4 (Fig. 5.8). Both of these groups show significant reduction in the yellow discoloration seen with the fibrin fiber filament groups. PGS tubes in both the unloaded collagen fiber sheet and empty lumen groups showed lower degrees of degradation compared to the fibrin filament containing groups.

5.3.3 Gait analysis results after 8 weeks implantation

SFI data are plotted for all groups in (Fig. 5.9). There is a clear drop in all groups during the first week after sciatic nerve removal and replacement with nerve guides or autograft. Improvements in SFI are seen at each time point compared to the previous for all groups. All groups showed similar levels of recovery to the autograft, a surprising result given that the electrophysiological data from CMAP measurements were so poor after 8 weeks in fibrin containing groups and the atrophy was so significant in these groups. By 8 weeks, SFI had recovered to values between -65 and -55 for all groups, but results were not different enough to conclude that there was any difference between groups for SFI recovery.

5.3.4 Histological analysis of explanted nerve tissue after 8 weeks NGC implantation

Figure 5.10 shows a longitudinal section taken from the steep GDNF gradient and no GDNF groups, containing fibrin filaments within the PGS coated PGA braided tube. A large clump of material is seen in the median section of the nerve graft that correlates with the bulging seen with the gross histological examination. There seems to be two separate regions of cellular behavior in this case, where broken up material is seen on the proximal side (left) compared to a large collagen positive stained clump on the distal (right) portion of the median region. It is very likely that the collagen positive region is the collagen sheet that has been compressed, either through the action of cellular traction or compression during initial loading. The fragmented region is likely the remains of the fibrin fibers, particularly if these were separated from the collagen sheet during loading as this material would be expected to degrade much more rapidly than the collagen once implanted.

The entire bulge region shows significant incidence of fibrosis surrounding the material clump in the median region. The precise cause of this incidence of fibrosis is unknown at this time as it could be the result of several potential causes. The high fibrosis seen could be a result of the host response to the potential contamination of the nerve guides. This will be better understood once the small repeat 8 week group is completed following Co60 irradiation to re-sterilize the samples. Should high fibrosis still remain present after the additional sterilization, the source of fibrosis would likely be a result of either extended persistence of fibrin filaments or host response to the xenograft materials used in the study. While it looks like fibrin fibers are possibly degraded in this histological slice, more slices will need to be analyzed to determine if this behavior is seen in other samples and to compare other timepoints to better see the persistence of fibrin filaments within the nerve guides at 4 and 12 weeks. The distal side of this slice shows higher incidence of scar tissue formation compared to the proximal end as seen by the higher levels of blue staining. This is consistent with our previous study using PGS coated PGA nerve guides, where distal ends were generally larger than the proximal end when gross histological analysis was performed. Cellular infiltration into the never guide looked very good until reaching the electrospun hydrogel fiber materials, which effectively acted as a plug preventing connection of the cellular ingrowth to the distal end.

Toludine blue stained cross sections (Fig. 5.11) show some shrinkage of the PGS coating only group nerve guide, which is somewhat unexpected given the results of the study from Chapter 4. It is possible that the coating of this batch degraded more rapidly or was thinner, causing the PGA braids to be exposed more rapidly and enabling the nerve guide to be susceptible to compressive forces. The unloaded collagen fiber sheet group shows no distinguishable region of collagen that lack cellular infiltration meaning that the density of collagen fiber sheets were low enough to enable cellular migration through the material. High magnification images of the cross sections (Fig. 5.12) show thicker myelin sheaths in the autograft, as seen in the previous study. The two nerve guide groups show similar myelin thicknesses with the collagen fiber sheet group having slightly higher density of myelinated axons measured (Fig. 5.13).

5.4 Conclusions

While it is unfortunate that the potential contamination or graft versus host response to fibrin filaments led to the loss of potential data demonstrating the effectiveness of GDNF uniform and gradient loading in collagen fiber sheets, this study has still been able to demonstrate that aligned electrospun collagen sheets do not prevent cellular migration through the material. This is important in that future studies can focus on usage of only the collagen sheets for loading and exclude the fibrin filaments. While fibrin filaments may potentially be able to improve nerve regeneration by providing rapidly degradable topographical cues, which would open up porosity for axonal growth cone infiltration to chase Schwann cells, the high labor cost of generating the discrete fibrin filaments and increased complexity of nerve guide preparation are not worth the effort. It is also important to consider that while topographical alignment cues from nanofibers have improved nerve regeneration, such nanofibers are able to present thousands of aligned pathways for directing cells, which is significantly higher than the filament loading level that can reasonably be achieved with fibrin filaments. A better potential method for incorporating 3D fiber guidance cues for Schwann cells may lie back in the beginning with the use of alginate fibers that have cell adhesive cues such as RGD conjugated to the polymer backbone since the alginate fibers form discrete micron-scale fibers when hydrated. Ultimately, the best near term strategy for using electrospun hydrogel fibers in nerve regeneration would be expected to be usage of only collagen fiber sheets with more controlled methods of gradient formation with a protective outer nerve guide such as the PGS coated PGA braids, which proved to be valuable in both nerve guide studies for improving nerve regeneration.

5.5 Figures

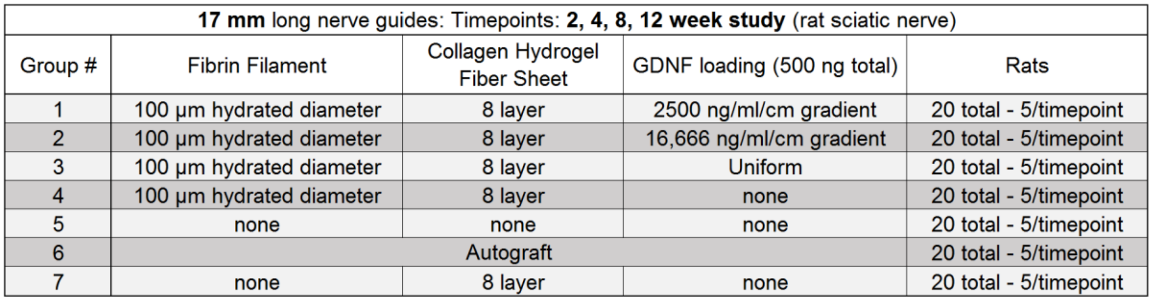

17 mm long nerve guides: Timepoints: **2, 4, 8, 12 week study** (rat sciatic nerve)

Group #	Fibrin Filament	Collagen Hydrogel Fiber Sheet	GDNF loading (500 ng total)	Rats
1	100 μm hydrated diameter	8 layer	2500 ng/ml/cm gradient	20 total - 5/timepoint
2	100 μm hydrated diameter	8 layer	16,666 ng/ml/cm gradient	20 total - 5/timepoint
3	100 μm hydrated diameter	8 layer	Uniform	20 total - 5/timepoint
4	100 μm hydrated diameter	8 layer	none	20 total - 5/timepoint
5	none	none	none	20 total - 5/timepoint
6	Autograft			20 total - 5/timepoint
7	none	8 layer	none	20 total - 5/timepoint

Figure 5-1: SYSU *in vivo* rat sciatic nerve defect animal study groups. Nerve guide conduit configurations are assembled to investigate the effect gradient steepness on regenerative outcome (G1 vs G2) and as compared to (G3) to characterize any impact the "candy store" effect might have on regeneration and if it can be avoided using gradient presentation of GDNF. Group 4 serves as an unloaded control to assess fiber addition alone. Group 5 serves as an empty nerve guide control and for comparison with the nerve guide studies of Chapter 4 and the autograft serves as an additional control. Group 7 tests the effect that addition of fibrin filaments might have on regeneration compared to collagen sheets alone (G7 vs. G4).

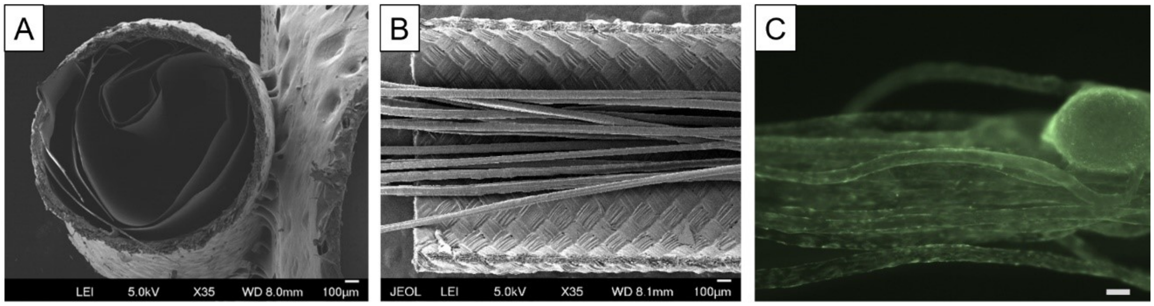

Figure 5-2: Loading of PGS coated braids with hydrogel fibers. Aligned collagen fiber sheet fills lumen of PGS coated braid and maintains open space interior to the sheets (a). Fibrin fibers provide longitudinal topographical guidance cues (b). Cellular outgrowth from DRG explant after 7 days culture shows migration of cells along rehydrated fiber bundles (c, scale bar: 150 µm).

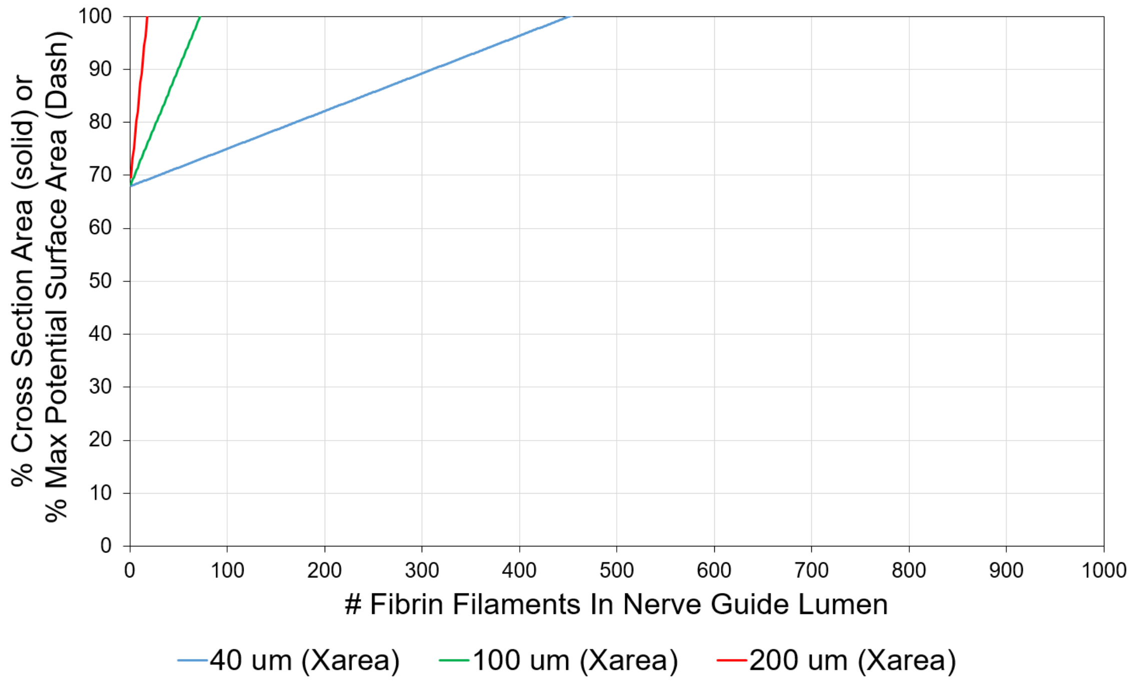

Figure 5-3: Fill density of lumen cross section as a function of fibrin filament loading level for 40, 100, and 200 µm hydrated fibrin filaments. Collagen sheets take up approximately 70% of internal cross-sectional space within nerve guide, leaving 30% for fibrin fiber filaments. As fiber filaments increase in diameter, maximum number of filaments possible to load in lumen are decreased (solid lines). Green lines indicate fibrin filament diameters used in NGC study, showing a maximum possible filament loading level of 73 filaments before all the space in nerve guide is occupied.

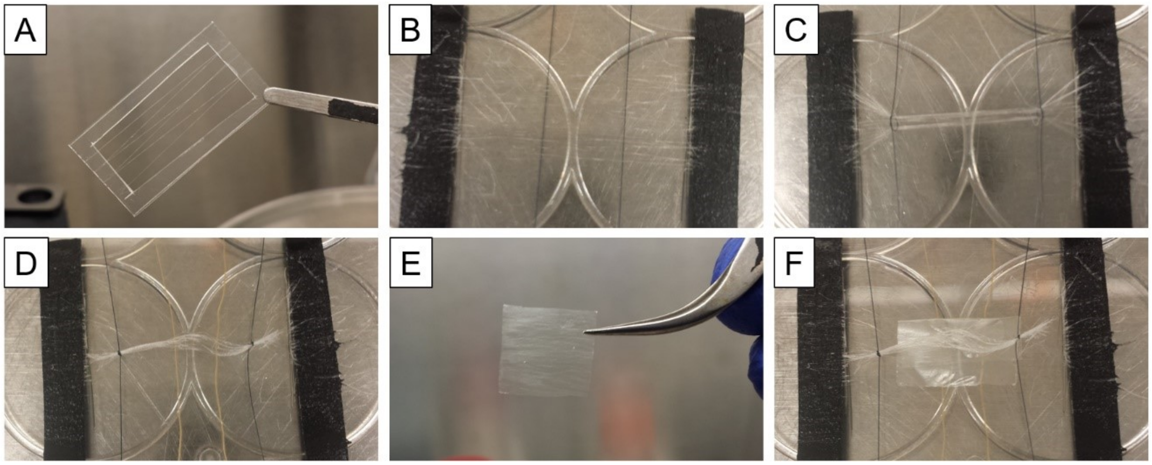

Figure 5-4a: Preparation of fibrin-collagen hydrogel fiber nerve guide. Nerve guide preparation. Fibrin fibers are spun for 1 min at 3.25 ml/hr flow rate and collected on 3 cm × 1.5 cm plastic frame, keeping 6-10 fibers separated from each other during wrapping and drying (a). Two suture guidelines (black) are taped down perpendicular to direction of fibrin filaments. Fibrin filament ends are pressed down from frame onto dual sided adhesive tape and detached from frame, repeat until 60 fibers have been laid down (b). Fibrin fiber bundle ends are tied together using sutures (c). Two (or three) secondary plain gut sutures are placed underneath bundles approximately 1/3 (and 1/2) the distance interior to the two suture ends (d). Air-dried collagen hydrogel fiber sheet (unloaded or GDNF loaded) (e) is placed underneath fibrin filament bundle (f).

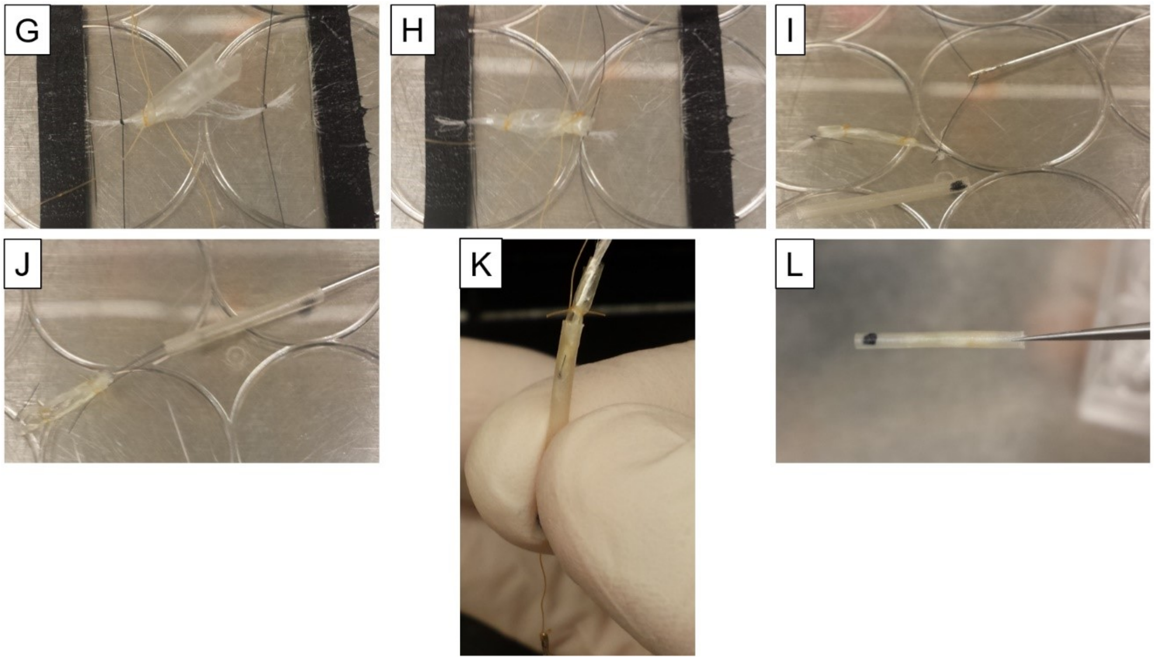

Figure 5-4b: Preparation of fibrin-collagen hydrogel fiber nerve guide. Nerve guide preparation. One end of collagen fiber sheet is carefully tied with plain gut suture, ensuring that fibrin filaments on that end are captured within the collagen wrap (g). Opposite end of collagen fiber sheet is tied (h). Excess suture is threaded through eye of sewing needle (i) and needle is drawn through PGS coated PGA braided tube (j). Sheet is carefully positioned into lumen of coated braid, ethanol can be used as a lubricant if needed, (k) and drawn through to form completed nerve guide (l).

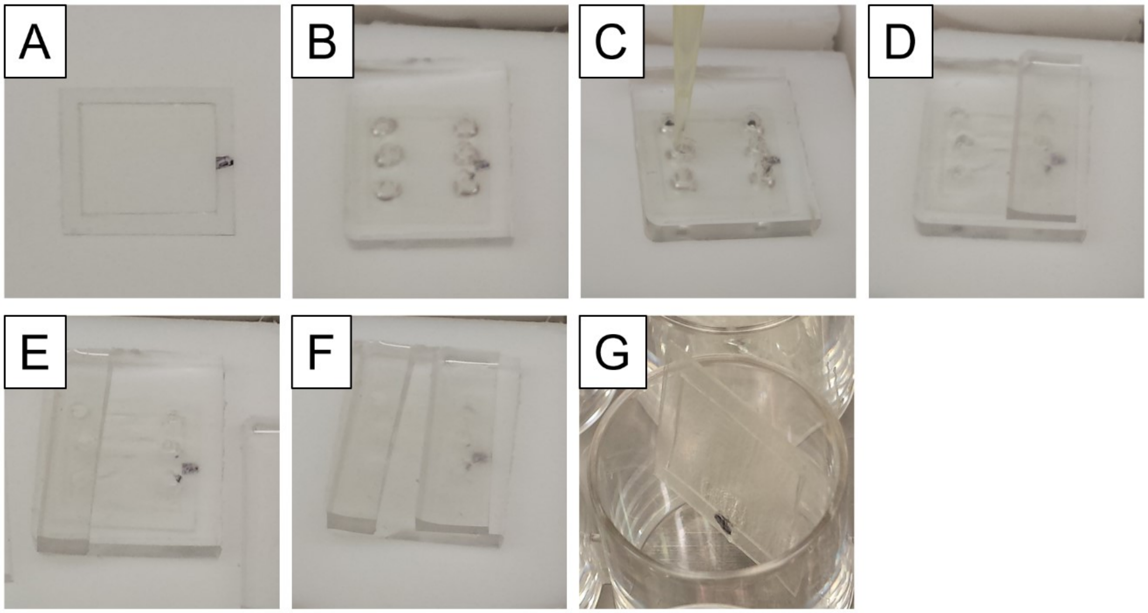

Figure 5-5: Diffusible gradient generation in collagen sheets utilizing modified Krick method. Diffusible gradients are prepared by placing dried collagen fiber sheets on Teflon surface (a). PDMS mold with triple set of 3 mm punch channels (yields ~2 mm diameter hole) is placed over top of collagen sheet frame (b) and sheets are rehydrated by pipetting 10 µl of DI water into each well (c). Cover placed over high concentration source wells and 10 µl of low concentration factor is pipetted into each of the three sink wells (d). Sink wells are covered and 10 µl of high concentration solution is added to each source well (e). Both source and sink wells are covered and samples are placed in 4°C for six hours to establish gradient (f, Fig. 5-6). PDMS covers and mold are removed and sheets are air dried while held vertical in 24-multiwell plate (g) and then loaded into nerve guides once dry.

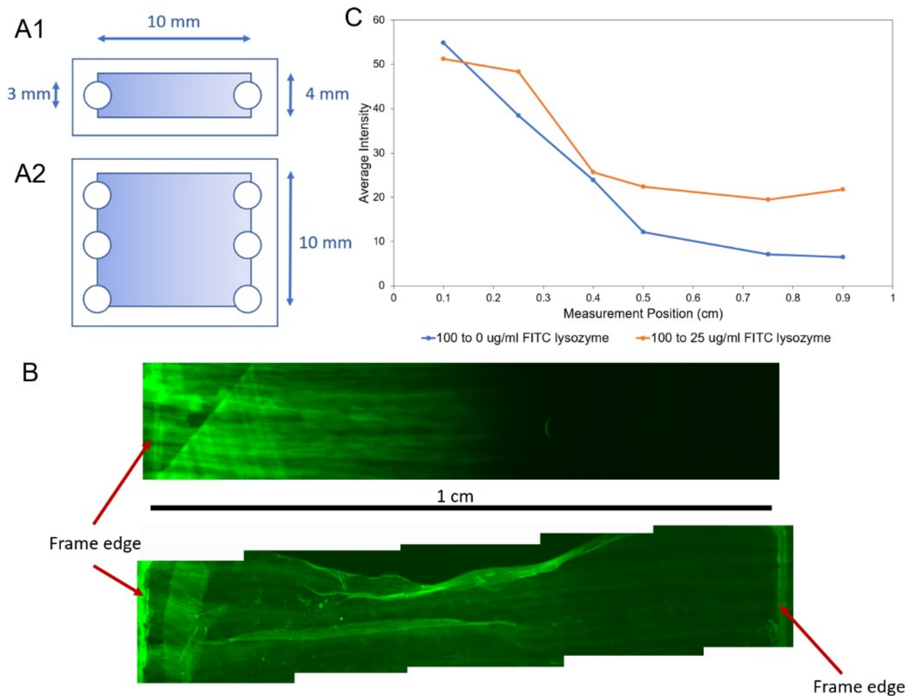

Figure 5-6: Testing of diffusible gradient generation in collagen fiber sheets using FITC-lysozyme and Krick method. Previous design from thesis of Dr. Kellin Krick was based on a 4 mm x 10 mm channel with single pair of source and sink drains for forming diffusible gradients (a1). Modification of this concept to incorporate the 1 cm x 1 cm collagen sheets was done by introducing two additional source and sink drains on either side of the PDMS mold used for gradient (a2). Through addition of 10 µl of 100 µg/ml FITC-lysozyme in each source drain and 10 µl of 0 or 25 µg/ml FITC-lysozyme to each sink drain, gradient parameters could be controlled to generate different gradient steepness visualized with fluorescence microscope images (b) and plotted as intensity versus position across the gradient (c).

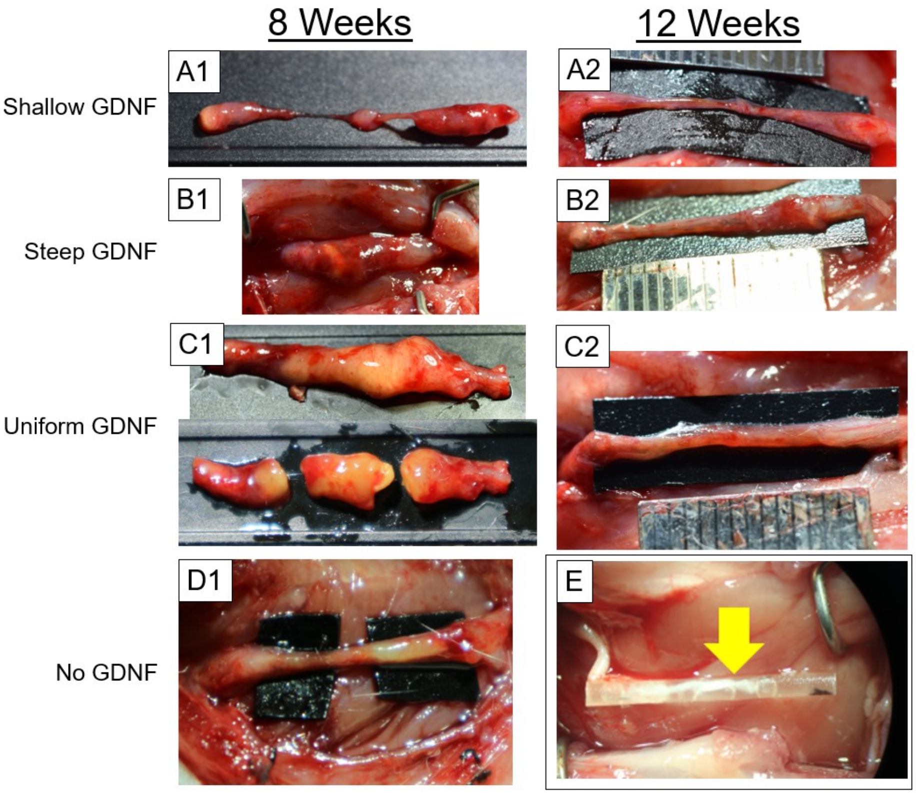

Figure 5-7: Gross histological examination of fibrin filament containing groups after 8 and 12 weeks. All fibrin filament containing groups showed extensive signs of either graft versus host response or contamination as indicated by the high prevalence of yellow infected tissue (c1). The elevated inflammatory response caused a significant increase in PGS braid degradation rate (a1, a2) when compared with initially implanted PGS braid (e). Samples at the 12-week time point looked slightly better (a2, b2, c2), possibly indicating that 8-week fibrin filaments were contaminated while 12-week were not. Distal end on right in all images.

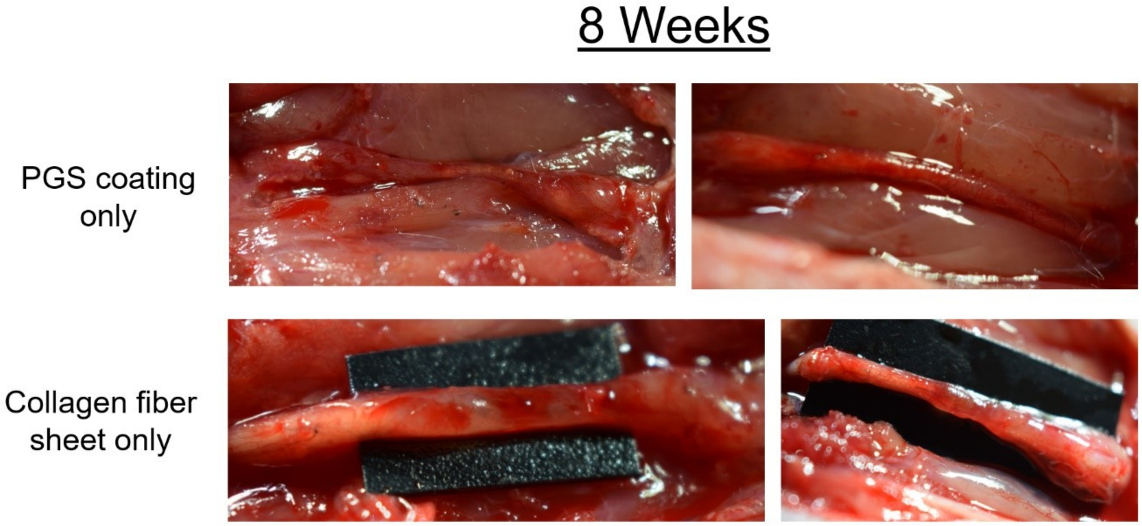

Figure 5-8: Gross histological examination of PGS coating only and unloaded collagen sheet only groups after 8 weeks. Unlike fibrin filament containing groups, the NGCs containing no filler or having only unloaded collagen fiber sheets did not show signs of infection or excessive inflammatory response after 8 weeks. Distal end on right in all images.

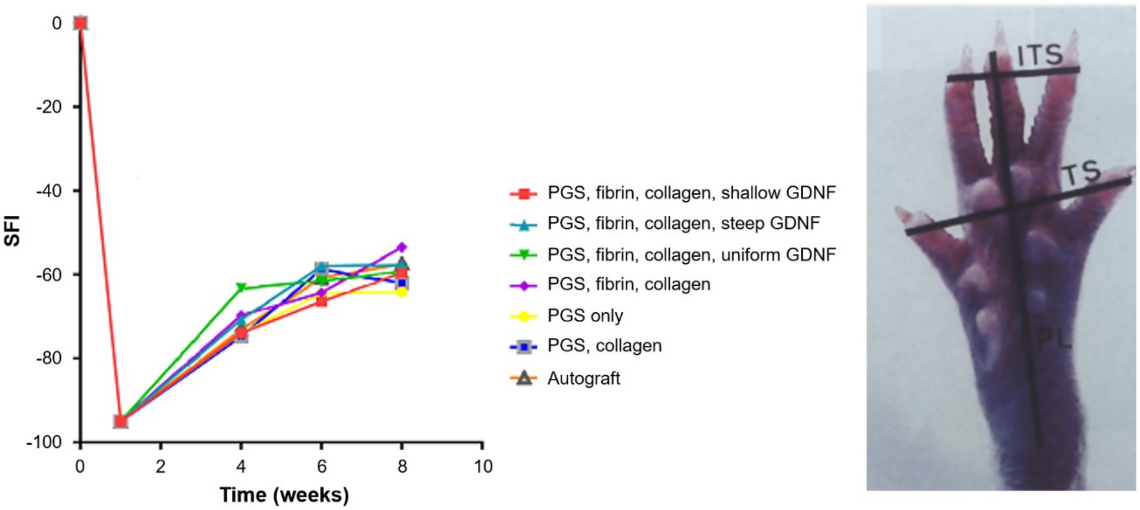

Figure 5-9: Sciatic functional index (SFI) results after 8 weeks NGC implantation. SFI results after 8 weeks (n = 4 per group) show little difference between nerve guide groups and autograft.

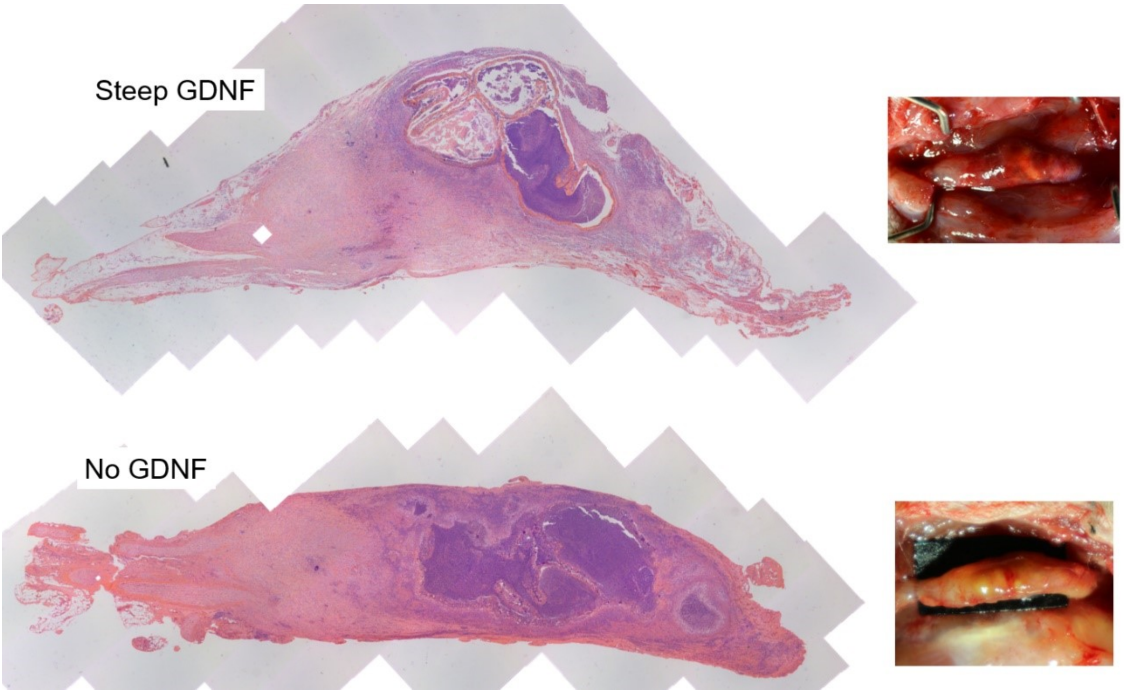

Figure 5-10: Longitudinal sections of steep GDNF and no GDNF groups stained with Masson's Trichrome after 8 weeks. Both of these fibrin filament groups show a highly collagenous clumping of material that is likely part of the massive inflammation or infection seen in these groups in the 8-week time point. The steep GDNF group (top) shows a region of broken material that may be the result of fibrin filaments degrading.

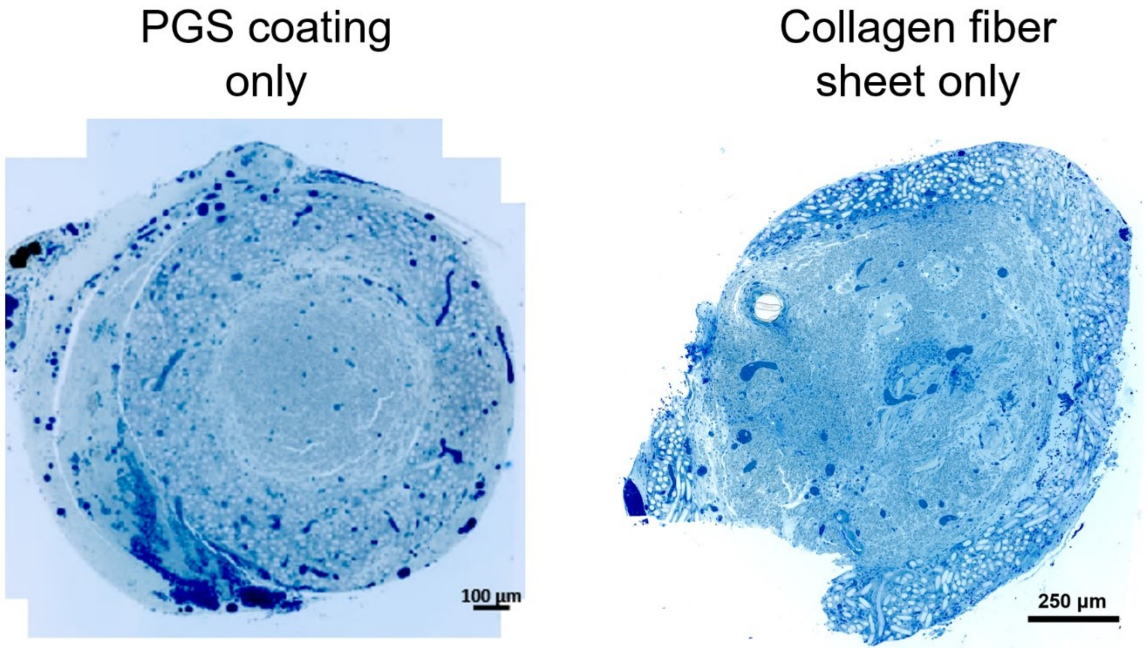

Figure 5-11: Toludine blue stained whole cross sections of PGS coating only and collagen fiber sheet only groups mid-graft after 8 weeks. PGS coating only group (left) shows some shrinkage compared to the collagen fiber sheet group. This shrinkage was not seen in the previous Secant study so it is possible that the batch of PGS used in this study more rapidly degraded, allowing the PGA braid to compress. Collagen fiber sheet only group shows no discrete regions lacking cellular infiltration, demonstrating that cells are able to successfully migrate through the collagen sheets.

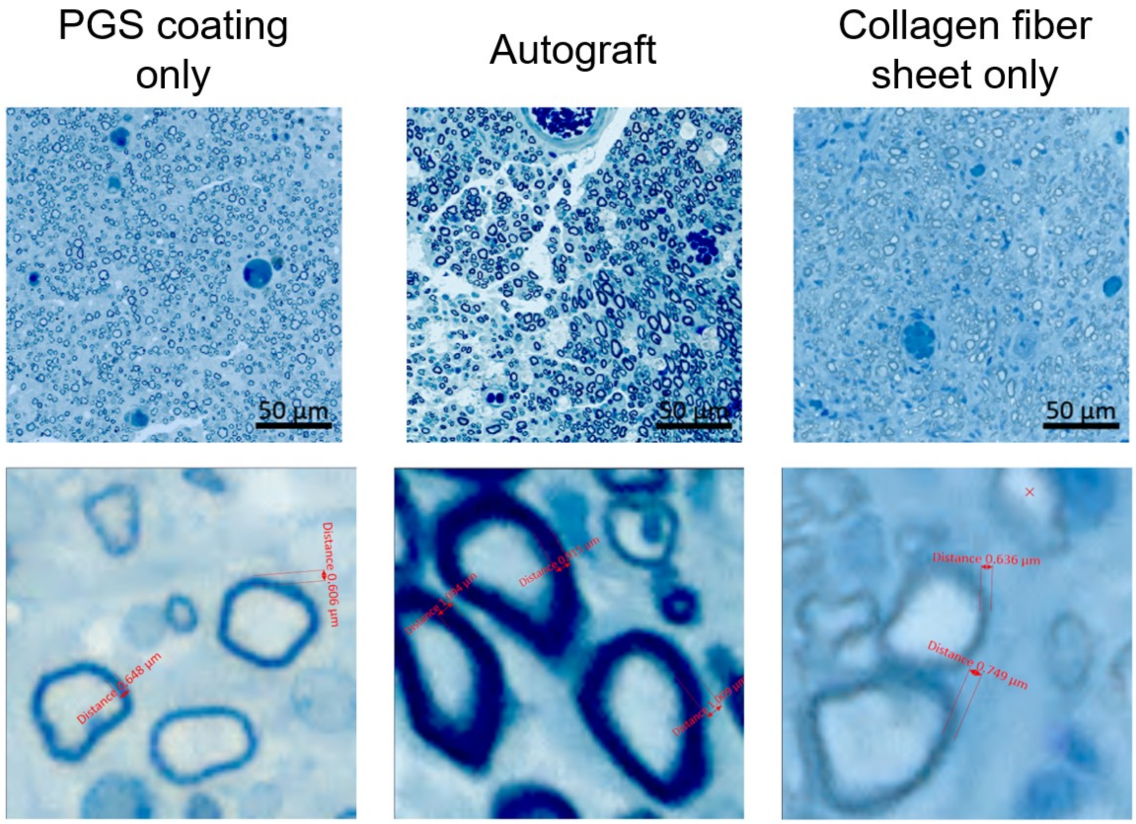

Figure 5-12: High magnification images of myelinated axons in PGS coating only, autograft, and collagen fiber sheet only groups after 8 weeks. Myelination quality looks similar between the two nerve guide groups (bottom) and there is a good distribution of myelinated axons throughout the ROI. The autograft shows thicker myelin formation than the nerve guide groups, which is consistent with the previous Secant study results of Chapter 4.

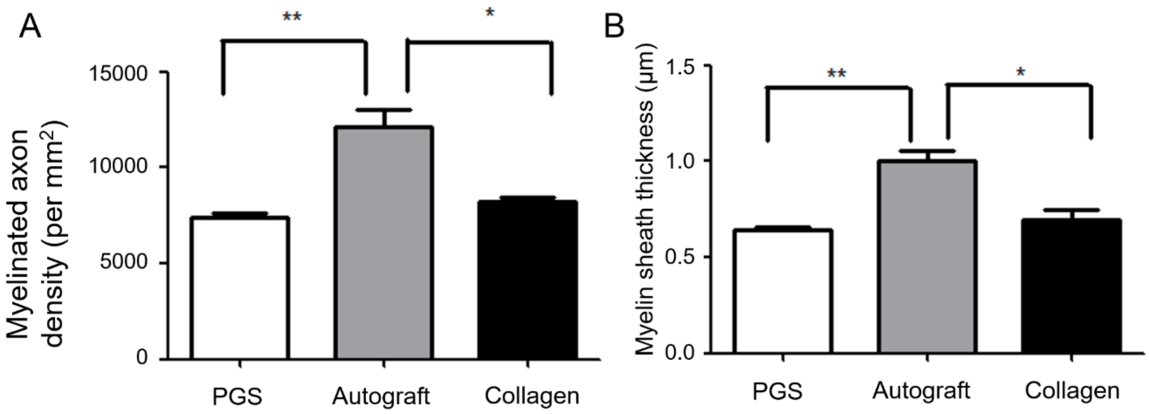

Figure 5-13: Myelinated axon density and myelin sheath thickness for unfilled PGS coated PGA braid, autograft, and collagen fiber sheet only groups after 8 weeks. Autograft highest density of myelinated axons per unit area from histological analysis of mid-graft cross sections stained with toluidine blue (a) while collagen fiber sheet containing groups show a small increase in myelinated axon density compared to the empty PGS coated braid. Myelin sheath thickness showed a similar trend (b).

5.6 References

1. Tannemaat MR, et al., *Differential effects of lentiviral vector-mediated overexpression of nerve growth factor and glial cell line-derived neurotrophic factor on regenerating sensory and motor axons in the transected peripheral nerve.* in *Eur J Neurosci*. 2008. p. 1467–1479.
2. Akassoglou K, et al., *Fibrin inhibits peripheral nerve remyelination by regulating Schwann cell differentiation.* in *Neuron.* 2002. p. 861–875.
3. Akassoglou K, et al., *Fibrin is a regulator of Schwann cell migration after sciatic nerve injury in mice.* in *Neurosci Lett.* 2003. p. 185–188.
4. Navaei-Nigjeh M, et al., *Enhancing neuronal growth from human endometrial stem cells derived neuron-like cells in three-dimensional fibrin gel for nerve tissue engineering: 3D Culture Of Hescs-Derived Neurons in Fibrin Gel.* in *J Biomed Mater Res A.* 2014. p. 2533–2543.
5. Wood MD, et al., *Fibrin gels containing GDNF microspheres increase axonal regeneration after delayed peripheral nerve repair.* in *Regen Med.* 2013. p. 27–37.
6. Pettersson J, et al., *Biodegradable fibrin conduit promotes long-term regeneration after peripheral nerve injury in adult rats.* in *J Plast Reconstr Aesthet Surg.* 2010. p. 1893–1899.
7. Koulaxouzidis G, et al., *Fibrin glue repair leads to enhanced axonal elongation during early peripheral nerve regeneration in an in vivo mouse model.* in *Naural Regen Res.* 2015. p. 1166–1171.
8. Ma S, et al., *Sciatic nerve regeneration using a nerve growth factor-containing fibrin glue membrane.* in *Neural Regen Res.* 2013. p. 3416–3422.
9. Kalbermatten D, et al., *New fibrin conduit for peripheral nerve repair.* in *J Reconstr Microsurg.* 2009. p. 27–33.
10. Kempton LB, et al., *Assessment of Axonal Growth into Collagen Nerve Guides Containing VEGF-Transfected Stem Cells in Matrigel.* in *Anat Rec Adv Integr Anat Evol Biol.* 2009. p. 214–224.
11. Matsumoto K, et al., *Peripheral nerve regeneration across an 80-mm gap bridged by a polyglycolic acid (PGA)–collagen tube filled with laminin-coated collagen fibers: a histological and electrophysiological evaluation of regenerated nerves.* in *Brain Res.* 2000. p. 315–328.
12. Yoshii S and Oka M. *Collagen filaments as a scaffold for nerve regeneration.* in *J Biomed Mater Res.* 2001. p. 400–405.
13. Xiao W, et al., *Rapid sciatic nerve regeneration of rats by a surface modified collagen–chitosan scaffold.* in *Injury.* 2013. p. 941–946.
14. Dienstknecht T, et al., *Type I Collagen Nerve Conduits for Median Nerve Repairs in the Forearm.* in *J Hand Surg.* 2013. p. 1119–1124.
15. Li S-T, et al., *Peripheral nerve repair with collagen conduits.* in *Clin Mater.* 1992. p. 195–200.

16. Bozkurt A, et al., *The role of microstructured and interconnected pore channels in a collagen-based nerve guide on axonal regeneration in peripheral nerves.* in in *Biomaterials.* 2012. p. 1363–1375.
17. Madduri S, et al., *Collagen nerve conduits releasing the neurotrophic factors GDNF and NGF.* in *J Controlled Release.* 2010. p. 168–174.
18. Seidi A, et al., *Gradient biomaterials for soft-to-hard interface tissue engineering.* in *Acta Biomater.* 2011. p. 1441–1451.
19. Burdick JA, et al., *Fabrication of Gradient Hydrogels Using a Microfluidics/Photopolymerization Process.* in *Langmuir.* 2004. p. 5153–5156.

Curriculum Vitae

Brian Patrick Ginn
Born December 3rd, 1985 in South Bend, IN

EDUCATION

Ph.D., Materials Science and Engineering
Johns Hopkins University
Baltimore, Maryland, USA
August 2017
GPA 3.9/4.0

Bachelor of Science, Materials Science and Engineering
Purdue University, West Lafayette, IN
May 2008

PUBLISHED WORK

- "The development of hydrogel microfiber scaffolds for peripheral nerve repair" Ph.D. dissertation submitted August 2017
- "Fabrication of 3-dimensional multicellular microvascular structures" Barreto-Ortiz S.F., Fradkin J., Eoh J., Trivero J., Davenport M., **Ginn B.**, Mao H.Q., Gerecht S. *FASEB,* 2015; 29(8): p. 3302-3314
- "Creating polymer hydrogel microfibres with internal alignment via electrical and mechanical stretching" Zhang S., Liu X,. Barreto-Ortiz S.F., **Ginn B.P.**, DeSantis N.A., Hutton D.L., Grayson W.L., Cui F.Z., Korgel B.A., Gerecht S., Mao H.Q. *Biomaterials*, 2014; 35(10): p. 3243-3251
- "A novel in vitro model for microvasculature reveals regulation of circumferential ECM organization by curvature" Barreto-Ortiz S.F., Zhang S., Davenport M., Fradkin J., **Ginn B.**, Mao H.Q., Gerecht S. *PLoS One,* 2013; 8(11): e81061
- "Characterization of a novel bioreactor system for 3D cellular mechanobiology studies" Cook C.A., Huri P.Y., **Ginn B.P.**, Gilbert-Honick J., Somers S.M., Temple J.P., Mao H.Q., Grayson W.L. *Biotechnology and Bioengineering*, 2016; 113(8): p. 3250-3259

- "Untitled implantable cardiac patch paper" Morrissette-McAlmon J., **Ginn B.P.**, Somers S., Mao H.Q., Grayson W.L., et al.. Under preparation
- "Untitled implantable vascular graft paper" Elliot M., **Ginn B.P**., Fukunishi T., Hibino N., Mao H.Q., Gerecht S. et al., Under preparation
- "Untitled fibrin scaffold backing for 3D printed cardiac tissue" Fukunishi T., Ong C.S., Zhang H., **Ginn B.P**., Mao H.Q., Hibino N., Under preparation
- "PGS coated PGA nerve guides regeneration paper" **Ginn B.P.**, Liu H., Lu S., Mi R., Haris J.J., Hoke A., Mao H.Q., Under preparation

PATENTS

Under Review:

- US20150118195 "Electro-Mechanically Stretched Micro Fibers and Methods of Use Thereof" Shuming Zhang, Hai-Quan Mao, Xi Liu, **Brian Patrick Ginn**

Pending Publication Number:

- "Engineering amniotic membrane composite for soft tissue repair" Huanhuan Liu, Hai-Quan Mao, Juan Wu, **Brian Ginn**
- "Hollow, Perfusable Small-Diameter Tissue Engineered Vascular Grafts" Morgan Elliot, Sharon Gerecht, **Brian Ginn,** Sebastian Barreto-Ortiz, Hai-Quan Mao

SKILLS AND TRAINING

- Design and production of biomaterial hydrogel scaffolds for tissue engineering applications including nerve, cardiac, muscle, vascular, ocular, and drug delivery
- Design and management of animal studies for both domestic and international collaborations
- Isolation and culture of mammalian cells including human, rodent, and stem cells
- Microscopy including use of fluorescence, confocal, and scanning electron microscopes
- Development of electrospun fiber materials including synthetic polymers and hydrogel fibers

- Directed undergraduate student researchers
- Interfacing and operation of industry-academic collaborations
- Experienced with analytical techniques including plate readers, ELISA, DSC, FTIR, X-ray diffractometry, compositional analysis using electron dispersive spectroscopy, mechanical testing using DMA or Instron tensile tester, calcium and pH probes, metallurgical sample preparation
- Training in clean room procedures and aseptic technique for biosafety cabinets
- Computer experience with Microsoft Office Suite, Zotero reference software, ImageJ, LabChart reader, ZEN microscopy software, CorelDraw

PRIOR PROFESSIONAL EXPERIENCE

Johns Hopkins University, Baltimore, MD, August 2011 – July 2017

Johns Hopkins University is one of the world leading universities in biomedical research and development. The close ties between the Johns Hopkins Hospital and University provides unique opportunities to push forward medical technology with emphasis on clinically translatable research through direct interaction with academic researchers and active clinicians.

Ph.D. Student

- Thesis research focused on development of novel aligned hydrogel microfiber electrospinning process using primarily biologically derived materials for use as 3D tissue engineering scaffolds
- Member of JHU Translational Tissue Engineering Center and Institute for NanoBiotechnology
- Generated fibrin fiber scaffolds with topographical guidance cues and mechanical properties matching native heart myocardium
- Developed peripheral nerve guides utilizing aligned fibrin and collagen hydrogel fiber and poly(glycerol sebacate) coatings of braided PGA tubes in collaboration with the Secant Group, LLC.

- Designed peripheral nerve guide animal studies for repair of rat sciatic nerve defects at Johns Hopkins and for international collaboration with Sun Yat-sen University, Guangzhou, China
- Created aligned transparent collagen electrospun fiber sheets for backing of amniotic membranes for use in ocular repair
- Engineered 0.6 mm ID perfusable hollow vascular grafts composed of longitudinally aligned and/or circumferentially aligned fibrin fibers
- Developed hydrogel fiber electrospinning protocols for fibrin, alginate, collagen, hyaluronic acid, gelatin, synthetics such as PLGA and PCL, and blends of these materials
- Engineered 3D PLGA microfiber bundle structure for bridging spinal cord injury gaps
- Created aligned alginate fiber wound dressings for use as a growth factor releasing platform during liver regeneration
- Presented work at internal and external conferences including INBT Symposia and Society for Biomaterials
- Wrote Research Strategy section of NIH RO1 grant for peripheral nerve regeneration
- Mentored three undergraduate students, one master's student, and three Baltimore inner city high school students during summer research program
- Lead teaching assistant for Biomaterials I upper level undergraduate class; supervised team of three other teaching assistants, lead office hours, organized gradebook, grading of exams and homework, and taught lectures during primary instructor travel

DEPUY SYNTHES, Warsaw, IN, October 2009 – August 2011

DePuy Synthes is focused on development of orthopaedic implants for hip, knee, and other skeletal injuries through metal-on-metal and metal-on-poly implants. Development at the time was being made on improving osseointegration through development and preparation of FDA resubmissions for revision products.

R&D Engineer I

- Developed next generation hydroxyapatite coatings through development of solution deposition process to replace existing plasma spray technologies
- Involved in scale up process of solution deposition hydroxyapatite from bench scale to pilot scale
- Analyzed HA, TCP, OCP, and other calcium phosphate coatings for structure and composition using SEM, EDS, FTIR
- Collaborated with University of Notre Dame, South Bend, IN to characterize coating compositional changes in cross section as a function of thickness using focused ion beam milling
- Optimized Kokubo treatment conditions for etching Ti-6Al-4V coupons and hip stems
- Revised existing protocols for environmental stability testing of CaP coatings
- Followed ASTM standards (C633) for testing of HA coating adhesive strength
- Responsible for dissolution and Ksp portions of CORAIL$^{®}$ Revision FDA submission
- Developed protocols for production of pure octacalcium phosphate (OCP) powders for powder diffraction XRD analysis
- Worked with outside consultants to develop computational models of CaP reactor solution flow dynamics